The impact of supernova feedback on the evolution of the ISM

Anabele-Linda Pardi

München

The impact of supernova feedback on the evolution of the ISM

Anabele-Linda Pardi

Dissertation
an der Fakultät für Physik
der Ludwig–Maximilians–Universität
München

vorgelegt von
Anabele-Linda Pardi
aus Baia-Mare, Romania

München, den 24. Februar 2017

Erstgutachter: Prof. Dr. Simon White
Zweitgutachter: Prof. Dr. Andreas Burkert
Tag der mündlichen Prüfung: März 30, 2017

Contents

List of Figures

List of Tables

Zusammenfassung

In dieser Arbeit wird die Entstehung und Vernichtung von molekularem Wasserstoff im turbulenten, magnetisierten, aus mehreren Phasen bestehenden interstellarem Medium (ISM) untersucht. Der Einfluss von stellaren Rückkopplungsprozessen auf die Entwicklung des ISM wird mit Hilfe von Simulationen in periodischen Boxen mit einer Ausdehnung von $(256\ \mathrm{pc})^3$ sowie mit Hilfe von teilweise periodischen, getreckten Boxen als Teil einer galaktischen Scheibe mit einer Größen von $0.5{\times}0.5{\times}{\pm}5\ \mathrm{kpc}^3$ inspiziert. Dazu wurde der drei-dimensionale adaptive Gittercode FLASH 4 verwendet. In den Simulationen sind Eigengravitation, Magnetfelder, Supernovae und chemische Prozesse der Spezies H^+, H, H_2, C^+ und CO berücksichtigt.

Der erste Teil der Arbeit behandelt die Entstehung von molekularem Wasserstoff und die Skalierung des Magnetfeldes mit der Dichte für verschiendene Magnetfeldanfangsbedingungen von 0, 6×10^{-3}, 0.3 und 3 μG. Das Gas wird duch Supernovae mit konstanter Explosionsrate getrieben. Je stärker das anfängliche Magnetfeld ist, desto homogener ist die Dichte- und Temperaturverteilung und desto geringer der Massenanteil an molekularem Gas.

Wir erweitern die Studie um die Korrelation zwischen den Supernova-Positionen und den Molekülwolken. Wir variieren den Anteil der Supernovae, die in dichtem Gas stattfinden, und der Anteil derer, die sich von der ursprünglichen Molekülwolke entfernen. Dieser Teil, bei dem Anfangsdichte und Supernova-Rate variiert werdem, beinhaltet ebenfalls Eigengravitation und Magnetfelder. Die Ergebnisse zeigen dass der Anteil der Sterne, die in dichten Regionen als Supernova explodieren, großen Einfluss auf die Struktur im ISM haben, in dem sie den Anteil des molekularen Wasserstoffes sowie den Volumenanteil heißen Gases reduzieren. Kleine Variationen der Supernovae in dichtem Gas erzeugen deutliche Unterschiede in der chemischen und thermischen Struktur. Diese Unterschiede hängen von den anderen Parameten wie der Magnetisierung, von Eigengravitation und der Supernova-Rate ab.

Im letzten Teil wird eine selbstkonsistente, variierende Supernova-Rate im Gegensatz zur konstanten Rate der vorherigen Kapitel verwendet, um die Entwicklung im ISM unter Berücksichtigung von Magnetfeldern, Eigengravitation und einem galaktischen Potential zu untersuchen. Es wird ein Schmidt-ähnliches Sternentstehungsmodell, wie es in vielen kosmologischen Simulationen zum Einsatz kommt, getestet. Es stellt sich heraus, dass bei der derzeitigen Implementierung die Kühlzeit der Supernova-Region kürzer als das Achtfache der Schalllaufzeit durch dieselbe Region ist, was in anderen Studien als Minimum

angegeben ist. Dieses Verhalten ist wichtig, da zwar in einigen Fällen Sternentstehungsraten erzielt werden, die mit der beobachteten Kennicutt-Schmidt-Relation übereinstimmen, in diesen Rechnungen jedoch kein heißes Gas erzeugt wird. Es werden Dichtegrenzwerte abgeleitet, für die die Injektion der Supernova-Energie bei einer gegebenen numerischen Auflösung sicherstellt, dass die Supernova expandieren kann, bevor die Energie weggekühlt wird. Es werden zwei mögliche Lösungsvorschläge für das Kühlproblem diskutiert. Zum einen können in einer realistischeren ISM-Implementierung massive OB-Sterne mit unterschiedlichen Lebenszeiten, die als Supernovae explodieren, aus den dichten Wolken herauswandern. Zum anderen kann in der Region, in der die Supernova injiziert wird, ein turbulentes Dichtefeld gesetzt werden, das durch die nicht aufgelösten Rückkopplungseffekte der Sterne hervorgerufen wird.

Abstract

The aim of this thesis is to investigate the formation and destruction of molecular gas as a component of the turbulent, multiphase, magnetised interstellar medium (ISM). In the pursuit of a better understanding of the impact of stellar feedback has on the evolution of the ISM, we use simulations of $(256\ \mathrm{pc})^3$ periodic boxes and $0.5\times0.5\times\pm5\ \mathrm{kpc}^3$ stratified disk slabs modelling local parts of the Galactic disk with the Eulerian, adaptive mesh refinement (AMR), three dimensional, magnetohydrodynamic code FLASH 4. The simulations include self-gravity, magnetic fields, supernova (SN) explosions and a chemical network following H^+, H, H_2, C^+ and CO.

The first part of the thesis focuses on the H_2 molecule formation and density-magnetic field scaling for various initial magnetic field strengths (0, 6×10^{-3}, 0.3, 3 μG) in an environment stirred by randomly placed SNe with a fixed rate. We find that with increasing initial field strengths the simulations develop an ISM with a more homogeneous density/temperature structure and with a decreasing H_2 mass fraction.

We extend this study to include SNe spatial correlated with their parental molecular clouds (MCs). With the intension to create a more realistic model, we vary the fraction of SNe exploding in peak density regions and the ones traveling away from the MCs. We include self-gravity, magnetic fields and also vary the initial gas density and the SN rate. Our results show that the fraction of SNe exploding in their natal MC have a significant impact on the structure of the ISM by reducing the H_2 mass fraction and the volume filling fraction of the hot gas up to an order of magnitude. Small variations of certain percentages of SN going off in MCs (depending on the magnetisation of the environment, on self-gravity and the SN rate) create dramatic transitions in the temperature and chemical structure of ISM.

The last part of the thesis is dedicated to the study of the self-consistent SN-driven ISM evolution (a more realistic implementation than the fixed SN rate) with an extended simulation volume, including magnetic fields, self-gravity and the Galactic potential. We test the Schmidt-type star formation recipe extensively used in cosmological simulations and we find that the current implementation does not meet the criterion that the cooling time of the supernova remnants (SNRs) should be at least eight times longer than the sound-crossing time. This is an important issue as some of the simulations produce star formation surface densities comparable to the Kennicutt-Schmidt law but fail to produce a hot phase. We also derive recommended densities for the injection regions that ensure that for a given resolution and star formation efficiency, the SNRs expand before they radiate

all their energy away. For practical reasons, we also put forward two potential solutions for the over-cooling problem like to model a more realistic ISM taking into account that a certain fraction of the massive OB stars travel away from their natal MCs and that they have different lifetimes or to introduce a turbulent field in the injection region that will rearrange the density structure due to stellar feedback mechanisms that cannot be resolved.

Chapter 1

Introduction

1.1 Star formation efficiency

Stars formation is a hot topic in contemporary astrophysics. Understanding the processes that transform gas into stars is the focus of substantial theoretical, observational and computational efforts, especially due to the link between star formation and galaxy formation and evolution. There are numerous unanswered questions about star formation (SF): When does it occur? What are the underlying physical processes and how is it related to the properties of galaxies? As Kennicutt phrased it in 1989 (Kennicutt, 1989): "An important problem in galactic structure and evolution is the relationship between the large-scale star formation rate (SFR) and the physical properties of the interstellar gas". Despite significant work over the decades in understanding this connection (in terms of observations, analytic modelling and simulations), it still remains a puzzle. The main reason is the complexity of the matter involved and the requirement to cover physical processes over a wide range of scales, densities and temperatures. This thesis contributes a few findings to this intricate picture.

An extensive number of simulations either include or were specifically developed to tackle challenges like the large variety of physical processes, or the temporal and spatial scales of star formation regulation and stellar feedback (for complete reviews see Dale, 2015; Naab and Ostriker, 2016). Cosmological-scale simulations treat star formation in different ways (by making the connection between star formation and local density thresholds or the molecular gas fraction, etc.) mainly because the star formation process cannot be resolved directly. The resolution of galactic-scale simulations allow the cold, dense gas (the site of star formation) to be resolved but not the detailed process of star formation itself. The same applies to simulations of vertical slabs of galactic disks (parsec-scale), although these can address more accurately physical processes like stellar turbulence, stellar feedback (including ionising radiation), and magnetic fields, and can also follow the chemical composition of the interstellar medium. Subparsec simulations ($\sim$ 0.1 pc) have the necessary resolution to capture the collapsing filaments and stellar cluster formation but they can address the fragmentation of the molecular filamentary structures only locally.

The interstellar medium (ISM, "the interstellar gas") is the scene for most of the mechanisms and the locus of star formation. This environment encompasses all the gas, the radiation and magnetic field, cosmic rays, etc. that can be found between the stars. Stars themselves play an important role since they have a constant massive impact on their surroundings during their lifespans through stellar feedback: protostellar jets, stellar winds and supernova explosions, and are thus crucial components in the gas cycle of a galaxy. Picture 1.1 depicts the cycle of interstellar matter in a galaxy. Stars form in giant molecular clouds (GMCs, the coldest and densest places in the galactic disk), they evolve, and through feedback, disrupt their parental molecular clouds (MCs), ionising them. The dispersed gas, now ionised or warm and neutral, cools and forms neutral hydrogen clouds which, when compressed, cause another MC to form. All these steps involve numerous physical processes occurring at various scales. In this work, after a short introduction to the generalities about the ISM and a few of its main components, I will present numerical simulations of a few hundreds of parsecs in scale, run in order to study the turbulent, multiphased, magnetised, SN-driven ISM. The aim of this study is to understand the impact of magnetic fields, self-gravity and SN feedback on the formation and destruction of molecular gas. In Chapter 3 we explore how magnetic fields alter the formation of molecular gas in the ISM. In Chapter 4, we extend this study to examine how the positioning of the SNe impacts molecular gas formation and in the last chapter, we improve the accuracy of the SN feedback implementation by studying a self-consistently driven, Schmidt-type ISM.

1.2 The interstellar medium (ISM)

Early discoveries about the local ISM included the dust clouds scattering the light of stars in their vicinity and the fact that most of the ISM consists of atomic hydrogen. However, one of the most important advances in the field was the idea that there is a direct connection between the ISM and the stars of a galaxy and that they evolve together, as a whole (Burbidge et al., 1957).

In the ISM, stars are born, they evolve and during their lifetimes a fraction of their mass is returned to their surroundings. This recycling process is illustrated in Fig. 1.1. Cores of GMCs collapse under the influence of gravity and form stars, usually in star clusters. Some stars evolve in their own cluster and can, through stellar feedback mechanisms like jets, winds and supernova explosions, disrupt the MC they formed in. Other stars can be ejected from their cluster through various processes and end up traveling hundreds (or even thousands) of parsecs (pc) away from their parental cloud (discussed in more details in Section 1.5). In any case, stars have a crucial impact on the environment surrounding them whether they heat, sweep up the gas or compress it.

The ISM as a whole is composed of a wide range of temperature and density components, including low density, hot, completely ionised gas ($T \sim 10^6$ K), cooler and denser partially ionised gas ($T \sim 10^4$ K), neutral hydrogen (H) regions ($T \sim 100$ K) and molecular hydrogen (H_2) gas ($T \sim 10$ K). A summary of the properties of these ISM components can be found in Table 1.1.

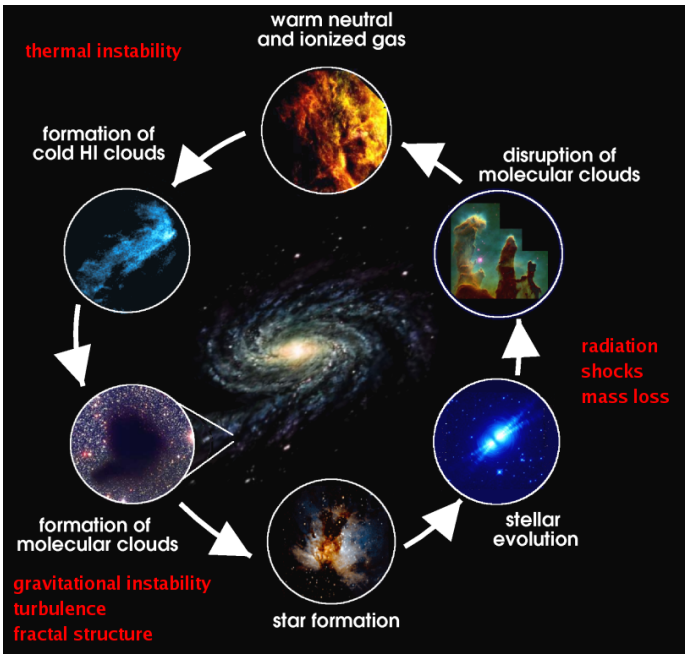

Figure 1.1: The life cycle of interstellar matter. Credit: the HEAT team (the High Elevation Antarctic Terahertz telescope).

Phase	H state	n [cm^{-3}]	T [K]	h [pc]	VFF [%]	mf [%]
Hot ionised medium (HIM)	H^+	10^{-3}-10^{-2}	10^5-10^7	> 1000	50	<1
Warm ionised medium (WIM)	H^+	0.1	∼8000	∼900	20	10
Warm neutral medium (WNM)	H	0.1-0.5	5500-8500	∼400	30	30
Cold neutral medium (CNM)	H	4-80	50-20	∼140	2-4	40
Molecular medium (MM)	H_2	100-10^5	<50	∼70	<1	20

Table 1.1: List of ISM phases and properties. From left to right: the name and the abreviation of the medium, the typical density, temperature, scale-height, the volume filling fraction (VFF) and the mass fraction (mf).

Due to the complex interaction between the different phases, the stellar feedback and the rest of the ISM, and because of the wide range of densities, temperatures and spatial scales, there is also a wide range of techniques needed to observe the different phases. The hot ionised medium (HIM) has scales above 1 kpc (roughly between 1.5 and 5 kpc) (Ferrière, 2001) and is believed to be created mainly by stellar feedback, especially SN explosions and shocks driven by stellar winds. It is a very hot environment but due to its low typical density ($10^{-3} - 10^{-2}$ cm^{-3}), even though it has a large volume filling fraction (VFF, $\sim 50\%$), its mass fraction (mf) is below 1%. The HIM emits in the X-ray and UV wave ranges.

The warm ionised medium (WIM) consists of ionised gas observed in Hα and microwave emission. It has a lower scale-height than the HIM, lower temperatures and an order of magnitude higher densities. Because the ionised gas is concentrated mainly around massive young OB-type stars (hot and luminous main-sequence stars with typical temperatures above 10^4 K (B) and 3×10^4 K (O) organised in clusters called "OB associations" containing 10-100 stars), it is believed that the radiation from the stars penetrates through the dense environment in the immediate vicinity and escapes into the warm neutral medium (WNM), ionising it. However, there is no clear consensus on the possible heating sources responsible for this (Osterbrock and Bochkarev, 1989; Reynolds et al., 1999).

While the warm neutral medium (WNM) is a diffuse component (with a typical number density of 0.1-0.5 cm^{-3}) and a large VFF (30%), the cold neutral medium (CNM) has much larger densities (up to 80 cm^{-3}) and is organised in compact clouds (with a much lower VFF, 4%). The CNM also makes up for most of the hydrogen mass in the ISM. The WNM and CNM can be observed in radio 21-cm emission (Giovanelli and Haynes, 2016; Alfvin et al., 2016).

1.3 Molecular clouds - cradles of star formation

Molecular clouds are the densest regions of the ISM, being mainly confined to the centre of the galactic disk (see Fig. 1.2). Their typical temperatures are about 30 K, their dimensions between 1 and 200 pc and their masses also vary from a few solar masses ($M_\odot$, $\sim 2\times10^{33}$g) up to 10^6 $M_\odot$. H_2 formation happens on the surface of dust grains because the H_2 molecules, when formed through H-H collision, are unable to efficiently radiate away their binding energy before the molecule dissociates. Dust grains mediate this process by absorbing the extra energy. Interstellar dust, besides being a catalyst for H_2 formation, is also involved in absorbing (and re-emitting) light at different frequencies up to an estimated 30% of all starlight in the Universe (Bernstein et al., 2002). Dust grains typically have dimensions of the order of microns (Weingartner and Draine, 2001) although their whole mass only amounts to about 1% of the total atomic hydrogen mass.

Due to its symmetry and lack of a permanent dipole field the H_2 molecules are difficult to detect. Observations of MCs use tracer molecules like carbon monoxide CO (2.6 mm), hydrogen cyanide HCN or C^+ ions depending on the situation. The most widely used tracer is CO as its low energy rotation transitions allow the probing of regions with temperatures

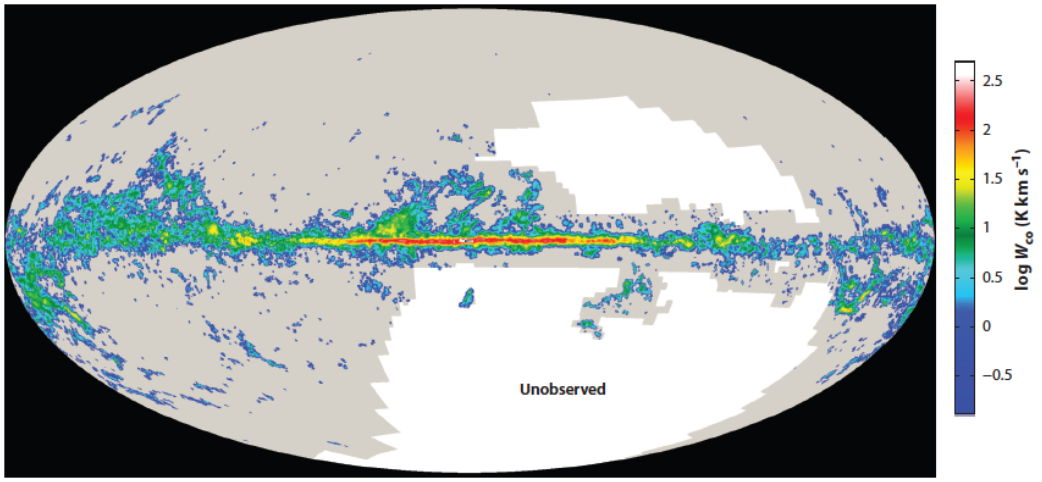

Figure 1.2: An image of ^{12}CO J=1-0 emission (at the transition from the first to the basic rotational state) constructed from the Centre of Astrophysics campaign to examine the high-latitude sky survey of Dame et al. (2001) and Mizuno and Fukui (2004). Image taken from Heyer and Dame (2015).

between 5 and 22 K. Figure 1.2 is an image of CO emission showing that the molecular hydrogen is mainly concentrated in a thin disk in the mid-plane of our galaxy.

MCs have irregular shapes - they can be filamentary in structure and contain self-gravitating, clumpy, dense cores. The densest molecular cores with typical dimensions of a few parsecs and densities above 10^5 cm^{-3} are the sites for star formation, also known as "protostellar disks". This is the first step of star formation in the ISM matter cycle, depicted in Fig. 1.1. Understanding the efficiency with which the molecular gas turns into stars is a complex multi-scale problem. The subject of this thesis is the study of the lifecycle of molecular gas in the ISM and the impact of SN feedback and magnetic fields on it.

1.4 Other components and important properties

Apart from the different components of the ISM described in the previous section, there is also the interstellar radiation field, which encompasses the UV and X-ray radiation from gas at $T > 10^5$ K, IR and far-IR emission from dust, emission from ionised gas at $T \sim 10^4$ K, cosmic microwave background (CMB) radiation, synchrotron emission from cosmic rays (CRs) and magnetic fields (described in detail in Section 1.6.3).

There are several important heating mechanisms in the ISM. One of the main ones is **photoelectric heating**. In the WNM and CNM, the electrons are stripped from dust grains and heat up the environment through collisions. They are produced through the photoelectric effect when the incident radiation (mid/far UV) hits the dust grains. The dis-

sociation of H_2 molecules by **UV radiation** is much more efficient at higher densities than photoelectric heating. It produces H atoms energetic enough to heat up the surrounding medium; however, the dissociation rate is relatively low, at only 15% (Draine and Bertoldi, 1996). Most of the time, the electrons are only excited to higher energy states and through relaxation they emit IR photons which have the ability to heat up the surrounding gas (collisional de-excitation). This process is also known as "UV pumping". **X-ray photons** can cause a chain of ionising events when absorbed by atoms and molecules and expel free electrons that can further ionise the surrounding medium; however, they are absorbed before reaching deep into the MCs.

At even higher densities, characteristic of the deep interior of MCs where shielding is efficient, **CRs** are the most efficient heating mechanism. They can ionise H atoms and H_2 molecules, which can further ionise the gas. Due to the enormous energy of the CR particles, they can travel long distances on galactic and intergalactic scales. Another heating mechanism is **chemical reactions** like the formation of H_2 from two H atoms, which is efficient in high density gas. The rotational/vibrational states the H_2 molecules are in immediately after formation can, via collisions, transfer energy to the environment. For more details on the heating mechanisms see Klessen and Glover (2016) and for details on modelling see Section 2.2.

The heating mechanisms are balanced out by radiative (involving photon emission) and adiabatic cooling. If we assume an optically thin regime with no chemical reactions happening, cooling just includes collisional excitation, de-excitation and spontaneous emission. **Collisional excitation and de-excitation** involves changes in the energy states of atoms and molecules; excited electrons cascade back to lower energy states by emitting photons that escape the environment. In the cold regions, cooling is dominated by the collisional excitation of C^+, the ground state of which has the fine structure transition ${}^2P_{1/2} - {}^2P_{3/2}$, which emits a far-IR 158 μm photon. There are also a multitude of species contributing to cooling as the temperature of the ISM rises (see Fig. B.3). The cooling rates in this regime (including the CNM) are sensitive to the electron fraction of the environment, decreasing over an order of magnitude for the electron fraction varying between 10^{-1} and 10^{-4}. At temperatures of about 1000 K, slightly higher than the typical temperatures of the WNM, the cooling is dominated by the Lymanα transition, causing a strong rise in the cooling rate. At higher temperatures, metal-ion collisions come into play at around 10^5 K, as hydrogen is becoming ionised. At about 10^7 K, the cooling rate starts to rise again due to free-free cooling.

The Generalised Loss Function ($\mathcal{L}$) is a function of the density (n) and temperature (T) of the gas and can be written as

$$\mathcal{L} = n^2\Lambda(T) - n\mathcal{H} \begin{cases} > 0 & \text{net cooling,} \\ < 0 & \text{net heating,} \\ = 0 & \text{equilibrium.} \end{cases}$$

where $\mathrm{n}^2\Lambda(T)$ is the cooling rate per unit volume and $\mathrm{n}\mathcal{H}$ is the heating rate per unit volume. The function $\Lambda(T)/T = \mathcal{H}/nT$ is visualised in Fig. 1.4 as a function of tempera-

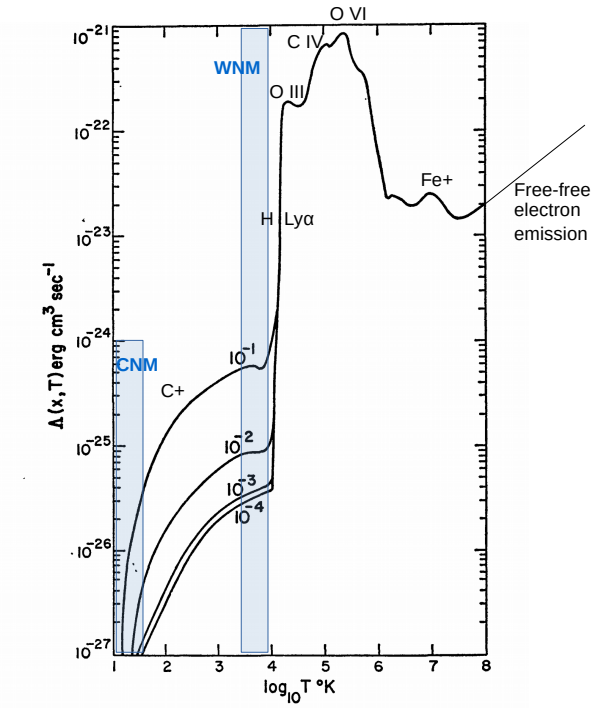

Figure 1.3: The ISM cooling function for various values of fractional ionisation. This plot is an adaptation of the original in Draine (1978), extended to include free-free electron emission, and to mark the CNM and WNM and add extra labels for C^+, Lyman α, etc.

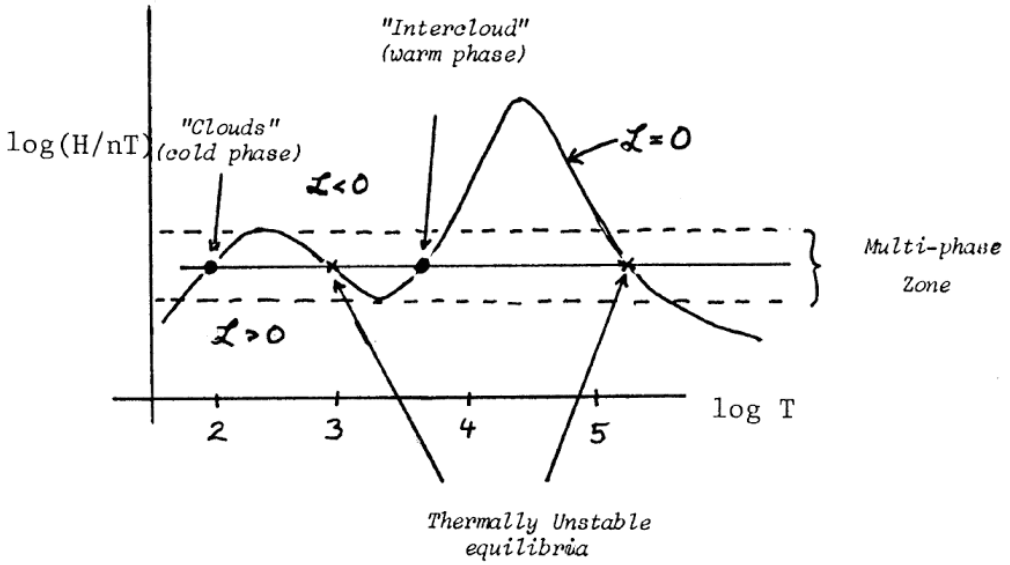

Figure 1.4: Equilibrium solutions for the interstellar gas with a constant heating rate $\mathcal{H}$ and constant pressure. Taken from Hollenbach and Thronson (1986).

ture. Here heating is balanced out by cooling, with the regions above the curve providing net heating and below the curve net cooling. There are four equilibrium solutions shown, two thermally stable (bullets) in the CNM and WNM and two thermally unstable (stars). The gas in the thermally unstable gas can be heated or cooled down rapidly by only small perturbations in density or temperature.

The two-phased ISM structure described above (the CNM and WNM coexisting in pressure equilibrium) was first suggested and described analytically at the end of the '60s (see e.g. Field et al., 1969; Goldsmith et al., 1969) and subsequently extended to encompass a third "hot" phase. The third phase with $T > 10^6$ K and low density (~ 0.002 cm^{-3}) is composed of overlapping SN bubbles, filling most of the volume of the ISM (McKee and Ostriker, 1977).

1.5 Runaway stars

Stars can be observed in the galactic halo, up to 100 kpc from the Galactic plane centre. We give a classification according to their peculiar velocities (motion relative to the Galactic rest frame). In order to provide a more accurate image of the typical distances and the parts of the Galaxy these stars escape from, Fig. 1.5 illustrates a schematic view of the Milky Way including the Galactic Centre (GC), the bulge, the Galactic disk and the Solar neighbourhood.

- Stars in general have velocity dispersions of ~ 3 km/s, due to turbulence in their parental MC. In Chapter 3 and 4 we will refer to them as "walkaway stars".

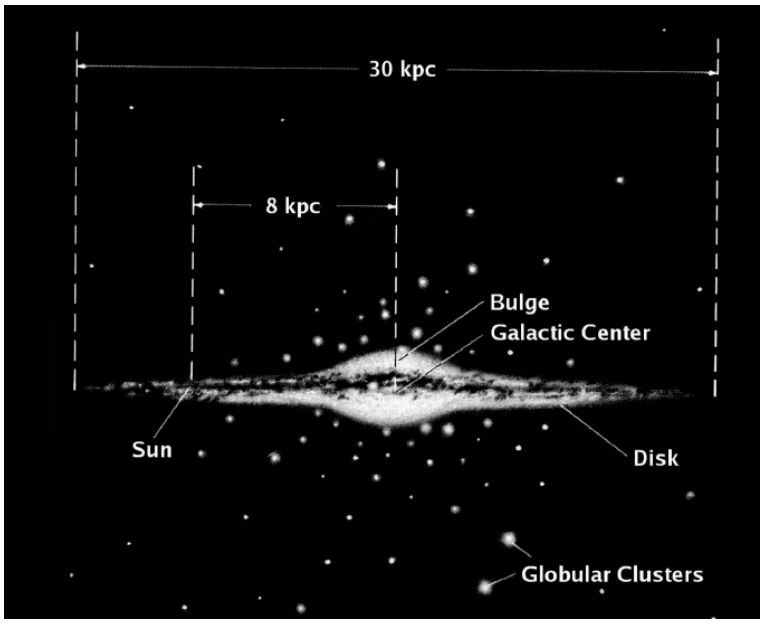

Figure 1.5: The Milky Way: schematic edge-on view. Credit: Freedman and Kaufmann (2008).

- Runaway stars (RAS) can be massive OB stars with peculiar velocity > 40 km/s (Oort, 1928; Blaauw, 1961) or high-speed low-mass stars with velocities comparable to the galactic escape velocity of 533 ± 54 km/s, at a radial distance of $R = 10$ kpc (Kenyon et al., 2014; Piffl et al., 2014).

- Hypervelocity stars (HVS) have peculiar velocities larger than 1000 km/s, which are close to the effective escape velocity at $R = 10$ pc, see Hills (1988). They are fast rotator stars with masses between 2.5 and 4 $M_\odot$ and are believed to be ejected from the Galactic Centre Black Hole (Hills, 1988). For a detailed description see Brown (2015).

- Semi-relativistic hypervelocity stars (SRHs) have peculiar velocities of about 10,000 km/s (Guillochon and Loeb, 2015).

There are several ejection mechanisms (stellar binary disruption scenarios) predicting different ejection velocities for stars (Silva and Napiwotzki, 2011). Here we present only the three most important ones[1].

[1]We also mention the following ejection mechanisms without a detailed description: (i) the binary-binary interaction, (ii) SN explosions that occur in the GC and can contribute to the number of HVS but can only induce relatively low ejection velocities, (iii) AGN jet interactions with individual stars.

1.5.1 SN mechanism or binary ejection mechanism (BEM)

The SN-induced binary disruptions scenario (Blaauw, 1961) assumes mass transfer/accretion (in the context of the single degenerate model). The ejection velocities are between 14-850 km/s, depending on a series of factors: the mass of the white dwarf (WD), the mass of the RAS and the orbital radius of the binary. For models and predictions about the largest ejection velocities (up to 1000 km/s) see Wang and Han (2009, 2010); Geier et al. (2015).

As most of the observed WD have masses lower than the Chandrasekhar limit (1.4 $M_{\odot}$), the accretion scenario must be true (single degenerate scenario). Two WD in a binary system can either merge and explode as a Type Ia (with no survivor companion) or accrete from one another and produce a survivor companion or a RAS. There are serious efforts in trying to find the surviving companion in Type Ia SN remnants (Marietta et al., 2000; Pakmor et al., 2008; Kerzendorf et al., 2009), in their bow-shocks, knowing that only very few cases would obliterate the WD in the SN explosion. However, recent binary population simulations show that about 70% of all close binaries produce RAS (Sana et al., 2012).

There are several ways to determine if a star is a surviving companion or not (see e.g. Marietta et al., 2000; Kasen and Ramirez-Ruiz, 2010; Garcia-Senz et al., 2012; Rimoldi et al., 2016), especially if the star is found in the remnant of a SN having either an unusual velocity (Han, 2008; Tauris, 2015), an unusual rotation due to tidal lock, or unusual brightness (which is sign of rejuvenation). However, it is remarkably hard to identify survivors of BEM observationally.

1.5.2 Dynamical ejection mechanisms (DEM)

RAS are usually OB stars and the RAS fraction increases with mass (the more massive stars have a higher chance of being RAS). We are particularly interested in this RAS subgroup and ejection mechanism and we model it in Chapters 3 and 4. Stars are born in star clusters where they can have many companions. Once they are identified as RAS, they can be traced back to their MC of origin from where one can deduce what caused the scattering of the star or of the binary.

There are massive stars with huge velocities traveling away from very young star clusters, so young that the SN scenario becomes unlikely. The most violent interaction between stars in a star cluster happens during the collapse of the cluster core. In the cluster, the most massive stars sink to the centre, a mechanism called "dynamical friction" (see Portegies Zwart et al., 2004), and the low mass stars are pushed to the outskirts. This is the core collapse state of the stellar cluster. During this phase, many binaries form, especially at the centre of the cluster where massive stars will pair up.

The dynamical ejection mechanism (DEM) was first put forward by Poveda et al. (1967), and it is currently believed that it is the main producer of the massive OB runaway stars observed. One can also compare the cluster core stellar population to the RAS population mass function. The RAS mass function is assumed to trace the mass function of the core

population, but still, it is a challenge to determine their birthplace.

1.5.3 The Hills mechanism

The Hills mechanism is the interaction of a star in a binary system with a black hole (BH) or a supermassive black hole (SMBH, Hills, 1988). This mechanism includes various possibilities: a binary system interacting with a BH, a BH binary interacting with a star, usually producing a HVS with an ejection velocity up to 1500 km/s (see Yu and Tremaine, 2003; Gualandris et al., 2005; Bromley et al., 2006; Kenyon et al., 2008), and a few more [2]. The estimated ejection rates are about $5\times\ 10^{-7}$/yr and at the moment there is no direct evidence for the BH origin theory. Any other property of HVSs apart from their velocities is hard to observe. However, their study is important as they link the outer part of the MW with the GC, probing the mass function, binary fraction and metallicity of the GC stellar population.

Due to their supposed origin, the HVS can help probe the Galactic potential (e.g. through changes in their trajectories). The largest deceleration the HVS would experience is in the central 200 pc region, see Kenyon et al. (2008). Only low mass stars can reach the galactic halo (due to their long lifespans) but massive HVS can become rejuvenated on the way through interactions with other stars (because unlike low mass HVS, massive HVSs are slowed down more efficiently).

1.5.4 Observations

RAS have a low likelihood of being observed in the solar neighbourhood, which represents an observational obstacle, and the volume that surveys should aim for to cover them has not yet been reached (there are $\sim$ 1000 RAS predicted within 1 kpc outside the solar neighbourhood). The observed RAS distribution can reflect their origin; however, the RAS and HVS distribution partially overlap. Yet, there are several useful observational constrains for identifying RAS: their number, rotation, trajectory (Brown, 2015), abundance pattern (Przybilla et al., 2008), stellar age, flight time and metallicity.

Further simulations of the RAS population, focusing on distinguishing characteristics produced in dynamical interactions in star clusters or type II SN disruptions through α element pollution (in the case of the SN disruption scenario) show that, in general, the kinematic properties of the released RAS are not sufficient to settle for one of the two competing mechanisms, BEM or DEM. α element pollution refers to finding traces of heavy chemical elements (up to iron) synthesised in massive stars through the capture of α particles (helium nuclei), before the type II SN explosion. Among recent observations we mention **ND 271791** (Schaffenroth et al., 2015), an observed HVS with a Galactic rest-frame velocity of 725 $\pm$ 195 km/s with traces of α elements (an indication that it was produced by the SN mechanism); **HIP 13962** (Tetzlaff et al., 2014), a binary supernova

[2](i) ejection by a binary SMBH system involving one star and one SMBH (in this case the ejection velocity of the star is $\sim$ 2000 km/s, independent of its mass) and (ii) ejection by a stellar mass BH involving the scattering of a stellar mass BH (see O'Leary and Loeb, 2008).

ejection candidate; **30 Doradus** (part of the VLT-FLAMES Tarantula survey), one of the most massive, young, active star forming regions in the local universe that can be resolved well enough to see the individual stars (Howarth et al., 2015; Ramirez-Agudelo et al., 2017).

Another way of identifying RAS is through their bow shocks, caused by the interaction of the star's wind with the ISM. For a bow shock to form, supersonic flows are required. They have an impact on the chemical enrichment of the ISM, the injection of energy and momentum and structure formation (Wilkin, 1996). Bow shocks have been observed around both young and old stars and are an excellent candidate for investigating RAS, stellar evolution (by calculating the mass-loss rate), the structure of the ISM and even magnetic fields (e.g. van Buren, 1993; Dgani et al., 1996).

1.6 Important physical processes

1.6.1 Stellar feedback

We discussed and illustrated in Fig. 1.1 the role stellar feedback plays in ISM matter recycling, encompassing the mechanisms involved when stars interact with their immediate environment. Among the most important feedback mechanisms are **stellar jets**, ejected away from gaseous disks falling onto protostars. The gas around the newborn star is blasted away in the form of thin beams likely with the influence of magnetic fields (Shepherd and Churchwell, 1996; Beuther et al., 2002; Pudritz, 2004). **Stellar winds** are continuous outflows of heated gas (at 20-2000 km/s) ejected from the upper atmosphere of stars. During its lifetime, a massive star can loose up to 50% of its initial mass (Meynet et al., 1994) and in some cases, its entire outer envelope, forming a Wolf-Rayet star (see Wolf and Rayet, 1867).

Massive stars, above 8 $M_{\odot}$, explode as Type II ("core collapse") SNe, enriching the ISM with metals (see Fig. 1.6 of the Crab Nebula). These are, likely, the most violent stellar feedback events, stretching out in their impact to galactic scales (Bagetakos et al., 2011). By depositing energies of the order of 10^{51} ergs into the surrounding gas, they can create massive bubbles of hot gas, which sweep up and shock heat the ISM, driving galactic scale outflows (Girichidis et al., 2016). On the other hand, they also play a major role in driving turbulence into the galactic disk (Mac Low and Klessen, 2004; Padoan et al., 2016) and in the production of the hot phase of the ISM. At smaller scales, if they explode inside their progenitor's parental MC, they can completely destroy the cloud.

1.6.2 Turbulence

Along with magnetic fields, turbulence is believed to be a supporting mechanism preventing gravitational collapse in MCs. Present at all scales, from galactic scales down to the dense clumps in the MCs, it is a fundamental ingredient that determines several properties of MCs, e.g. lifetime, morphology and the rate of star formation (see review by Ballesteros-Paredes et al., 2007). Turbulence is dynamically important from scales of MCs to molecular

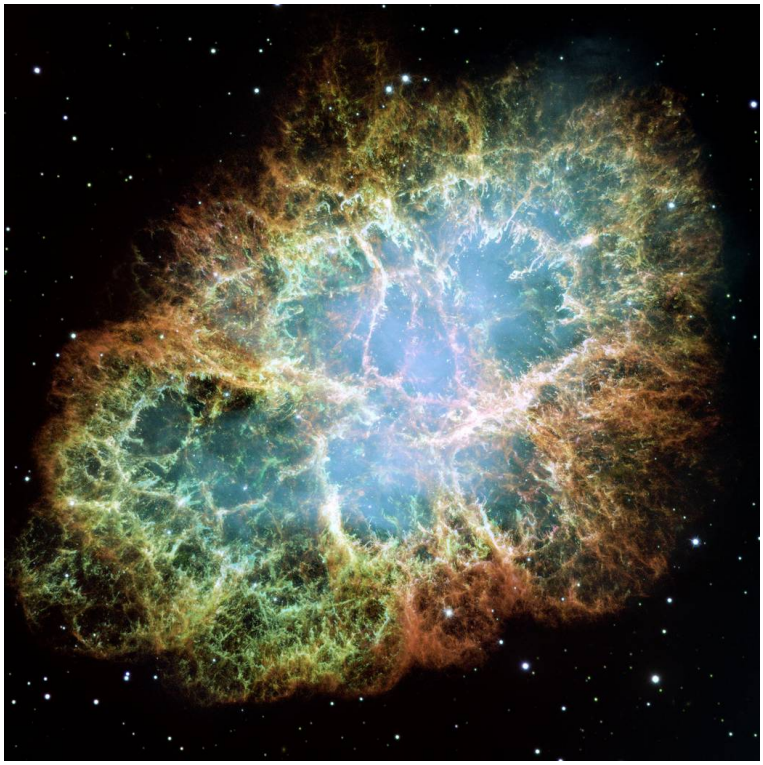

Figure 1.6: A composite HST image of the Crab Nebula with [O I] λ 6300 in blue (the central part remnant characteristic of post-shock gas), [S II] $\lambda\lambda$ 6717,6731 in green (tracing gas of densities between 100 and 10^4 cm^{-3}) and [O III] λ 5007 shown in red (tracing gas with temperatures between 1-1.7 $\times 10^4$ K). Credit: NASA, ESA, J. Hester, A. Loll (ASU)

cores as kinetic energy cascades down from larger to smaller scales (Ballesteros-Paredes et al., 1999; Mac Low and Klessen, 2004).

Turbulence in MCs, when supersonic (i.e. when able to compress the cold and dense gas) can sweep up and compress enough gas for it to become gravitationally unstable and undergo collapse, forming new stars. However, as turbulence and magnetic energy are in rough equipartition with the gravitational binding energy in MCs (see e.g. Federrath et al., 2011b; Federrath and Klessen, 2013), they can provide the necessary support against cloud collapse. This support could explain the observed low rate of MC collapse (Zuckerman and Evans, 1974; Zuckerman and Palmer, 1974).

Turbulence in the warm diffuse ISM, even though transonic (Heiles and Troland, 2003), can drive large density fluctuations, because once the gas is in the thermally unstable regime it can cool rapidly. SNe, one of the main sources of supersonic flows in the ISM, drive shock waves and produce hot bubbles. Not only does the energy injected by SN explosions produce the hot phase of the ISM and drive outflows and fountains (connecting the Galactic disk and the Galactic halo), it also contributes through turbulence to the mixing and stirring of the ISM.

1.6.3 Magnetic fields

Magnetic fields have been suggested to affect the dynamics of the ISM and star formation in various ways.

A popular distinction is between weak and strong field models. Weak field models (Elmegreen, 2000; Mac Low and Klessen, 2004) are based on the hypothesis that the formation of MCs is controlled by turbulent flows that compress the gas, with the magnetic field too weak to stop the collapse. Still, even in that case, the fields can modify the gas dynamics (and consequently the star formation activity) of molecular clouds (e.g. Vazquez-Semadeni et al., 2005; Price and Bate, 2008). Strong field models (Mouschovias, 1976; Kudoh and Basu, 2007) rely on the magnetic fields being the dominant mechanism controlling the formation and evolution of molecular clouds and star formation. In this case, the magnetic field is thought to be strong enough initially to prevent wholesale gravitational collapse of the cloud (see, however, Ballesteros-Paredes and Hartmann, 2007). Gravitational fragmentation and collapse in this scenario may be enabled via turbulent compression in combination with ambipolar diffusion (the decoupling of the neutral particles from the charged ones in the plasma, interacting with the magnetic field) (Kudoh and Basu, 2008), or an accumulation of additional matter along field lines (Chen and Ostriker, 2014; Heitsch and Hartmann, 2014).

Observational information on the magnetic field of the Milky Way and on nearby and distant galaxies, as well as cosmic magnetic fields, has increased recently due to the improvement of observational methods (Beck and Wielebinski, 2013). **Zeeman splitting**, for example, occurs when an external magnetic field interacts with the magnetic dipole of atoms, displacing their energy levels and giving rise to uniformly spaced multiplet splitting of their spectral lines. It is one of the most direct methods for measuring galactic magnetic fields and it has been widely used since the first measurements of magnetic fields in sunspots

(Spencer, 1965). The downside of the method is that it does not work for very low density regions. However, the effect is detectable in MCs, star-forming regions and SN remnants (Crutcher et al., 1993; Li and Henning, 2011). **Dust polarisation** (Hildebrand, 1988; Lazarian, 2003) consists of dust grains, elongated in shape, aligned with their major axis perpendicular to the magnetic field lines (alignment associated with paramagnetic relaxation or radiative torques, see Hoang and Lazarian, 2008). By measuring the polarisation degree and angle, the Planck mission constructed the first full sky dust polarisation map showing the magnetic field structure in both the diffuse ISM and star forming MCs (Planck Collaboration, 2012; Planck Collaboration et al., 2013). The **Faraday effect** (Burn, 1966) is the rotation of the polarisation of light induced by the magnetic field component aligned with the orientation of the electromagnetic radiation. The rotation of the rays (even linearly polarised radio waves) is a function of the strength of the magnetic field along the line-of-sight. The disadvantage of the method is that, because the rotation angle is dependent on the sign of the field direction, it cannot be detected if the field is tangled; ordered fields are necessary, characterised by morphological consistency. **Synchrotron emission** is a type of non-thermal radiation emitted when charged particles with relativistic velocities (mainly electrons) are accelerated radially, spiralling around magnetic field lines. The spectrum emitted depends on the strength of the magnetic field component perpendicular to the line of sight (Mao et al., 2012; Yoast-Hull et al., 2013). We also mention **optical and far-IR polarisation** (Hoang and Lazarian, 2008) and **spectral-line linear polarisation** (Goldreich and Kylafis, 1981). For more details on these methods see Crutcher (2012) and Beck and Wielebinski (2013).

Usually, since different methods retrieve different components of the magnetic field in different media, a combination of the listed methods is needed for accurate measurements. Therefore, optical, far-IR and sub-mm dust polarisation studies have shown that the magnetic field is aligned with the Galactic plane (Pavel et al., 2012). Synchrotron emission analysis gives an average field strength of 6 ± 2 μG in the local neighbourhood and 10 ± 3 μG at a 3 kpc radius from the Galactic centre (Beck, 2001). More recent studies of radio continuum all-sky surveys combined with thermal electron models and an assumed cosmic ray distribution reveal an average field strength of $\sim 2\mu$G for the regular field (large scale field) and ~ 3 μG for the random field (local field), in the solar neighbourhood (Sun and Reich, 2010; Jansson and Farrar, 2012).

In the diffuse ISM of the Milky Way, the magnetic field is estimated to be around 10 μG along the line-of-sight (Crutcher, 2012). In the denser regions, such as MCs, there are examples supporting both the strong and weak magnetic field theories. On the one hand, the magnetic field has been observed to be regular and strong enough to resist turbulence. In Crutcher (2004), two examples are discussed: L183 with a magnetic field strength in the plane of the sky of ~ 80 μG and a line-of-sight field strength of < 16 μG, and DR 21(OH), a high mass star forming region consisting of two compact cores (Woody et al., 1989) with an estimated total field strength of 1.1 mG. On the other hand, more recent work shows evidence for many MCs being supercritical, with magnetic fields that are too weak ($\sim 28\mu$G along the line-of-sight) to provide support against collapse (see Crutcher et al., 2009, 2010b,a; Crutcher, 2012).

Crutcher et al. (2010b), in his Bayesian analysis of molecular Zeeman measurements, showed that at densities between 10 and 10^7 cm^{-1}, the field strength displays strong variations. However, it has been shown by the PLANCK mission Planck Collaboration (2013a,b) that, statistically, the alignment of the field is parallel to low density structures below $\log_{10}(N_{\rm H}/{\rm cm}^{-2})\sim$ 21.7 in the diffuse ISM, and it tends to be aligned perpendicularly in regions with densities above this threshold.

According to observations, the mean orientation of the magnetic field in the Milky Way is mainly parallel to the Galactic plane and nearly azimuthal (Heiles, 1996), consistent with induction in a system possessing strong differential rotation (Roberts and Yuan, 1970). The Galactic magnetic field has two components: the large scale (ordered) and the random component (Rand and Kulkarni, 1989; Han et al., 2006; Beck, 2007), with the mean component being of order 1.4-2 μG and the random field about 5-6 μG (Kulsrud and Zweibel, 2008).

There is a tight link between the magnetic field and the motion of the plasma through the dynamo effect. A dynamo is a system that converts the kinetic energy of the plasma flow into magnetic energy. There are several types of dynamo depending on the type of the plasma flow, the scales of the turbulence and the parameters that describe the plasma: the Reynolds number $R_{\rm e}$ (the ratio between the inertial and viscous forces), the magnetic Reynolds number $R_{\rm m}$ (the ratio between induction and diffusion) and the magnetic Prandtl number $P_{\rm m}$ (the ratio between the viscous and the magnetic diffusion rate):

$$R_{\rm e} = \frac{VL}{\nu}, \tag{1.1}$$

$$R_{\rm m} = \frac{VL}{\eta}, \tag{1.2}$$

$$P_{\rm m} = \frac{\nu}{\eta} \tag{1.3}$$

with V the characteristic velocity scale of the flow, L the characteristic linear dimension, ν the kinematic viscosity and η the magnetic diffusivity.

Dynamos can be classified in two major groups according to how strong the plasma flow is: kinematic dynamos (when the plasma motion is dominant and the magnetic field is negligible) and nonlinear dynamos (when the magnetic field channels the flow through the Lorentz force). For a detailed description of this classification see the review by Brandenburg (2007). The kinematic dynamos, according to the type of flow can be turbulent or laminar. The laminar dynamos depending on the behaviour of the magnetic field in the vanishing magnetic resistivity regime can be slow (the magnetic field decays) or fast (the magnetic field remains finite). The turbulent dynamos can be small-scale, when the magnetic energy grows at comparable scales with the scale of the turbulence, and large-scale, when the magnetic energy is amplified at larger scales than the turbulence scale. This classification is summarised by Fig. 1.7.

The flows responsible for the main dynamo action in galaxies are differential rotation and SN-driven turbulence. For more details see Pariev et al. (2007); Sur et al. (2007).

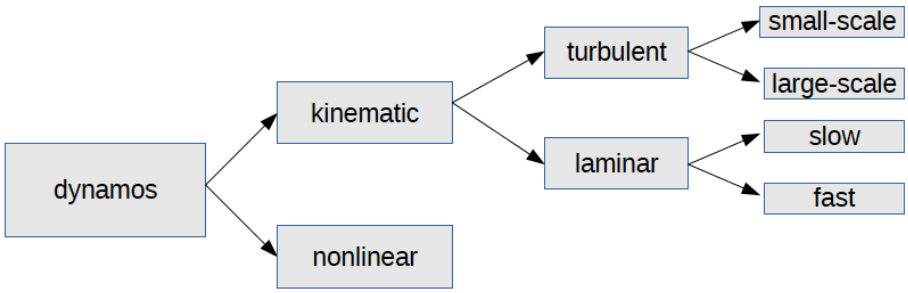

Figure 1.7: General dynamo classification.

Chapter 2

Modelling the ISM: Numerical methods

The Flash code is a 3D, Eulerian, adaptive mesh refinement (AMR), MHD code Fryxell et al. (2000); Dubey et al. (2008). The AMR is handled by the PARAMESH library. We refer to Walch et al. (2015) for a more detailed picture of the code described in this section.

2.1 The MHD equations

We solve the following MHD equations using the directionally split 3 (5)-wave MHD Bouchut HLL3R (HLL3R) solver (Bouchut et al., 2010; Waagan et al., 2011):

$$\frac{\partial \rho}{\partial t} + \nabla \cdot (\rho \mathbf{v}) = \mathbf{0}, \tag{2.1}$$

$$\frac{\partial E}{\partial t} + \nabla \cdot \left[\left(E + \frac{\mathbf{B^2}}{8\pi} + \frac{P}{\rho} \right) \mathbf{v} - \frac{(\mathbf{B} \cdot \mathbf{v})\mathbf{B}}{\mathbf{4}\pi} \right] = \rho \mathbf{v} \cdot \mathbf{g} + \mathbf{\dot{u}_{chem}} + \mathbf{\dot{u}_{inj}}, \tag{2.2}$$

$$\frac{\partial \mathbf{B}}{\partial t} - \nabla \times (\mathbf{v} \times \mathbf{B}) = \mathbf{0}, \tag{2.3}$$

with the total energy density:

$$E = u + \frac{\rho \mathbf{v^2}}{2} \frac{\mathbf{B^2}}{8\pi}, \tag{2.4}$$

and

$$\nabla \cdot \mathbf{B} = \mathbf{0}, \tag{2.5}$$

where t denotes time, ρ the mass density, $\mathbf{v}$ the velocity vector, $\mathbf{B}$ the magnetic field, $P = (\gamma - 1)u$ the thermal pressure along with the adiabatic index $\gamma = 5/3$ and the internal energy density u. $\mathbf{g}$ is the gravitational acceleration that combines self-gravity and the effect of external potential (see below), E is the total energy density, $\dot{u}_{\rm chem}$ is the rate of change in the internal energy density accounting for radiative cooling and diffuse heating.

$\dot{q}_{\rm inj}$ and $\dot{u}_{\rm inj}$ are the mechanical and thermal injection rates per unit volume from stellar feedback.

2.2 Chemistry

The simplified chemical network follows the evolution of five chemical species (H^+, H, H_2, C^+, CO) and free electrons. We do not assume chemical equilibrium, and therefore, we solve the continuity equation for each chemical species i included in the network:

$$\frac{\partial \rho_i}{\partial t} + \nabla \cdot (\rho_i \mathbf{v}) = \mathbf{C_i}(\rho, \mathbf{T}, \chi) - \mathbf{D_i}(\rho, \mathbf{T}, \chi) \tag{2.6}$$

where C_i and D_i account for the creation and destruction of species, being functions of density, gas temperature and abundances. The hydrogen chemistry is described by Glover and Mac Low (2007a,b); Micic et al. (2012), and it accounts for collisional ionisation, ionisation by X-rays and cosmic rays, radiative recombination, etc. The treatment of H_2 assumes its formation on dust grain surfaces and its destruction mainly by cosmic ray ionisation, collisional dissociation in hot gas or photo-dissociation by the interstellar radiation field (for a more detailed description see Walch et al., 2015). The CO chemistry is based on the simplified treatment developed by Nelson and Langer (1997).

Because we do not assume chemical equilibrium, our non-equilibrium (atomic and molecular) cooling function Λ is a function of temperature, density, abundances of chemical species and their evolution in time. This approach is the opposite of the collisional ionisation equilibrium approximation (CIE), which is more suitable for optically thin plasma and its own radiation in the absence of a significant external radiation field that could effect the ionisation balance of the gas. However, we use this approximation for the cooling by metals in the hot, ionised gas with $T > 10^4$ K, see Gnat and Ferland (2012).

We account for heating processes like radiative heating by cosmic rays, X-rays, the interstellar radiation field, photoelectric heating from dust grains and polycyclic aromatic hydrocarbons (PAHs). In addition, we include the heating from H_2 formation and H_2 photodissociation (for details see Glover and Mac Low, 2007a,b; Glover and Clark, 2012) We also model the attenuation of the ISFR by dust absorption, by H_2 and CO self-shielding and the shielding of H_2 and CO. All this is included using the TreeCol algorithm developed by Clark et al. (2012) in order to accurately calculate the column densities of H^+, H_2 and CO. Full details of the implementation of the chemical network and the coupling of TreeCol with FLASH are described by Walch et al. (2015) and Wünsch et al. (in preparation).

In the simulations we consider an interstellar radiation field of $G_0 = 1.7$ Habing (1968); Draine (1978), the X-ray ionisation and heating rates based on Wolfire et al. (1995) and a cosmic ray ionisation rate of $\xi = 3 \times 10^{-17} \mathrm{s}^{-1}$. For all simulations the gas has solar metallicity with abundances $\mathrm{x_{O,tot}} = 3.16 \times 10^{-4}$, $\mathrm{x_{Si^+}} = 1.5 \times 10^{-5}$, and $\mathrm{x_{C,tot}} = 1.41 \times 10^{-4}$ Sembach et al. (2000) and a constant gas-to-dust mass ratio of 10^2.

2.3 Self-gravity and the external gravitational potential

The gravitational acceleration of the gas has two components: the gravitational acceleration due to the gas self-gravity and due to the stellar component of the galactic disk. By solving the Poisson equation for the gas (with the method described in detail by Walch et al., 2015) we compute the gravitational potential:

$$\Delta\Phi = 4\pi G\rho \tag{2.7}$$

with Φ the gravitational potential and G= 6.67×10^{-8} cm^3 g^{-1} s^{-2} Newton's constant.

The gravitational acceleration due to the stellar component of the disk, $g_{\rm ext}(z)$ is modelled by an external potential. To paint a clear picture of the setup of the simulations we use the external potential from (Chapter 5), and we model a stratified gaseous disk with a density distribution:

$$\rho(z) = \rho(0)exp\left[-\left(\frac{z}{h_{\rm z}}\right)^2\right] \tag{2.8}$$

with $h_{\rm z} = 60$pc being the scale-height of the disk and ρ_0 the density in the mid-plane of the disk.

For computing the external potential we assume an isothermal sheet (Spitzer, 1942) and a Maxwellian distribution of stars within it. The vertical distribution of the stars as function of the radial distance to the galactic centre (R) and the scale-height (z) is:

$$\rho(R,z) = \rho_\star(R,0)sech^2\left(\frac{z}{2z_{\rm d}}\right) \tag{2.9}$$

with $z_{\rm d}$ being the vertical scale-height of the stellar disk, chosen to be 100 pc and $\rho_\star(R,0)$ the density of the stellar component in the mid-plane.

After solving the Poisson equation for the gravitational potential of the stellar disk, one can compute the gravitational acceleration due to the stellar component:

$$g_{\rm ext}(z) = -\frac{\partial\Phi_\star}{\partial z} \tag{2.10}$$

2.4 Star formation

2.4.1 Fixed SN rate

One option in implementing the SN explosions is to rely entirely on the Kennicutt-Schmidt law (Kennicutt, 1998) and to derive a fixed SN rate for the given initial density of the simulation. To estimate it, we calculate the mean surface density of gas in the simulation volume, $\Sigma_{\rm gas} = \rho_i L$, where ρ_i is the initial mass density of the gas and L is the dimension of the simulation volume. We then determine the corresponding star formation rate surface

density $\Sigma_{\rm SFR}$ using the Kenicutt-Schmidt relation. Finally, we assume a Salpeter initial mass function (IMF) Salpeter (1955), with a low-mass cutoff at 0.01 $M_\odot$ and a high-mass cutoff at 60 $M_\odot$, to find the number of massive stars that will explode as Type II SN. This procedure yields 1 SN for every 100 $M_\odot$ of stars formed, and so the final SN rate in the volume is given by

$$\dot{N}_{\rm SN} = 2.5 \times 10^{-6} \left(\frac{L^2}{1\,{\rm pc}^2} \right) \left(\frac{\Sigma_{\rm gas}}{M_\odot {\rm pc}^{-2}} \right)^{1.4} {\rm Myr}^{-1}. \tag{2.11}$$

For each SN we inject thermal energy of $E_{\rm SN} = 10^{51}$ erg into the medium in a spherical region adjusted to encompass 800 $M_\odot$ of gas. The radius $R_{\rm inj}$ of this region is required to be resolved with at least four cells.

In previous studies (Gatto et al., 2015; Walch et al., 2015), we have explored the influence of SN positioning on the evolution of the ISM. The four methods that we tested were random SN positioning, peak positioning (the SN are placed at the peaks in the density field), mixed positioning (a combination of random and peak driving), and clustered positioning.

The treatment of the SN positioning is as follows:

- Random driving assumes that the SNe (Type II) are randomly distributed in the disc following a Gaussian distribution with a scale-height of 50 pc. This approach allows the modelling of massive OB-type stars that travel outside the molecular clouds they were born in.

- In peak driving, the Type II SNe are positioned in peak density regions, following a scenario where all the massive stars explode in their mother MC.

- For mixed driving, the SNe locations are a mix of 50% random and 50% local peak positioning. For a detailed analysis of the percentage of random and peak density placements of the SNe and how they impact the ISM see Chapter 3.

- Clustered driving is based on the idea that OB-type stars are born in clusters and the positions of the SNe, at the end of their lives, are correlated as well. The clusters have a 40 Myr lifetime (Oey and Clarke, 1997) and the number of SNe in each cluster is based on a truncated power law (Clarke and Oey, 2002) with a time between individual explosions of 40 Myr, within the cluster. The clustering methods we compare to account for 80% Type II SN with a 50 pc scale-height and the rest Type Ia SNe with 325 pc scale-height (Hill et al., 2012). 40% of the Type II SNe explode in random locations while 60% explode in clusters. For more details on the implementation see Walch et al. (2015).

With clustered positioning, 60% of the SNe occur in clusters (the positions of which are random) and the remaining 40% are individual SNe inserted at random positions. We found in those studies that simulations carried out with peak and mixed SN positioning lead to substantial cooling of the SN remnants in dense regions, and hence produce very

little hot gas. They also drive turbulence at a relatively low level and just a small amount of H_2 can form. On the other hand, random or clustered positioning of the SNe results in H_2 mass fractions that are in reasonable agreement with observational estimates (Honma et al., 1995; Krumholz and Matzner, 2009). Simulations with random or clustered positioning also reproduce the large volumes occupied by hot diffuse gas that are predicted by the classical three-phase ISM model (McKee and Ostriker, 1977) and result in velocity dispersions for the individual phases that are in much better agreement with observations (Girichidis et al., 2016).

2.4.2 Schmidt-type SN driving

A more accurate approach is to aim for self-consistent SN driving instead of having a fixed SN rate. Following Schmidt (1959, 1963); Young (1987) and the constraint that the star formation rate (SFR) in MCs $\sim \rho^n$ with $n \in (1, 2)$ and ρ being the local gas density, and later the estimate for collisions between MCs giving the SFR $\sim \rho^{3/2}$ (Larson, 1969), we want to retrieve a SFR that is proportional to the local density and star formation efficiency ($\varepsilon_{\rm SFR}$) and inversely proportional to a characteristic time scale.

In order to find the regions where we can assume star formation is going to occur, we perform a series of tests, similar to the checks implemented by Bate et al. (1995); Federrath et al. (2010); Gatto et al. (2016):

- We look for cells that exceed a certain density threshold $\rho > \rho_{\rm crit}$. We calculate this density threshold by imposing the Jeans length:

$$\lambda_{\rm J} = \left(\frac{\pi c_{\rm o}^2}{G\rho_{\rm crit}}\right)^{1/2} \tag{2.12}$$

  with $c_{\rm o}$ the isothermal sound speed, to be resolved within at least four cells, in order to avoid spurious fragmentation in numerical collapse calculations (the Truelove criterion, see Truelove et al., 1997). However, for MHD free-fall isothermal collapse, Heitsch et al. (2001) argue that it needs to be resolved with eight cells at least. With an accretion radius $r_{\rm acc} = 4 \times \Delta x \sim 16$ pc when resolved with the highest level of refinement, the Jeans length becomes:

$$\lambda_{\rm J} = \left(\frac{\pi k_{\rm B} T}{m_{\rm p}} \frac{1}{G\rho_{\rm crit}}\right)^{1/2} = 2 \times r_{\rm acc} \simeq 32{\rm pc} \tag{2.13}$$

  From this relation, considering T = 300 K (the typical temperature of the cold stable phase), the critical density $\rho_{\rm crit} \sim 2 \times 10^{-22}$ g/cm^{-3} (see also Hennebelle and Iffrig, 2014).

- We take a spherical region of radius $r_{\rm acc}$ around the cell with $\rho > \rho_{\rm crit}$, and we resolve it with the highest level of refinement.

- We make sure the gas inside the $r_{\rm acc}$ area is Jeans-unstable.

- The gas inside this region has to be converging towards the centre ($\bigtriangledown \cdot \mathbf{v} < \mathbf{0}$).
- This region has to gravitationally bound so we look for the gravitational potential minimum in the centre of the region.
- We avoid the formation of two overlapping star forming regions. If we find two cells with $\rho > \rho_{\rm crit}$ within a distance that would make the two creation regions overlap, we calculate the mass enclosed in both regions and form only the more massive one.

After finding a region that fulfils all the checks, we calculate the mass of the gas enclosed in the collapsing region ($M_{\rm reg}$). Assuming a certain fixed star formation efficiency ($\varepsilon_{\rm SFR}$) we can calculate the expected star formation rate of the region:

$$SFR_{\rm ex} = \varepsilon_{\rm SFR} \frac{M_{\rm reg}}{t_{\rm ff}(\rho)} \tag{2.14}$$

with $t_{\rm ff}$ being the free-fall time, the typical timescale for a spherically symmetric, homogeneous cloud to collapse under the influence of its own gravity:

$$t_{\rm ff}(\rho) = \left(\frac{3\pi}{32 G \rho} \right)^{1/2} \tag{2.15}$$

and ρ, the average density of the region.

Assuming a Salpeter initial mass function (IMF, see Salpeter, 1955), with a low-mass cutoff at 0.01 $M_\odot$ and a high-mass cutoff at 60 $M_\odot$, we find that one star for every 100 solar masses will be massive enough to explode as a Type II SN. The total number of massive stars (equivalent to the number of SNe that will explode subsequently) in the collapsing region in the time interval Δt is

$$N_{\rm SN} = \frac{SFR_{\rm ex}}{100 \times M_\odot} \cdot \Delta t = \varepsilon_{\rm SFR} \frac{M_{\rm reg}}{100 \times M_\odot} \frac{\Delta t}{t_{\rm ff}(\rho)} \tag{2.16}$$

with $M_{\rm reg} = V_{\rm reg} \times \rho$ and $V_{\rm reg} = 4\pi r_{\rm acc}^3/3$, $r_{\rm acc} = 16$ pc fixed, $N_{\rm SN} \sim \rho^{3/2}$ (Schmidt, 1959, 1963; Young, 1987; Katz, 1992). The free-fall time is about 6.5 Myr (2.1×10^{14} s) for a region with the average density equal to the critical density (10^{-22} g/cm^{-3}) and the typical time-step Δt is of the order of $10^{10} - 10^{11}$ s (see Fig. C.1, left panel, Appendix C.1). Because the free-fall time is several orders of magnitude higher than the average time-step (see Fig. C.1, right panel, AppendixC.1) we adopt a statistical approach following Kim et al. (2011). We generate a random number from a uniform distribution $a \in [0, 1)$ and check for $a \in [0, \frac{\Delta t}{t_{\rm ff}}]$. For each region where the selection criterion is met, we allow the SNe to explode.

Very high density regions will have a shorter free-fall time ($t_{\rm ff}$), raising the ratio $\Delta t / t_{\rm ff}(\rho)$ and the probability for the region to undergo star formation. If the area does not explode at a certain time step only due to the statistical criterion, it will accumulate more gas until the probability of it exploding is high enough.

2.5 SN feedback

Type II SN explosions have maybe the strongest environmental impact out of all the stellar feedback mechanisms. They consist of an instantaneous release of $\sim 10^{51}$ ergs heating up the gas in their vicinity and sweeping it up with supersonic velocity. In the early phase of the SNR, immediately after the detonation, an extremely hot bubble forms around the centre, expanding into the ISM driven by enormous thermal pressure. Because of the very high pressure difference between the inside of the bubble and the gas around it, the supernova remnant (SNR) expands freely into the surrounding gas with the radius of the bubble $R_{\rm fr} = v \times t$ where v is the velocity of the ejecta. In the same time, a reverse shock starts to form, moving towards the centre of the SNR in the frame of the ejecta and outwards in the lab frame. Between the shocked ISM (situated right behind the outward moving blast wave) and the shocked SN ejecta (situated right behind the reverse shock wave) a contact discontinuity is formed, which is a surface between the two different media having comparable velocities and pressures but different densities. At the end of this first phase, called **the free expansion phase**, the swept up gas mass becomes approximately equal to the ejected mass at detonation.

After the reverse shock passes, the interior of the SNR is heated to very high temperatures, making energy losses by radiation negligible. This leads to the remnant expanding adiabatically into the surrounding environment, compressing it. The end of the second phase, the **adiabatic Sedov-Taylor phase** (Taylor, 1950; Sedov, 1959), occurs when radiative losses become dominant and the cooling gas right behind the shock wave forms a thin shell. The time it takes for this shell to form depends on the injected energy (E_{51} notation for 10^{51} ergs) and the number density of the ambient medium ($\rm n_0$), just like the radius and the velocity of the SNR:

$$R_{\rm st} = 22.6 pc E_{51}^{0.29} n_0^{-0.42} \tag{2.17}$$

$$v_{\rm st} = 202 kms^{-1} E_{51}^{0.07} n_0^{0.13} \tag{2.18}$$

(see Kim and Ostriker, 2015c)

After a short transition phase, the SNR enters a pressure-driven radiative phase, at the time the cooling time-scale of the formed shell is comparable to the age of the SN bubble, and the remnant is powered only by the pressure inside the bubble. This phase is called the **pressure driven snowplow phase**. Once the pressure within the SNR decreases to being comparable to the pressure of the ambient medium, the remnant enters the **momentum driven snowplow phase**. When the speed of the shock wave becomes of the same order of magnitude as the sound speed of the environment, the shock wave transforms into a sound wave and and begins fading away.

This description is valid for SNe exploding in the unmagnetised ISM. A magnetised environment can have a significant impact on the evolution of a SNR. When deriving the Sedov-Taylor solutions from the Rankine-Hugoniot jump conditions after adding the magnetic pressure to the momentum-flux conservation and the magnetic energy to the

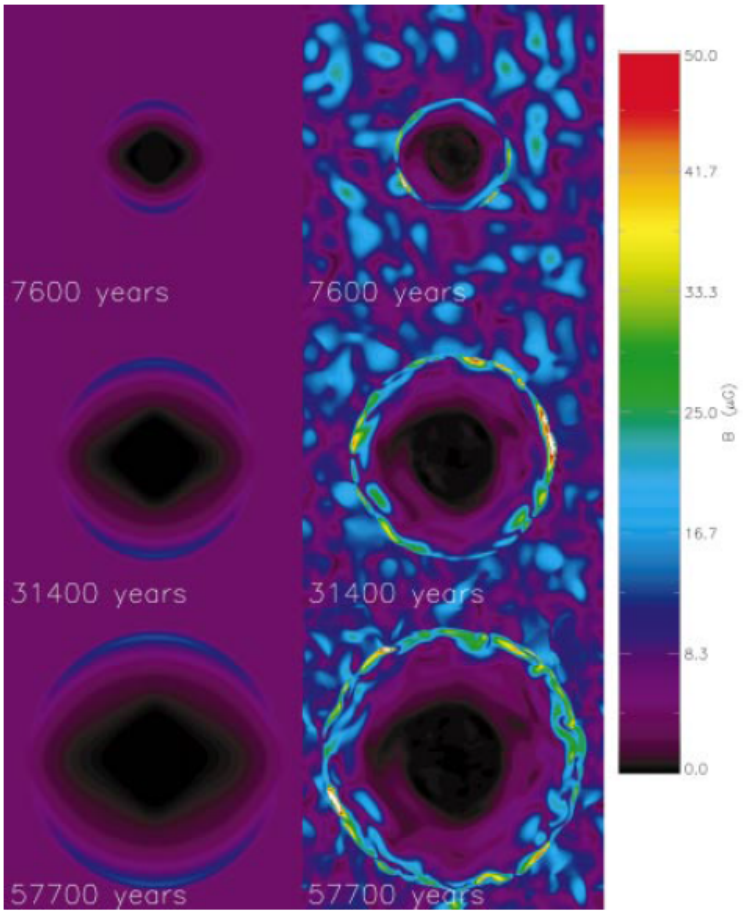

Figure 2.1: The total magnetic field strength for a 2D cut of a SNR in a uniform (left panels) and turbulent ISM (right panels), from Balsara et al. (2001). The magnetic field is oriented along the x-axis.

energy-flux conservation, when considering that the thermal pressure inside the hot remnant (during the Sedov-Taylor phase) clearly dominates over the magnetic pressure, the results are comparable to the Sedov-Taylor solutions for the unmagnetised case. The magnetised environment starts having a significant impact on the SNR during the pressure and momentum-driven snowplow phase. Numerical simulation of SN explosions in magnetised environments (see Fig. 2.1 from Balsara et al., 2001) show that the SNR becomes elongated in the direction parallel to the magnetic field while in the perpendicular direction the shock front thickens while more gas mass can be supported by thermal and magnetic pressure in comparison to just thermal pressure (see also Hanayama and Tomisaka, 2006).

Because in our simulations, due to a limited resolution of 1 pc/cell (at best), we are unable to model the free expansion phase of the SN explosions, we inject a fixed amount of energy $E_{\rm inj} = 10^{51}$ ergs in the form of thermal energy for each exploding SN.

Chapter 3

The impact of magnetic fields on the chemical evolution of the supernova-driven ISM

This chapter is bublished in Pardi et al. (2017), MNRAS 465, 4611-4633.

3.1 Introduction

Magnetic fields are ubiquitously observed in the interstellar medium (ISM; e.g. Han, 2009; Crutcher, 2012; Beck and Wielebinski, 2013) and they are expected to impact the dynamical evolution of the gas on galactic scales (e.g. Han, 2004; Frau et al., 2012; Alves et al., 2014). Therefore a good understanding of the connection between magnetic fields, ISM structure, and star formation is crucial for a complete theory of the dynamical and chemical evolution of the ISM (see McKee and Ostriker, 2007; Crutcher, 2012).

Supernovae (SNe) play an important role in the evolution of the ISM, possibly regulating the formation of a structured multi-phase ISM (e.g. Kim and Ostriker, 2015a; Tan et al., 2014; Gatto et al., 2015; Walch et al., 2015; Girichidis et al., 2016; Gatto et al., 2016; Peters et al., 2016b,a) and also the evolution and structure of the magnetic fields (Gent et al., 2013b). SN feedback leads to a multitude of complex mechanisms like the formation of the hot phase of the ISM (Cox and Smith, 1974; McKee and Ostriker, 1977), the driving of turbulence (Mac Low and Klessen, 2004; Klessen and Glover, 2016), local dispersal of gas (McKee and Ostriker, 1977; Mac Low et al., 2005; de Avillez and Breitschwerdt, 2007; Joung et al., 2009) or the formation of colliding flows that regulate MC formation and the formation of stars (Heitsch et al., 2011; Hennebelle et al., 2008; Banerjee et al., 2009). The impact of SNe location and spatial as well as temporal clustering has been extensively studied in both stratified boxes (Hill et al., 2012; Gent et al., 2013b; Kim et al., 2013; Walch et al., 2015; Girichidis et al., 2016) and homogenous boxes with open, mixed and periodic boundary conditions (Balsara et al., 2004; Mac Low et al., 2005; Slyz et al., 2005; Gatto et al., 2015; Li et al., 2015a). In particular Gatto et al. (2015) show

that the positioning and clustering of SN have significant impact on the structure of the ISM. Explosions predominantly in intermediate and low density environments favour the formation of a three-phase ISM with properties similar to the observed ones in the solar neighbourhood.

Recent magnetohydrodynamical (MHD) simulations that focused on the impact of magnetic fields and turbulent flows in the ISM indicate that magnetic fields reduce the amount of dense and cold gas formed (Hill et al., 2012), delay H_2 formation (Walch et al., 2015), reduce star formation and fragmentation of massive cores significantly (Peters et al., 2011; Hennebelle et al., 2011; Hennebelle and Iffrig, 2014) and determine the filamentary structure orientation along the field lines (Nakamura and Li, 2003; de Avillez and Breitschwerdt, 2005), even though only the cold, dense regions are magnetically dominated. Recently, Padoan et al. (2016) have shown that MCs have a mean magnetic field enhanced by a factor of two relative to the mean magnetic field of their simulation. Other studies have also shown that the magnetic field has little impact on the scale height of magnetised disks galaxies (Hill et al., 2012) and a weak effect on outflows (Girichidis et al., 2016). However, those models did not follow the chemical evolution of the ISM (except for Girichidis et al., 2016). Instead temperature and density cuts were used to distinguish between the different ISM phases. Walch et al. (2015) showed that these simple cuts are insufficient to investigate the ISM phases and dynamics, in particular for the cold molecular phase. As this is the phase with the strongest magnetic fields as well as the phase in which star formation occurs, it is important to follow the evolution of the magnetised ISM together with its chemical evolution.

In this study, which is part of the SILCC project (SImulating the Life-Cycle of molecular Clouds[1]), we investigate the interplay between the chemical evolution of the SN-driven ISM and the magnetic field evolution. We use three-dimensional magnetohydrodynamical simulations including a chemical network and shielding from an interstellar radiation field, to explore how magnetic fields alter the formation of molecular gas in the ISM. We present the details of the simulations, the list of simulations and the initial conditions in Subchapter 3.2. We discuss the morphological evolution of the simulations in Subchapter 4.3. The chemical evolution is described in Subchapter 4.4 together with the magnetic field evolution and the influence of self-gravity. In this chapter we also evaluate the thermal, magnetic and kinetic energy density (Subchapter 3.4.1). In Subchapter 3.4.2 we show the magnetic field scaling and present our conclusions in Subchapter 4.7.

3.2 Simulations and initial conditions

All simulations cover a box volume of $(256\ \mathrm{pc})^3$. We start with atomic gas of solar composition, at a uniform temperature of $T = 5000$ K and with a uniform number density of $n_i = 0.5\,\mathrm{cm}^{-3}$. This yields a gas surface density of $\Sigma_{\mathrm{gas}} = 4.1\,M_\odot\,\mathrm{pc}^{-2}$ for the box, and a total gas mass of $2.9 \times 10^5\,M_\odot$, comparable to the mass of a giant molecular cloud (Hughes et al., 2010).

[1] see the SILCC website: `www.astro.uni-koeln.de/silcc`

No.	Sim. name	SN rate [Myr^{-1}]	$B_{\rm init}$ [μG]	Numerical resolution [cells]	Physical resolution [pc/cell]	Self-gravity
1	KS-lowB-L4	1.2	6×10^{-3}	64^3	4	no
2	KS-lowB	1.2	6×10^{-3}	128^3	2	no
3	KS-lowB-L6	1.2	6×10^{-3}	256^3	1	no
4	KS-medB	1.2	0.3	128^3	2	no
5	KS-highB	1.2	3	128^3	2	no
6	KS	1.2	0	128^3	2	no
7	KS-SG	1.2	0	128^3	2	yes
8	KS-lowB-SG	1.2	6×10^{-3}	128^3	2	yes
9	KS-medB-SG	1.2	0.3	128^3	2	yes
10	KS-highB-SG	1.2	3	128^3	2	yes
11	KS-medB-lateSG	1.2	0.3	128^3	2	from $t = 150$ Myr

Table 3.1: List of simulations and parameters. From left to right we list the name of the simulation, SN rate, initial magnetic field strength, numerical resolution, physical resolution, and whether or not the simulations were carried out with self-gravity.

We adopt a fiducial, fixed-grid resolution of 128^3 cells across the domain, equivalent to a uniform cell size of 2 pc. To test the resolution effects, we ran additional simulations at a uniform resolution of 64^3 (labeled L4) and 256^3 (labeled L6) cells (see Appendix A.1, Fig. A.2).

To study the evolution of the magnetic fields, we carry out runs with three different values for the initial magnetic field strength: a low value of 6×10^{-3} μG, an intermediate value of 0.3 μG and a high value of 3 μG (comparable to observations in the local ISM). We note, however, that even our strong initial magnetic field is at the lower limit of what observations suggest for the atomic gas.

The role of self-gravity in shaping the ISM has been discussed by Walch et al. (2015), who show that without it, it is impossible to obtain reliable estimates of dense and molecular gas. However, recently, Padoan et al. (2016) have seen little influence from self-gravity in a very similar simulation setup to ours. In this study, we run all simulations with and without self-gravity (with the exception of the simulations run as part of our convergence testing, described in Appendix A.1). In addition, we compare one simulation with self-gravity switched on from $t = 0$ to one simulation in which we let the ISM first evolve without self-gravity and then switch it on after 150 Myr. As this procedure has been used in previous studies (see e.g. Padoan et al., 2016; Ibáñez-Mejía et al., 2016) we describe the morphological and chemical differences between these two cases in Appendix A.2. A full list of the simulations is given in Table 3.1. The names of the simulations specify the supernova rate in SNe/Myr given by the Kennicutt-Schmidt relation via Eq. 5.3 (KS), the initial magnetic field strength (no label for runs with $B_{\rm init} = 0$, lowB for runs with a weak initial field, medB for the runs with $B_{\rm init} = 0.3\,\mu$G and highB for the runs with $B_{\rm init} = 3\,\mu$G. To the name, the level of refinement of the simulation (L4, L6) or a suffix for self-gravity

(from $t = 0$ as SG and from $t = 150$ Myr as lateSG) is added where appropriate.

3.3 Morphological evolution

The initial homogeneous distribution of atomic hydrogen is rapidly stirred by expanding SN shells. The explosions disperse the gas locally and compress the regions between the shells that will form high density structures and molecular hydrogen. Randomly placed SNe result in a highly structured medium with large variations in column density (from 10^{-5} to 10^{-1} g/cm^2) and a significant fraction of the simulation volume filled with hot gas. This is in agreement with previous findings (see Hennebelle and Iffrig, 2014; Gatto et al., 2015; Walch et al., 2015; Girichidis et al., 2016).

Figure 3.1 depicts the morphological differences of the ISM between KS (top row), KS-lowB (second row), KS-medB (third row) and KS-highB (bottom row). We compare column density projections after 50, 100, 150 and 200 Myr of evolution. There are no significant structural differences between KS and KS-lowB but the medium and high initial field strength simulations show fewer clumpy structures (see the discussion in Subchapter 4.4). While the column density in the first three simulations varies by at least four orders of magnitude, in KS-highB it varies by only two orders of magnitude.

In Fig. 3.2 we highlight the structural differences between the runs with and without self-gravity, all at 150 Myr. We show the column densities for KS and KS-SG (left column), KS-lowB and KS-lowB-SG (second column), KS-med and KS-med-SG (third column) and KS-highB and KS-highB-SG (right column). The simulations including self-gravity form very dense structures confined to a small volume while in the runs without self-gravity the structures are less dense and occupy a larger volume. The same can be seen in Fig. 3.3 where the H_2 column density is shown. However, KS-highB and KS-highB-SG are clearly different. Because of the strong magnetic fields the gas cannot be compressed and collapse to high densities. As a results only traces of H_2 can be found (see Subchapter 4.4).

In Fig. 3.4 we present the time evolution in density slices (through the densest region in the box) and the magnetic field strength with the field lines over-plotted for KS-lowB (top two rows), KS-medB (third and forth row) and KS-highB (bottom two rows). For KS-lowB, even after a very short time (50 Myr), the ISM becomes very inhomogeneous with densities ranging over 5 orders of magnitude (from 10^{-27} to 10^{-22} g/cm^3) and the magnetic field varying by 3 orders of magnitude (from 10^{-3} to 1 μG). Overall, the highest magnetic field strength is found in dense gas. In runs KS-lowB and KS-medB, the combination of the strong turbulent motions and the weakness of the magnetic field lead to the field becoming highly tangled. This is an expected result, consistent with the ideal MHD assumption where the magnetic field is dragged along with the gas. In simulation KS-highB (Fig. 3.4 bottom row) the magnetic field strength remains high during the entire simulation. The magnetic field lines are less tangled and due to the strength of the field, compression is less efficient and the ISM is more homogeneous.

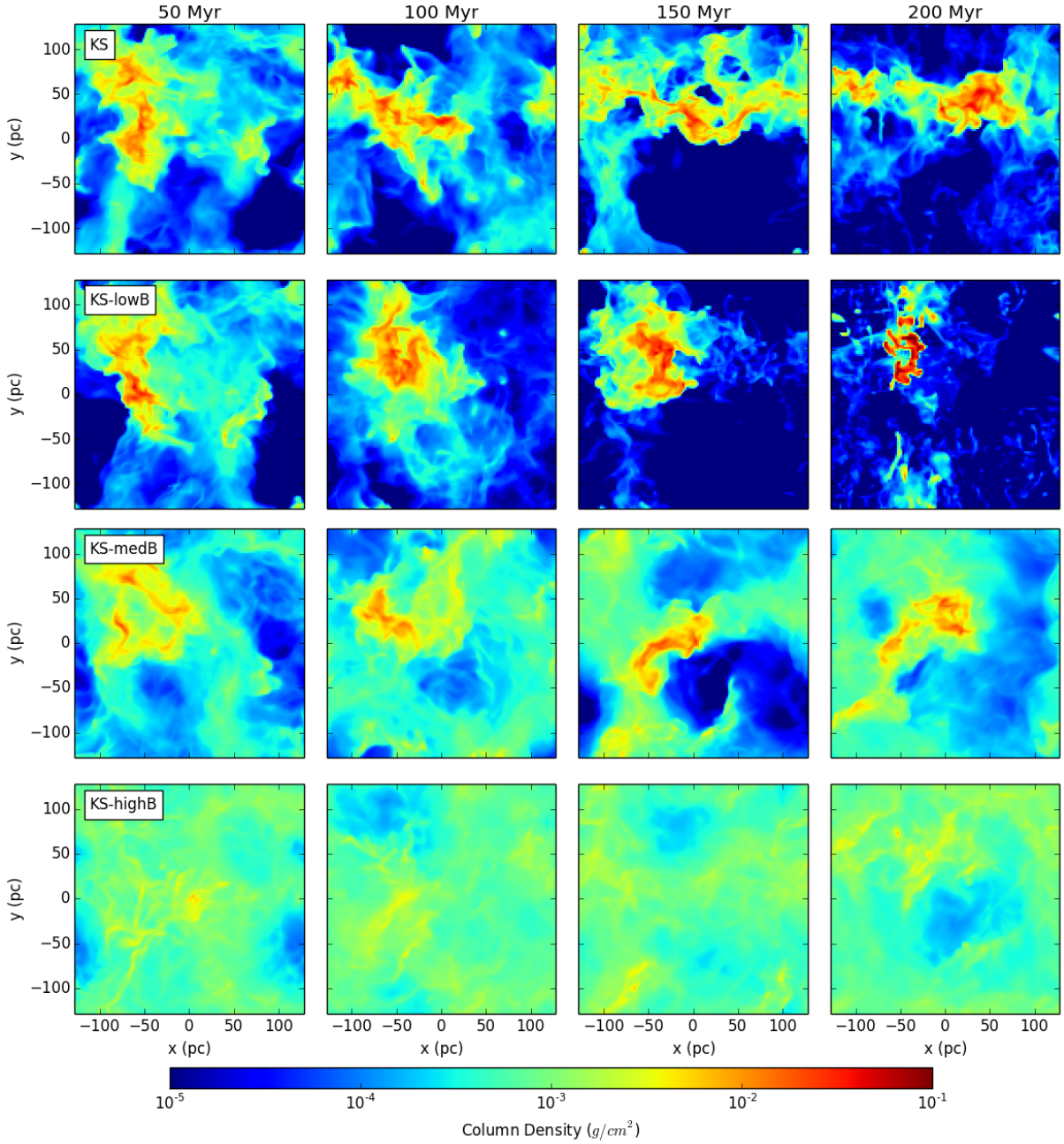

Figure 3.1: Time evolution of the column density for runs KS (*top*), KS-lowB (*second row*), KS-medB (*third row*) and KS-highB (*bottom row*) at 50, 100, 150 and 200 Myr (from left to right). The densest clumps develop in the KS-lowB simulation after 100 Myr while KS-highB has the most homogeneous ISM structure. The structural differences between KS and KS-lowB are discussed in Subchapter 4.4.

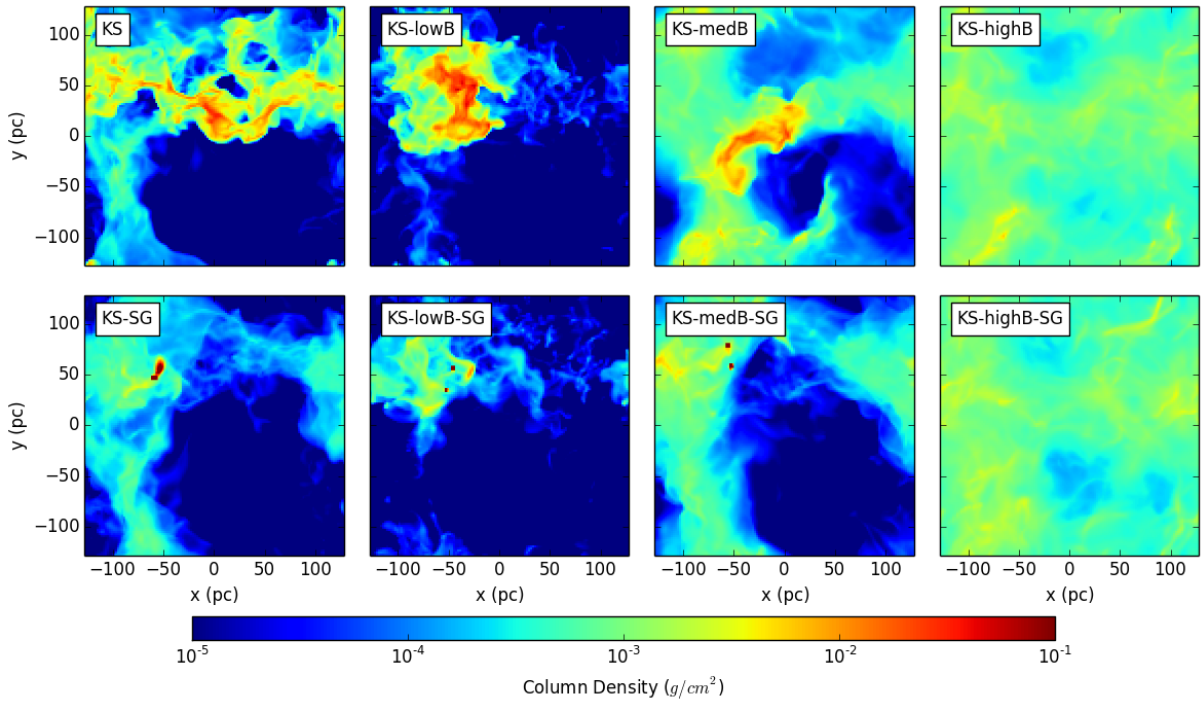

Figure 3.2: Column density comparison of simulations KS, KS-lowB, KS-medB and KS-highB (*top row*) and self-gravity simulations KS-SG, KS-lowB-SG, KS-medB-SG and KS-highB-SG (*bottom row*), all at 150 Myr. With self-gravity the dense structures are much more compact. KS-highB-SG is an exception: the ISM is much more homogeneous and resembles the ISM in KS-highB.

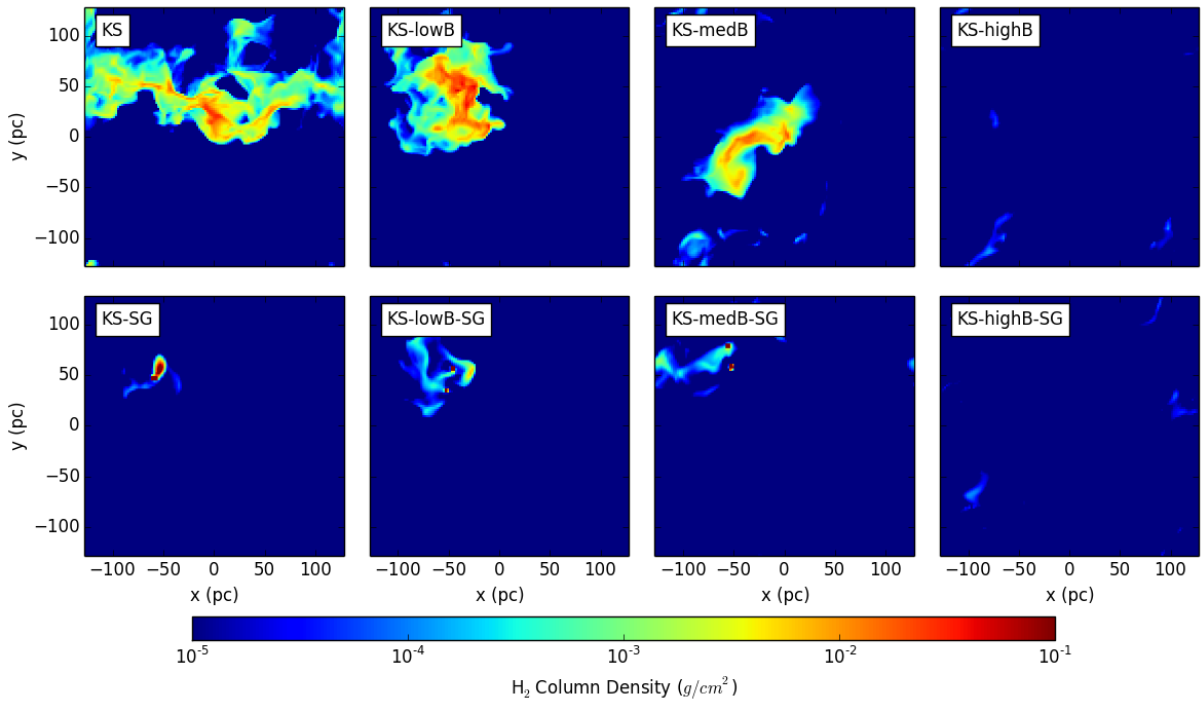

Figure 3.3: Same as Fig. 3.2 but for the H_2 column density, all at 150 Myr. Without self-gravity, the H_2 is contained in relatively extended clouds while with self-gravity almost all the H_2 is concentrated in a few very compact clumps. However, in runs KS-highB and KS-highB-SG very little H_2 is formed.

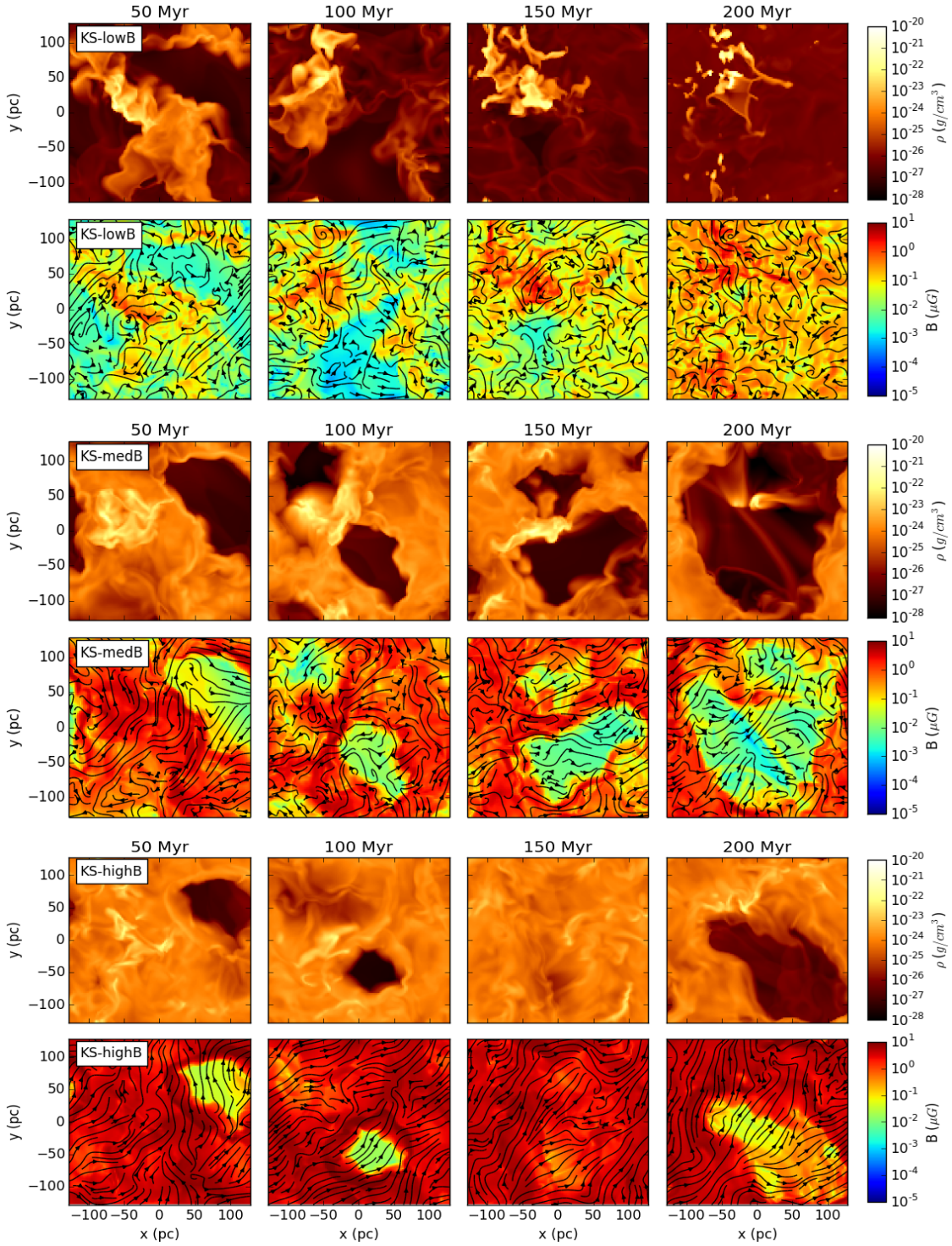

Figure 3.4: Time sequence showing density slices passing through the densest region in the simulation and oriented parallel to the z axis (rows 1, 3, 5) and the corresponding magnetic field strengths (rows 2, 4, 6), with magnetic field lines over-plotted. Results are shown for output times of 50, 100, 150 and 200 Myr and for runs KS-lowB (*top two rows*), KS-medB (*middle two rows*) and KS-highB (*bottom two rows*). There is a strong correlation between the density and magnetic field strength. The magnetic field in KS-lowB is highly tangled due to the turbulent motion of the gas.

3.4 Chemistry and magnetic field evolution

In a turbulent environment, with the magnetic field "frozen into" the gas, the fluid motion drags along the magnetic field, twisting and folding it. Turbulent compression[2] quickly amplifies the magnetic field at small scales (Kazantsev, 1968; Subramanian, 1997) until the saturation scale is reached (Egan et al., 2016), when there is a statistical balance between the kinetic and magnetic energy. This effect is seen in the weak and medium strength simulations. In order to reach this saturation limit, the system needs several dynamical times (Piontek and Ostriker, 2007; Hennebelle et al., 2011; Federrath et al., 2011a; Hill et al., 2012; Schober et al., 2015).

We show the average volume weighted and mass weighted magnetic field evolution in Fig. 3.5 (top and middle panels) for all magnetic runs. The volume weighted magnetic field in KS-highB is constant over time. In KS-medB the field is amplified over the first 20 Myr and then remains constant. On the other hand, the seed field in KS-lowB is amplified over a much longer time, more than 150 Myr. Self-gravity does not significantly influence the saturation field strength in any of the simulations. The volume weighted mean magnetic field saturates at about 0.2 μG for KS-lowB, at 1 μG for KS-medB and at 3 μG for KS-highB. The mass weighted mean magnetic field (Fig. 3.5 middle panel) shows a similar behaviour although the saturated values are higher: ~ 1 μG for KS-lowB, 2 μG for KS-medB and 4 μG for KS-highB. Self-gravity in KS-medB and KS-lowB induces significant fluctuations in the mass weighted field strength, almost an order of magnitude, which emphasises the scaling of the field strength with gas density (shown also in Fig. 3.18). The gas can reach higher densities and magnetic field strengths in the self-gravitating runs (see Subchapter 3.4.1 and 3.4.2). However, in all the simulations, the mean magnetic field strength is weaker than in the solar neighbourhood (6 ± 2 μG, see Beck, 2001).

We analyse the chemical state of the ISM by focusing on the time evolution of the H_2 mass fractions. As there is only a few percent of mass in H^+, the remaining gas mass is in atomic form. Our simulations' resolution limits prevent meaningful conclusions about CO formation (more details are given in Appendix A.1, Fig. A.1). The evolution and the strength of the magnetic field is tightly linked to the evolution of H_2. In Fig. 3.5 (bottom panel), the H_2 formed in KS-highB and KS-highB-SG is less than 2% of the total mass throughout the simulations (seen also in Fig. 3.3). In our setup, high magnetic fields can suppress the formation of H_2.

Figure 3.6 shows the mass and volume weighed density and temperature probability distribution functions (PDFs) of the simulations without self-gravity. The density PDFs of the unmagnetised, initially low and medium field strength runs reach a density higher than 10^{-21} g/cm^3 while the PDF of KS-highB is much narrower ($\rho_{\rm max} \approx 10^{-22}$ g/cm^3). As a result, the minimum temperature of the gas in KS-highB is much higher: around 100 K, in comparison to 20-30 K in the other simulations. The lack of high density gas in the KS-highB run also has a pronounced impact on the formation of H_2, explaining the small

[2]Note that as our simulations do not account for the effects of Galactic rotation, they are unable to probe any further amplification that may occur due to the α-Ω dynamo.

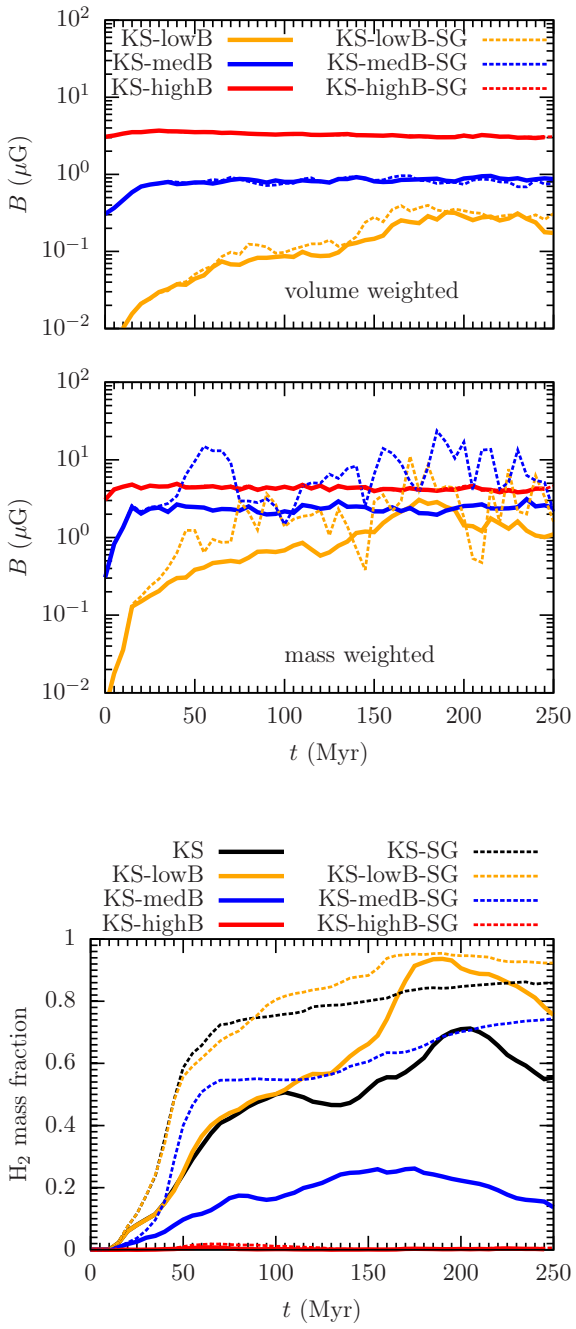

Figure 3.5: Magnetic field evolution over time (volume weighted *top panel* and mass weighted *middle panel*) and H_2 mass fraction evolution over 250 Myr (*bottom panel*). We show the runs: KS (solid black line), KS-lowB (solid orange line), KS-medB (solid blue line), KS-highB (solid red line), KS-SG (dashed black line), KS-lowB-SG (dashed orange line), KS-medB-SG (dashed blue line) and KS-highB-SG (dashed red line). The average magnetic field of KS-highB is almost flat at 3 μG while the field in KS-medB and KS-lowB are being amplified. Although including a very weak initial magnetic field actually aids the formation of H_2, increasing the field strength to values closer to the observations leads to a significant suppression of H_2 formation, to the point where there is barely any H_2 formed in runs KS-highB or KS-highB-SG.

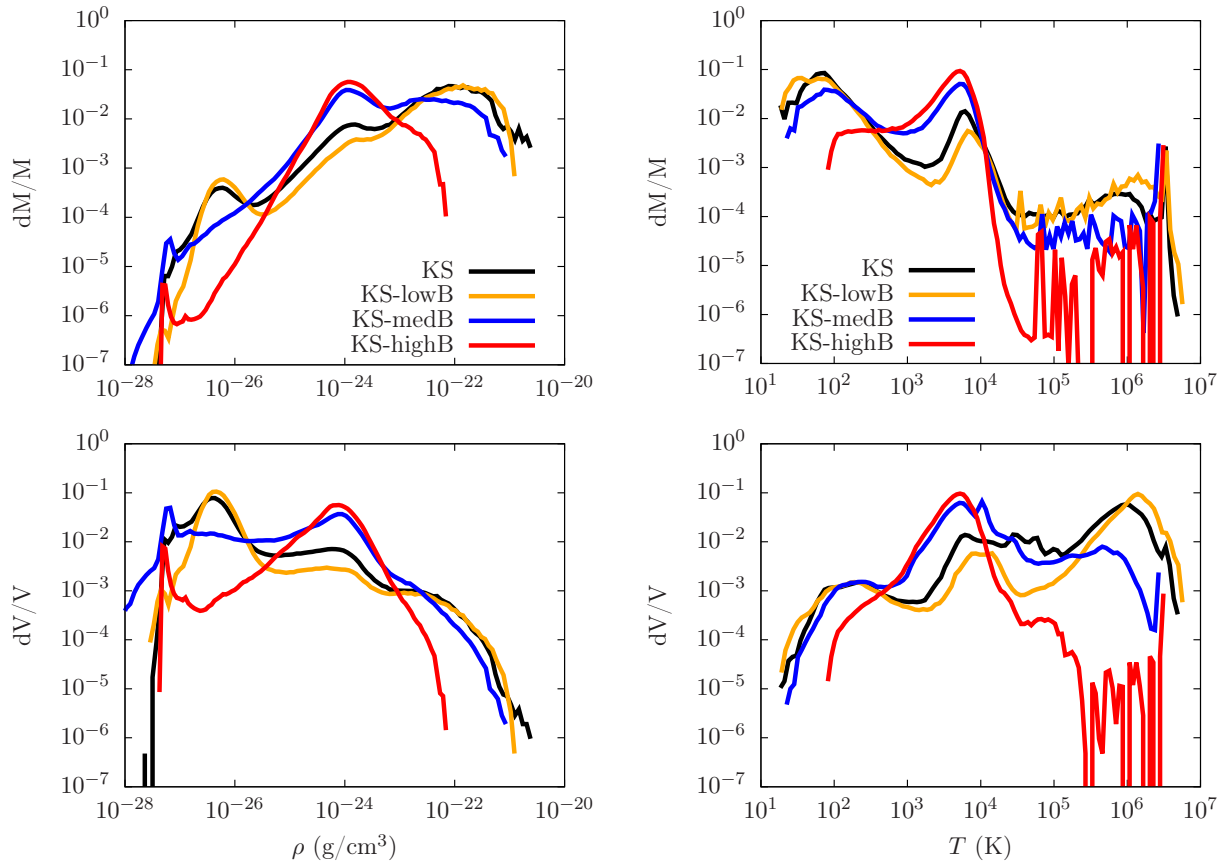

Figure 3.6: Mass weighted (*top left panel*) and volume weighted (*bottom left panel*) density PDFs and mass (*top right panel*) and volume weighted (*bottom right panel*) temperature PDFs of KS (black), KS-lowB (yellow line), KS-medB (blue line) and KS-highB (red line), all at 150 Myr. In both cases, the PDF of KS-highB is narrower at high densities and low temperatures while there is very little hot and low density gas in this simulation.

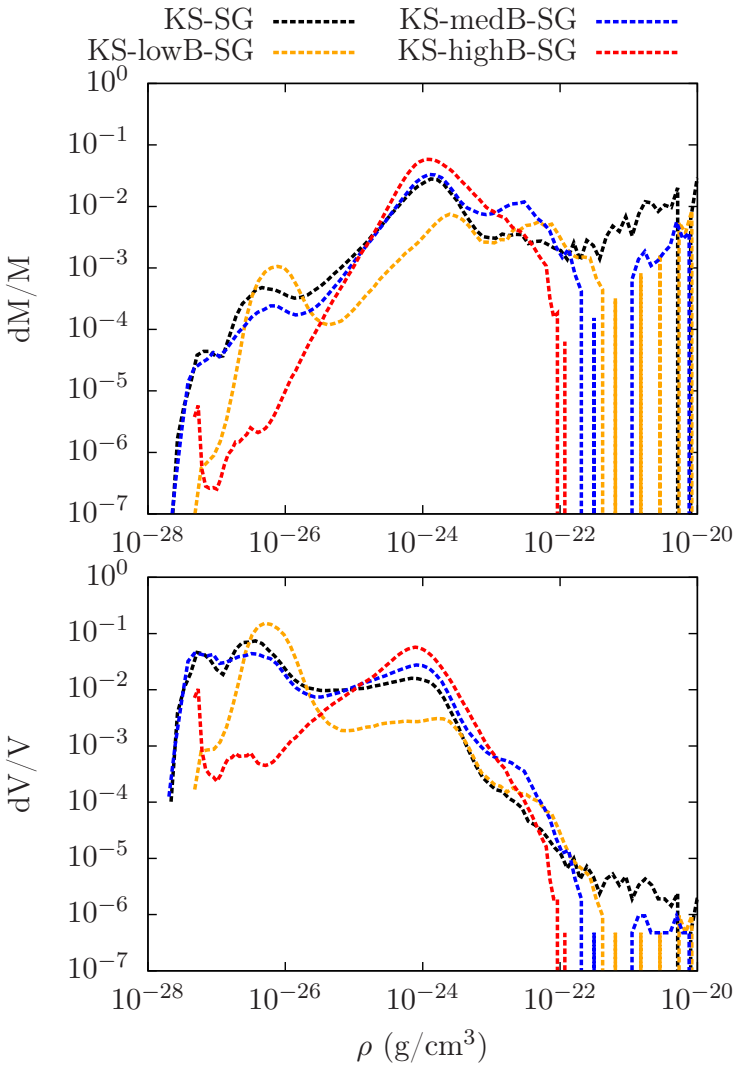

Figure 3.7: Mass weighted (*top panel*) and volume weighted (*bottom panel*) density PDFs of KS-SG (black dotted line), KS-lowB-SG (yellow dotted line), KS-medB-SG (blue dotted line) and KS-highB-SG (red dotted line), all at 150 Myr. The PDF of KS-highB-SG is much narrower and unlike the other PDFs does not show a peak at 10^{-26} g/cm^3.

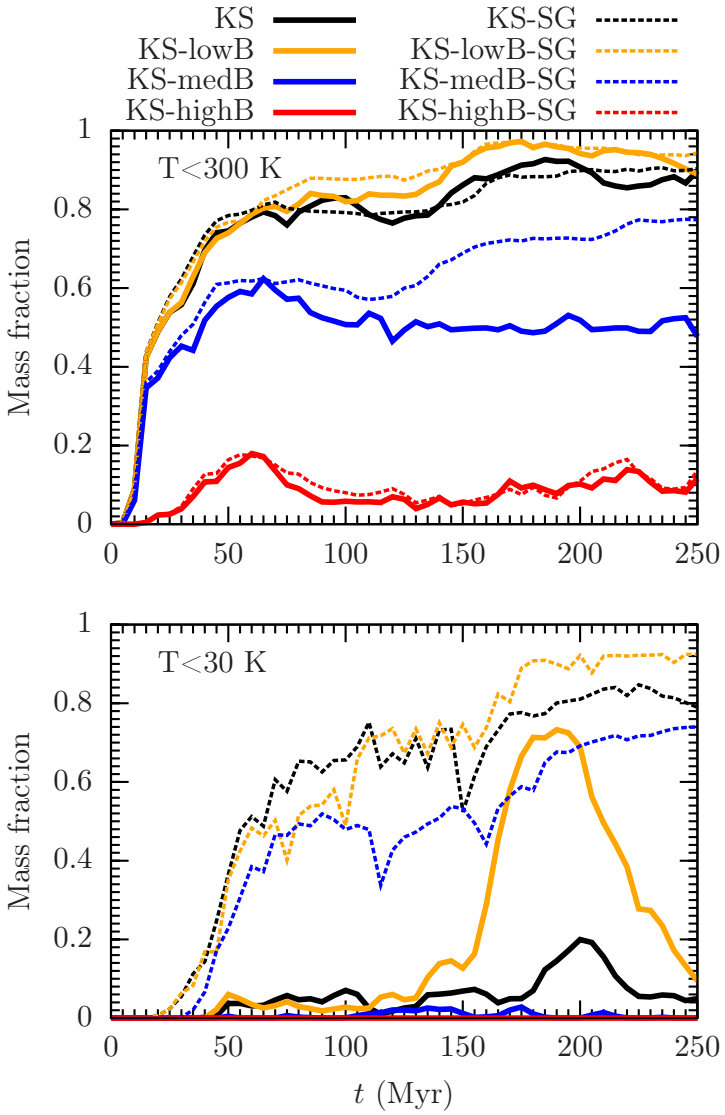

Figure 3.8: Mass fraction evolution of the cold gas ($T < 300$ K, *top panel*) and very cold gas ($T < 30$ K, *bottom panel*) for all the simulations (same colour-coding as in Fig. 3.5). While in the cold gas regime the mass fractions in KS and KS-lowB are similar, the very cold gas mass fraction starts diverging soon after 100 Myr and in KS-lowB, the very cold gas reaches a fraction almost four times higher than in KS.

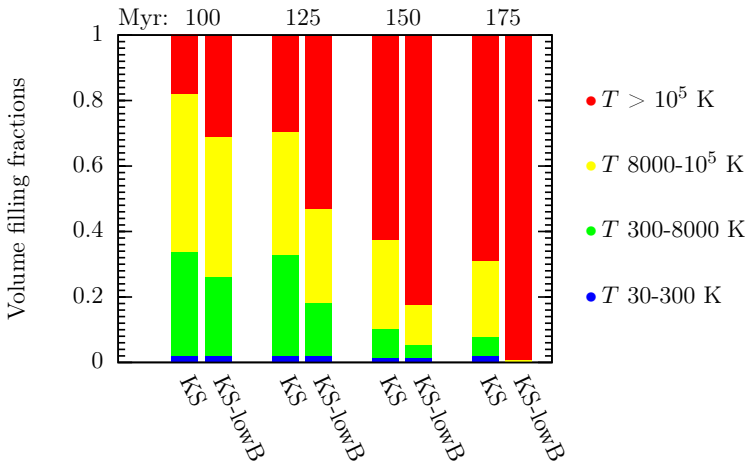

Figure 3.9: Volume filling fractions at 100, 125, 150 and 175 Myr (averaged over 4 Myr). Colour-coding: blue - cold gas ($T \in [30; 300)$ K), green - cool gas ($T \in [300; 8000)$ K, yellow - warm gas ($T \in [8000; 10^5)$ K) and red - hot ionised gas ($T \geq 10^5$ K) for KS and KS-lowB. The cool and warm gas VFFs are higher for KS while the hot gas VFF comes to completely dominate in KS-lowB by 175 Myr.

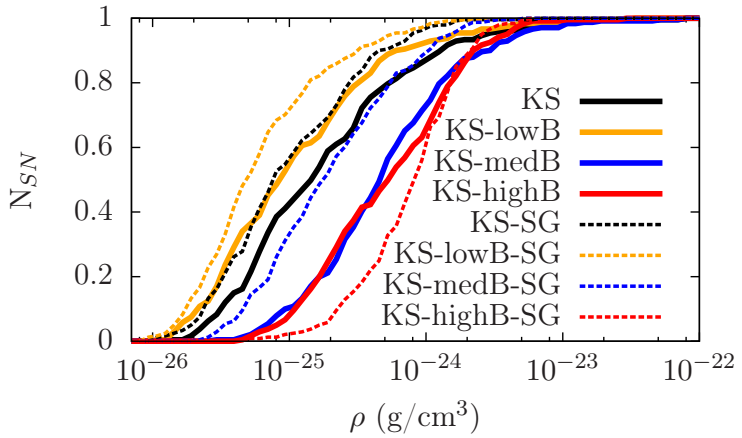

Figure 3.10: Cumulative histogram of the number of SNe as a function of the environment they explode in. Same colour-coding as in Fig. 3.5 and Fig. 3.8. The SNe in KS-lowB (and KS-lowB-SG) explode in a more diffuse ISM than the ones in KS (and KS-SG).

Sim. name weighing	f_{H_2}	f_H	B [μG] mass	B [μG] volume	B (H^+) [μG] mass	B (H) [μG] mass	B (H_2) [μG] mass	B (T_1) [μG] mass	B (T_2) [μG] mass	B (T_3) [μG] mass	$f_{\beta<1}$
KS	0.5	0.4									
KS-lowB	0.6	0.3	1.2	0.5	0.5	1	1.2	1.5	1.2	0.9	0.07
KS-lowB-L4	0.6	0.4	0.4	0.07	0.3	0.5	0.3	0.3	0.4	0.4	0.002
KS-medB	0.2	0.7	2.2	0.8	1.8	2	2.3	1.9	2.7	2	0.3
KS-highB	10^{-3}	0.9	4	3.2	4	4	4.4	4.4	3.9	5.5	0.7
KS-SG	0.8	0.2									
KS-lowB-SG	0.9	0.1	3	0.3	0.9	1.7	3	4	2.5	2.5	0.01
KS-medB-SG	0.6	0.4	6.5	0.8	2.4	3	8.8	22	11.6	2.7	0.16
KS-highB-SG	$0.8{\cdot}10^{-3}$	0.97	4.04	3.2	4.3	4	5.2	4.7	4.2	5.3	0.7

Table 3.2: List of simulations with the H_2 and H mass fractions, mass and volume weighted magnetic field intensity, mass weighted magnetic field in H^+, H and H_2, mass weighted magnetic field in T_1 <30 K, $T_2 \in [30; 300)$ K and $T_3 \in [300; 8000)$ K and the mass fractions for which $\beta < 1$ for all the simulations at 150 Myr.

fraction of $\sim 2\%$ that we see for the KS-highB and KS-highB-SG runs. The much more homogeneous ISM we see in Fig. 3.1 is a result of most of the mass and volume of the gas in KS-highB being around 10^{-24} g/cm^3 (discussed also in Subchapter 3.4.1) and temperature of 10^4 K. In comparison, the other simulations show distinct density PDF peaks at 10^{-26}, 10^{-24} and 10^{-22} g/cm^3, indicative of a three-phase ISM. In KS and KS-lowB, most of the simulation box is filled with 10^6 K gas while most of the mass is at 10^2 K.

The fact that the PDF of KS-highB falls off so steeply at the high density and low temperature end can have several reasons. The random distribution of the SNe in a 3 μG magnetised environment is apparently not enough to stir the gas efficiently in the simulation. The compression of the gas is too low to form high density, long-lived structures that would permit the substantial formation of H_2. The current simulation setup fails to create a hot phase as well. A more efficient way of driving turbulence would be clustered SNe generating stronger coherent motions. Extending the simulation box to a stratified box with open boundaries and an external background potential would both allow for coherent acceleration towards the centre of the potential as well as allowing the SNe to expand further without the spatial restrictions of the periodic box (see also the discussion in Subchapter 3.4.1).

In Fig. 3.7 we show the mass and volume weighted density PDFs for the simulations with self-gravity. The main features are the same as for the simulations without self-gravity. The main systematic difference is the high-density tail that corresponds to gravitationally dominated regions.

Returning to Fig. 3.5, in the runs without self-gravity, higher magnetic fields result in lower H_2 mass fractions (at 150 Myr, 60% in KS-lowB, 25% in KS-medB and 1% in KS-highB). The H_2 mass fractions in the simulations with self-gravity reach 50% - 70% after only 50 Myr and much higher values after 150 Myr, compared to the runs without self-gravity (90% in KS-lowB-SG, 60% in KS-medB-SG and about 1% in KS-highB-SG). The evolution of the H_2 mass fractions in KS and KS-lowB is very similar until about 100 Myr. After this point, the evolutionary trend is very similar but the H_2 mass fraction is lower in KS than in KS-lowB. The same holds for KS-SG and KS-lowB-SG which diverge at 90 Myr. To illustrate why we see this counter-intuitive difference between the hydro and KS-lowB simulations in H_2 we show in Fig. 3.8 (top panel) the mass fraction of the cold ($T < 300$ K) and the very cold ($T < 30$ K, bottom panel) gas. The cold gas in both KS and KS-lowB (as well as in KS-SG and KS-lowB-SG) has similar mass fractions ($\sim$ 90%) while in the $T < 30$ K regime KS-lowB increases and peaks at around 200 Myr at a four times higher value than KS.

This difference occurs due to a systematic effect (tested with simulations using different random positioning for the SNe). Even though an initial field of $6 \times 10^{-6}\mu$G is too weak to make a considerable difference in the structure and chemical evolution of the ISM at the beginning of the simulation, as the field is being amplified, dense magnetised regions are being formed through compression. More compact dense structures are formed in KS-lowB in comparison to the filamentary structures of KS, seen also in Fig. 3.3, upper row, first two panels (the aspect of the dense clumps in KS-lowB and KS are consistent in the y-z direction as well). The magnetic tension in these clumps prevents the dense gas from being

dispersed as easily as in the KS simulation, keeping the molecular hydrogen more confined and hence better shielded.

The cold, dense molecular gas is embedded in the cool ($T \in [300; 8000)$ K) and warm ($T \in [8000; 10^5)$ K) surrounding environment (see Fig. 3.3) and the fact that the H_2 molecules reside in smaller clumps in KS is shown also by the higher cool and warm gas volume filling fraction (VFF) compared to KS-lowB. In Fig. 3.9 we present a series of averaged (over 4 Myr) VFFs for KS and KS-lowB at 100, 125, 150 and 175 Myr. Significant differences in cool (yellow column) and warm (green column) gas VFFs appear around 100 Myr, shortly before the H_2 mass fractions starts to diverge. The difference in the structure of the dense gas up to this point is enough to make the self-shielding of the molecular gas more efficient in contrast to the smaller clumps in KS. This effect can be seen in the self-gravity runs as well.

Because the sequence of SNe is fixed in space and time, they typically explode in higher density regions in run KS. In Fig. 3.10 we present the cumulative histogram of the number of SNe as a function of the density of the environment they explode in. There is a clear difference between KS and KS-lowB (also KS-SG and KS-lowB-SG) showing that the SNe in KS-lowB (and KS-lowB-SG) explode in a more diffuse ISM than in KS (and KS-SG), leading to much denser clumps containing much more molecular gas (see Fig. 3.1 second row, 150 and 200 Myr) and an increasingly high hot gas VFF over time (see Fig. 3.9 at 150 and 175 Myr). The structure of the ISM in the KS-lowB simulation, at later stages, points to the onset of thermal runaway (described in detail by Gatto et al., 2015).

According to Honma et al. (1995) in the Milky Way, the H_2 mass fraction varies from $\simeq 50\%$ around the galactic centre to $\simeq 2\%$ at 9.5 kpc distance away from the centre. In a more recent study, Pineda et al. (2013) show an average H_2 mass fraction of $\sim 50\%$ when taking into account the CO-dark H_2 gas component. By varying the initial magnetic field between 0 and 3 μG we obtain H_2 mass fractions ranging from 0.1% (KS-highB and KS-highB-SG) to 90% (KS-lowB-SG). The H_2 mass fraction we obtain after 150 Myr are in the observed range for KS-medB (20%). If we consider a H_2:H surface density ratio we obtain a 0.29 average value for KS-medB at 150 Myr, consistent with the observed values of $0.1 - 1$ (Schruba et al., 2011).

We test the dependence of the amplification of the magnetic field and the H_2 mass fraction evolution on the resolution in Appendix A.1. The magnetic filed is slightly stronger for higher resolution, whereas the amount of H_2 is converged at our fiducial resolution. We also investigate the differences between a simulation in which self-gravity acts during the entire evolution and a run in which we first allow SNe to generate a structured ISM before switching on self-gravity at t= 150 Myr. We find that self-gravity switched on at a later time in the simulation leads to isolated dense clumps embedded in a lower density gas than the MCs formed with self-gravity from the beginning of the simulation (see Appendix A.2).

Figure 3.11 shows the evolution of the mass weighted magnetic field over time (left column) and the mass fractions (right column) in different temperature regimes. From the top to the bottom we show the low, medium and high initial field simulations. In the top left panel, the magnetic field in KS-lowB is stronger for colder gas (at 150 Myr the field is about 1.5 μG in $T < 30$ K, 1.2 μG in $T \in [30; 300)$ K and 0.9 μG in $T \in [300; 8000)$ K). In

the self-gravity simulation the variation of the magnetic field in the cold ($T \in [30; 300)$ K) and very cold ($T < 30$ K) regime is about one order of magnitude. In the top right panel, the mass fraction in the very cold gas becomes high after the first 20 Myr (40%) in the self-gravity run while it takes ~ 200 Myr for the same mass fraction to be reached without self-gravity (see also Fig. 3.5).

In Fig. 3.11 left middle panel (for KS-medB and KS-medB-SG) strong magnetic field variations in the very cold regime can be noticed for KS-medB (from below 0.1 to about 6 μG). This can be related to the fact that the mass fraction of the very cold gas is very low (Fig. 3.11 right middle panel) remaining less than 2% over the time of the simulation. Also the magnetic field in the cold and very cold gas in KS-medB-SG is fluctuating by almost an order of magnitude above the field strength in the corresponding temperature regime in KS-medB. This is consistent with the mass fraction in $T < 30$ K temperature regime that can reach 40% in KS-medB-SG due to the strong compression of the gas.

In KS-highB and KS-highB-SG, the magnetic field has approximately the same strength in all the temperature regimes (Fig. 3.11, bottom panels). Here self-gravity does not have an impact on the strength of the field. There is less than 1% gas with $T < 30$ K in the simulations, hence the magnetic field in this temperature regime in KS-highB-SG is present only for a short time around 50 Myr. Most of the gas is at $T \in [300; 8000)$ K with a mass fraction close to unity.

The magnetic field is stronger in colder temperature regimes and in denser regions. For our simulations, in the cold phase ($T \leq 300$ K, $\rho \simeq 10^{-21}$ g/cm^3) the magnetic field is around 4 μG, consistent with the observations of Beck and Wielebinski (2013). In the warm diffuse medium the observations show a field strength of a few μG, similar to our results in KS-medB (2 μG) and KS-highB (4 μG).

In Fig. 3.12, we show the mass fractions (in the same temperature regimes as shown in Fig. 3.11), the H_2, H and H^+ mass fractions and the volume filling fractions at 150 Myr, averaged over $\pm$ 2 Myr. Stronger magnetic fields significantly decrease the mass fractions of cold gas and H_2 and significantly increase the mass fraction and VFF of warm gas. We notice this trend independent of self-gravity. The main effect of self-gravity is to increase the mass fraction of the coldest (and densest) gas component (grey bars in Fig. 3.12) and the H_2 mass fractions (light blue bars). There is also a trend towards higher VFFs of the hot gas in runs with self gravity (red bars on the bottom panel of Fig. 3.12). This is a result of SNe going off in low density regions (as also seen in Gatto et al., 2015; Li et al., 2015a). According to Snowden et al. (1998) the hot gas VFF is $\simeq$ 60% while Heiles and Troland (2003) give $\simeq$ 50% for the warm neutral gas and $\simeq$1.5% for the cold gas. In all the simulations the hot gas VFF varies between 0.1 % (KS-highB) and 90% (KS-lowB-SG) while the KS-medB simulations reproduces best the observations (the same simulation that obtains the best match to the H_2 mass fraction). When comparing the top and middle panels of Fig.3.12 we notice that there is no one-to-one correlation between the very cold gas and H_2 mass fractions (also shown by Walch et al., 2015). Even though the trend with the initial magnetic field is similar, for the runs without self-gravity the ratio of mass fractions of the very cold gas and H_2 is 13% for KS, 19% for KS-lowB and 4% for KS-medB. In comparison to the self-gravity runs where this ratio is much higher: 65% for

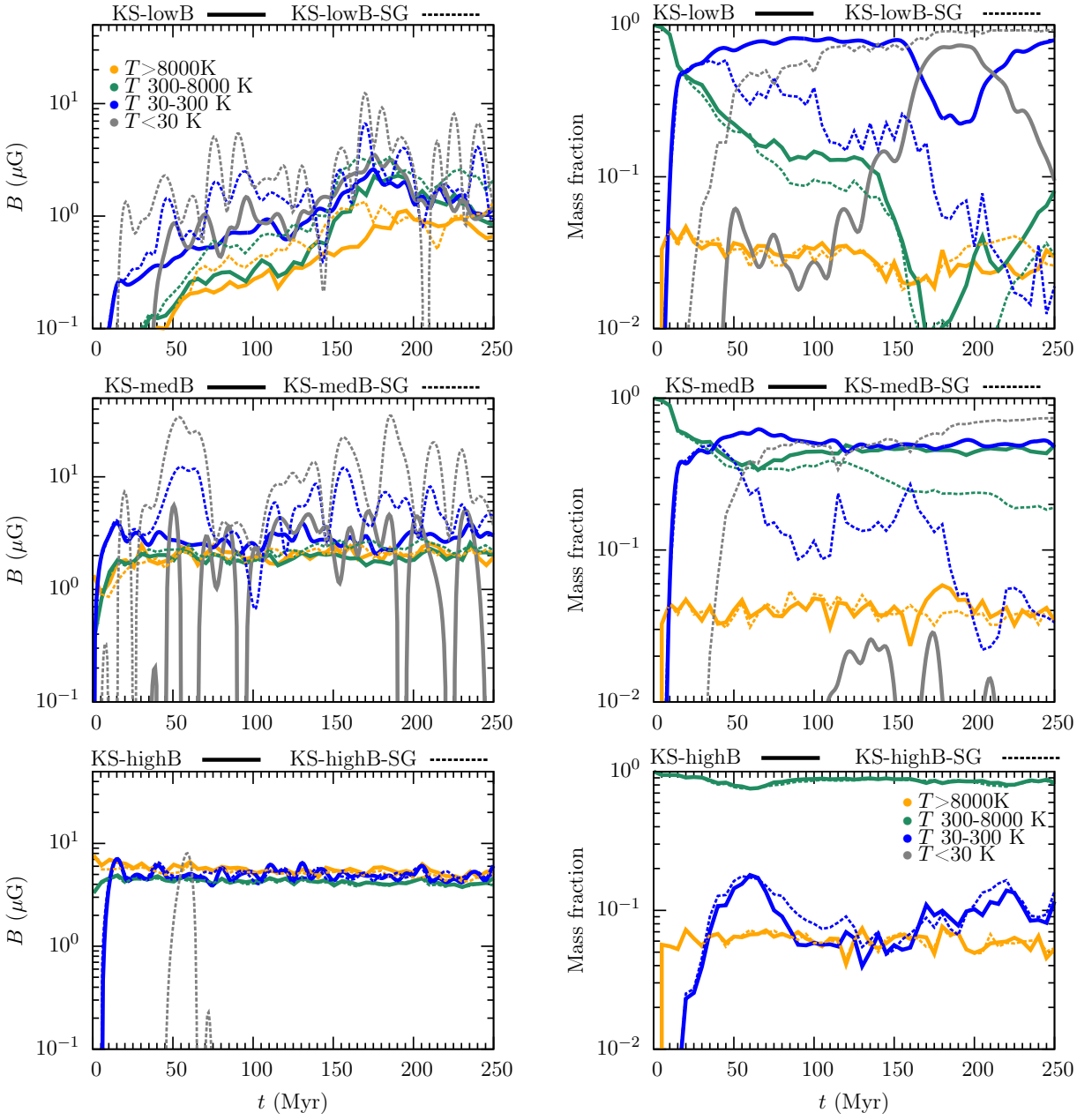

Figure 3.11: Time evolution of the mass weighted magnetic field strength for KS-highB, KS-medB and KS-lowB (solid lines) and KS-highB-SG, KS-medB-SG and KS-lowB-SG (dashed lines) in different temperature regimes (grey for $T < 30$ K, blue for $T \in [30; 300)$ K, green for $T \in [300; 8000)$ K and orange for $T \geq 8000$ K)- *left column*. The corresponding mass fraction evolution in the *right column* with the same line styles and colour-coding. The lower the temperature of the medium, the higher the average magnetic field in these regions. We interpret this as a consequence of flux freezing, since the mean density of the cold phase is much higher than that of the intermediate or warm phases.

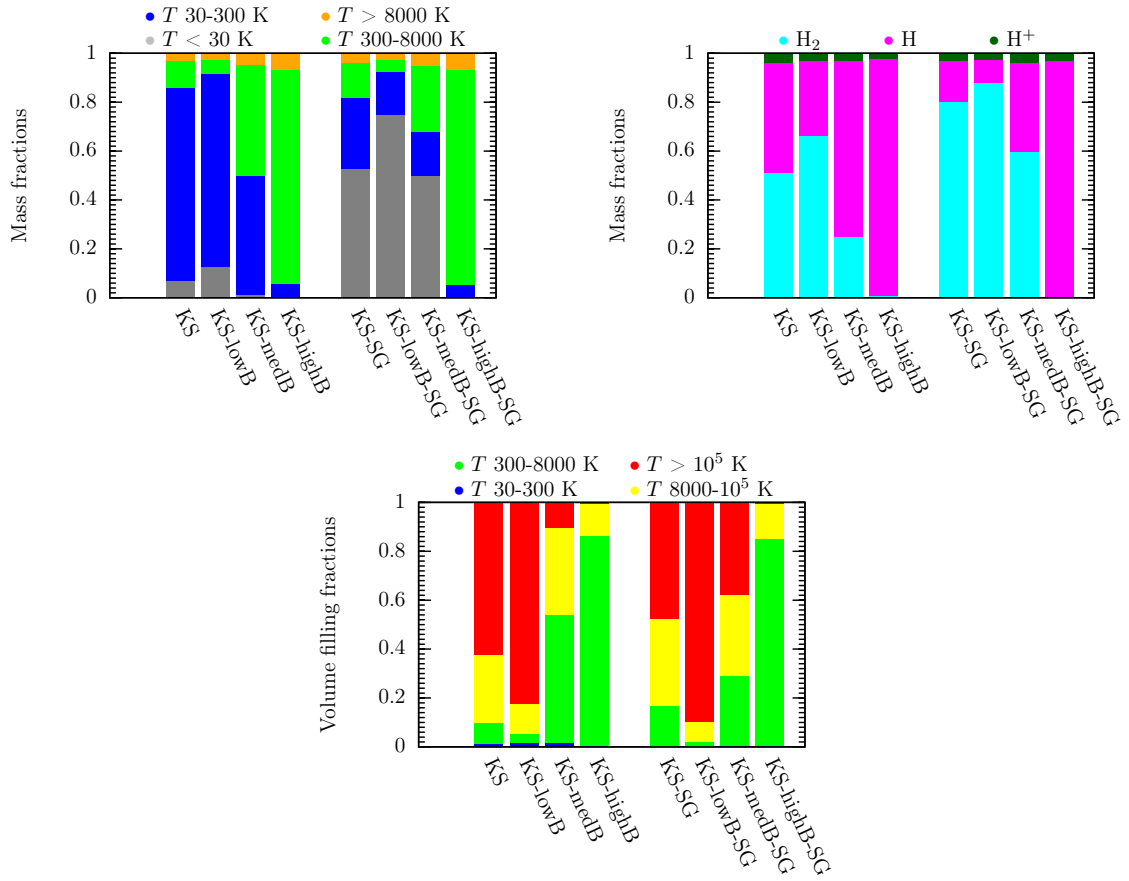

Figure 3.12: Temperature regime mass fractions (*top left panel*), H_2, H and H^+ mass fractions (*top right panel*) and volume filling fractions (*bottom panel*) at 150 Myr (averaged over 4 Myr) Colour-coding: grey - very cold gas ($T < 30$ K), blue - cold gas ($T \in [30; 300)$ K), green - cool gas ($T \in [300; 8000)$ K, yellow - warm gas ($T \in [8000; 10^5)$ K) and red - hot ionised gas ($T \geq 10^5$ K), the orange mass fractions correspond to temperatures above 8000 K, light blue - H_2, magenta - H and dark green - H^+. High magnetic fields result in low cold gas, low H_2 mass fractions, high VFFs of warm gas and low VFF of hot gas. Self gravity increases the mass fraction of the colder gas component and slightly increases the hot gas VFF. There is no tight correlation between the very cold gas and H_2 mass fraction.

KS-SG, 85% for KS-lowB-SG and 83% for KS-medB-SG.

In Fig. 3.13 we present the average H_2, H and H^+ mass weighted magnetic field (from top to bottom). In H_2 the magnetic field is the strongest: after 150 Myr the field is 1.2 μG in KS-lowB, 2 μG in KS-medB and 4.5 μG in KS-highB. Again self-gravity results in fluctuations in the mass weighted field (also seen in Fig. 3.5, middle panel). Due to the efficient formation of the very high density gas, the magnetic field can be locally amplified to over 10 μG. In atomic and ionised hydrogen, self-gravity does not impact the magnetic field significantly. In atomic hydrogen the magnetic field is about 1 μG in KS-lowB, 2 μG in KS-medB and 4.5 μG in KS-highB. The hot ionised gas is formed when the atomic gas is heated by SN blasts. Characterised by low densities and high temperatures, in this regime the field is the weakest: 0.5 μG in KS-lowB, 1.8 μG in KS-medB. In the case of KS-highB, the magnetic field strength is very similar in all temperature regimes with 4 μG in the hot gas at 150 Myr.

For the further characterisation of the physical state of our model ISM, we show the volume and mass weighted root mean square (RMS) of the Mach number in Appendix A.3, Fig. A.7.

3.4.1 Pressure components

We present a diagram of thermal, magnetic and ram pressure as a function of density on top of the mass weighted pressure-density distribution (Fig. 3.14) for the hydro runs (top row), the magnetic simulations without self-gravity (middle row) and with self-gravity (bottom row). The initial field strength increases from left to right. We take the median pressure for each density bin (equal in log space and a number of 35 between 10^{-25} and 10^{-20} g/cm^3). The upper limit of the bars represents the 75th percentile and the lower one the 25th percentile. We average over 4 Myr around 150 Myr. The colour map shows the mass of the gas, which indicates how the gas is distributed between the thermally unstable regime, the stable warm and the stable cold branch. The hydro simulations reach a higher maximum density (see Fig. 3.6 left panels) and contain less thermally unstable gas than the magnetised boxes. This thermally unstable gas represents between 10% (low initial field) and 90% (high initial field) of the total gas mass. According to Heiles and Troland (2003), 30% of the mass fraction of the solar neighbourhood is thermally unstable (from the Millennium Arecibo 21 cm survey) which is very close to the thermally unstable gas mass fraction we obtain in the KS-medB and KS-medB-SG runs.

The grey dotted line represents the approximate density we can resolve. Applying the Truelove criterion Truelove et al. (1997) in the simulations with self-gravity, the Jeans length should be resolved with at least 4 cells in order to avoid spurious fragmentation in numerical collapse calculations. For a fixed 8 pc Jeans length the critical density scales linearly with the temperature. From Fig. 3.6 right panel we see that there is a considerable amount of gas at $T = 100$ K in all the simulations and for this temperature the maximum density we can resolve is about 2.6 $\times 10^{-22}$ g/cm^3.

The highest density reached in the simulations depends on the magnetisation of the environment: 1.65×10^{-21}g/cm^3 in KS-lowB (same as KS-medB) and 1.64×10^{-22} g/cm^3

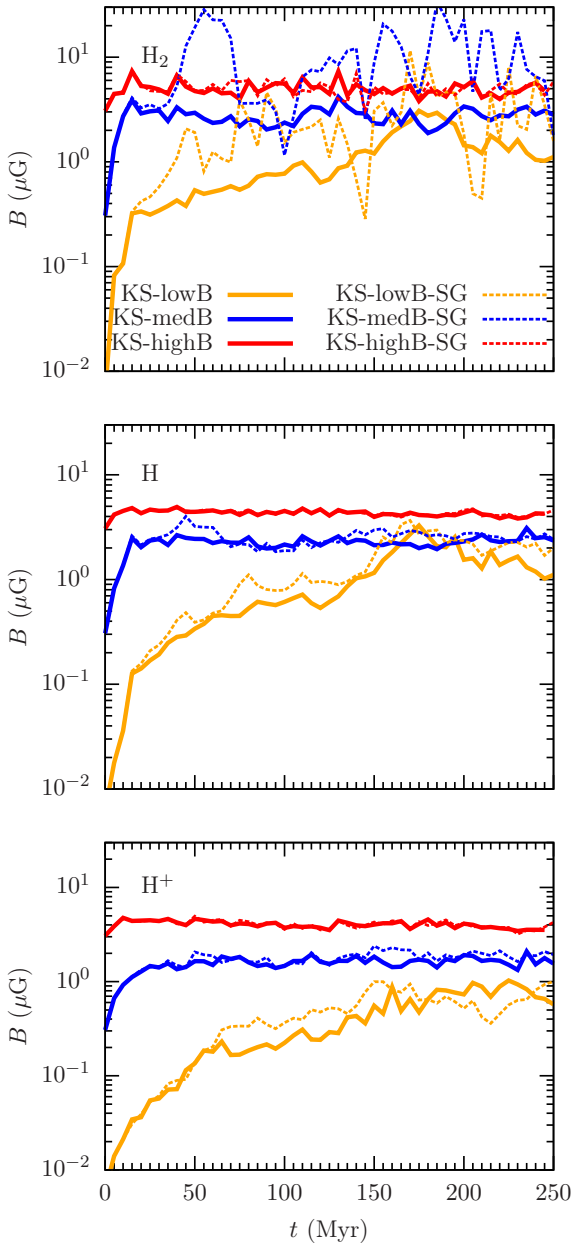

Figure 3.13: Mass weighted magnetic field evolution in H_2 (*top panel*), atomic H (*middle panel*) and H^+ (*bottom panel*). KS-lowB (solid orange line), KS-medB (solid blue line), KS-highB (solid red line), KS-lowB-SG (dashed orange line), KS-medB-SG (dashed blue line) and KS-highB-SG (dashed red line). The magnetic field reaches up to 10 μG in H_2 with self-gravity while for KS-medB the field is around 3 μG in H and 2 μG in H^+.

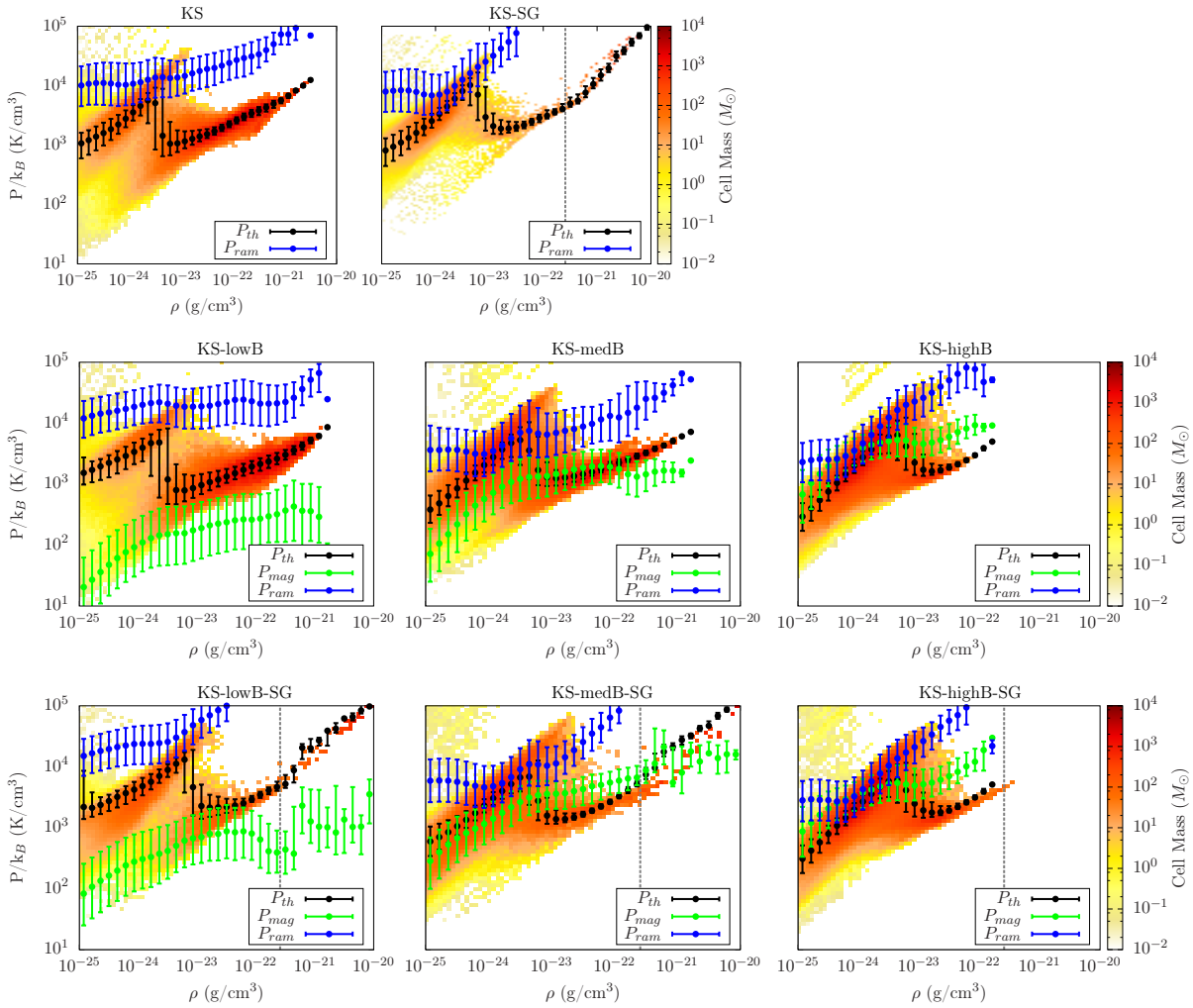

Figure 3.14: Pressure-density phase plots with mass colour-coding at 150 Myr. *Top row*: KS (left) and KS-SG (right), KS-lowB (left), *middle row*: KS-medB (middle) and KS-highB (right) and *bottom row*: KS-lowB-SG (left), KS-medB-SG(middle) and KS-highB-SG (right). The black points stand for the median thermal pressure, green for the median magnetic pressure and blue for the ram pressure averaged over 148-152 Myr, with the bar limits representing the 25th and 75th percentile. The grey dotted line represents the maximum density we can resolve according to the Truelove criterion, computed assuming a temperature of 100 K. The stronger the initial field, the lower the maximum density that can be reached. Ram pressure dominates over the thermal and the magnetic pressure in all the simulations, over the entire density regime. Self-gravity allows the gas to reach a much higher maximum density.

in KS-highB (shown also in Fig. 3.1).

As discussed earlier, the KS-highB-SG model does not develop as high densities as its counterparts at lower field strengths. There could be several reasons for this behaviour. First, we notice that the density structure in model KS-highB-SG is much more uniform than for lower field strengths. This suggests that the magnetic field "cushions" the effect of the supernova explosions, preventing efficient compressions and sweep-up of gas to large (column) densities. Second, the accumulation length along the (strong) field may be too short in our box to allow the build-up of a column density large enough for self-gravity to dominate. This column density is determined by the critical mass-to-flux ratio, which for a sheet of infinite extent results in $N_c = B/(2\pi mG)$, with the critical column density N_c, the magnetic field strength B, and the particle mass m (Crutcher, 2012). In numbers, this corresponds to

$$N_c = 3.7 \times 10^{20} \left(\frac{B}{\mu G}\right) \text{ cm}^{-2}, \tag{3.1}$$

at a mean molecular weight of $\mu = 1$. For our strongest field of 3μG, this corresponds to $N_c = 1.1 \times 10^{21}$ cm^{-2}, yet the mean column density in our simulation box is $N = 3.9 \times 10^{20}$ cm^{-2}. In other words, due to the strong magnetic field, the only way to build up high column densities is by flows *along* the field lines, resulting in the mean column density dictating the onset of gravitational instability as well as H_2 formation (e.g. Bergin et al., 2004). Conversely, in the models without, or with sufficiently weak magnetic fields, motions perpendicular to the field lines can contribute to the build-up of (local) column densities, enhancing the shielding, and allowing for gravitational collapse (see also discussion in Heitsch and Hartmann, 2008).

For the low initial field simulations, up to a density of 10^{-24} g/cm^3, the thermal pressure is more than two orders of magnitude higher than the magnetic pressure and one order of magnitude lower than the ram pressure, $P_{\rm ram} = \rho v^2$. This is the region where the gas has high temperatures and it is frequently heated by SN blasts. Keep in mind, however, that the mean magnetic field strength is resolution dependent (see Appendix A.2). Between 10^{-24} and 10^{-23} g/cm^3, in the thermally unstable regime, the thermal pressure drops significantly while the magnetic pressure keeps rising. However, the magnetic pressure remains always lower than the thermal pressure in KS-lowB and KS-lowB-SG (see Fig. 3.4). In the KS-medB case the two pressures are comparable in the cold regime while still dominated by turbulence. In KS-highB, the magnetic pressure is high enough in all density regimes to dominate over the thermal pressure but remains below the ram pressure.

Self-gravity allows the formation of denser structures, hence a more than one order of magnitude difference in the maximum density reached between KS-lowB, KS-medB and KS-highB (top row) and the self-gravity runs (bottom row) develops. Above $\rho \sim 10^{-23}$ g/cm^3 the ram pressure grows approximately linearly with density in these simulations indicating that v^2 does not vary as a function of ρ. In all simulations, $P_{\rm ram}$ is the dominant energy component. For KS-lowB-SG, the magnetic pressure grows with density up to $\sim 10^{-22}$ g/cm^3 and then flattens while the thermal pressure grows linearly. In KS-medB-SG we notice similar general trends in the scaling of magnetic pressure. How-

ever, $P_{\rm mag}$ is overall higher and exceeds $P_{\rm ram}$ for 10^{-23} g/cm^3 $\leq \rho \leq$ 10^{-22} g/cm^3. In KS-highB-SG the magnetic pressure exceeds the thermal one over the entire density range.

The plasma-β parameter (the ratio of the thermal to magnetic pressure $\beta = P_{\rm th}/P_{\rm mag} = 8\pi P_{\rm th}/B^2$) is shown in Fig. 3.15. We present slices of the temperature and the corresponding plasma-β through the densest region in the simulation box for different times. The top two rows are for KS-lowB and the bottom two rows for KS-highB. Locally, in the extreme cases, regions with very low temperatures correspond to low plasma-β and also extremely high temperature regions correlate with very high plasma-β (see the upper tails in Fig. 3.16). However, overall this correlation is not obvious for intermediate temperatures (e.g. in the upper two rows, the regions with temperatures above 10^4 K correspond to high plasma-β, but in the bottom rows temperatures lower than 10^4 K do not have a one-to-one correspondence to low plasma-β values).

We illustrate in Fig. 3.16 a two-dimensional histogram of the plasma-β parameter as function of temperature, with the black line indicating the $\beta = 1$ limit. For KS-lowB, the scatter in β is very large (4 to 5 orders of magnitude) in any temperature regime, showing that the magnetic field is still being amplified at this time, even in the cold, dense clumps. In contrast, in KS-highB, most of the gas is magnetically dominated. However, the same large scatter in β can be seen for temperatures between 10^3 and 10^4 K. This region corresponds to the peak in the volume and mass weighted density PDFs (see Fig. 3.6).

Figure 3.17 is a two-dimensional histogram of the plasma-β parameter as a function of density. In the top row we plot β for the simulations without self-gravity with increasing magnetic field strength from the left to the right and on the bottom row, the corresponding simulations with self-gravity, all at 150 Myr. The black points at 10^{-24} g/cm^3 represent the initial states of the simulations. Because of the very low initial seed field, the initial plasma-β of KS-lowB and KS-lowB-SG is about $\beta = 2 \times 10^6$. Most of the mass in the intermediate and low initial field simulations shifts from a large β towards the $\beta = 1$ limit and below (for KS-medB and KS-medB-SG) which reflects the amplification of the field via the dynamo effect and compression of the gas in combination with flux-freezing. In KS-highB and KS-highB-SG the gas is initially completely magnetically dominated and over time due to the SNe that inject thermal energy into the ISM, some of the gas reached higher plasma-β values. However, during the time of the simulations, 70% of the gas mass is magnetically dominated.

For the simulations without self-gravity the magnetically dominated gas mass is larger with stronger magnetic field (7% in KS-lowB, 30% in KS-medB and 71%in KS-highB). For the self-gravity simulations, the KS-highB-SG mass fraction with $\beta < 1$ is very similar to KS-highB. In KS-lowB-SG and KS-medB-SG the very dense clumps formed early in the simulations (see Fig. 3.1) have high thermal pressures leading to a lower mass fraction of the magnetically dominated gas (1% in KS-lowB-SG and 16% in KS-medB).

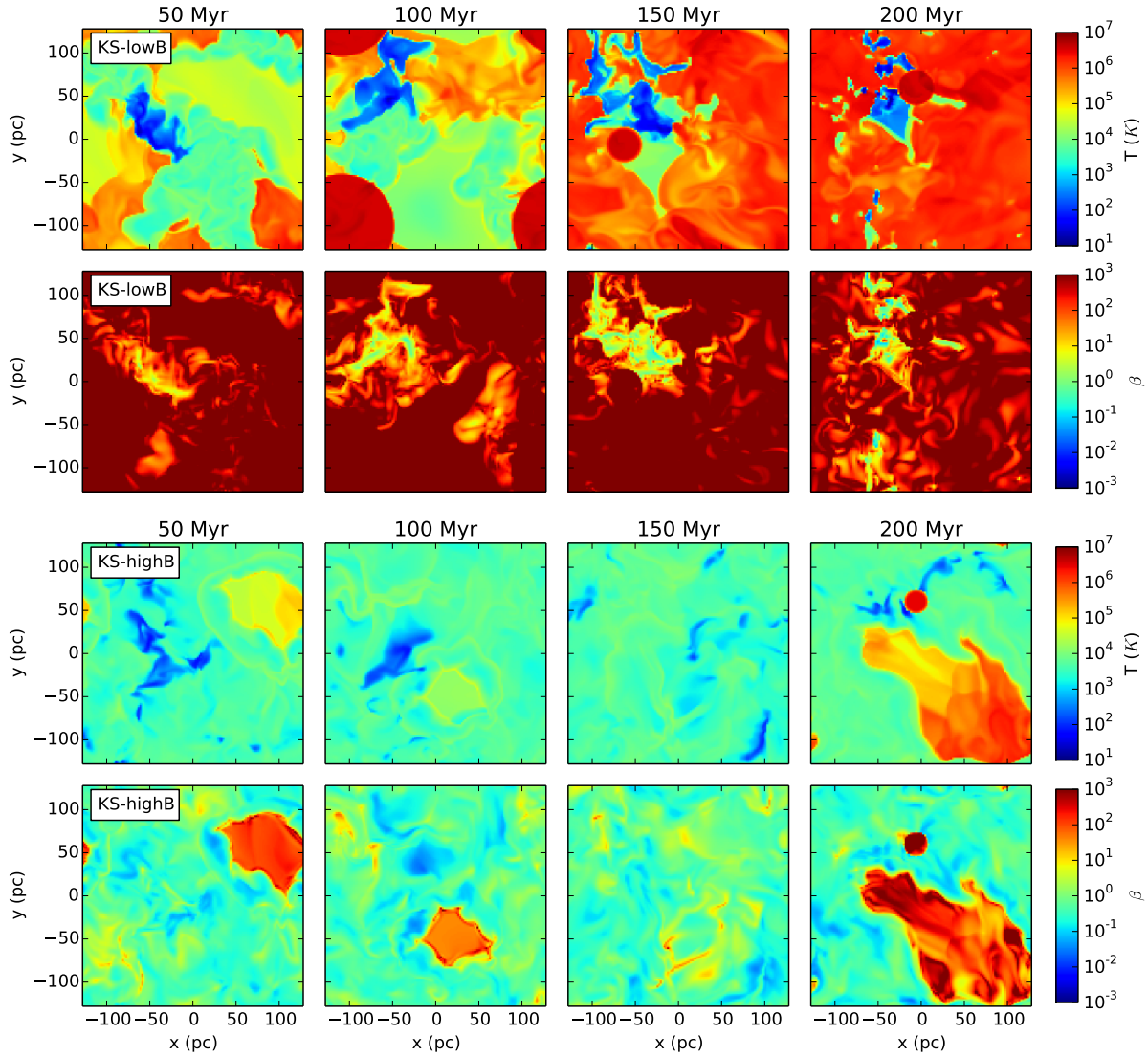

Figure 3.15: Time sequence of temperature slices through the plane defined by the densest region along the z axis (*top row*) at 50, 100, 150 and 200 Myr and the plasma-β parameter (*second row*) for KS-lowB, same for KS-medB (*third* and *fourth row*) and KS-highB (*fifth* and *bottom row*). High temperature and high plasma-β (low temperature and low plasma-β) are well correlated only locally, for extreme temperatures.

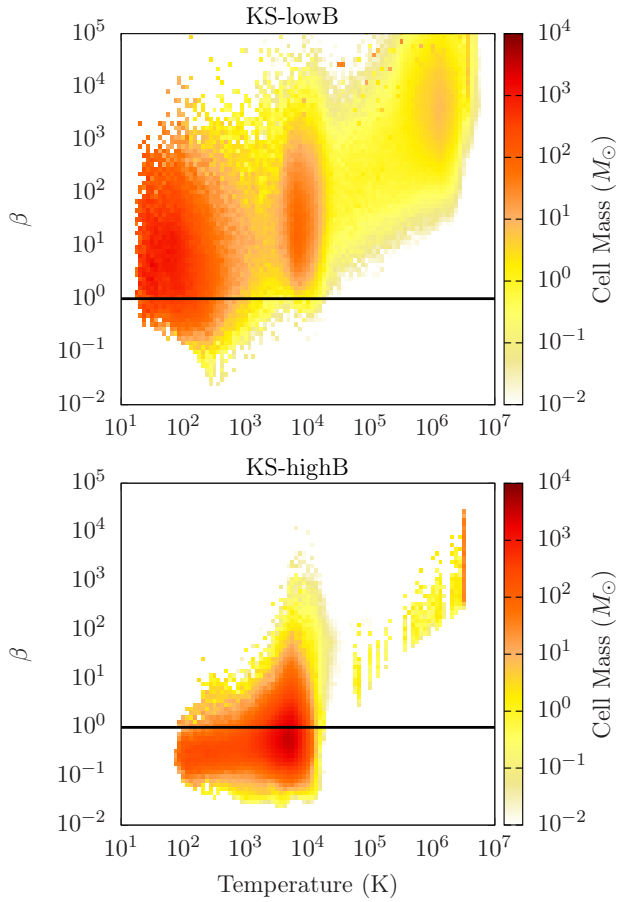

Figure 3.16: Plasma-β parameter as a function of temperature at 150 Myr for KS-lowB (*top panel*) and KS-highB (*bottom panel*). While only a small mass fraction lies below $\beta = 1$ in KS-lowB, most of the gas in KS-highB is magnetically dominated.

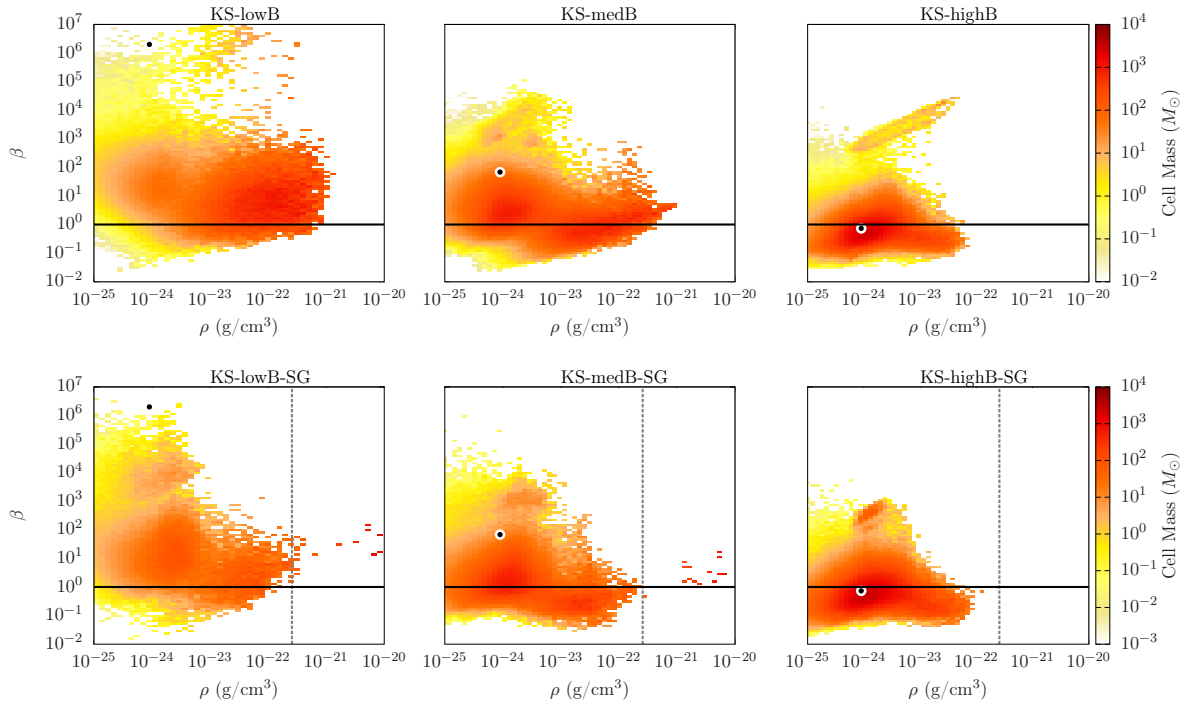

Figure 3.17: Plasma-β as a function of density at 150 Myr. In the *top row* we show KS-lowB (left), KS-medB (middle) and KS-highB (right). In the *bottom row*: KS-lowB-SG (left), KS-medB-SG (middle) and KS-highB-SG (right). The black line marks the limit $\beta = 1$. The black point at 10^{-24} g/cm^3 represents the initial state of the simulation. The grey dotted line represents the maximum density we can resolve according to the Truelove criterion. The stronger the initial field the more the magnetic pressure dominates over the thermal pressure in the dense gas. With self-gravity we obtain very dense structures with high thermal pressures. There is less mass below $\beta = 1$ with self-gravity in comparison to the simulations without self-gravity.

3.4.2 Magnetic field scaling with density

The energy balance between kinetic and magnetic energy in simulations depends on two factors: the magnetic field amplification and dissipation. Recent studies describe the amplification of a magnetic seed field due to gravitational collapse through the small-scale turbulent dynamo (Sur et al., 2010; Federrath et al., 2011b; Peters et al., 2012; Schober et al., 2012). Unfortunately, in this paper, we cannot discuss the mechanisms that lead to the amplification of the magnetic field in detail because of limited resolution. The magnetic field evolution has been studied in detail in isothermal environments with 1024^3 and 2048^3 cells (see Kritsuk et al., 2009; Jones et al., 2011; Federrath et al., 2014a) but our demanding thermodynamics makes a resolution of 512^3 cells already hard to achieve (see Appendix B). Another reason is the wide temperature range and the chemistry of the ISM model which makes it difficult to recover key parameters for describing the dynamo (Magnetic Prandtl number $P_{\rm m}$, Reynolds number $R_{\rm e}$, Magnetic Reynolds number $R_{\rm m}$, (for details see Kritsuk et al., 2011; Schober et al., 2012). In addition, we face numerical dissipation of the magnetic field without specifically including diffusive terms in the MHD equation. Tests of decaying supersonic MHD turbulence have been conducted by Kritsuk et al. (2011) on state-of-the-art MHD codes. The study shows that the magnetic energy in all codes drops by 6% to 30% over 0.2 turnover times, after the turbulent driving stops. As the initial conditions are identical, this difference is only due to the intrinsic numerical dissipation of the MHD solvers. However, Lazarian (2013) concluded the numerical diffusivity can account for fast magnetic reconnection which removes the magnetic field from the turbulent plasma during star formation. In this sense, numerical dissipation could provide a good representation of reconnection diffusion.

In our case, the situation is more complex. Our simulations are not isothermal and we introduce motions by SN explosions. Hence, the dynamical driving scales as well as the scales on which magnetic dissipation and amplification occur are not as well defined as in idealised turbulence simulations with, e.g. Ornstein-Uhlenbeck driving (see, e.g. Eswaran and Pope, 1988). The magnetic field amplification and dissipation occurs in gas with very different densities and temperatures because SNe go off in an already highly structured, magnetised, multi-phase ISM.

In Fig. 3.18 we show a 2D profile of the magnetic field as a function of density, at 150 Myr, with the mass color-coded. We over-plot the median volume weighted magnetic field with the bars representing the 75th and 25th percentile and average the field over 4 Myr (between 148-152 Myr). The scaling in the runs without self-gravity is very similar to the one in the simulations with self-gravity, which is shown here.

There is a large scatter in the magnetic field values for a given density suggesting that the gas is driven by turbulence rather than channeled by the magnetic field. This is the case in all our simulations, as seen in Fig. 3.14; the ram pressure dominates over the magnetic and thermal pressure (see also de Avillez and Breitschwerdt, 2005). At low densities, below 10^{-24} - 10^{-25} g/cm^3, the gas is frequently heated by the SN. Every time the SNe blasts blow away the gas they swipe along the field lines too, so the low density tail of the scaling reflects the way we introduce turbulence into the simulations.

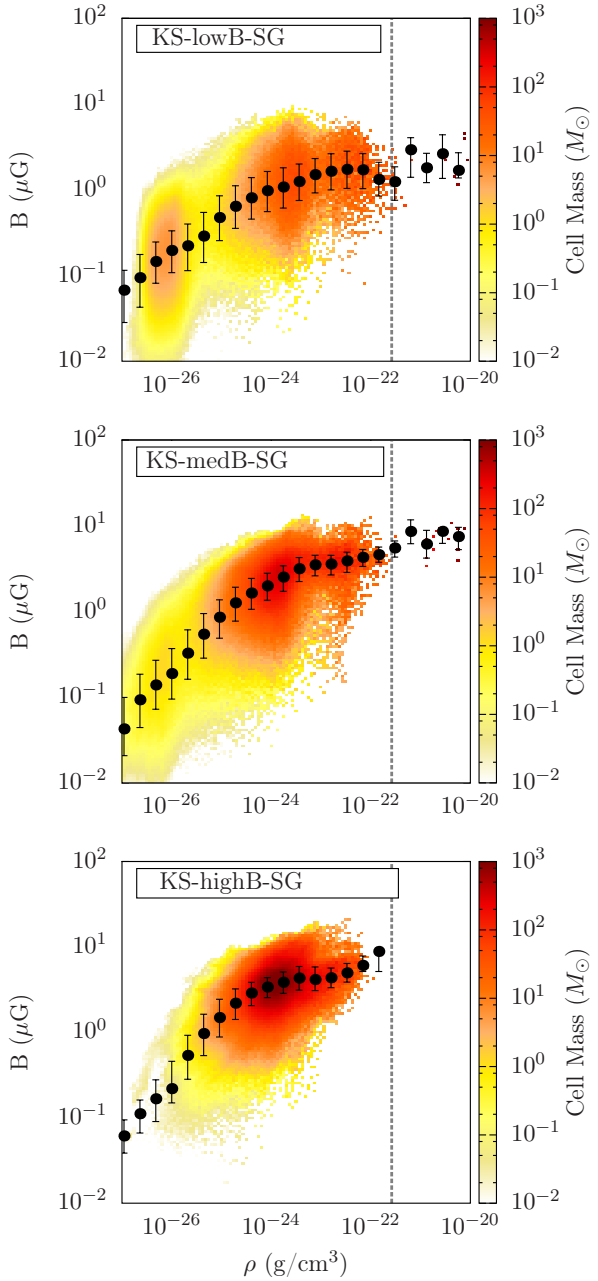

Figure 3.18: Scaling of the magnetic field with density for KS-lowB-SG around 150 Myr (black dots)- *top panel*, KS-medB-SG (*second panel*) and KS-highB-SG (*bottom panel*). The grey dotted line represents the maximum den sity we can resolve according to the Truelove criterion. There is a large scatter in the magnetic field strength with density indicating that the gas in the box is dominated by the kinetic energy density.

The magnetic field strength does not increase with ρ over the entire density range. Above $\sim 10^{-24}\,\mathrm{g/cm^3}$ the scaling flattens. This flattening could be a numerical artefact due to the limited resolution and a missing dynamo effect in dense regions, which are confined to small spatial scales and thus unresolved at higher densities.

Due to the numerical limitations, it is difficult to compare our scaling to other previous studies (Li et al., 2015b; Collins et al., 2011). Furthermore, we have only a small number of molecular clouds formed in our simulations. However, we compare the magnetic field strength in the high density gas to the observations of Crutcher (2012) and even though the magnetic field in our densest resolved structures is lower than the upper limit of the line-of-sight magnetic field, we are within the observed range.

3.5 Conclusions

We use the 3D magnetohydrodynamic code FLASH in version 4 to study the structure of the magnetised, multiphase interstellar medium and focus on the connection between magnetic fields and the chemical composition. We use periodic boxes with a volume of $(256\,\mathrm{pc})^3$ with different initial magnetic field strengths of 6×10^{-3}, 0.3 and $3\,\mu$G. SNe are injected as individual explosions at a fixed rate at random locations. We focus on the chemical evolution following mainly ionised, atomic and molecular hydrogen over a total simulation time of 250 Myr. Our results can be summarised as follows:

- The mass weighted magnetic field in simulations with low and medium initial field strengths saturate at 1-3 μG. In simulations including self-gravity the field strength reaches up to $\sim$10 μG. The time to reach saturation is $\sim$ 20 Myr for a medium initial field and about five to eight times larger for very weak initial fields. Our strong initial field of $3\,\mu$G is already above the dynamically reached saturation limit and remains unchanged. Increasing the resolution indicates that the field strength in our simulations is not converged.

- The dense molecular clouds and structures show magnetisations of the order of $1 - 10\,\mu$G, consistent with the range of of field strengths observed in molecular clouds.

- For the fixed supernova rate and identical positions for all simulations the initial field strength has a strong impact on the resulting structure of the interstellar medium. Starting from a homogenous warm phase, the runs with low and medium initial fields evolve into a multi-phase interstellar medium with tangled magnetic fields and well defined cold, warm and hot phases. The simulations with the lowest initial field strength develop the highest hot gas volume filling fractions ($\sim$ 80%) and have the highest mass fraction in cold and molecular gas.

- The simulations with high initial fields do not develop into a distinct multi-phase ISM. Instead, they remain dominated by warm gas at densities close to the mean density, permeated by a coherent large-scale magnetic field. In those simulations

very little molecular hydrogen is formed. The injected SNe do not provide sufficient dynamical driving in order to form long-lived dense structures that are able to resist the opposing magnetic pressure long enough to exceed the cooling time and the time for H_2 formation.

- Self gravity increases the fraction in molecular gas for low and intermediate magnetic fields but has only a moderate impact on the overall multi-phase structure.
- The mass fraction of magnetically dominated gas ($\beta \equiv P_{\rm th}/P_{\rm mag} < 1$) increases with the initial strength of the magnetic field ranging from 7% for $B_{\rm init} = 6\,{\rm nG}$ to 70% for $B_{\rm init} = 3\,\mu{\rm G}$.

Chapter 4

The impact of massive runaway stars on the shaping of the ISM

4.1 Introduction

For more than half a century, the dynamics of stars has sparked interest and curiosity (Oort, 1928; Blaauw, 1961; Poveda et al., 1967). Runaway stars are defined as O- and B-type stars with large peculiar velocities, larger than 40 km/s (Blaauw, 1961). There are two main mechanism for the formation of runaway stars. The first mechanism is the binary supernova scenario (Blaauw, 1961; Eldridge et al., 2011): a runaway and a neutron star are produced when a (Type Ia or Type II) SN explodes within a binary system. Runaway stars formed through this mechanism have a high rotational velocity and enhanced helium abundance. Observations show that at least 50∼80% of B- and O-type stars are multiples (Chini et al., 2012). The second mechanism is the dynamical ejection (Poveda et al., 1967; Fujii and Portegies Zwart, 2011; Perets and Subr, 2012) scenario: the gravitational interactions between stars in a dense, young cluster cause the ejection of runaways.

Whether runaway stars or stars with lower peculiar velocities (of ~ 15 km/s, see Tetzlaff et al., 2011), it seems like the majority of OB stars explode as Type II SNe from a few tens of parsecs to even thousands of parsecs away from their birthplaces. There have been simulations carried out (Portegies Zwart et al., 2007; Perets and Subr, 2012), as well as observations (Zinnecker and Yorke, 2007; Tetzlaff et al., 2011), but still the exact percentages of OB stars traveling away from their birth places and more importantly the velocities that most of them have when leaving their birth molecular cloud (MC) are still unknown. There is hope that the Gaia project will shed some light on these fractions soon. However, there is evidence of Type II SNe exploding in various environments: low-density gas (Rogers and Pittard, 2013), HII regions (Dale et al., 2014; Walch and Naab, 2015), old SN remnants (Gatto et al., 2015) or molecular gas (Fukui et al., 2003; Hewitt and Yusef-Zadeh, 2009).

Type II SNe, in general, have been shown to have a crucial impact on the shaping of the ISM (see e.g. Gatto et al., 2015; Walch et al., 2015; Girichidis et al., 2016; Gatto et al.,

2016; Pardi et al., 2017) by introducing turbulence (Mac Low and Klessen, 2004; Klessen and Glover, 2016), forming colliding flows (Heitsch et al., 2011; Hennebelle et al., 2008; Banerjee et al., 2009) or creating the hot phase of the ISM (Cox and Smith, 1974; McKee and Ostriker, 1977). Detailed simulations have been carried out in order to study the impact of SNe location along with their spatial and temporal clustering (Hill et al., 2012; Gent et al., 2013b; Kim et al., 2013; Walch et al., 2015; Girichidis et al., 2016; Balsara et al., 2004; Mac Low et al., 2005; Slyz et al., 2005; Gatto et al., 2015; Li et al., 2015a), showing that the positioning (and clustering) of SNe has a major impact on the structure of the ISM.

Magnetic fields have also been studied and observed in the interstellar medium (ISM; e.g. Han, 2009; Crutcher, 2012; Beck and Wielebinski, 2013). It was found that they impact the dynamical evolution of the gas on galactic scales (e.g. Han, 2004; Frau et al., 2012; Alves et al., 2014). In the previous chapter we showed that even just the turbulent component of the magnetic field can affect drastically the amount of molecular hydrogen formed and hence has a crucial impact structure and life-cycle of MCs.

The role of self-gravity in shaping the ISM has been discussed by Walch et al. (2015), who, using hydrodynamical simulations as well, showed that without self-gravity, it is impossible to obtain reasonable estimates of dense and molecular gas. However, recently, Padoan et al. (2016) have seen little influence from self-gravity in a very similar simulation setup. There are also studies in which self-gravity is turned on after a certain equilibrium is reached or after the point when the influence of initial conditions is lost (see e.g. Padoan et al., 2016; Ibáñez-Mejía et al., 2016). In the previous chapter we discussed the differences between considering self-gravity at the beginning of the simulations and the late switch on and found that the ISM evolution is significantly different. We showed that in the case when self-gravity is switched on after chemical equilibrium is reached produces isolated dense structures without any embedding gas.

Walch et al. (2015) and Gatto et al. (2016) showed how the chemistry and ISM structure changes with different fractions of SNe exploding in peak density regions. Here, we extend this study to the magnetised ISM and including self-gravity, using three-dimensional MHD simulations including a chemical network and shielding from an interstellar radiation field, to explore how magnetic fields and self-gravity alter the formation of molecular gas in the ISM with different fractions of SNe exploding in peak densities. We present the details of the simulations, the list of simulations and the initial conditions in Subchapter 4.2. We discuss the morphological evolution of the simulations in Subchapter 4.3 and the impact of the SN peak fractions (PF) on the chemical composition, volume filling fraction (VFF) and thermal pressure of runs with and without self-gravity in Subchapter 4.4. We show the strength of the magnetic field in different media and the plasma-β parameter in Subchapter 4.5. In Subchapter 4.6 we discuss the structure of the ISM in higher initial density runs and we present our conclusions in Subchapter 4.7.

4.2 Simulations and initial conditions

We use an approach very similar to what was described in the previous chapter. We implement SN explosions at a fixed rate just like previously.

All simulations cover a box volume of $(256\ \mathrm{pc})^3$. We start with atomic gas of solar composition, at a uniform temperature of $T = 5000$ K and with a uniform number density of $n_\mathrm{i} = 0.5$ and $3\,\mathrm{cm}^{-3}$. This yields a gas surface density of $\Sigma_\mathrm{gas} = 4.1\,M_\odot\,\mathrm{pc}^{-2}$ and $\Sigma_\mathrm{gas} = 24.3\,M_\odot\,\mathrm{pc}^{-2}$ for the box, and a total gas mass of $3 \times 10^5\,M_\odot$ and $16 \times 10^5\,M_\odot$ respectively (comparable to the mass of a giant molecular cloud, see Hughes et al., 2010). We adopt a fiducial numerical resolution of 128^3 cells (L5), equivalent to a physical resolution of 2 pc/cell.

We run simulations with different fractions of the SNe exploding in peak density regions (see Table 4.2). A fraction of 100% represents a scenario in which all the SNe explode in density peaks, modelling an ISM in which none of the massive (OB-type) stars travel out of their parental MC before they explode as Type II SNe. On the other hand, the fully random positioning (likely, close to 0% peak fraction) would model an ISM in which the massive stars have a very high probability to travel away from their MC. Due to the dimensions of the simulated volume, $(256\ \mathrm{pc})^3$, if we consider a runaway star with a peculiar velocity of 30 km/s and a lifetime of 10 Myr (O type star with $M = 13\ M_\odot$), the star would travel about 300 pc in its lifetime. As B type stars live longer and massive stars can have smaller and larger peculiar velocities than 30 km/s, the distance they travel varies largely but as long as it is comparable to the size of our simulation box, a random distribution of SNe captures the variety of massive stars and peculiar velocities meaningfully. The peak fractions between 0% and 100% represent intermediate scenarios, from the one in which most likely all the massive stars travel away from their birth place, to the extreme case in which none of them do.

4.3 Morphological evolution

SNe explosions introduce turbulence in an initially homogeneous, atomic hydrogen environment. The compressed gas between the SN shells forms high density structures and molecular hydrogen, while SNe exploding inside these structures can disperse the gas and destroy the formed clouds.

Figure 4.1 shows the morphological differences of the ISM between different fractions of peak-exploding SNe, in an unmagnetised and magnetised environment, with and without self-gravity. We compare column density projections after 100 Myr for 10%, 30%, 70% and 90% peak-exploding SNe (first row) showing that with higher peak fraction (PF) less dense structures are formed. In the second row, we present the same peak-fractions but in a magnetised environment. The trend here is the same, smaller peak fractions lead to the formation of regions with higher density. Compared to the unmagnetised simulations, the magnetic runs produce a more homogeneous ISM (see discussion in the previous chapter).

The third (not magnetised) and fourth row (magnetised) in Fig. 4.1 represent the same

No.	Sim. name	peak fr. %	n_i [cm^{-1}]	SN rate [Myr^{-1}]	B [μG]	self-gravity
1	p0	0	0.5	1.2	0	no
2	p0B	0	0.5	1.2	0.3	no
3	p10	10	0.5	1.2	0	no
4	p10B	10	0.5	1.2	0.3	no
5	p20	20	0.5	1.2	0	no
6	p20B	20	0.5	1.2	0.3	no
7	p30	30	0.5	1.2	0	no
8	p30B	30	0.5	1.2	0.3	no
9	p40	40	0.5	1.2	0	no
10	p40B	40	0.5	1.2	0.3	no
11	p50	50	0.5	1.2	0	no
12	p50B	50	0.5	1.2	0.3	no
13	p60	60	0.5	1.2	0	no
14	p60B	60	0.5	1.2	0.3	no
15	p70	70	0.5	1.2	0	no
16	p70B	70	0.5	1.2	0.3	no
17	p80	80	0.5	1.2	0	no
18	p80B	80	0.5	1.2	0.3	no
19	p90	90	0.5	1.2	0	no
20	p90B	90	0.5	1.2	0.3	no
21	p100	100	0.5	1.2	0	no
22	p100B	100	0.5	1.2	0.3	no
23	sg-p0	0	0.5	1.2	0	yes
24	sg-p0B	0	0.5	1.2	0.3	yes
25	sg-p10	10	0.5	1.2	0	yes
26	sg-p10B	10	0.5	1.2	0.3	yes
27	sg-p20	20	0.5	1.2	0	yes
28	sg-p20B	20	0.5	1.2	0.3	yes
29	sg-p30	30	0.5	1.2	0	yes
30	sg-p30B	30	0.5	1.2	0.3	yes
31	sg-p40	40	0.5	1.2	0	yes
32	sg-p40B	40	0.5	1.2	0.3	yes
33	sg-p50	50	0.5	1.2	0	yes

Table 4.1: List of simulations and parameters. From left to right we list the name of the simulation, the peak fraction, the initial density of the gas, the SN rate, initial magnetic field strength and whether or not the simulations were carried out with self-gravity.

No.	Sim. name	peak fr. %	n_i [cm^{-1}]	SN rate [Myr^{-1}]	B [μG]	self-gravity
34	sg-p50B	50	0.5	1.2	0.3	yes
35	sg-p60	60	0.5	1.2	0	yes
36	sg-p60B	60	0.5	1.2	0.3	yes
37	sg-p70	70	0.5	1.2	0	yes
38	sg-p70B	70	0.5	1.2	0.3	yes
39	sg-p80	80	0.5	1.2	0	yes
40	sg-p80B	80	0.5	1.2	0.3	yes
41	sg-p90	90	0.5	1.2	0	yes
42	sg-p90B	90	0.5	1.2	0.3	yes
43	sg-p100	100	0.5	1.2	0	yes
44	sg-p100B	100	0.5	1.2	0.3	yes
45	P0	0	3	14	0	no
46	P0B	0	3	14	0.3	no
47	P20	20	3	14	0	no
48	P20B	20	3	14	0.3	no
49	P40	40	3	14	0	no
50	P60	60	3	14	0	no
51	P60B	60	3	14	0.3	no
52	P80	80	3	14	0	no
53	P80B	80	3	14	0.3	no
54	P100	100	3	14	0	no
55	P100B	100	3	14	0.3	no
56	sg-P0	0	3	14	0	yes
57	sg-P0B	0	3	14	0.3	yes
58	sg-P20	20	3	14	0	yes
59	sg-P20B	20	3	14	0.3	yes
60	sg-P40	40	3	14	0	yes
61	sg-P40B	40	3	14	0.3	yes
62	sg-P60	60	3	14	0	yes
63	sg-P60B	60	3	14	0.3	yes
64	sg-P80	80	3	14	0	yes
65	sg-P80B	80	3	14	0.3	yes
66	sg-P100	100	3	14	0	yes
67	sg-P100B	100	3	14	0.3	yes

Table 4.2: List of simulations and parameters. From left to right we list the name of the simulation, the peak fraction, the initial density of the gas, the SN rate, initial magnetic field strength and whether or not the simulations were carried out with self-gravity.

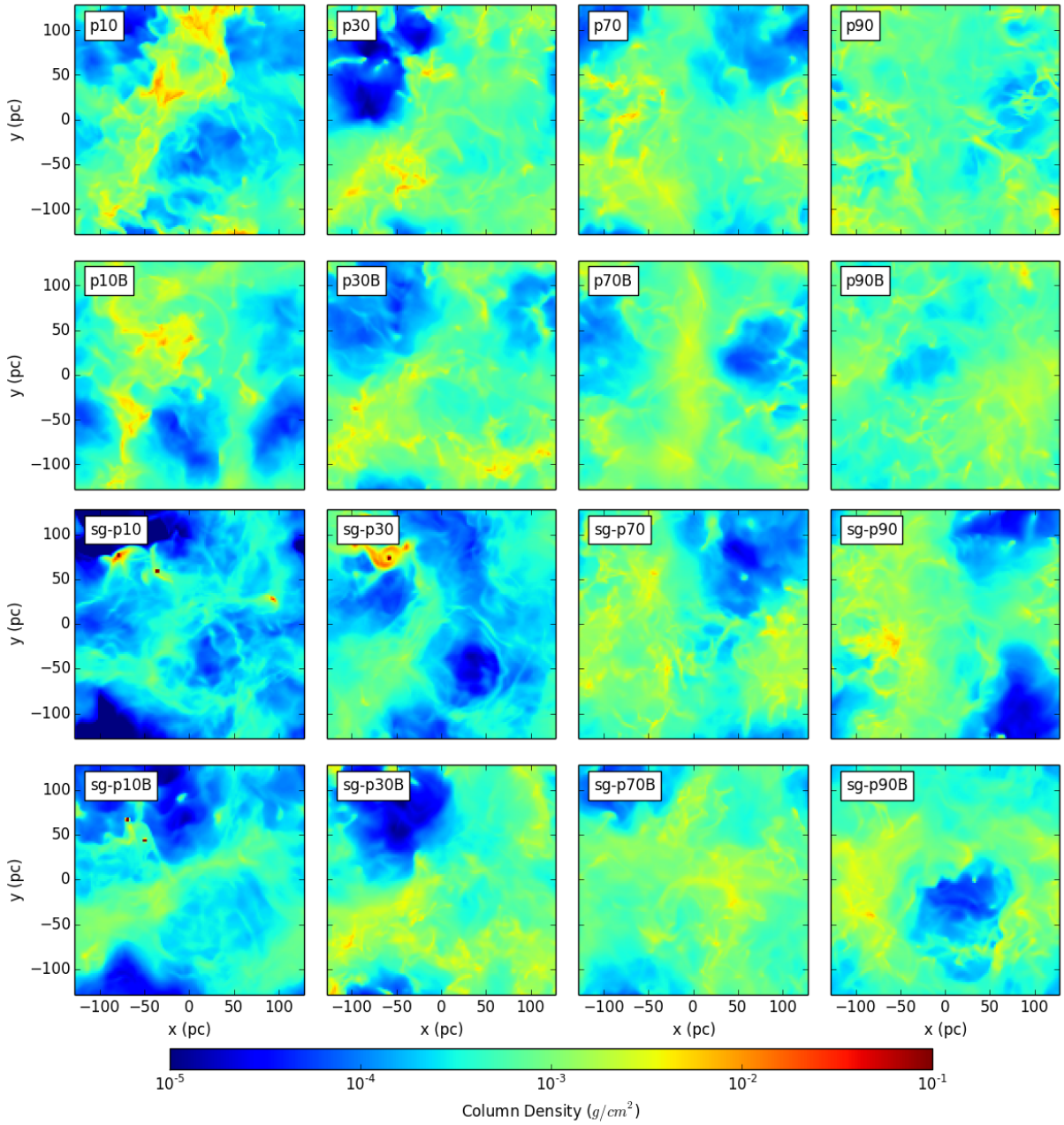

Figure 4.1: Column densities of runs p10, p30, p70, p90 (*first row*), the runs with the same peak fraction but with magnetic fields (*second row*), with self-gravity (*third row*) and self-gravity with magnetic fields (*last row*), all at 100 Myr. The ISM is more homogeneous with a higher peak fraction, and for the same peak fraction in the magnetised runs. Self-gravity determines the rapid formation of very dense and cold molecular blobs at low peak fractions (sg-p10 and sg-p30), but in an initially magnetised environment these clumps are absent for a peak fraction of 30%.

column density projections (with the same peak fractions) but for simulations including self-gravity. With 10 and 30% peak fractions, small and very dense clumps are formed, reaching column densities one order or magnitude higher in comparison to the maximum column density reached without self-gravity. In low peak fraction runs, the volume filled with hot and low density gas is high, while the cold dense gas is concentrated in very small areas (see also Gatto et al., 2015). The ISM formed with high SN peak fractions is much more homogeneous because a higher number of SNe explode in these peak densities and can more efficiently disperse them. This dramatic difference is reflected in the average H_2 mass fractions and VFFs, described in detail in Subchapter 4.4.1.

We show in Fig. 4.2 the mass and volume weighted density probability distribution functions (PDFs) of the simulations without self-gravity (with peak fractions of 10%, 30%, 70% and 90%, left panels) and with self-gravity (same peak fractions, right panels). We show the temperature PDF's in Appendix B.1, Fig. B.1. In the left panels of Fig. 4.2, the PDFs have three distinct peaks, at 10^{-27}, 10^{-24} and 10^{-22} g/cm^3, indicative of the three-phase ISM. The peak at 10^{-27} g/cm^3 is higher for a PF of 10% and 30%, dropping almost an order of magnitude for higher PFs, while the third peak, at 5×10^{-23} g/cm^3, does not exist. This is in concordance with Fig. 4.1, first row which shows that the ISM is more homogeneous when stirred with a high PF driving. Low peak fractions determine a higher 10^{-22} g/cm^3 peak, and the maximum reached density is higher (for p10 the maximum density is 5.6×10^{-22} g/cm^3 while for p30 it is 2×10^{-22} g/cm^3 and 1.8×10^{-22} g/cm^3 for p70 and p90). In the magnetised simulations (left panels, dashed lines) the peaks at 10^{-24} and 10^{-22} g/cm^3 are more balanced and the maximum densities of these simulations are lower compared to the unmagnetised ones: for p10B the maximum density is a factor of two lower than in p10 as well as for p90B compared to p90.

The ISM formed in the simulations including self-gravity and magnetic fields is more homogeneous than without magnetic fields (Fig. 4.1, third and bottom row) This can be seen as well in the upper right panel of Fig. 4.2. In the regions of density between 10^{-24} and 10^{-22} g/cm^3, simulations sg-p10B, sg-p70B and sg-p90B have PDFs between the values of sg-p10 and sg-p70, sg-p90. sg-p10 and sg-p30 reach maximum densities of orders of 10^{-19} g/cm^3, more than one order of magnitude higher than in sg-p70 and sg-p90.

4.4 Results and discussions

We focus on the time evolution of the H_2, H and H^+ mass fractions to analyse the chemical state of the ISM. For explanations on the resolution limitation for the analysis of CO, see Chapter 3, Appendix A.1. We let the simulations run for 150 Myr (except p60B which runs only 80 Myr) and for each run we average the quantities over the last 100 Myr of evolution, obtaining each point in Fig. 4.3, 4.5, 4.9, 4.10, 4.11 etc. The full evolution of the H_2 mass fractions for the fiducial and self-gravity runs are presented in Appendix B.2.

The evolution of chemical species is tightly linked to the balance between dense structure formation (by gas compression between SN shells) and destruction (by dense gas dispersion due to SN explosions, hence the SN peak fraction). As shown Chapter 3 mag-

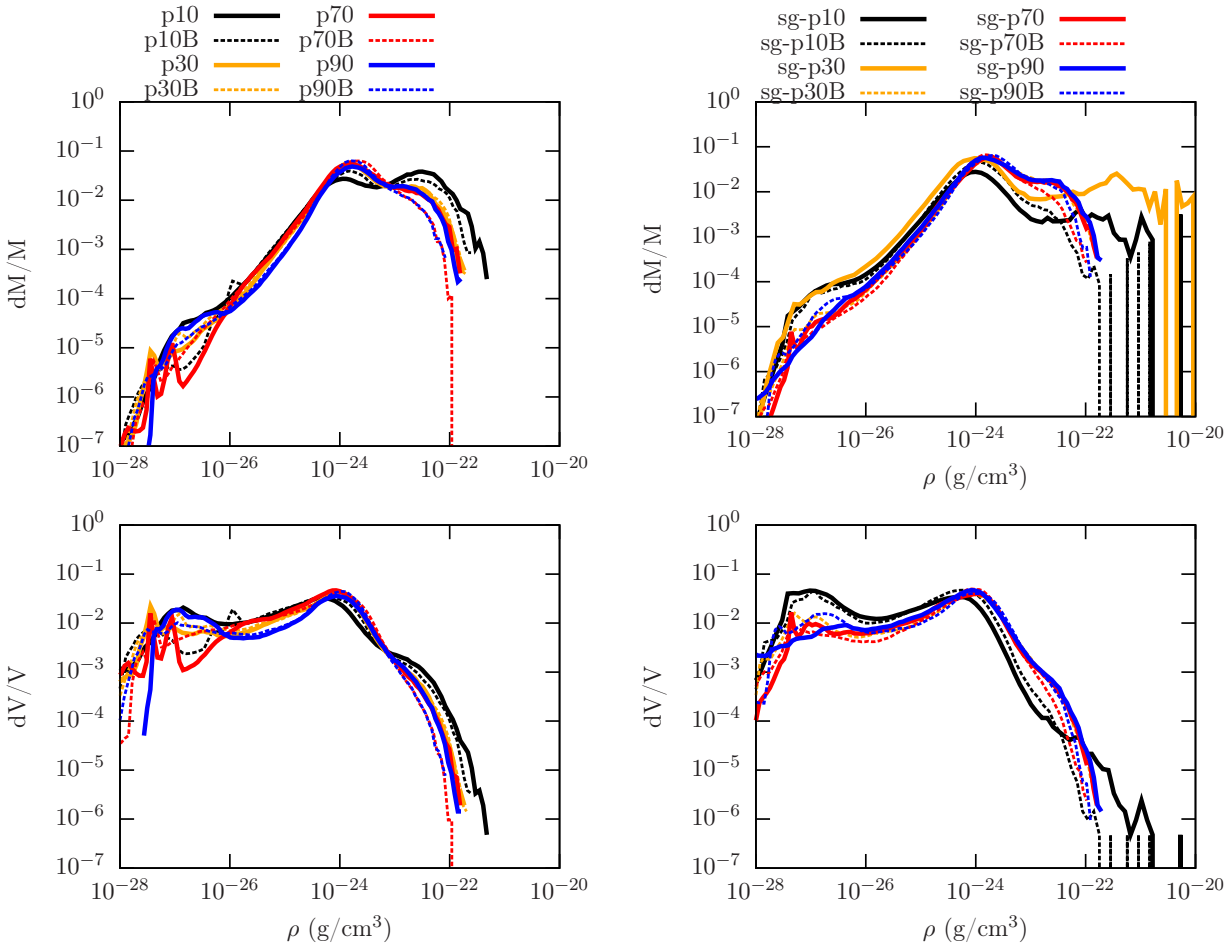

Figure 4.2: Mass weighted (*top left panel*) and volume weighted (*bottom left panel*) density PDFs of the fiducial runs (left row) and self-gravity runs (right row) with peak fractions of p10 (solid black line), p10B (dotted black line), p30 (solid orange line), p30B (dotted orange line), p70 (solid red line), p70B (dotted red line), p90 (solid blue line) and p90B (dotted blue line), all at 100 Myr. For the fiducial runs, the larger the peak fraction the lower the reached maximum density, and magnetic fields lower this maximum density even more. For the self-gravity runs, only sg-p10, sg-p10B and sg-p30 form the very dense clumps seen in Fig. 4.1.

netic fields play a significant role in the efficiency of both the formation (dense clumps are less efficiently compressed perpendicular to the field lines due to the magnetic pressure) and destruction of MCs (the magnetic tension within the clumps prevents the gas from being dispersed as easily as the unmagnetised MCs).

4.4.1 Fiducial runs

In Fig. 4.3 (upper left panel) we show the H_2, H and H^+ mass fractions formed in runs without self-gravity, with different peak fractions, with (triangles) and without (circles) magnetic fields, of the simulations with $n_i = 0.5$ cm^{-3}. The H_2 mass fractions range over three orders of magnitude, decreasing with the increasing fraction of SNe exploding in peak density regions. From ∼50% H_2 mass fraction for randomly exploding SNe to 0.3% in all peak density exploding SNe. There is a steep transition between 0% and 20% peak fraction which corresponds to an equivalent drop of the hot gas VFF. When the PF is 0%, randomly placed SNe explode in lower density gas, efficiently compressing it and causing it to cool and form H_2. Higher peak fractions than 20% lead to SNe efficiently dispersing the dense gas and lowering the H_2 mass fractions.

To illustrate the H_2 mass fraction transition in more depth, in Fig. 4.4 we show the cumulative histogram of the number of SNe as a function of the environment they explode in, for peak fractions of 10, 30, 50, 70 and 90%. Overall, in higher peak fraction simulations the SNe explode in higher density gas: in p10, 80% of the SNe explode in gas with density below $2\times\ 10^{-24}$ g/cm^3 while in p30, 80% of the SNe explode in gas of density below $4\times\ 10^{-23}$ g/cm^3. This steep increase in the distribution between 2 and 3×10^{23} g/cm^3 corresponds to the average density of the gas filling most of the volume of the box. While in p10 and p10B this increase occurs at lower densities due to the boxes being dominated (in volume) by lower density gas (see Fig. 4.1 and discussions in Subchapter 4.6).

The magnetised average H_2 mass fractions are about a factor of two lower than in the unmagnetised runs (see Table B.2). The average mass and volume weighted magnetic fields (Fig. 4.3, upper right panel) are almost constant in different peak fraction runs, being only slightly stronger in the randomly stirred ISM due to a better compression of the dense structures. The mass weighted magnetic field has an average of 2 μG, while the volume weighted average is 0.8-0.9 μG. Because the magnetic pressure in the dense clump is resisting compression perpendicular to the field lines (see Chapter 3) the H_2 mass fractions in the magnetised environment are lower than the unmagnetised runs for almost all PFs. The evolution of the magnetic field for different PFs is shown in Appendix , Fig. B.4. Overall, we find that the different peak fractions do not affect significantly the magnetic field evolution.

In the lower left panel of Fig. 4.3 we show the volume filling fractions (VFFs) of cold gas ($T \in [30 - 300)$ K), cool gas ($T \in [300 - 8000)$ K), warm ($T \in [8000, 3 \times 10^5)$ K) and hot gas ($T > 3 \times 10^5$ K). The transition in the hot gas VFF between 0% and 20% PF is of one order of magnitude (from 30% to 3%) while the transition in cold gas VFFs is milder (from 2% to 0.8%). This trend correlates well with the transition in the H_2 mass fractions and with the cumulative histogram in Fig. 4.4, where we show that more SNe

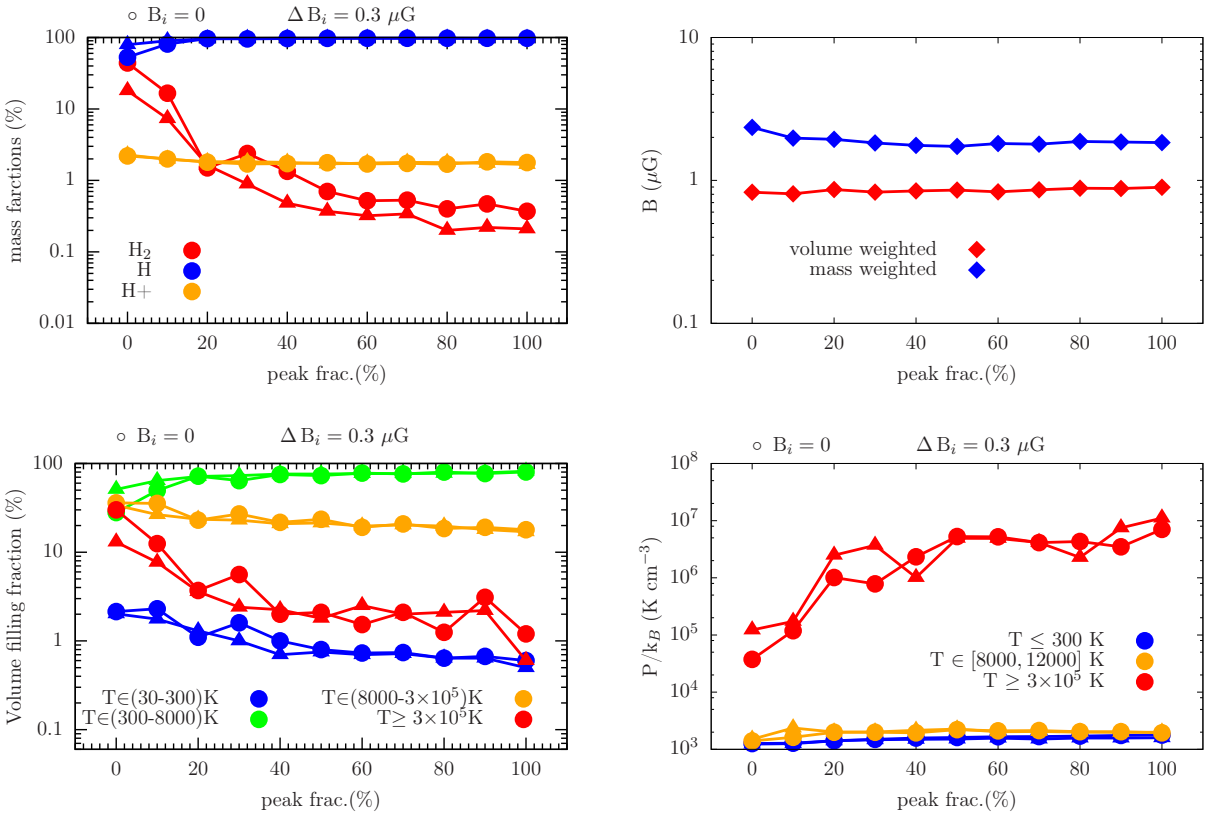

Figure 4.3: Average H_2, H and H^+ mass fractions (*top left panel*, H_2-red, H-blue and H^+-yellow, circle for $B_i = 0$ μG and triangles for $B_i = 0.3$ μG), volume (red diamonds) and mass weighted (blue diamonds) average magnetic field strength (*top right panel*), VFF (*bottom left panel*, cold-blue, cool-green, warm-orange and hot gas-red) and average thermal pressure (*bottom right panel*, in $T \leq 300$ K - blue, $T \in [8000, 12000]$ K- orange and $T \geq 3 \times 10^5$ K- red) comparison for the fiducial simulations with different peak fractions. There is a transition in H2 mass fractions at 10-40% peak fractions. The H2 mass fractions in the magnetised runs are always lower than the others. The mass weighted magnetic field saturates at about 2 μG regardless of the peak fraction, same for the volume weighted field (saturated below 1 μG). The hot gas VFF is decreasing with increasing peak fractions. The average thermal pressure in the hot stable regime is higher for the magnetised runs up to a peak fraction of 50%.

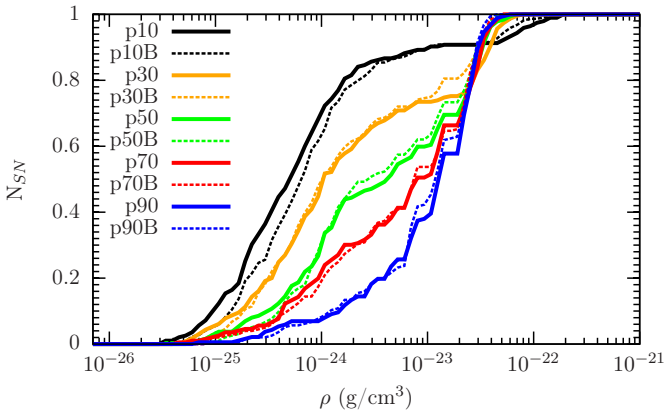

Figure 4.4: Cumulative histogram of the number of SNe as a function of the environment they explode in. With higher peak fractions the SNe explode in higher density gas.

explode in less dense gas for lower PFs. Except for p0(B) and p10(B), the hot gas VFFs for magnetised and unmagnetised runs are not very different, even though the H_2 mass fractions vary considerably. The cumulative histogram shows that indeed the SNe in p10 explode in lower density environments than the SNe in p10B, and this is backed up by the hot gas VFF being higher for p10 by almost a factor of two in comparison to p10B. However, only the randomly stirred unmagnetised box has a higher warm gas VFF, all the rest being clearly dominated by cool gas (VFFs higher than 70%).

In the lower right panel of Fig. 4.3 we show the thermal pressure in hot ($T \geq 3 \times 10^5$ K), stable warm ($T \in [8000, 12000]$ K) and stable cold ($T \leq 300$ K) phases of the gas for the different SN peak fraction runs. The thermal pressure in the stable warm and cold gas is relatively constant while the thermal hot gas pressure is much higher, varying over three orders of magnitude, increasing with the peak fraction. As discussed in Gatto et al. (2015), the increase of the hot gas thermal pressure corresponds to the decrease of the hot gas VFF with higher PF. The high hot gas thermal pressure reflects the young age of the SN remnants that contribute to the hot phase. The transition between p0 and p20 is marked by an increase of the thermal pressure in hot gas (5.2×10^{-12} to 1.4×10^{-10} K/cm^3) which for p0B and p20B is between 1.7×10^{-11} and 3.4×10^{-10} K/cm^3, a factor of two higher.

4.4.2 Self-gravity

We show in Fig. 4.5 (upper left panel) the H_2, H and H^+ mass fractions, the mass and volume weighted magnetic field (upper right panel), the VFFs (lower left) and the thermal pressures in different phases of the gas (lower right panel), all for simulations with $n_i = 0.5$ cm^{-3}, including self-gravity. In the H_2 mass fractions we see the same transition as in the runs without self-gravity, but at a different SN PF. Due to self-gravity, a 10-20% peak fraction is not high enough to disperse the dense clumps formed. Here the transition

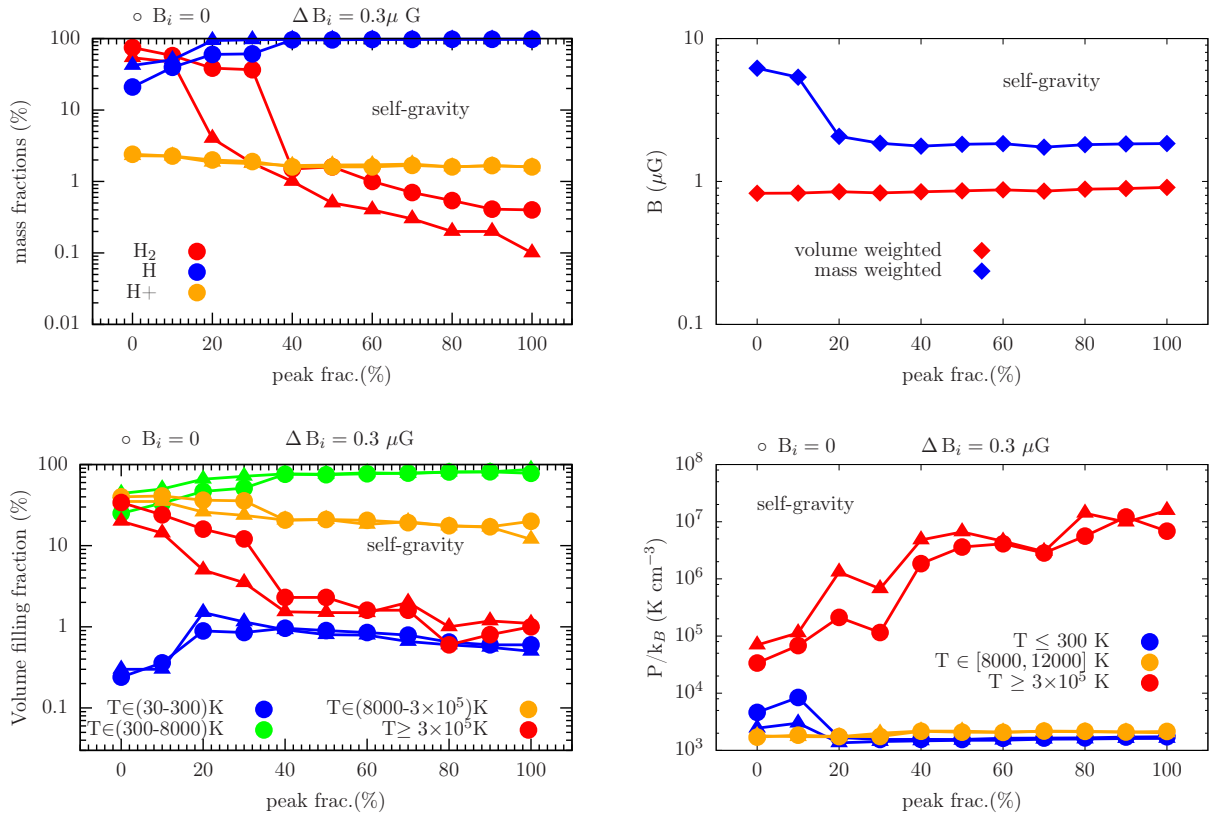

Figure 4.5: Same as in Fig. 4.3 but for self-gravity including simulations. The drop in H_2 is more abrupt than in the runs without self-gravity and for the unmagnetised runs it is shifted to 30-40% PF. The mass weighted magnetic field is also much higher for 0-20% PF than in the simulations without self-gravity.

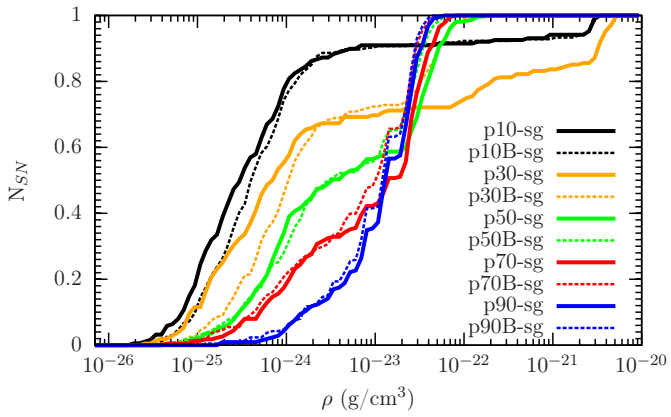

Figure 4.6: Cumulative histogram of the number of SNe as a function of the environment they explode in. The lower the peak fraction, the more SNe explode in less dense gas.

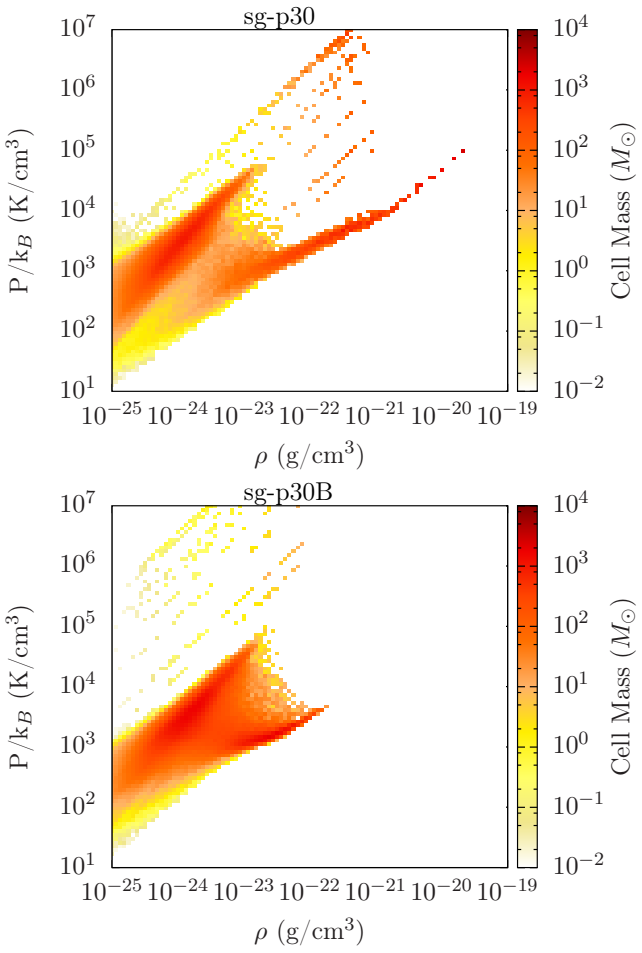

Figure 4.7: Pressure-density phase plots with mass colour-coding at 100 Myr for sg-p30 (*top panel*) and sg-p30B (*bottom panel*). Most of the gas in sg-p30 lies on the hot and low density branch or on the cold branch at high densities, while in sg-p30B the very cold and high density branch is missing.

happens between 30% and 40% for the unmagnetised runs and at 10-40% in the magnetised ones. As the SN peak fraction decreases, the H_2 mass fractions vary dramatically between 75% (sg-p0), 36% (sg-p30), 1.5% (sg-p40) and 0.4% (sg-p100, for more details see Table B.2). Figure 4.6, the cumulative histogram of the number of SNe as a function of the environment they explode in for peak fractions of 10, 30, 50, 70 and 90%, shows that while 80% of the SNe in sg-p10 explode in less than 10^{-24} g/cm^3 gas, only 40% of the total SNe in sg-p40 explode below this value. The steep increase in the distribution remains between 2 and 3×10^{23} g/cm^3 as for the runs without self-gravity (see Fig. 4.4), but here four simulations make an exception: p10(B)-sg and p30(B)-sg. These, as well as p0(B)-sg and p20(B)-sg have much higher hot gas VFF than the rest of the runs. This "plateau" is also stretched over four orders of magnitude (in comparison to only two for the fiducial p10(B), see Fig. 4.4) due to the bigger difference between the cold and hot gas VFF (two orders of magnitude).

In the case of the magnetised simulations, the transition in H_2 happens more gradually, between sg-10B and sg-p40B. While the volume weighted magnetic field is constant for every peak fraction (0.9 μG), the mass weighted field is as strong as 6.2 μG for sg-p0, 5.3 μG for sg-p10 and 2 μG for sg-p20. This shows that the magnetic field, due to flux-freezing, is strongest in the densest regions, corresponding to the highest H_2 mass fractions. The transition profile of H_2 looks just like the mass weighted magnetic field strength for the same peak fractions. While the very dense blobs are formed in the unmagnetised runs between sg-p0 and sg-p30, the magnetic field prevents the formation of such dense structures by making the compression of the gas less efficient. Therefore, because the dense clumps in p0B to p30B are less dense than the ones formed in p0 to p30, a 20% PF is more efficient in dispersing the magnetised clumps than the unmagnetised ones. This leads to the one order of magnitude difference in H_2 between sg-p20 and sg-p20B and even larger difference between sg-p30 and sg-p30B, more than an order of magnitude.

To depict more clearly the difference in the ISM formed in the magnetised and unmagnetised runs, we show in Fig. 4.7 the pressure-density please-plots for sg-p30 (top panel) and as-p30B (bottom panel) at 100 Myr. We can distinguish here the 3 phases of the ISM, the hot low density branch (from below 10^{-25} to 10^{-23} g/cm^3), the cold phase branch (from 10^{-23} g/cm^3 to the maximum density reached in the simulation) and the thermally unstable regime between these two branches. The main difference between the ISM in the two simulations is that in sg-p30 most of the gas can be found either on the hot branch (high pressures and low densities) or on the cold branch (high densities and high pressures) with the maximum density reached being over 10^{-20} g/cm^3. In sg-p30B, even though the two branches stand out, the maximum density of the cold gas is much lower (just above 10^{-22} g/cm^3) and there is much more gas at intermediate densities, showing a more homogeneous ISM (also seen in Fig.4.1, third and forth row).

We show in Appendix B.3, Fig. B.4 that the evolution of the magnetic field is influenced significantly by self-gravity only in the mass weighted case for sg-p0B. Self-gravity induces large fluctuations in the mass weighted field strength due to the scaling of the field strength with gas density. The gas can reach higher densities in sg-p0B which means higher magnetic field strengths. However, for higher peak fractions the maximum density is not significant

enough to make a difference.

In Chapter 3 we showed that magnetic fields as strong as in this study decrease significantly the mass fraction of cold gas and increase the mass fraction of warm gas (for a 0% PF). They also show that the main effect of self-gravity is to increase the coldest and densest gas component ($T < 30$ K) and the H_2 mass fraction, which is in agreement with our findings.

Just as the H_2 mass fractions are lower in the magnetised runs, the hot gas VFFs are also lower, being consistent with a more homogeneous ISM. The average hot gas VFFs are higher than in the fiducial runs up to a PF of 40%. For these PFs, the magnetised ISM has on lower hot gas VFFs of about a factor of two (p0(B)-sg and p10(B)-sg) or three (p20(B)-sg and p30(B)-sg). This difference shows the impact of the magnetic field not only on the chemistry but also on the structure of the ISM by producing higher VFFs of warm gas and lower VFF of hot gas than the unmagnetised runs. With self-gravity, only the simulations with a PF higher than 30% are clearly dominated by cool gas (in comparison to almost all the simulations without self-gravity). With smaller and more compact dense structures, the embedding environment consists of less dense and hotter gas.

The thermal pressure (Fig. 4.5, bottom right panel) in the cold gas is higher in sg-p0 and sg-p10 than in the other simulations reaching 10^7 K/cm^3. In the hot gas, the thermal pressure is slightly higher in the magnetised runs and transitions from 10^5 K/cm^3 in sg-p0B to 2×10^7 K/cm^3 in sg-p20B.

Comparing our results to observations, the H_2 mass fraction according to Honma et al. (1995) and Pineda et al. (2013) varies from $\simeq 50\%$ around the galactic centre to $\simeq 2\%$ at 9.5 kpc distance away from the centre. We obtain H_2 mass fractions in agreement with observations for peak fractions lower than 40%. The VFF is predicted to be $\simeq 60\%$ for hot gas (Snowden et al., 1998), $\simeq 50\%$ for the warm neutral gas and $\simeq 1.5\%$ for the cold gas (Heiles and Troland, 2003). The simulations that best reproduces these observational values are p0-sg and p0B-sg, even though they underestimate the cold gas VFF. sg-p20 reproduces well the VFF of the cold gas but underestimate the VFF of the hot gas by a factor of three. The thermal pressure in the cold neutral medium (CNM) and warm Neutral medium (WNM) are in concordance with the observations, between 10^3 and 10^4 K cm^{-3} (Wolfire et al., 2003; Gaensler et al., 2008; Jenkins and Tripp, 2011). However, the thermal pressure of the hot ionised phase (HIM) that we obtain for peak fractions of over 40% is comparable to the one observed in starburst galaxies, which have much higher star formation rates than in our simulations (Lehnert et al., 2013). This could be an artefact of our simulation setup. The periodic boundary condition boxes do not allow for outflows or fountain flows which would form in highly pressurised ISMs. We can not count for vertical stratification to allow the ISM to evolve into hydrostatic equilibrium with the galactic potential. Moreover, the star formation rate in our boxes is constant, whereas in more realistic models it would readjust and maybe decrease.

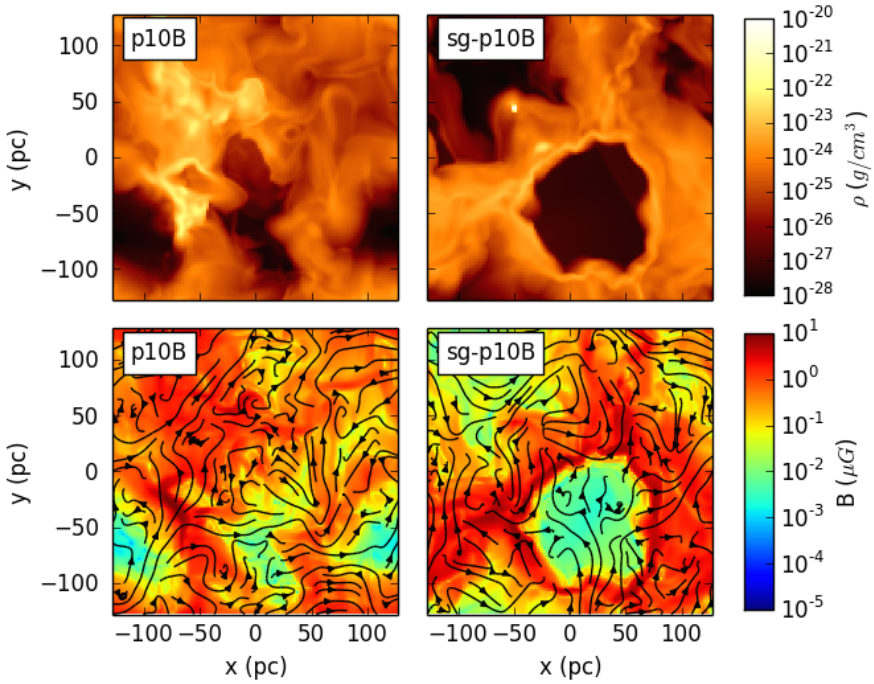

Figure 4.8: Density slices passing through the densest region in the simulation and oriented parallel to the z-axis (*first row*) for p10B and sg-p10B at 100 Myr. In the *second row* we show the corresponding magnetic field strength with magnetic lines over-plotted. There is a strong correlation between the density and the magnetic field strength.

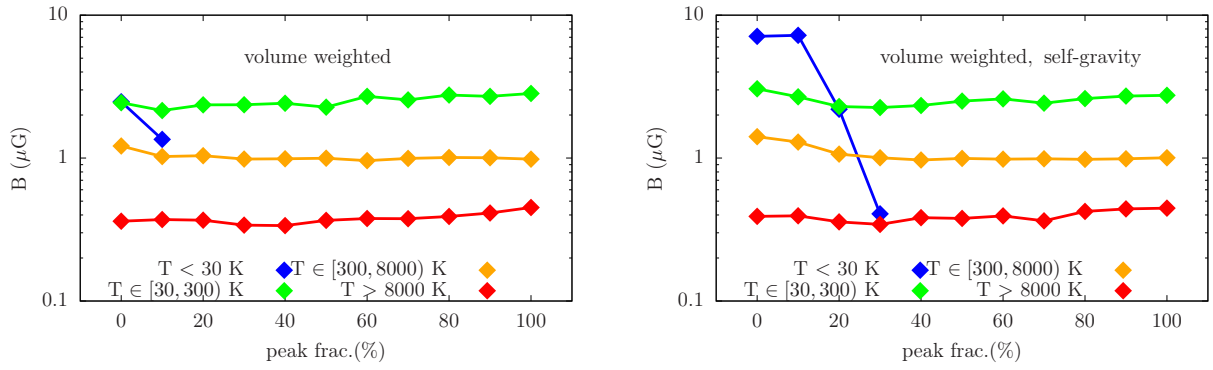

Figure 4.9: Average volume weighted magnetic field in very cold gas $T < 30$ K (blue diamonds), cold gas $T \in [30, 300)$ K (green diamonds), cool gas $T \in [300, 8000)$ K (yellow diamonds), warm and hot gas $T \geq 8000$ K (red diamonds) for the runs without self-gravity (*left panel*) and with self-gravity (*right panel*). The field is stronger in colder temperature regimes for both sets of simulations.

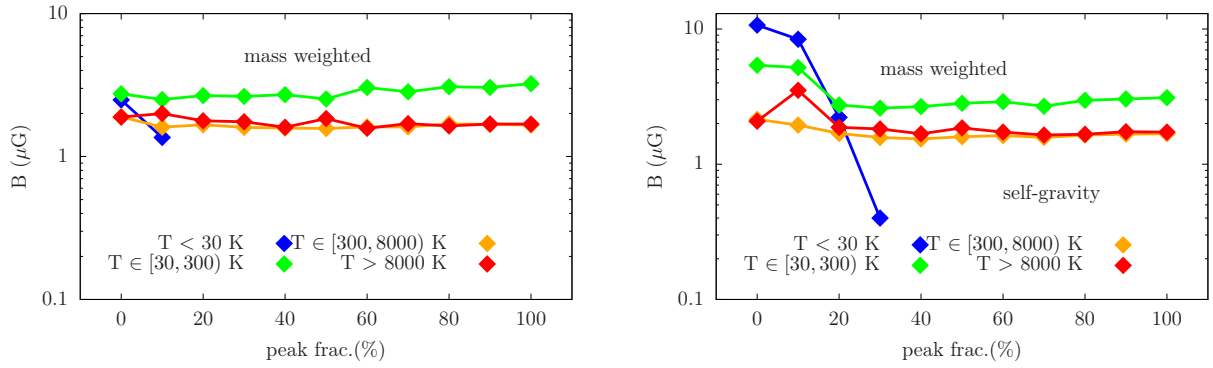

Figure 4.10: Same as Fig. 4.9 but for mass weighted magnetic field. The field strength is very similar for the warm and hot temperature regimes. The field strength increases with decreasing temperatures of the gas.

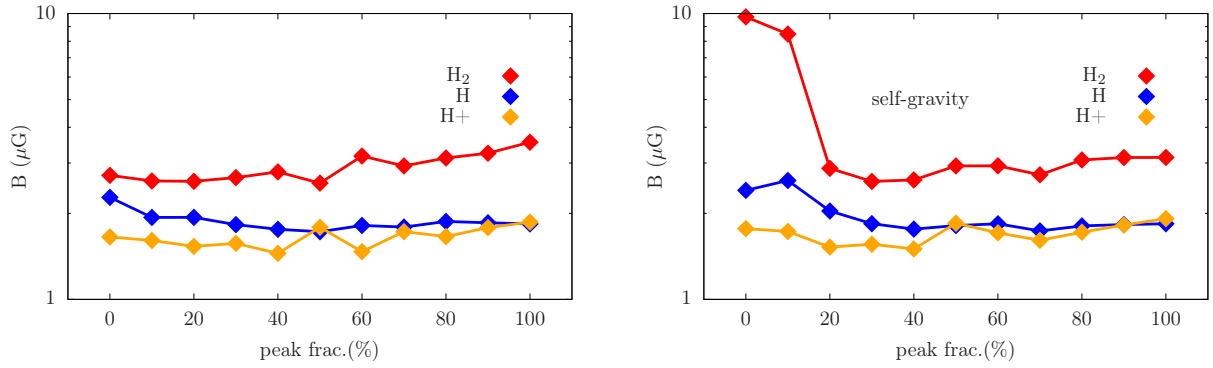

Figure 4.11: Average mass weighted magnetic field strength for different peak fractions in H_2 (red diamonds), H (blue diamonds) and H^+ (yellow diamonds) for the simulations without self-gravity (*left panel*) and with self-gravity (*right panel*). The magnetic field is the strongest in H_2.

4.5 The magnetic field strength

In Fig. 4.8 we present density slices (through the densest region of the box) and the magnetic field strength with the magnetic field lines over-plotted for p10B and sg-p10B, at 100 Myr. The ISM is by this time very inhomogeneous covering eight orders of magnitude in density (from 10^{-28} to 10^{-20} g/cm^2) and six orders of magnitude in magnetic field (from 10^{-5} to 10 μG). There is a strong correlation between the dense regions and the strongest magnetic field, consistent with the "frozen-in" scenario where the magnetic field is moving along with the gas. The turbulence introduced by the expanding SN blasts sweeps away the gas, which drags the magnetic field with it, efficiently twisting and tangling it. There is little difference between the magnetic field strength in p10B and sg-p10B, because the very dense regions formed under self-gravity occupy a very small volume. However, we will discuss these differences in more detail below.

Figure 4.9 shows the volume weighted magnetic field in different temperature regimes (very cold $T < 30$ K, cold $T \in [30, 300)$ K, cool $T \in [300, 8000)$ K, warm and hot gas $T \geq 8000$ K) for the runs without self-gravity (left panel) and with self-gravity (right panel). There are only a few points for the very cold regime because only in p0B, p10B, sg-p0B, sg-p10B, sg-p20B and sg-p30B there is gas having lower temperatures than this. The average field is relatively constant for warm and hot gas (0.4 μG), cool gas (1 μG) and cold gas (2-3 μG). This shows that the volume weighted average field is stronger for colder gas in both sets of simulations. The fields in the self-gravity runs sg-p0B and sg-p10B in the very cold regime are more than a factor of two higher than the field in the cold gas and in the very cold gas of p0B.

The average mass weighted magnetic field is shown in Fig. 4.10 for the fiducial runs (left panel) and the self-gravity runs (right panel). In the cool and warm gas, the field strength is very similar in both sets of simulations and quite constant with varying PF at ~ 2 μG. The main difference is that when including self-gravity for low peak fractions the magnetic field is very strong in the dense structures it is "frozen" into, becoming almost an order of magnitude stronger in the very cold gas for sg-p0B and sg-p10B. The field is also stronger in the cold gas at low peak fractions (5 μG) in comparison to higher peak fractions (3 μG) and to the fiducial p0B and p10B. Even though the mass weighted field strength in sg-p20B and sg-p30B equals the field strength of larger peak fractions in the cold gas, it seems to be enough to considerably reduce the H_2 mass fractions in comparison to the unmagnetised runs (see Fig. 4.5).

In Fig. 4.11 we show the average H_2, H and H^+ mass weighted magnetic field for the fiducial runs (left panel) and the self-gravity simulations (right panel). The strongest field is in H_2 in both cases while in H the field is only slightly stronger than in H^+. While the field is relatively constant in H_2 for the fiducial runs (for different peak fractions) at about 2-3 μG, in sg-p0B and sg-p10B the field reaches 10 μG before it drops to 3 μG and stays constant for higher peak fractions. We can see a similar trend for H in the self-gravity runs sg-p0B and sg-p10B.

Observations show that the magnetic field strength in the diffuse ISM is about 10 μG (Crutcher, 2012) and in denser regions between ~ 16 μG and 1.1 mG (Crutcher, 2004;

Woody et al., 1989). In our simulations the strongest mass weighted magnetic field is reached in the self-gravity runs in dense, very cold ($T < 30$ K) H_2 gas and it is about 10 μG for the runs with 0 and 10% peak fractions. Even though this field strength can be considered a lower limit of what is observed in these conditions, it is strong enough to make a significant difference in the H_2 mass fractions of the self-gravity runs.

Because of magnetic flux-freezing, the fluid motion and the magnetic field are tightly linked, and turbulent compression can therefore amplify the magnetic field at small scales (Kazantsev, 1968; Subramanian, 1997) until the saturation scale is reached (Egan et al., 2016). The small-scale turbulent dynamo can amplify a magnetic seed field during gravitational collapse (Sur et al., 2010; Federrath et al., 2011b; Peters et al., 2012; Schober et al., 2012). As just stated in Chapter 3, we cannot discuss the mechanisms that lead to the amplification of the magnetic field because of limited resolution, numerical dissipation, and the complexity of our simulations. In terms of our resolution, previous studies have been carried out with 1024^3 and 2048^3 cells (Kritsuk et al., 2009; Jones et al., 2011; Federrath et al., 2014a), resolution hard to achieve given the complexity of our simulations. The wide temperature range and the different chemical species we track make it difficult to recover parameters like the Magnetic Prandtl number $P_{\rm m}$, Reynolds number $R_{\rm e}$ or the Magnetic Reynolds number $R_{\rm m}$, useful for describing the dynamo (Kritsuk et al., 2011; Schober et al., 2012). Moreover, we face the numerical dissipation of the magnetic field even though we do not specifically include diffusive terms in the MHD equation.

4.5.1 Plasma-β

The plasma-β parameter (the ratio of the thermal to magnetic pressure $\beta = P_{\rm th}/P_{\rm mag} = 8\pi P_{\rm th}/B^2$) is shown in Fig. 4.12 for p0B, p20B and p40B (upper row) and the self-gravity runs sg-p0B, sg-p20B and sg-p40B (bottom row). We show here the plasma-β as a function of the density of the gas with mass colour-coding at 100 Myr, with the black line indicating the $\beta = 1$ limit and the mass fraction that is magnetically dominated $M(\beta < 1)/M_{tot}$ being the total mass of gas in which the magnetic pressure is higher than the thermal pressure normalised to the entire mass of the box.

There is a huge scatter in β for different density regimes. The lower limit of the plasma-β parameter is in general 0.1, meaning that the magnetic pressure is at most ten times larger than the thermal pressure, with the exception of p0B and sg-p0B (where β decreases to 0.05). The percentage of the mass in the simulation that is magnetically dominated ($\beta < 1$) seems to be comparable for 20% and 40% PF however, the magnetised gas fraction in p0B is a factor of almost four higher than in sg-p0B.

In the simulation without self-gravity, due to more SNe exploding in peak density regions, the dense clumps harbouring the strongest magnetic field are being dispersed more efficiently. The thermal pressure is also increasing with the peak fraction (see Fig. 4.4) leading to a lower magnetically dominated mass fraction (39% in p0B, 23% in p20B and 15% in p40B).

In the case of the self-gravity runs, the dependence of the magnetically dominated mass fraction on peak fraction is not so straight forward. The H_2 mass fraction are very high

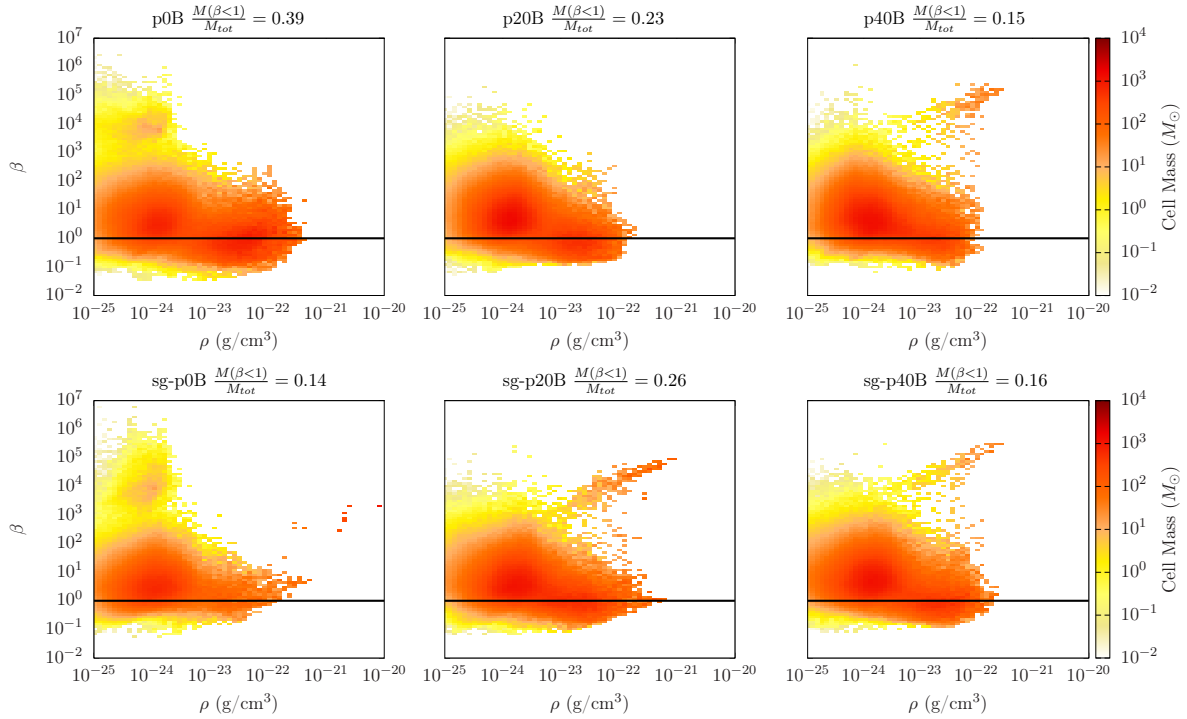

Figure 4.12: Plasma-β as a function of density at 100 Myr. In the *top row* we show p0B (left), p20B (middle) and p40B (right). In the *bottom row*: sg-p0B (left), sg-p20B (middle) and sg-p40B (right). The black line marks the limit $\beta = 1$. For the simulations without self-gravity field, with higher peak fractions the percentage of mass below $\beta = 1$ is lower. For the runs with self-gravity the highest magnetically dominated mass fraction is obtained in sg-p20B.

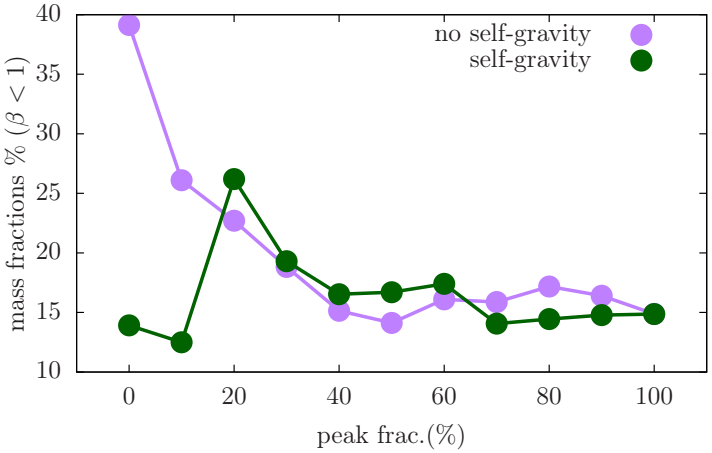

Figure 4.13: Average mass fractions with plasma-$\beta < 1$ for the simulations with self-gravity (dark-green circles) and without self-gravity (purple circles) for different peak fractions. While the magnetically dominated gas mass fractions decrease with increasing peak fractions for the runs without self-gravity, the ones with self gravity have a maximum at a peak fraction of 20%.

for low peak fractions. In these simulations, the clumps are very dense and forming at over 10^{-21} g/cm^3 with very high thermal pressure (see left panel, second row of Fig. 4.12) leading to a low percentage of mass with $\beta < 1$. The less dense these structures become with increasing peak fractions, the more significant the magnetic pressure becomes: there is 20% of mass below $\beta < 1$ at 100 Myr in sg-p20B (Fig. 4.12 middle panel, second row). The fact that 20% PF is a maximum in the magnetised mass fraction can be clearly seen in Fig. 4.13, where we show the averaged mass fraction of gas having a plasma-β lower than unity. In contrast to the runs without self-gravity for which the magnetically dominated mass fraction decreases with peak fraction (from 40% in p0B to 15% at p100B), the self-gravity runs have a maximum of 26% at 20% peak fraction. For higher peak fractions than this, the SN exploding inside the dense regions can efficiently disperse both the gas and the magnetic field leading to a decrease in the magnetically dominated mass fractions. The 20% PF seems to create the perfect conditions for a large fraction of the mass to become magnetically dominated: this PF is low enough not to prevent dense structures to form (sg-p20B has an average of 4% H_2 mass fraction and quite a high hot gas VFF of $\sim$50%) but is high enough not to permit these structures to become so dense and compact that the thermal pressure would exceed 2×10^3 K/cm^3.

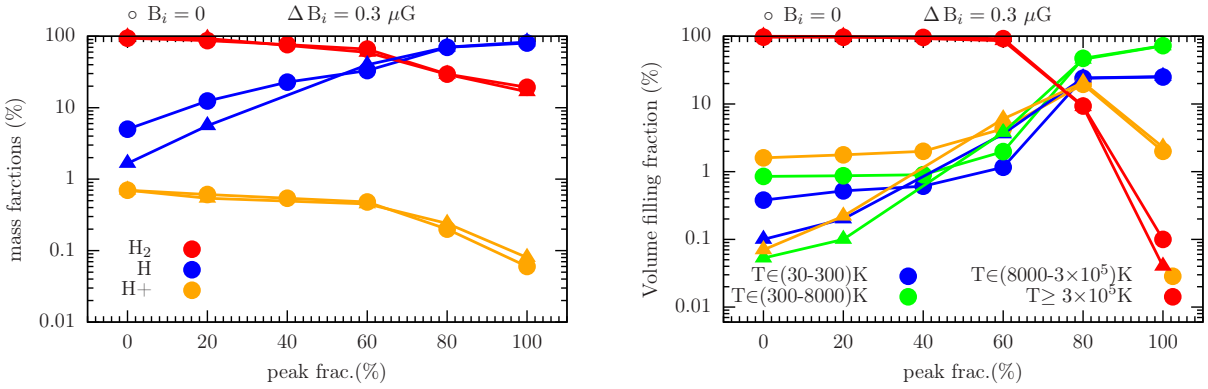

Figure 4.14: Average H_2, H and H^+ mass fractions (*left panel*, H_2-red, H-blue and H^+-yellow, circle for $B_\mathrm{i} = 0\ \mu$G and triangles for $B_\mathrm{i} = 0.3\ \mu$G) and VFF (*right panel*, cold-blue, cool-green, warm-orange and hot gas-red) for the runs with $n_i = 3$ cm^{-1}. Up to about 60% peak fractions the simulation boxes seem to be in thermal runaway with very high H_2 mass fractions and hot gas VFFs.

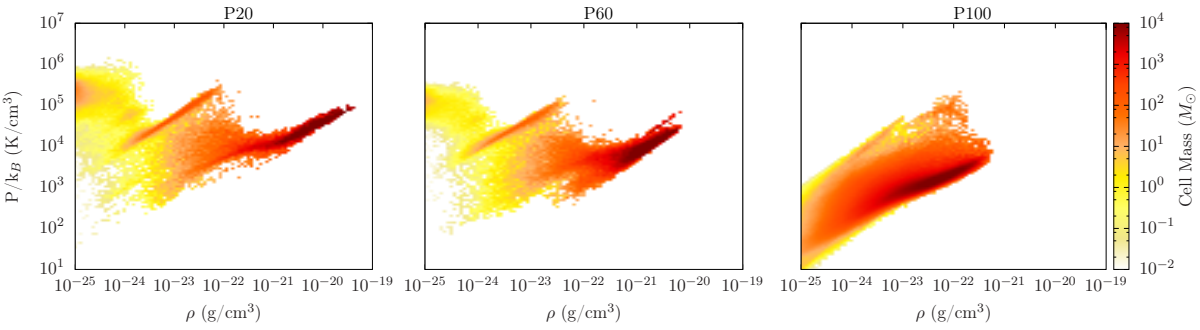

Figure 4.15: Pressure-density phase plots with mass colour-coding at 100 Myr for P20 (*left panel*), P60 (*middle panel*) and P100 (*right panel*). With lower the peak fraction more gas lies in the cold branch and at higher densities.

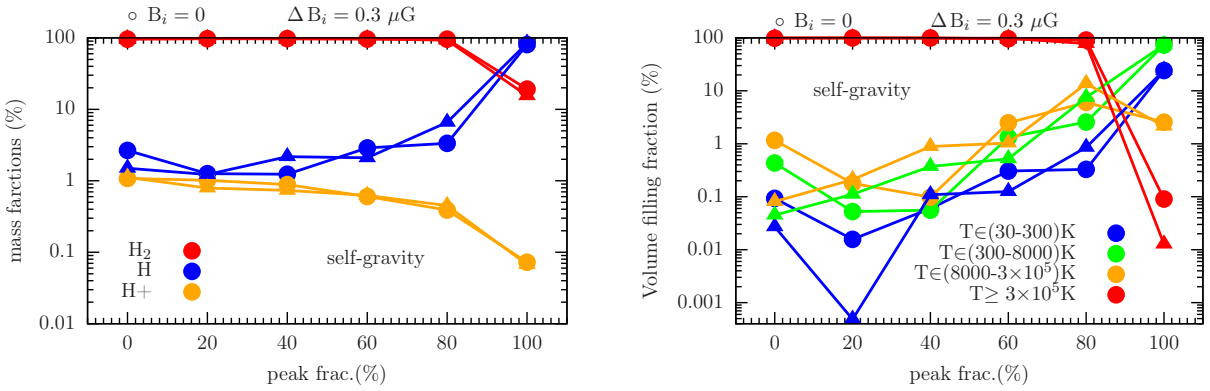

Figure 4.16: Same as Fig. 4.14 but for simulations including self-gravity. Only the sg-P100 and sg-P100B are not in thermal runaway.

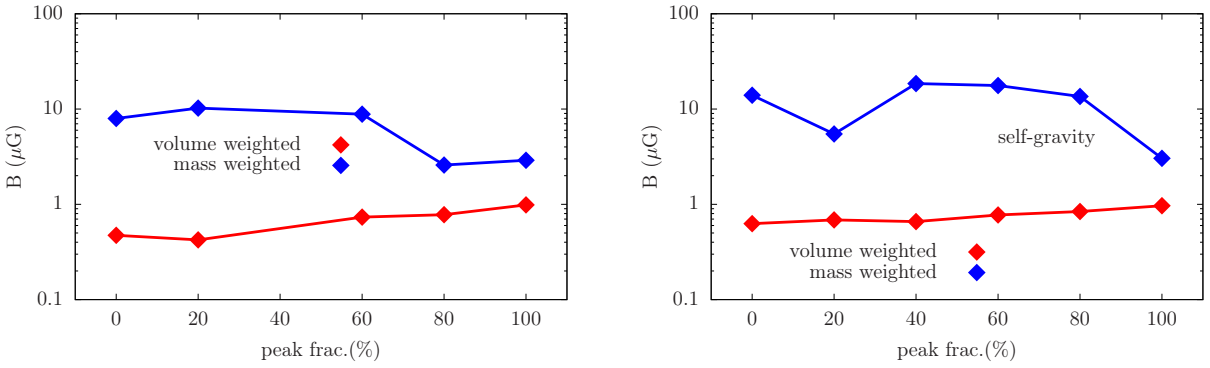

Figure 4.17: Average volume (red diamonds) and mass weighted (blue diamonds) magnetic fields for the runs with $n_i = 3$ cm^{-1} without (*left panel*) and with self-gravity (*right panel*). The volume weighted magnetic field increases slightly with PF. The mass weighted field in the simulations without self-gravity is decreasing at a PF higher than 60% while for the self-gravity runs there is little correlation with PF.

4.6 Higher initial density and SN rate

Figure 4.14 shows the chemical evolution (left panel) and the VFFs (right panel) for simulation with $n_i = 3$ cm^{-1} and a (Kennicutt-Schmidt) SN rate of 14 Myr^{-1} (see Table 4.2). Up to a peak fraction of 40%, the H_2 mass fraction is very high, close to 90%. The same holds for the VFF of the hot gas due to the fact that almost all the mass in these simulations is at densities greater than 10^{-20} g/cm^3 (see Fig. 4.15). The phases of the ISM in these simulations are not in pressure equilibrium, having most of the volume filled by low density and high temperatures gas (described in detail by Gatto et al., 2015). The SNe explode in a highly pressurised environment which is not able to cool. Due to the periodic boundary conditions, the gas is confined without having the option of driving outflows. The cold, very dense clumps form because the gas is compressed very efficiently and ends up being surrounded by over-pressurised, hot gas. As their spatial extent is very small, we are unable to resolve them with more than a few cells, therefore the high H_2 mass fractions and hot gas VFF represent unrealistic, upper limit values.

For larger than 40% peak fractions, we see a decrease in the H_2 mass fractions, from 90% in P0 to 20% in P100, corresponding to a dramatic decrease in the hot gas VFF. For P60, the maximum density is about 10^{-20} g/cm^3, much lower than in P0 (see Fig. 4.15, middle panel), and the H_2 mass fraction is consequently lower as well ($\sim$ 70%). For P100, the maximum density drops another order of magnitude (to 10^{-21} g/cm^3) and the gas is more evenly distributed in the density range. Even though the cool gas becomes dominant for 80%-100% peak fractions (Fig. 4.14), the H_2 mass fractions for the same runs do not drop to more than 20%. This might be an indication that our SNe are not strong enough to efficiently destroy the dense clumps even though all of the SNe explode within them. If the densities in the injection region of the SN explosion are too high and the total mass in this region becomes of the order of thousands of solar masses, the injection temperature can be as low as 10^6 K. This would result in the injected thermal energy almost immediately being radiated away. In order to avoid over-cooling, Gatto et al. (2015) have implemented a momentum injection mechanism. If this is the case and we are facing over-cooling in the high initial density and high peak fraction simulations, we assume that much lower H_2 mass fractions can be reached with momentum injection at the SN explosions.

Self-gravity leads to a shift in the transition peak fractions from 60 - 80% (in simulations without self-gravity) to 80 - 100%. This is expected as the density of the clumps is much higher than in the runs without self-gravity. If the H_2 mass in the case without self-gravity was as high as 94% for PF up to 20% and decreased for higher PFs, the H_2 mass fractions in the simulations including self-gravity are about 97% for almost all the simulations except for P100 and P100B which produce a lower amount of H_2, $\sim$ 20%. The same radical trend is present in the hot gas VFFs. If previously, for P80 the VFF of hot gas was about 10% with most of the box being dominated by cool gas, with self-gravity, sg-P80 still maintains a 91% of the box engulfed in hot gas. Even though there is no clear trend dictated by the magnetised simulations, there are a few exceptions: the VFF of hot gas in sg-P80B is 14% lower than in sg-P80 and in the case of sg-P100B it is an order of magnitude lower than in sg-P100 (0.01% compared to 0.1%).

The average volume and mass weighted magnetic fields are presented in Fig. 4.17 for the runs without self-gravity (left panel) and with self-gravity (right panel). The volume weighted field looks very similar in both cases, varying from 0.5 to 1 μG, increasing with the PF (see for details Table B.3). The average mass weighted magnetic field, in the runs without self-gravity is around 10 μG up to a PF of 60%, followed by a decrease to about 3 μG. In the self-gravity runs, the mass weighted field varies between ~ 5 and 20 μG, without a clear dependence on the PF. The decline of the mass weighted field in the simulations without self-gravity is correlated with the decrease in the H_2 mass fractions and hot gas VFFs. In the self-gravity runs, the mass weighted field correlates with the transition in this case as well. However, at 20% PF, there is a factor of three difference with respect to sg-P0B and sg-P40B, with no apparent correlation but a decrease in the VFF of the cold gas. Because these quantities are averaged over 100 Myr, this discrepancy might mean that one of the very dense clumps got hit by a SNe and the gas was dispersed enough to account for a decrease in the (already small) cold gas VFF and mass weighted magnetic field, but not enough to make a difference when it comes to the average H_2 mass fraction and hot gas VFF.

4.7 Conclusions

We use the 3D magnetohydrodynamic code FLASH in version 4 to study the structure of the magnetised, multiphase interstellar medium and focus on the effect that different fractions of SNe have when placed in density peaks. As it is not fully understood what the fraction of stars traveling away from their parent cloud before exploding as type II SNe is, and how many of them explode in the cluster they are born in, we model scenarios by varying the peak fraction SNe to study their impact on the evolution of the ISM. We use periodic boxes with a volume of $(256\,\mathrm{pc})^3$ with and with our self-gravity, with two initial densities: $n = 0.5$ and 3 cm^{-1} and magnetic fields of 0 and 0.3 μG. Our results can be summarised as follows:

- For the fiducial runs ($n_i = 0.5$ cm $^{-3}$) the fraction of SNe exploding in their parent MC has a significant impact on the structure of the ISM. A variation in the peak fraction between 0 and 20% causes more than an order of magnitude difference in the H_2 mass fraction (from 40% to 2%).The same happens with the hot gas VFF (30% to 3%). The mass weighted average magnetic field of 2 μG is however in the lower observational limit, strong enough to determine a lower H_2 mass fraction for almost all PFs of about a factor of two. The thermal pressure increases from 5.2×10^{-12} to 1.4×10^{-10} K/cm^3, and is a factor of two higher for the magnetised runs.

- When including self-gravity, the transition happens at higher PFs, between 30-40%, due to the denser and smaller clumps formed in these simulations. The H_2 mass fraction decrease is much more dramatic, plummeting from 36% for sg-p30 to 1% when increasing the PF by only 10%. The magnetised ISM shows a smoother transition, for the same PFs (between 10-40%) because of a more homogeneous environment. The

average magnetic field in lower PFs than 20% is a factor of three higher ($\sim 6\mu$G) than for higher PFs. This transition changes the situation where the boxes have comparable cool, warm and hot gas VFFs (about 20%, 30% and 40% in sg-p0) to completely cool gas dominated ISMs (for higher PFs than 40%). The thermal pressure transitions over 3 orders of magnitude, increasing with the PFs, reaching values observed for starburst galaxies for higher than 40% PFs (between 10^6 and 10^8 K/cm^3).

- The magnetic field strength is highest in high density regions, in agreement with flux-freezing. The average volume weighted and mass weighted field are approximately equal and constant with PF (3μG) for the fiducial runs, with the field being weaker in hotter temperature regimes. Self-gravity determines a clear distinction between less than 20% PF and the rest of the simulations. The more efficient compression of the dense gas at low PFs saturates the average magnetic field at about 10 μG in the cold gas (< 30 K) and H_2.

- The plasma-β parameter decreases with increasing PF from 40% to 1.5% in the fiducial runs. In the simulations including self-gravity, it reaches a peak of $\sim 30\%$ at a PF of 20%. Because of the very dense clumps formed at low PFs, the magnetic pressure is high but the thermal pressure in these clumps is even higher. As the PF increases to 30% the thermal pressure decreases allowing a maximum plasma-β. For larger PFs, the maximum density of dense clumps declines and the magnetic field declines in strength as well.

- Most of the high density simulations ($n_\mathrm{i} = 3$ cm^{-3}) are in thermal runaway, having their volume filled with low density and high temperature gas, highly pressurised. This keeps the H_2 mass fractions close to 100% for lower than 20% PFs and the hot gas VFFs close to 100% for lower than 60%. The transition in chemistry and VFF is shifted to higher PFs compared to the fiducial runs: 60-80% (with a factor of two in H_2 and one order of magnitude in the VFF of hot gas). Self-gravity shifts this transition to even higher PFs: 80-100%.

- The fact that the thermal pressure is higher than the observations show in the solar neighbourhood (for the fiducial runs) and the over-pressurised simulations with higher initial density ($n_\mathrm{i} = 3$ cm^{-3}) can be an artefact of our simulation setup. Open boundary conditions would allow the boxes to breath and would avoid thermal runaway.

- The placement of the SNe makes a staggering difference in the evolution of the ISM. Even though the results are partially influenced by the simulation setup, the fact that major changes can occur in the chemistry and structure of the ISM with only a few percent of the SNe exploding in different positions underlines the importance of further studies for an accurate modelling of the ISM.

Chapter 5

Pitfalls in the ISM occurring with the Schmidt-type Supernova driving

The question of how stars form is of great interest in the contemporary astrophysics. The processes involved in the transformation of gas into stars have been heavily studied in the last 25 years. For a recent and complete review see Naab and Ostriker (2016).

Cosmological scale simulations treat star formation in different ways, mainly because the star formation process cannot be resolved directly. One way is to make the connection between the star formation rate density and the gas above a certain threshold density while assuming a star formation efficiency on a given time-scale, depending on the local density of the gas (Schmidt-type, see Schmidt (1959) and Springel and Hernquist (2003)). Another way is simply to link the star formation rate to gas which is above a certain density threshold (see e.g. Schaye and Dalla Vecchia (2008); Schaye (2015); for more examples and discussions see also Hopkins et al. (2013)) or to the molecular gas fraction (following observational findings of, e.g. Wong and Blitz, 2002; Bigiel et al., 2008; Leroy et al., 2008; Kennicutt and Evans, 2012; Feldmann et al., 2012; Monaco et al., 2012).

The resolution of galactic-scale simulations allows the cold, dense gas (the site of star formation) to be resolved but not the detailed processes of star formation. The main aim of these simulations is to link the local physics of the ISM and the star formation regulation on larger, kpc scales (e.g. Krumholz et al., 2009; Benincasa et al., 2016). One of the models investigates the dynamical equilibrium aspect of galactic evolution while studying the balance between ISM weight and pressure support as well as the energy balance between feedback and heating/cooling processes (Ostriker et al., 2010; Kim et al., 2011; Ostriker and Shetty, 2011; Kim and Ostriker, 2015b). These studies imply that the star formation rate surface density is proportional to the weight of the ISM. Another factor that can support the gas in the outer regions of the disk is the turbulence induced by the galactic shear which leads to a limited star formation (see models of Elmegreen and Parravano, 1994; Schaye, 2004; McNally et al., 2009). Furthermore, there are extensive high resolution simulations of isolated galaxies aimed at exploring dense star-forming gas (Dobbs, 2008; Tasker and Tan, 2009; Hopkins et al., 2011; Dobbs et al., 2011; Renaud et al., 2013; Benincasa et al., 2016). However, galaxy-scale simulations can not resolve more than star cluster formation

at most and thus they still have to consider various star formation recipes.

The same applies to simulations of vertical slabs of galactic disk simulations (parsec scales), which however, can address physical processes more accurately like stellar turbulence see (see Mac Low and Klessen, 2004) and feedback (including ionising radiation, stellar outflows and winds and SN explosions, see e.g. Agertz et al., 2013; Mac Low, 2013), magnetic fields (Shu et al., 1987) and in addition can follow the chemical composition of the ISM (Walch et al., 2015).

Turbulence, especially on large scales, and the way it impacts star formation depends strongly on the stellar feedback implementation. Stellar feedback has the potential to reduce star formation significantly (by up to a factor of 10, see simulations of Hopkins et al., 2011). Magnetic fields have been suggested to affect the dynamics of the ISM and star formation in various ways: they can modify the star formation activity of molecular clouds (Vazquez-Semadeni et al., 2005; Price and Bate, 2008) or prevent the gravitational collapse of the cloud (Ballesteros-Paredes and Hartmann, 2007; Chen and Ostriker, 2014; Heitsch and Hartmann, 2014).

Numerous studies have shown that the location and time at which feedback is introduced into the simulation are very important (Hill et al., 2012; Shetty and Ostriker, 2012; Gent et al., 2013b; Kim et al., 2013). The way SN explosions are injected into the ISM strongly impact the star formation rate, see de Avillez and Breitschwerdt (2005); Joung et al. (2009); Walch et al. (2015); Girichidis et al. (2016). They distributed the SNe randomly in the disk and found that this SN positioning drives gaseous outflows and leads to high gas velocity dispersion in good agreement with observations. The SNe were also placed in exact (or partial) correlation with peak density regions leading to the mid-plane confinement of the galactic disks and significant reduction of the star formation rates due to the systematic destruction of dense regions, for details see Hennebelle and Iffrig (2014). The clustering of SNe was also studied and it was shown that it retrieves the disk structure, in agreement with observations. Another conclusion of these studies is that the implementation of the supernova explosions impact strongly the ISM evolution.

In order to bypass the internal dynamics modelling of very dense systems like stars embedded in gas clouds, Bate et al. (1995) developed 'sink' particles (self-gravitating objects encompassing several SPH, smoothed particle hydrodynamics, gas particles). Gas particles passing within a certain 'accretion radius' of the formed sink particle are accreted (linear and angular momenta and the mass of the accreted particles are added to the sink), modelling the gravitational collapse and accretion in turbulent molecular clouds and cores. While the sink particle implementation in SPH codes has been improved (e.g. Hubber et al., 2013), work has also been done introducing sink particles in Eulerian codes (Federrath et al., 2010; Gong and Ostriker, 2012; Gatto et al., 2016). In numerical simulations, sink particles become an excellent tool for measuring properties like the SFR, star formation efficiency $\varepsilon_{\rm SFR}$ or the mass distribution of stars. In comparison to the fixed SN rate simulations, sink particle proved to produce outflows in the cases the SFR is high enough to form a high VFF of hot gas. However, when adding stellar winds to the sink implementation, Gatto et al. (2016) showed that, even though the sink particles are constantly accreting mass, winds can quench the gas accretion.

No.	Sim. name	$\Sigma_{\rm gas}$ $[M_\odot/{\rm cp}^2]$	$\varepsilon_{\rm SFR}$	$\rho_{\rm crit}$ 10^{-22} [g/cm^3]	$r_{\rm inj}$ [cells]	B [μG]	$M_{\rm tot}$ $\times 10^6 [M_\odot]$
1	S10-e10	10	0.1	2	5	0	2.5
2	S10-e10-mag	10	0.1	2	5	0.3	2.5
3	S10-e03	10	0.03	2	5	0	2.5
4	S10-e30	10	0.3	2	5	0	2.5
5	S30-e10	30	0.1	2	5	0	7.5
6	S30-e10-c4	30	0.1	2	4	0	7.5
7	S30-e10-c2	30	0.1	2	2	0	7.5
8	S30-e10-ld	30	0.1	0.02	5	0	7.5
9	S50-e10	50	0.1	2	5	0	12.5

Table 5.1: List of simulations and parameters. From left to right we list the name of the simulation, the initial surface density, the star formation efficiency, the critical density, the injection radius, the value of the initial magnetic field and the total gas mass.

In this study, we investigate the effects of the Schmidt-type SN driving (described in Chapter 2) in subgalactic-scale stratified disks with various gas surface densities ($\Sigma_{\rm gas}$) and $\varepsilon_{\rm SFR}$. We are interested in the characteristics of the evolved ISM when stirred by the Schmidt-type supernova driving at a few hundred pc scales. We present the details of the simulations and parameters (with the numerical methods described in Chapter 2 and the star formation recipe described in Subchapter 2.4.2). We discuss the morphological evolution of the simulations, the $\Sigma_{\rm SFR}$ and chemical evolution in Subchapter 5.2. In Subchapter 5.3 we analyse in depth the missing outflow problem, in Subchapter 5.4 we present alternatives for overcoming the caveats of the model (theoretical estimates of the density of the injection region, accounting for the displacement of massive OB stars from their parental MC or the implementation of stellar winds) and summarise our conclusions in Subchapter 5.5.

5.1 Simulations and initial conditions

For all simulations, the gas density profile is described in detail in Walch et al. (2015) and Gatto et al. (2016) being uniform in x and y and following a Gaussian distribution in the z-direction. The initial temperature in the disk mid-plane is $T = 4500$ K and the gas is initially composed of atomic hydrogen. Assuming vertical pressure equilibrium, the gas at high altitudes can reach $T = 4\times 10^8$ K with the gas being partially or fully ionised.

We present the evolution of stratified disks with $\Sigma_{\rm gas} = 10, 30$ and $50\,M_\odot\,{\rm pc}^{-2}$. For the simulations with $\Sigma_{\rm gas} = 10\ M_\odot\ {\rm pc}^{-2}$ we consider different fixed star formation efficiencies: 3, 10 and 30%, and we run one simulations with an initial magnetic field oriented along the x axis of 0.3 μG (in the mid-plane) which scales with the density as $B(z) = B(0)\sqrt{\rho(z)/\rho(0)}$. For all simulations we assume a constant accretion radius of $r_{\rm acc} = 4$ cells and vary the SN injection radius, $r_{\rm inj} = 5, 4$ and 2 cells for the simulation with $\Sigma_{\rm gas} = 30\,M_\odot\,{\rm pc}^{-2}$, in order

to probe the effect of its dimension on the average density of the collapsing regions. We also run one simulation with a lower density threshold $\rho_{\rm crit} = 2\times10^{-24}$ g/cm^{-3} (S30-e10-ld) to explore the impact on the outflows and $\Sigma_{\rm SFR}$.

A complete list of the simulations in given in Table 5.1 starting with their names, specifying the initial surface density of the disks (S10, S30 and S50 for $\Sigma_{\rm gas} = 10, 30$ and $50\,M_\odot\,{\rm pc}^{-2}$), the star formation efficiency (e03, e10 and e30 for $\varepsilon_{\rm SFR}$ of 3%, 10% and 30%). To the names there are suffixes attached for the low density threshold simulation (ld for $\rho_{\rm crit} = 2 \times 10^{-24}$ g/cm^{-3}), the different SN injection radii (c4 and c2 for $r_{\rm inj} = 4$ and 2) and the magnetic run (mag, $B = 0.3$ μG). We also specify the total mass of the gas in the simulation $\rm M_{tot}$.

In order to partially support the disk against gravitational collapse towards the mid plane, we introduce turbulence with the largest modes k = 1 and k = 2 corresponding to the full and half box size. The turbulent energy input is evolved with an Ornstein-Uhlenbeck random process (Eswaran and Pope, 1988) and it is switched off once the first SN event occurs. For more details see Gatto et al. (2016).

5.2 Morphological evolution and qualitative discussions of the simulations

We run all the simulations for 125 Myr (except the ones with different SN injection radii). After an initial time of about 8 Myr, the turbulent motion results in structures dense enough to undergo collapse and form stars. The simulations form stars during the entire time of the runs, but at different rates and with different time gaps between the star formation events. This also yields in the different clustering of the SNe; the average number of SNe/event varies between 28 in S10-e03 to 4906 in S50-e10. In table Table 5.2 we list these averages, the H_2 mass fractions, the average density of the injection region, the injection temperature and the average observed $\Sigma_{\rm SFR}$ for the main simulations, except the ones with different SN injection radii. We also show the average time-steps, the average free-fall, cooling and the sound-crossing times to which we will refer in the discussions of Subchapters 5.3 and 5.4.

Figure 5.1 presents the time evolution of the column densities for the fiducial run (left panel) and the magnetised simulation (right panel). The presence of magnetic fields has been shown to delay the formation of dense structures and keep the accumulated gas at lower densities in comparison to the unmagnetised simulations (Walch et al., 2015; Girichidis et al., 2016; Pardi et al., 2017) due to the magnetic pressure that opposes the compression of the gas perpendicular to the field lines. Because of flux-freezing, the magnetic field is stronger in denser regions, Fig. C.2 (left panel, Appendix C.2) shows that the average mass weighted magnetic field reaches up to 10 μG while the field in H_2 gas can get as high as 30 μG. Due to the lower densities in the collapsing regions of the magnetised run (also seen by Hennebelle and Iffrig, 2014), the free-fall times are longer in these areas. Hence, the star formation events are less massive ($\sim$ 62 SN/event in S10-e10-mag in comparison to 73 in S10-e10, see Table 5.2) and the overall energy injected into the ISM

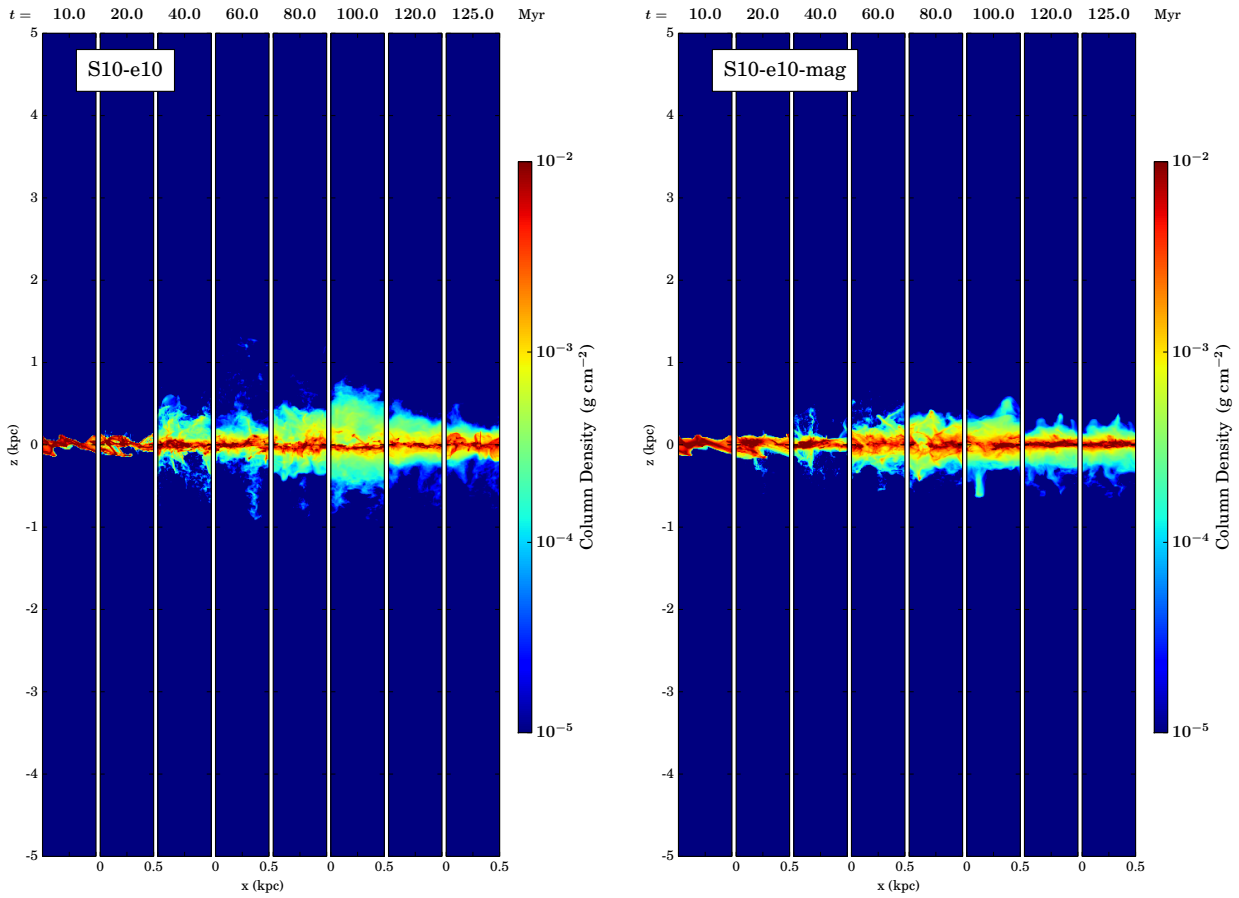

Figure 5.1: Column density sequence for S10-e10 (*left panel*) and S10-e10-mag (*right panel*) at 10, 20 40, 60, 80, 100, 120 and 125 Myr. There are no major differences in the dynamical evolution of the disk between the two simulations.

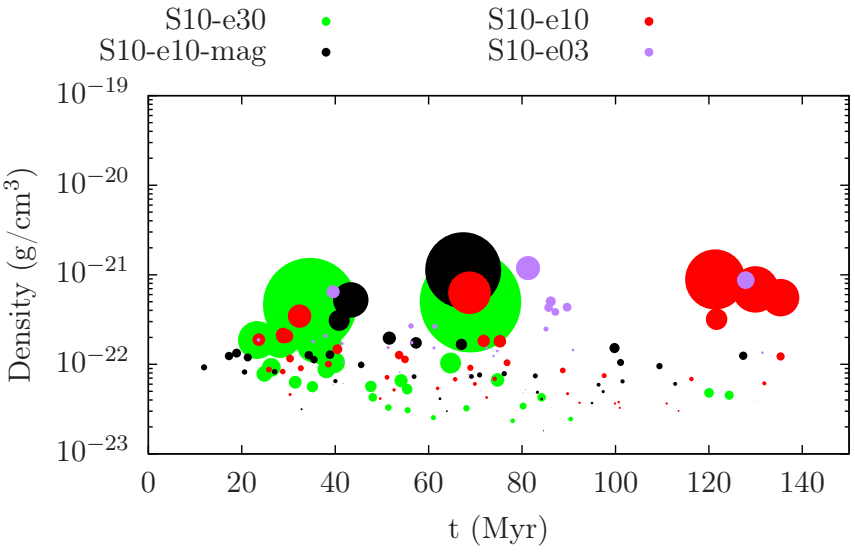

Figure 5.2: The average density of the environment the SNe explode in at the time of the explosion. The radius of the circles is scaled with the number of SNe/event for S10-e30 (green circles), S10-e10-mag (black circles), S10-e10 (red circles) and S10-e03 (purple circles).

is lower.

To illustrate this difference better we show in Fig. 5.2 the comparative average density of the collapsed regions, with the radii of the circles scaled with the number of SNe for the runs with $\Sigma_{\rm gas} = 10\,M_\odot\,{\rm pc}^{-2}$. In S10-e10-mag (black circles), the SN explosion events occur relatively early, after only 10 Myr and they grow in mass and number of massive stars rises progressively until about 70 Myr into the simulation. After 70 Myr, there is a steep decrease in star formation which coincides with the drop in magnetic field strength in H_2 and the average mass weighted field (see Fig. C.2, Appendix C.2). The magnetised simulation displays this behaviour due to the statistical approach in the star formation implementation. Numerous collapsing regions form but if they do not explode, they end up merging in time and forming more massive regions with a higher probability of triggering star formation events. This happens in both S10-e10 and S10-e10-mag but the difference is that in the magnetised case the ISM is overall more homogeneous, for details see Chapter 3. Hence, once a very massive region explodes, like the event at 70 Myr, it disperses easier the dense gas of the surroundings. However, our results are in agreement with previous studies showing that the magnetic field, on these scales, does not impact perceptibly the dynamical evolution of the disk (Walch et al., 2015; Girichidis et al., 2016)

In Fig. 5.3 we present the time evolution of the column densities for different star formation efficiencies: 3% (S10-e03, left panel) and 30% (S10-e30, right panel). The average densities of the collapsing regions in S10-e03 are a factor of two higher than the average densities in S10-e30 (see Table 5.2), however, the average number of SN per event is lower than in the fiducial run by more than a factor of two (28 in comparison to 73 in S10-e10),

No.	Sim. name	no. SN per event	H_2 mf.	ρ ($\times 10^{-22}$) [g/cm^3]	$T_{\rm inj}$ ($\times 10^6$) [K]	$\Sigma_{\rm SFR}$ [M$_\odot$ yr^{-1} kcp^{-2}]	Δ t [Myr]	$t_{\rm ff}$ [Myr]	$t_{\rm cool}$ [Myr]	$t_{\rm c}$ [Myr]
1	S10-e10	73	0.28	1.5	2.5	0.009	0.0035	7.1	0.09	0.16
2	S10-e10-mag	61.7	0.17	1.3	2.5	0.0067	0.0035	7.4	0.1	0.16
3	S10-e30	144.1	0.12	1	7.5	0.0125	0.0032	8.4	0.38	0.1
4	S10-e03	28	0.47	2	0.7	0.0031	0.004	6.8	0.025	0.3
5	S30-e10	613.5	0.6	11.4	2.5	0.1075	0.0026	4.1	0.03	0.16
6	S30-e10-ld	1361	0.6	29.5	2.5	0.33	0.0026	2.9	0.024	0.16
7	S50-e10	4906	0.75	86.1	2.5	1.752	0.0022	1.4	0.004	0.16

Table 5.2: From left to right we list the name of the simulation, the average number of SNe/event, the average H_2 mass fraction, the average density of the injection region, the injection temperature and the average observed $\Sigma_{\rm SFR}$. In the last four columns we specify the average time-steps, the average free-fall times, the average cooling times and the sound-crossing times.

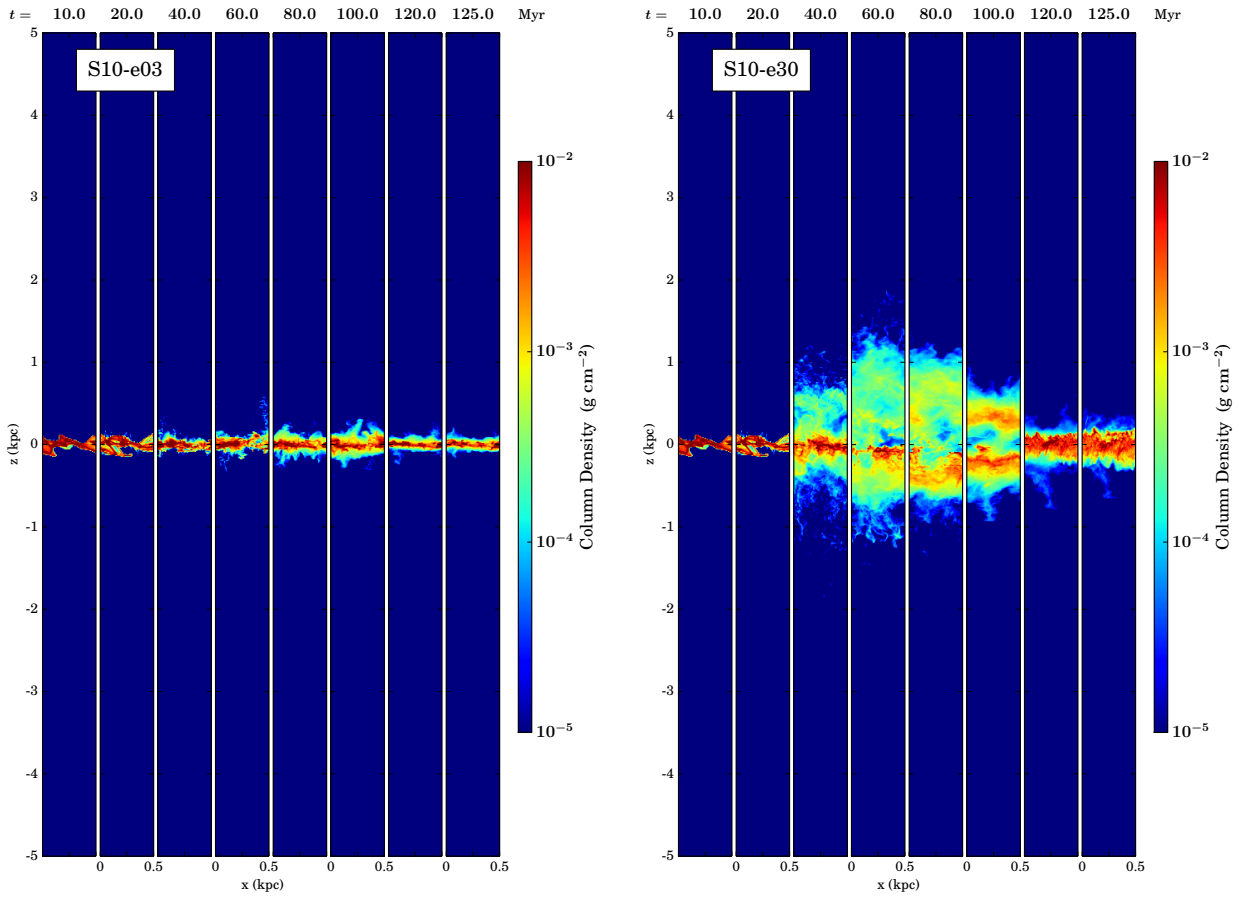

Figure 5.3: Column density sequence for S10-e03 (*left panel*), and S10-e30 (*right panel*). With 3% star formation efficiency the gas is even more confined to the mid-plane than in the fiducial run S10-e10. With 30% efficiency the average number of SN/event is a factor of two higher than in S10-e10, evicting more gas from the mid-plane.

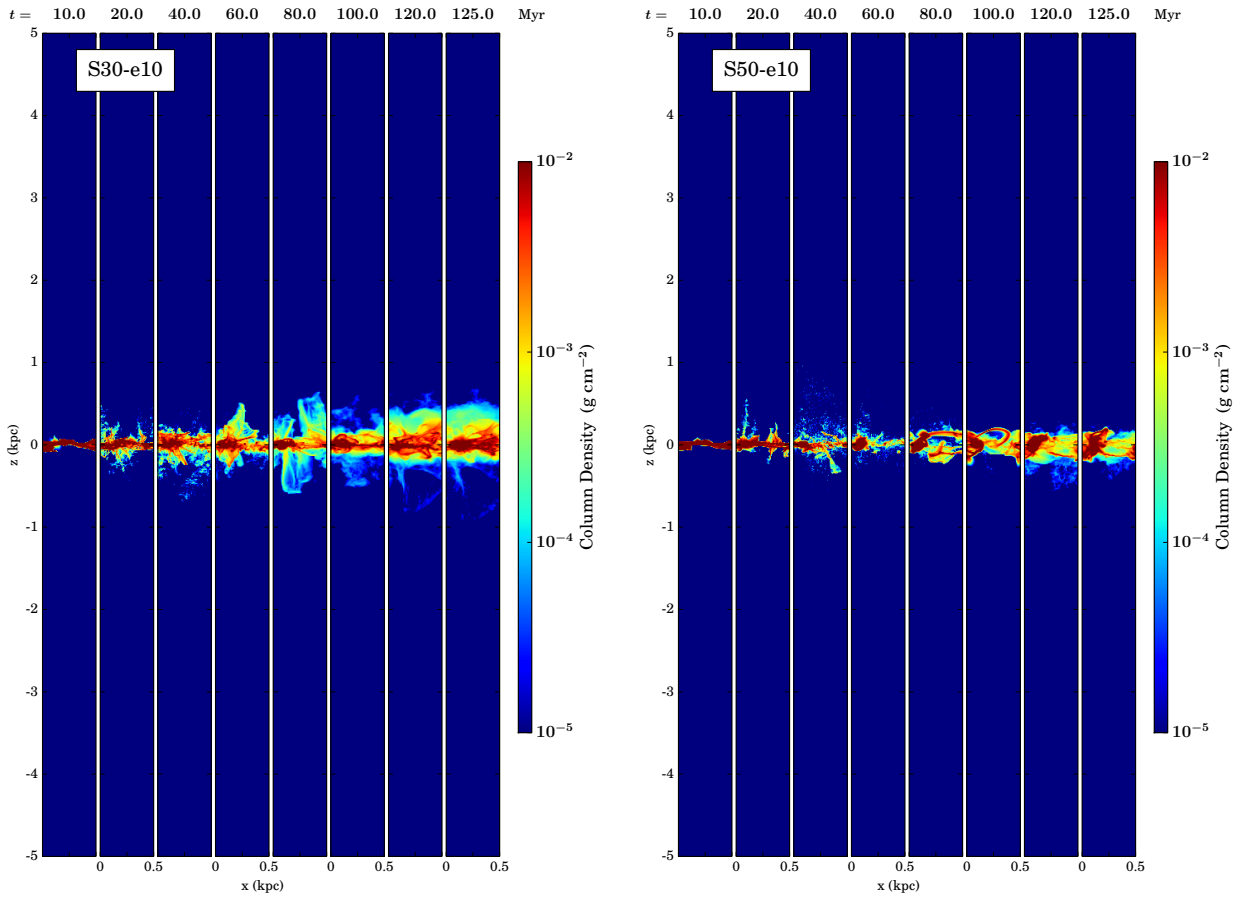

Figure 5.4: Column density sequence for S30-e10 (*left panel*) and S50-e10 (*right panel*). Both simulations show little gas in galactic fountains. The larger the initial density of the box, the more confined the gas is to the galactic mid-plane.

while in S10-e30, the events are two times more massive than in S10-e10 (144). This is illustrated in Fig. 5.2 where the star formation events in S10-e03 (purple circles) occur at higher densities but they are much smaller in comparison to the events in S10-e30 (green circles) and fewer. As a consequence, the run with $\varepsilon_{\rm SFR} = 3\%$ results in the gas being even more confined to the disk than in S10-e10 while a $\varepsilon_{\rm SFR}$ of 30% is able to push the gas out to ± 1 kpc from the mid-plane, just for it to collapse again towards the mid-plane after 120 Myr.

Figure 5.4 shows the time evolution of the column densities for $\Sigma_{\rm gas} = 30$ (left panel) and $50 M_\odot$ pc^{-2} (right panel). The maximum densities in the mid-plane of these simulations reach values of $\sim 2.5 \times 10^{-19}$ g/cm^3 and in both cases there are few to no gaseous outflows. In S50-e10, after 60 Myr, a large accumulation of gas forms in the left part of the disk and it remains roughly in the same position during the rest of the simulations time, without being destroyed. We present in Fig. 5.5 the number of massive stars exploding as SNe in each starburst event for the different $\Sigma_{\rm gas}$ runs. The number of SNe (and the injected

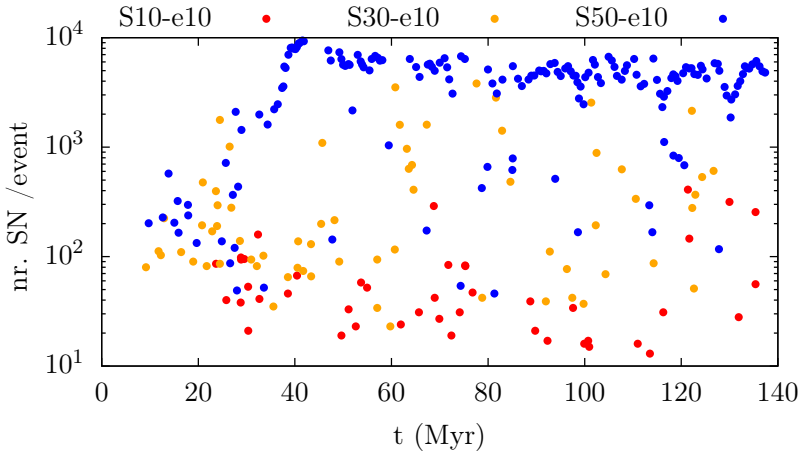

Figure 5.5: The number of SNe exploding per star formation event for different initial surface density runs, over a time of 140 Myr: S10-e10 (red dots), S30-e10 (orange dots) and S50-e10 (blue dots). The average number of SNe/event scales with the initial surface density of the simulations.

energy in the collapsing regions) increases with the surface density: most of the events in S10-e10 have fewer than 200 SNe/event while S50-e10 has more than 3000 SNe/event and most of these events happen inside the dense clump formed at 60 Myr. However, the disks seem to be more and more confined to the mid plane with increasing initial surface density.

We calculate the "instantaneous" SFR surface density which represents the total mass of the stars forming in all the collapsing regions in a certain time frame (free parameter) within the disk mid-plane area:

$$\Sigma_{\mathrm{SFR_{inst}}} = \frac{1}{A} \sum_{j=1}^{N_{\mathrm{event}}} M_{\mathrm{reg,j}} \frac{\varepsilon_{\mathrm{SFR}}}{dt_1} \; [M_\odot \mathrm{yr}^{-1} \mathrm{kpc}^{-2}], \tag{5.1}$$

where A = (0.5 kpc)^2, N_{event} is the number of collapsing regions, M_{reg} is the mass of the collapsing region and $\varepsilon_{\mathrm{SFR}}$ is the star formation efficiency of the simulation and dt_1 is 1 Myr.

Following the assumptions of Gatto et al. (2016), we can estimate an "observable" SFR surface density $\Sigma_{\mathrm{SFR_{OB}}}$. Knowing how many OB stars we form in each collapsing region (1/100 $M_\odot$) while considering an average of 10 Myr lifetime for each of them, we compute

$$\Sigma_{\mathrm{SFR_{OB}}} = \frac{1}{A} \sum_{j=1}^{N_{\mathrm{SN_{obs}}}} \frac{100 \times M_\odot}{dt_{2,\mathrm{j}}} \; [M_\odot \mathrm{yr}^{-1} \mathrm{kpc}^{-2}], \tag{5.2}$$

where $N_{\mathrm{SN_{obs}}}$ is the number of the massive OB stars that can be observed (considering they have a 10 Myr lifetime, dt_2). This approach allows a direct comparison to observable

measurements like tracing the SFR with Hα emissions.

Figure 5.6 shows the evolution of $\Sigma_{\mathrm{SFR_{inst}}}$ (columns of $dt_1 = 1$ Myr) and $\Sigma_{\mathrm{SFR_{OB}}}$ (red line) for S10-e10 and S10-e10-mag (first row), S10-e30 and S10-e03 (middle row), S30-e10 and S50-e10 (bottom row). We also show the average $\Sigma_{\mathrm{SFR_{OB}}}$ (blue dashed line) and compare it to the expected value of Σ_{SFR} (grey dashed line) derived from the Kennicutt-Schmidt (KS) relation for a certain surface density:

$$\frac{\Sigma_{\mathrm{SFR}}}{M_{\odot}\mathrm{yr}^{-1}\mathrm{kpc}^{-2}} = 2.5 \times 10^{-4} \left(\frac{\Sigma_{\mathrm{gas}}}{M_{\odot}\mathrm{pc}^{-2}} \right)^{1.4} \mathrm{Myr}^{-1}. \tag{5.3}$$

The dense regions start collapsing earlier in the magnetised run in comparison to S10-e10, but the average Σ_{SFR} is 25% lower than in S10-e10, and it overlaps with the predicted KS Σ_{SFR}. A significant decrease in the $\Sigma_{\mathrm{SFR_{OB}}}$ takes place at about 70 Myr followed by smaller $\Sigma_{\mathrm{SFR_{inst}}}$ values, in concordance with Fig. 5.2.

The average $\Sigma_{\mathrm{SFR_{OB}}}$ varies according to the star formation efficiency: S10-e30 has a $\Sigma_{\mathrm{SFR_{OB}}}$ of 86% above the KS while S10-e03 has a $\Sigma_{\mathrm{SFR_{OB}}}$ of 57% lower. With increasing initial gas surface densities, the average $\Sigma_{\mathrm{SFR_{OB}}}$ becomes higher than the KS value (for S30-e10 by more than a factor of three and S50-e10 by almost a factor of thirty).

In Fig. 5.7 we plot the average $\Sigma_{\mathrm{SFR_{OB}}}$ for each simulation as function of the initial gas surface density along with the KS relation (Kennicutt, 1998). The variation within the S10 simulations is between 56% below the KS relation for the 3% $\varepsilon_{\mathrm{SFR}}$ run and 78% above for the 30% $\varepsilon_{\mathrm{SFR}}$ runs. With increasing initial surface densities the average Σ_{SFR} are further away from the KS relation.

We also show the H_2 mass fraction evolution (Fig. 5.8, top panel) and the hot gas VFF (Fig. 5.8, bottom panel) of the simulations. The H_2 mass fraction varies substantially for some simulations (three orders of magnitude for S10-e30, two orders of magnitude for S10-e10-mag) and it is seemingly constant for e.g. S30-e10 or S50-e10. The highest H_2 mass fraction is obtained in S50-e10 (0.75, see Table 5.2), probably in the dense MC that forms at 60 Myr (see Fig. 5.4) and which survives through the simulation in spite of the high number of SNe/event. The same situation applies to S30-e10 which produces a 60% H_2 mass fraction. These simulations have a very high hot gas VFF ($\sim$ 80% at the beginning of the runs) due to the collapse of the disk under its own weight, up a thickness of about 82 pc. The SN feedback in S50-e10 is inefficient in dispersing the collapsing regions and accountable for the high hot gas VFF (calculated at $\pm$ 100 pc around the mid plane). In the case of S30-e10, some dense gas is being dispersed when the SNe go off later in the simulation (see Fig. 5.4) causing a decrease in the VFF (from 80% to 1% after 100 Myr).

The average H_2 mass fraction in S10-e10 is 0.28 while the hot gas VFF starts decreasing considerably after 30 Myr. The H_2 in S10-e10-mag reaches 30% at a later time than in S10-e10 and settles at a lower average of 13%. The fact that the formation of H_2 is delayed and suppressed in the magnetised ISM has been extensively analysed and discussed in Chapter 3. The sudden drop at 70 Myr corresponds to a massive star formation event that was able to disperse about 20% of all the H_2 formed in the disk at that time. After this event it takes about 60 Myr for the H_2 mass fraction to reach the previous level of 30%.

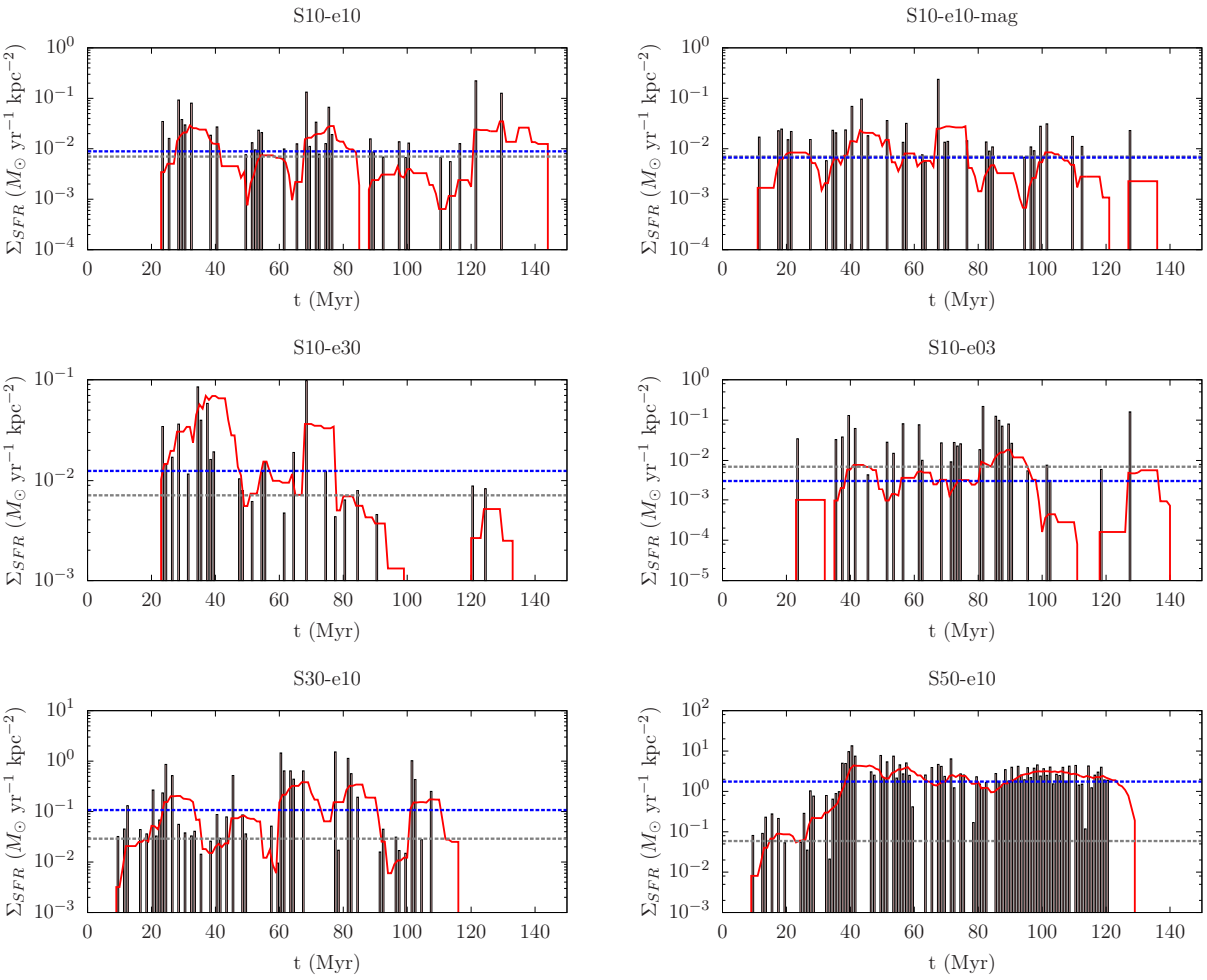

Figure 5.6: Evolution of $\Sigma_{\mathrm{SFR_{inst}}}$ (light pink columns) and $\Sigma_{\mathrm{SFR_{OB}}}$ (red line) for S10-e10 (*first row, left panel*), S10-e10-mag (*first row, right panel*), S10-e30 (*middle row, left panel*), S10-e03 (*middle row, right panel*), S30-e10 (*bottom row, left panel*) and S50-e10 (*bottom row, right panel*). The grey dotted line represents the Σ_{SFR} we would expect from the Kennicutt-Schmidt relation for the corresponding surface density and the blue line is the average $\Sigma_{\mathrm{SFR_{OB}}}$. The average $\Sigma_{\mathrm{SFR_{OB}}}$ increases with increasing star formation efficiency and increasing initial surface density.

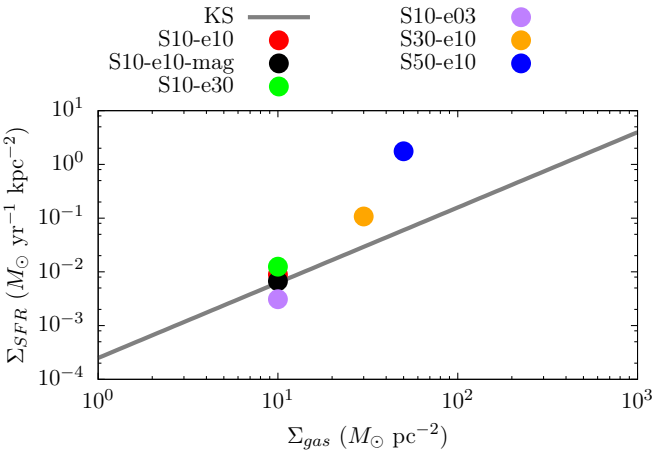

Figure 5.7: Mean SFR surface density as function of total gas surface density for S10-e10 (red circle), S10-e10-mag (black circle), S10-e30 (green circle), S10-e03 (purple circle), S30-e10 (orange circle), S50-e10 (blue circle) and for the Kennicutt-Schmidt relation (grey line). While the simulation with initial surface density of 10 $M_\odot$/pc^2 lie very close to the KS relation (with small variations with $\varepsilon_{\rm SFR}$), the increase in the initial surface density determines a larger deviation from KS.

However, the hot gas VFF has a similar behaviour to the unmagnetised run.

In S10-e30, after the initial artificial stirring of the gas, the H_2 fraction decreases considerably and during the simulation time, varies over three orders of magnitude. The average H_2 mass fraction is 12%, much lower than in the rest of the simulations. The same behaviour can be seen in the VFF: dramatic drop after 30 Myr (after the first SNe explode) followed by strong variations due to the warm gas being pushed outside the ±100 pc limit (see Fig. 5.3).

The Schmidt-type driving seems to give results in agreement with the Kennicutt-Schmidt relation only for the $\Sigma_{\rm gas} = 10\,M_\odot\,{\rm pc}^{-2}$ simulation. For higher surface densities, even though the SFR scales with the density ($N_{\rm SN} \sim \rho^{3/2}$), we retrieve a $\Sigma_{\rm SFR}$ higher than the KS predictions. The high H_2 mass fraction and the inefficiency of the SN feedback to produce sustained gaseous outflows point to the fact that solely instantaneous SN explosions, strongly correlated with peak density regions, fail to create a realistic ISM.

Even though the Schmidt-type SN driving is very different from the fixed SN rate feedback, implemented and discussed by Walch et al. (2015) and Girichidis et al. (2016), we find a similar lack of outflows as in the case of the peak density correlated fixed SN rate driving. More details of a comparison between our $\Sigma_{\rm gas} = 10\,M_\odot\,{\rm pc}^{-2}$ simulations and different fixed SN drivings in disks with almost identical initial conditions and comparable $\Sigma_{\rm gas}$ can be found in Appendix C.3.

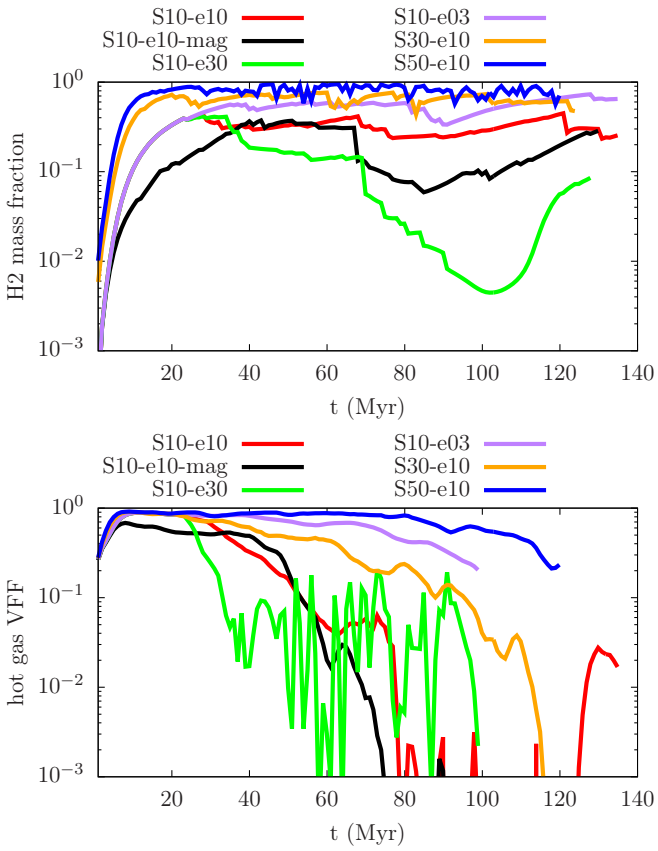

Figure 5.8: H_2 mass fraction (*top panel*) and hot gas VFF (calculated in the $\pm$ 1 kpc about the mid-plane) comparison (*bottom panel*) of the simulations: S10-e10 (red line), S10-e10-mag (black line), S10-e30 (green line), S10-e03 (purple line), S30-e10 (orange line) and S50-e10 (blue line). The high surface density runs (S50-e10 and S30-e10) produce the most H_2, along with the low star formation efficiency run, and have the largest hot gas VFF.

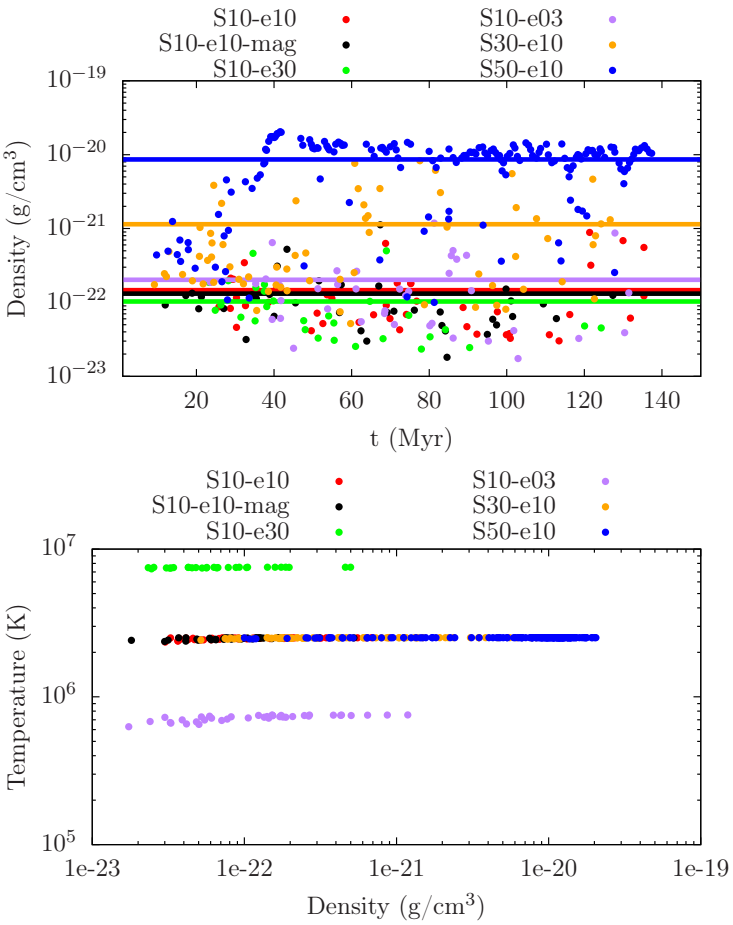

Figure 5.9: The (average) density of the regions the SN explodes in (the lines are averages over all the SN explosions, *top panel*), and the injection temperatures (*bottom panel*). Only the S10-e3 simulation has injection temperatures below 10^6 K.

5.3 Why are there no outflows?

The common trend in the column density time evolutions in Fig. 5.1, 5.3 and 5.4 is that there are no significant outflows produced in any of these simulations. We only observe fountain flows in S10-e30 up to a scale height of 1.5 kpc. Previous studies of SN-driven galactic disks (with very similar setups) have shown that randomly positioned and clustered SNe can eject hot gas up to 3 kpc (Hill et al., 2012), and a significant fraction of the gas up to 2 kpc (Gent et al., 2013a; Girichidis et al., 2016). Observations show that galactic outflows vary in scale-height between 1 and 20 kpc (see the review of Veilleux et al., 2005).

We show in Fig. 5.9 (top panel) the average densities of the environment the SNe explode in for all the simulations, and the temperature at the injection of the SN feedback as function of density (bottom panel). The average densities cover two orders of magnitude (between 10^{-22} and 10^{-20} g/cm^3); they are higher with increasing initial surface density,

when the $\varepsilon_{\rm SFR}$ is constant (S10-e10: $1.5{\times}10^{-22}$ g/cm^3, S30-e10: $11.4{\times}10^{-22}$ g/cm^3 and S50-e10: $86.1{\times}10^{-22}$ g/cm^3, see Table 5.2), and with decreasing $\varepsilon_{\rm SFR}$ for the same surface density (S10-e30: $1{\times}10^{-22}$ g/cm^3 and S10-e03: $2{\times}10^{-22}$ g/cm^3). However, the injection temperature is constant, regardless of the density of the collapsing region or surface density (see Table 5.2). It is dependent only on the $\varepsilon_{\rm SFR}$. In high density regions, due to strong radiative cooling, at an injection temperature $T_{\rm inj} < 10^6$ K, the injected energy is immediately lost, causing over-cooling (e.g. Stinson et al., 2006; Creasey et al., 2011; Gatto et al., 2013). The injection temperature of S10-e03 is lower than the $T_{\rm inj} = 10^6$ K limit.

The reason the injection temperature is dependent only on the $\varepsilon_{\rm SFR}$ is because it is calculated as

$$T_{\rm inj} = \frac{N_{\rm SN} \times E_{\rm SN}}{k_{\rm B}} \frac{2}{3} \frac{m_{\rm p}}{M_{\rm reg}}, \tag{5.4}$$

where $E_{\rm SN} = 10^{51}$ erg and $m_{\rm p} = 13au/21$ with au $= 1.6726231{\times}10^{-24}$ (g) (Blondin et al. 1998).

From Eg. 5.4 and Eg. 2.16 we find

$$T_{\rm inj} = \frac{\frac{M_{\rm reg}\times\varepsilon_{\rm SFR}}{100\times M_\odot}}{k_{\rm B}} \times E_{\rm SN} \frac{2}{3} \frac{13au}{21 M_{\rm reg}} \sim \varepsilon_{\rm SFR}. \tag{5.5}$$

We also calculate the radiative cooling time $t_{\rm cool}$ and the sound crossing time $t_{\rm s}$ (the time needed for a sound wave to cross the injection region):

$$t_{\rm cool} = \frac{1}{n_{\rm H_2}^2 \Lambda(T,\rho)} \frac{E_{\rm inj}}{V_{\rm inj}}, \tag{5.6}$$

$$t_{\rm s} = \frac{r_{\rm inj}}{c_{\rm o}} = \frac{r_{\rm inj}}{\sqrt{\frac{\gamma k_{\rm B} T_{\rm inj}}{m_{\rm H_2}}}}, \tag{5.7}$$

where $c_{\rm o}$ is the sound speed in the injection region, $n_{\rm H_2}$ in cm^{-3} is the average number density of the region (we assume that the gas is molecular), $\Lambda(T,\rho)$ is the cooling function (in erg cm^3 s^{-1}), $E_{\rm inj}$ is the total thermal energy injected in the SNe and $V_{\rm inj} = \frac{4}{3}\pi(r_{\rm inj})^3$ which in the fiducial case is $\sim 2\times10^4$ pc^3, $\gamma = 7/5$ is the adiabatic index and $m_{\rm H_2}$ is the mass of a single H_2 molecule.

Only when the sound-crossing time scale $t_{\rm s}$ across the injection region is shorter than the radiative cooling time $t_{\rm cool}$ the thermal feedback is effective. This is a necessary criterion in order for the thermal energy not to be radiated away before the expansion of the SN remnant. According to Creasey et al. (2011); Dalla Vecchia and Schaye (2012), the ratio of $t_{\rm cool}/t_{\rm s}$ has to be larger than eight in order to ensure that numerical over-cooling is avoided.

For the simulations with the same $\varepsilon_{\rm SFR}$ (S10-e10, S30-e10 and S50-e10), we show the average time-steps, the cooling times for each SN event and the sound-crossing time in Fig. 5.10, top panel. The average cooling times decrease with increasing $\Sigma_{\rm gas}$ (S10: 0.1 Myr, S30: 0.03 Myr and S50: 0.004 Myr, see Table 5.2) and only eight of the starburst events in S10-e10 have longer cooling times than the sound crossing time (which is 0.16 Myr),

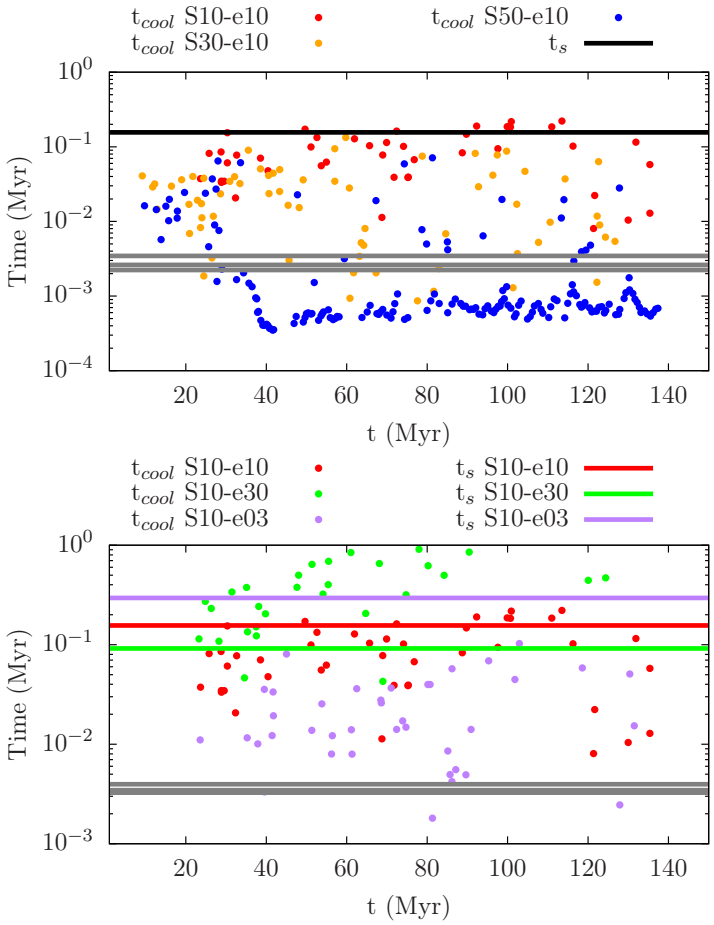

Figure 5.10: Comparison of the sound-crossing times, cooling times and time-steps for the simulations with 10% $\varepsilon_{\rm SFR}$ (*top panel*), and the simulations with $\Sigma_{\rm gas} = 10\,M_{\odot}\,{\rm pc}^{-2}$ and different $\varepsilon_{\rm SFR}$ (*bottom panel*). We show the sound-crossing time (black line), the average time-steps (grey lines), and the cooling times for each event in S10-e10 (red dots), S30-e10 (orange dots) and S50-e10 (blue dots). In the bottom panel, the sound-crossing times depend on the $\varepsilon_{\rm SFR}$ and are represented for S10-e10 (red line), S10-e30 (green line) and S10-e03 (purple line), along with the cooling times of the events (dots with the same colour coding). The grey lines are the average time-steps. The only run for which the cooling times of the events are longer than the sound-crossing time is S10-e30.

meaning that almost all the SN blasts cool down before they expand into the surrounding environment. S30-e10 has a few events for which the cooling time is shorter than the average time-steps, pointing to the fact that our time resolution is too low in order to properly resolve the radiative cooling time. In the case of S50-e10, most of the SN events are unresolved having cooling times up to an order of magnitude shorter than the average time-steps.

We present the same comparison for the runs with the same $\Sigma_{\rm gas}$, but different $\varepsilon_{\rm SFR}$ (see Fig. 5.10, bottom panel). For these simulations, the sound-crossing time is higher for lower $\varepsilon_{\rm SFR}$ (S10-e30: 0.1 Myr, S10-e10: 0.16 Myr and S10-e03: 0.3 Myr) because the sound speed, for a fixed injection radius, depends only on the $\varepsilon_{\rm SFR}$ (see Eq. 5.14). For S10-e03, even though only two events have lower cooling times than the average time-steps, all of them lie below the sound-crossing time. With the exception of two, all events satisfy $t_{\rm cool}/t_{\rm s} > 1$; however, for only three of them the $t_{\rm cool}/t_{\rm s} > 8$ criterion is fulfilled.

5.4 Overcoming the cooling problem

With higher surface density, the SNe events are increasingly unresolved. Our simulations are heavily affected by numerical overcooling which leads to an unrealistic (too cold) ISM, an over-prediction of the SFR, and results in a lack of outflows. In order to overcome these caveats, we propose several options.

5.4.1 Theoretical estimates for environmental densities

There are three time scales (the time-step Δt, the cooling time $t_{\rm cool}$ and the sound-crossing time $t_{\rm s}$) which have to obey two rules: $t_{\rm cool} > \Delta t$ and $t_{\rm cool}/t_{\rm s} > 8$. According to the Courant-Friedrichs-Lewy (CFL) condition:

$$\frac{u \times \Delta t}{\Delta x} \leq C \tag{5.8}$$

where u is the total signal speed (motion of the gas and sound speed in the HD simulations and in addition the magnetic speeds in the MHD run), Δx is the length of a cell and C in our case has a fixed value of 0.9. From Eq. 5.9 the time-step becomes

$$\Delta t \leq \frac{C \times \Delta x}{u} \tag{5.9}$$

which represents the upper limit of for the time-step. In order to decrease the time-step Δt and increase the probability for $t_{\rm cool} > \Delta t$ for high density runs like S50-e10 (see Fig. 5.10, top panel), one can

- Impose a lower C. However, small decrements of C would rapidly make the simulations run much slower.
- Increase the resolution of the simulations.

- Increase the sound speed $c_{\rm o}$ of the environment the SNe explode in.

Moreover, knowing that the total injection energy is $E_{\rm inj} = N_{\rm SN} \times 10^{51}$ ergs:

$$E_{\rm inj} = \frac{M_{\rm reg}\varepsilon_{\rm SFR}}{100 M_\odot} \times 10^{51} \tag{5.10}$$

and that $\mathrm{V}_{\rm inj} = M_{\rm reg}/\rho$, from Eq. 5.6, the cooling time can be written as:

$$\begin{aligned} t_{\rm cool} &= \frac{1}{n_{\rm H_2}^2 \Lambda(T,\rho)} \times \frac{M_{\rm reg}\varepsilon_{\rm SFR}}{100 M_\odot} \times 10^{51} \times \frac{\rho}{M_{\rm reg}} \\ &= \frac{\rho \times \varepsilon_{\rm SRF}}{n_{\rm H_2}^2 \Lambda(T,\rho)} \frac{10^{51}}{100 M_\odot} \end{aligned} \tag{5.11}$$

Considering that for $T > 10^6$K, $\Lambda(T,\rho)$ is approximately $2.5{\times}10^{-23}$ erg cm^3 s^{-1}, that $\mathrm{n_{H_2}} = \rho/m_{\rm H_2}$ with $m_{\rm H_2} = 3.34 \times 10^{-24}$ g, that 1 $M_\odot = 1.98 \times 10^{33}$ g, and that 1 Myr$= 3.2 \times 10^{13}$s, $t_{\rm cool}$ becomes:

$$t_{\rm cool} = 0.7 \times 10^{-23} \frac{\varepsilon_{\rm SFR}}{\left(\frac{\rho}{\rm g/cm^3}\right)} \ \text{(Myr)} \tag{5.12}$$

being a function of the $\varepsilon_{\rm SFR}$ and the density of the collapsing region.

From Eq. 5.4 and 5.7 we can also express $t_{\rm s}$ as:

$$\begin{aligned} t_{\rm s} &= r_{\rm inj} \left(\frac{\gamma k_{\rm B}}{m_{\rm H_2}} \frac{N_{\rm SN} \times 10^{51}}{k_{\rm B}} \frac{2}{3} \frac{m_{\rm p}}{M_{\rm reg}} \right)^{-1/2} \\ &= r_{\rm inj} \left(\frac{\gamma m_{\rm p}}{m_{\rm H_2}} \frac{2}{3} \frac{M_{\rm reg} \times \varepsilon_{\rm SFR}}{100 M_\odot} 10^{51} \frac{1}{M_{\rm reg}} \right)^{-1/2} \\ &= r_{\rm inj} \varepsilon_{\rm SFR}^{-1/2} \left(\frac{\gamma m_{\rm p}}{m_{\rm H_2}} \frac{2}{3} \frac{10^{51}}{100 M_\odot} \right)^{-1/2} \end{aligned} \tag{5.13}$$

Considering that $\gamma = 7/5$, $m_{\rm p} = 13/21 \times 1.67 \times 10^{24}$g, $t_{\rm s}$ in Myr becomes:

$$t_{\rm s} = 0.8 \times 10^{-22} \left(\frac{r_{\rm inj}}{\rm cm} \right) \varepsilon_{\rm SFR}^{-1/2} \ \text{(Myr)} \tag{5.14}$$

In Fig. 5.11, we show the cooling and sound-crossing time dependence of the density for a $\varepsilon_{\rm SFR}$ of 10% (top panel), 30% (middle panel) and 3% (bottom panel), on different injection radii. For a given $\varepsilon_{\rm SFR}$, the sound-crossing time is directly proportional to the injection radius, while the cooling time is inversely proportional to the density of the injection radius. This will lead to a value $\rho_{\rm eq}$ for the density when the cooling time and sound-crossing time are equal. The density limit $\rho_{\rm eq}$ is increasing with the $\varepsilon_{\rm SFR}$ (for 10% $\varepsilon_{\rm SFR}$, $\rho_{\rm eq} = 5 \times 10^{-23}$ g/cm^3 and for 3% $\varepsilon_{\rm SFR}$, $\rho_{\rm eq} = 9 \times 10^{-24}$ g/cm^3).

One can also estimate a recommended density for which the $t_{\rm cool}/t_{\rm s} > 8$ criterion is fulfilled (we note that to reach this condition one must assume that the average density of the injection region and the local density where we compute the cooling time are comparable):

$$\rho_{\rm rec} = 0.01 \frac{\varepsilon_{\rm SFR}^{3/2}}{\left(\frac{r_{\rm inj}}{\rm cm}\right)} \tag{5.15}$$

We depict in Fig. 5.12 the values for the recommended density $\rho_{\rm rec}$ that can be resolved as function of injection radius and $\varepsilon_{\rm SFR}$. The $\rho_{\rm rec}$ values are colour coded and encompass densities from 10^{-25} to 10^{-21} g/cm^3 with distinctive lines for 10^{-24} (light-yellow line), 10^{-23} (red line) and 10^{-22} g/cm^3 (black line). As shown by Eq. 5.15, $\rho_{\rm rec}$ increases with decreasing injection radius (for a fixed $\varepsilon_{\rm SFR}$) and with increasing $\varepsilon_{\rm SFR}$ (for a fixed injection radius).

Our goal is to increase $\rho_{\rm rec}$ as the average densities of SNe events are or order 10^{-22} g/cm^3 for $\Sigma_{\rm gas} = 10\ M_\odot$ pc^{-2}, 10^{-21} g/cm^3 for $\Sigma_{\rm gas} = 30\ M_\odot$ pc^{-2} and even 10^{-20} g/cm^3 for $\Sigma_{\rm gas} = 50\ M_\odot$ pc^{-2} (see Fig. 5.9, top panel). We can do this in three ways:

- *Increase the star formation efficiency ($\varepsilon_{\rm SFR}$).* We have shown in Fig. 5.10 that the only simulation that has a higher cooling time than the average sound-crossing time is S10-e30, and it is also the only run in which the SN feedback lifts warm gas up to a scale-height of $\sim$ 1 kpc (see Fig. 5.3, right panel). However, the $\varepsilon_{\rm SFR}$ is an observationally constrained local parameter which according to recent studies (see e.g. Lada, 2016) varies between 30% in dense cores and 2% in giant molecular clouds (GMCs). In this sense, the maximum reasonable value for the $\varepsilon_{\rm SFR}$ would be around 30%.

- *Decrease $r_{\rm inj}$.* This can be done with better resolution. In our case, increasing the level of refinement to only 2 pc/cell is very computationally expensive. An option would be to study the Schmidt-type driving in periodic boxes of only a few hundred parsecs in dimension (see Chapter 3 and 4). This setup would allow us to obtain resolutions of 1 pc/cell which corresponds to an injection radius of 4 pc (for 4 cells). With 4 pc injection radius and an $\varepsilon_{\rm SFR}$ of 30%, we could resolve densities above 10^{-22} g/cm^3 (see Fig. 5.12). However, the drawback of the setup would be that we cannot follow the outflows.

- *Lower the average density of the collapsing regions.* This will lead to the increase of the Jeans length ($\lambda_{\rm J}$) and the free-fall time ($t_{\rm ff}$) of the collapsing region. We have run an additional simulation with the same initial parameter as S30-e10 but we lowered the critical density to $\rho_{\rm crit} = 2 \times 10^{-24}$ g/cm^3, below the recommended density given by Eq. 5.15 for $\varepsilon_{\rm SFR}$= 10% and $r_{\rm inj}$ = 5 cells = 20 pc ($\rho_{\rm rec} \sim 6 \times 10^{-24}$ g/cm^3), in run S30-e10-ld.

  Lowering the density threshold determines a higher SFR and a higher average number of SNe/event (1361 in comparison to the less than half, 613 SN/event in S30-e10), and it results in more warm gas being elevated to higher scale height (see Fig. C.5

where we show a dynamical evolution of the disk over 110 Myr). However, we see the formation of a MC that can hardly be dispersed due to inefficient SN feedback. The average $\Sigma_{\rm SFR}$ in this case is 0.33 $M_\odot$ yr^{-1} kcp^{-2}, more than three times higher than for S30-e10 (see Fig. 5.13), placing S30-e10-ld even further away from the KS law.

- Another option we suggest is to *redistribute the density of the gas in the injection region.* Due to stellar winds and radiation, it is reasonable to assume that the environment in the injection region has a lower average density than what we obtain. Observation show that subparsec filaments are effected by trans- and supersonic turbulence (Arzoumanian et al., 2013; Li et al., 2014) and small scale zoom-in simulations like Seifried and Walch (2015) introduce an additional turbulent velocity field in star forming filaments corresponding to a Kolmogorov type spectrum.

5.4.2 Modelling a more realistic ISM

Another way to deal with the overcooling problem would be to model the ISM in a more realistic way. The classic Schmidt-type driving that we discussed so far assumes a perfect correlation between the SNe and the densest cell in the injection region. There are extensive studies and simulations showing that the majority of OB stars can explode as Type II SNe from a few tens of parsecs to even thousands of parsecs away from the MC they were born in (Portegies Zwart et al., 2007; Zinnecker and Yorke, 2007; Tetzlaff et al., 2011; Perets and Subr, 2012). There is also evidence that Type II SNe explode in various types of environment: low-density gas (Rogers and Pittard, 2013), HII regions (Dale et al., 2014; Walch and Naab, 2015), old SN remnants (Gatto et al., 2015), or molecular gas (Fukui et al., 2003; Hewitt and Yusef-Zadeh, 2009).

In our simulations, the injection region is highly structured from the density point of view. We ran additional test simulations varying the injection radius (4 cells S10-c4 and 2 cells S10-c2). We find that with decreasing injection radius, the average density of the collapsing regions becomes higher (see Fig. 5.14). This points to the fact that most of the mass in the injection regions is highly concentrated towards the centre. The way in which we look for collapsing regions is to find the cell with $\rho > \rho_{\rm crit}$ and we define the injection region around this cell hence, in time, we can expect more gas to flow towards the centre. When considering an injection radius half the size (2 pc) the average density of the region rises with almost an order of magnitude (3×10^{-21} g/cm^3, in comparison to 4×10^{-22} g/cm^3 for $r_{\rm inj} = 4$ cells).

In Fig. 5.15 we show the density of all the cells in the injection region for the areas that are collapsing but have not yet exploded in S30-e10, between 12 and 18 Myr. The densities in the injection region can range over five orders of magnitude (between 10^{-26} and 10^{-21} g/cm^3). As time passes, this density range becomes narrower due to the additional mass accumulated until the SN detonation. However, there is a high possibility for any displaced SNe about the centre of the injection region to explode in much less dense gas, decreasing considerably the chances of numerical overcooling.

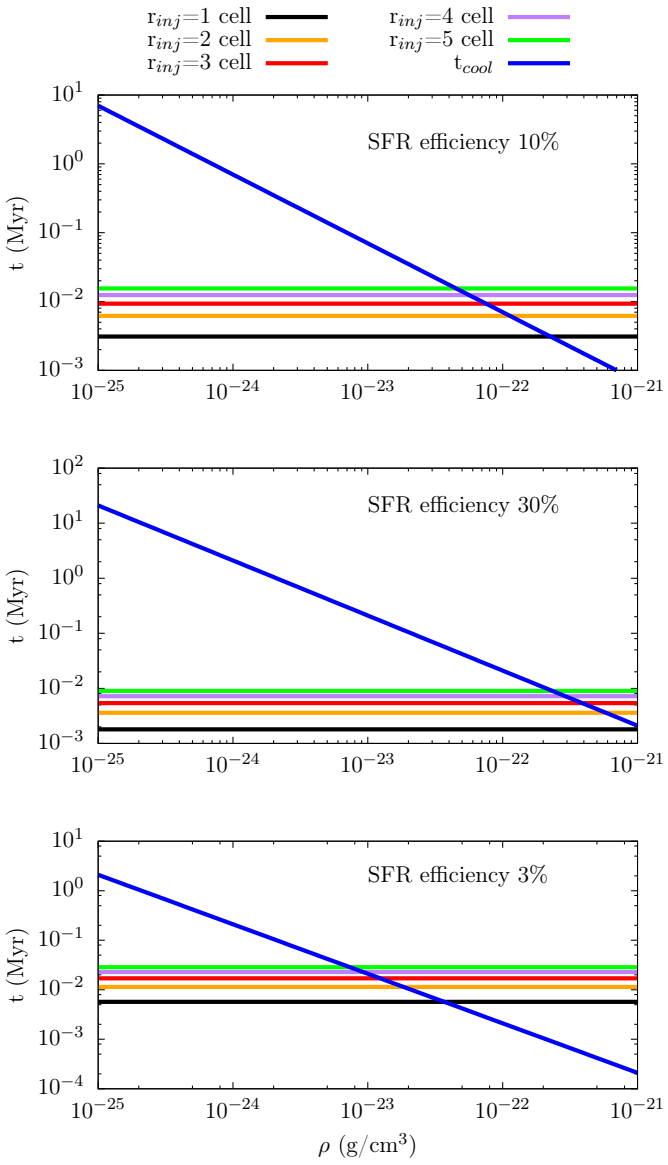

Figure 5.11: Cooling times and $r_{\rm inj}$-dependent sound-crossing times for different $\varepsilon_{\rm SFR}$ (10% *top panel*, 30% *middle panel* and 3% *bottom panel*). We represent the sound crossing time for $r_{\rm inj}$ = 1 cell (black line), 2 cells (orange line), 3 cells (red line), 4 cells (purple line), 5 cells (green line), and the cooling time $t_{\rm cool}$ (dark-blue line). For one specific $\varepsilon_{\rm SFR}$, $t_{\rm s}$ is decreasing for smaller $r_{\rm inj}$, while $t_{\rm cool}$ is decreasing with higher ambient densities. The critical ambient density for which $t_{\rm cool}$ becomes equal to $t_{\rm s}$ is lower for low ε_{SFR}.

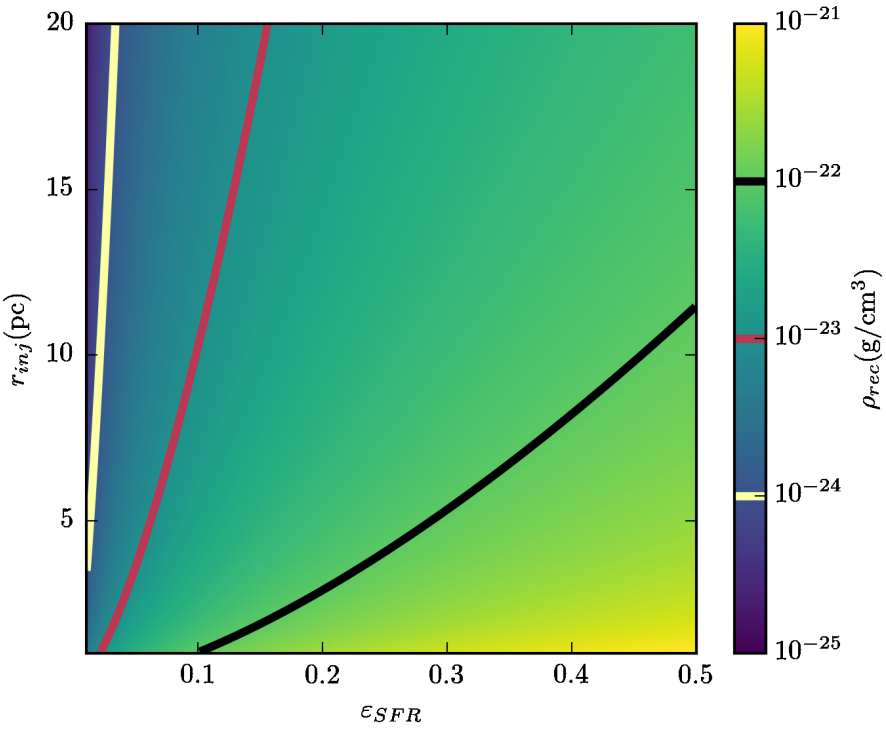

Figure 5.12: Values for the recommended density $\rho_{\rm rec}$ that can be resolved as function of injection radius and $\varepsilon_{\rm SFR}$. The $\rho_{\rm rec}$ values are colour coded from 10^{-25} (dark-blue) to 10^{-21} g/cm^3 (yellow) with distinctive lines for 10^{-24} (light-yellow line), 10^{-23} (red line) and 10^{-22} g/cm^3 (black line). $\rho_{\rm rec}$ increases with decreasing injection radius (for a fixed $\varepsilon_{\rm SFR}$) and with increasing $\varepsilon_{\rm SFR}$ (for a fixed injection radius).

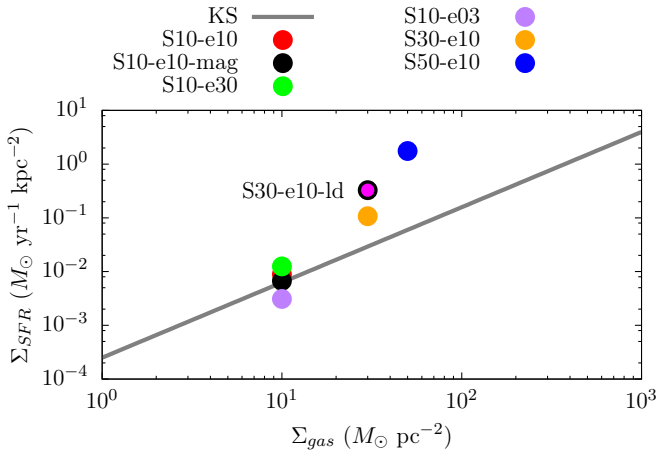

Figure 5.13: Same as Fig. 5.7 but with the additional average $\Sigma_{\rm SFR}$ of S30-e10-ld (magenta dot in black circle). A lower density threshold determines a higher $\Sigma_{\rm SFR}$ placing the simulation further away from the expected $\Sigma_{\rm SFR}$ from the KS relation.

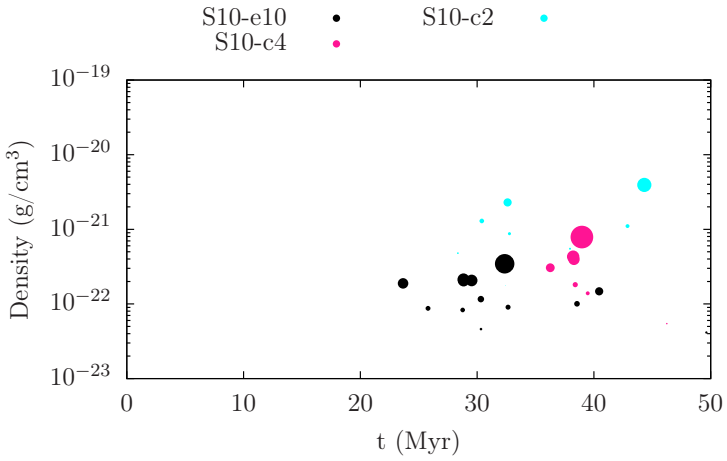

Figure 5.14: Density of the environment the SNe explode in, with the radii of the circles scaling with the no. of SNe/event, for different dimensions of the injection radius (5 cells - black circles, 4 cells - pink circles and 2 cells - cyan circles) for S10-e10, and the density of the cells inside the injection region ($r_{\rm inj}$ = 5 cells) for S30-e10-box. The smaller the injection radius the denser the medium the SNe go off in.

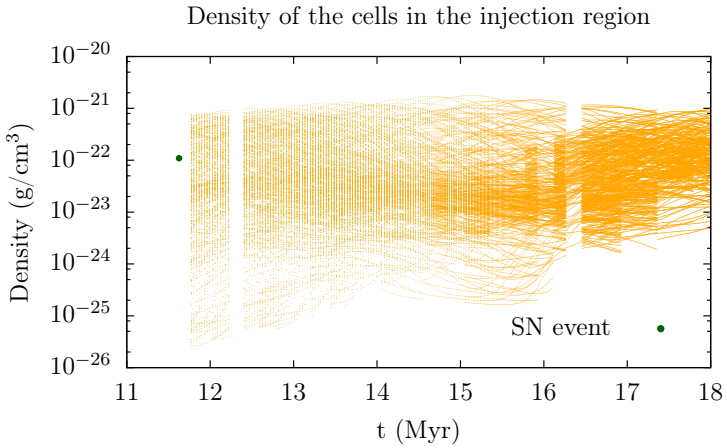

Figure 5.15: The densities of all the cells within the accretion radius for the collapsing regions between 12 and 18 Myr (orange dots), with the average density of a star formation event shortly before 12 Myr (green dot) added for reference. The densities in these regions can range over five orders of magnitude with this interval decreasing in time, as more mass is accreted until the SN detonation.

Moreover, all the SNe in our simulations explode at the same time while the lifetime of stars scales with their mass. If we do a rough estimate and divide the mass range we use for all the Type II SNe (from 8 to 60 $M_\odot$, see Smartt (2009, 2015)) and distinguish between two classes of $M_1 = [8, 34) M_\odot$ and $M_2 = (34, 60] M_\odot$, using the Salpeter IMF (Salpeter, 1955), we find that out of the total number of SNe exploding at an event, 90% will be of class M_1 and 10% of class M_2. If we also extend the $t \sim M^{-3}$ scaling to all the core collapse SNe progenitors, we find that the most massive stars have an average lifetime of the order of 0.8 Myr, while the less massive ones can live on average 10 Myr. If we assume that the class M_2 stars explode at the moment of the collapse, we are left with 90% of SNe exploding at a later time-step.

Without the strong correlation between the SNe and the peak density regions along with the instantaneous detonation of the SNe, we are confident we can create a hot phase. Following Naab and Ostriker (2016), one can calculate the expected value for a SN to explode in the hot gas within the shell of a previous SN explosion (N_{hot}). This scenario ensures that a hot stable phase is created before the isolated SN remnants rapidly cool away. Knowing that at the end of the Sedov-Taylor phase, at the time of the shell formation, the maximum amount of hot gas has been produced, N_{hot} represents the probability for another SN to explode within the Sedov-Taylor radius of an older SN remnant in a homogeneous ISM and assuming a certain SN density rate. Applying these calculations to our simulation setup, we find that the expected N_{hot} for an initial $\Sigma_{gas} = 10\, M_\odot$ pc^{-2} is 38% (for the gas enclosed within a volume of $500 \times 500 \times 200$ cp^3). This value drops to 20% for $\Sigma_{gas} = 30$ and 50 $M_\odot$ pc^{-2}.

5.4.3 Comparison to simulations using sink particles

Following Gatto et al. (2016), we ran one simulation with almost identical initial conditions to S30-e10, but with sink particles (S30-sink) for 40 Myr. In the search for a collapsing region, the area around the over-critical density passes the same checks describes in Subchapter 2.4. The critical density and the injection region are the same as in S30-e10. Once a collapsing region is found, the sink particle is created immediately and it can accrete mass continuously during its lifetime. In these simulation, the SN feedback implementation is identical to the fiducial runs, however, we include stellar wind feedback. Calculating the total mechanical luminosity for all the stars and the total mass lost in the winds, this mass is added to the injection region and subtracted from the sink particles' masses (for details on implementation see Gatto et al. (2016)). The wind feedback is injected in the form of kinetic energy, evenly distributed within the injection area.

The average $\Sigma_{\mathrm{SFR_{OB}}}$ retrieved for S30-sink is about three times higher than the $\Sigma_{\mathrm{SFR_{OB}}}$ obtained for S30-e10 (0.28 compared to 0.1). However, it is comparable to S30-e10-ld (0.33). In Fig. 5.16, we show the dynamical evolution of the disk through consecutive column density panels. In comparison to s30-e10-ld, after 40 Myr (see Fig. C.5, Appendix C.4) the combination of winds and subsequent SN injected in the sink particles' positions can drive outflows for which the gas reaches scale-heights of 5 kpc above and below the mid-plane. It was discussed by Gatto et al. (2016) that the effect of stellar winds is to reduce both the SFR and outflows, limiting the mass accretion by efficiently cleaning out the local environment around the sinks.

The main difference between S30-e10-ld and S30-sink is that, when comparing the mass accreted by the sink particles, the average is about four orders of magnitude lower than the mass in the injection region when the SNe explode in S30-e10-ld. In the sink particle simulations, only the mass of the gas with densities above the ρ_{crit} threshold is contributing to star formation and the subsequent mass that is accreted onto the sink particles remains in the grid, while in our simulations we include the entire gas there is around the cell exceeding the ρ_{crit} threshold within an r_{acc} radius. Furthermore, the sink particles accrete mass over time (while our starburst events are instantaneous), and they move around the disk increasing the chances for a SN to explode in a low density environment. This leads to a huge difference in average density at the time of SN detonation. In Fig. 5.17, we show the cooling times for all the SNe in S30-sink (often exploding within the same sink particle) and the few SNe events in S30-e10-ld until 40 Myr into the simulation, along with the average sound-crossing times. Most of the SN detonations in S30-sink are orders of magnitude above the sound crossing-time, with only a few SNe being affected by over-cooling. Once a sink is formed, mass is accreted onto it, and when a massive enough star forms, a SN explodes which leads over time to a lot of single SN events going off in low density environments, in comparison to the instantaneous detonation of a large number of SNe in a peak density region. In S30-e10-ld, the events occurring until 40 Myr are all over-cooled.

Because the single SNe in S30-sink are not overcooling due to the environment they explode in, and there are several generations of SNe exploding in the already formed hot

phase by 40 Myr, powerful outflows can be launched.

5.5 Conclusions

We use the 3D magnetohydrodynamic code FLASH in version 4 to study the structure of the magnetised, multiphase interstellar medium stirred by the Schmidt-type SN driving. We use stratified disks in a volume of $0.5 \times 0.5 \times \pm 5$ (kpc)^3 with different initial surface densities of $\Sigma_{\rm gas} = 10, 30$ and $50\,M_\odot\,{\rm pc}^{-2}$, and with different fixed star formation efficiencies (3%, 10% and 30%). We focus on the dynamical evolution of the disks and on the average SFR surface densities over a total simulation time of 125 Myr. Our results can be summarised as follows:

- The morphological evolution of the simulations show that even though the Schmidt-type driving seems to give results in agreement with the Kennicutt-Schmidt relation for $\Sigma_{\rm gas} = 10\,M_\odot\,{\rm pc}^{-2}$, the simulations produce little to no gaseous outflows. In the simulations with $\Sigma_{\rm gas} = 30$ and $50\,M_\odot\,{\rm pc}^{-2}$, the gas becomes very dense ($2.5{\times}10^{-19}$ g/cm^3) and confined to the mid-plane, while the only case in which gas in lifted to 1 kpc is the high $\varepsilon_{\rm SFR}$ run, S10-e30.

- For the $\Sigma_{\rm gas} = 10\,M_\odot\,{\rm pc}^{-2}$ runs, the average $\Sigma_{\rm SFR}$ increases with the $\varepsilon_{\rm SFR}$ (varying between 86% above and 57% below the KS relation), while the simulations with higher initial $\Sigma_{\rm gas}$ have the average $\Sigma_{\rm SFR}$ increasingly further and away from the expected KS relation (a factor of three larger for S30-e10 and a factor of thirty for S50-e10).

- The injection temperature of the SNe depends only on the star formation efficiency, meaning that with increasing initial $\Sigma_{\rm gas}$ the collapsing regions become denser, and even though the number of the SNe/event is rising as well (from 73 in S10-e10, 613 in S30-e10 to 4906 in S50-e10), the SNe are inefficient in destroying the formed clumps. In S10-e03 the SNe cool immediately after the injection, as the temperature at detonation is below the 10^6 K.

- In order for the SNe not to radiate away their energy before the remnant expands, the cooling time has to be at least eight times longer than the sound-crossing time. For this criterion to be met, we derive a theoretical density that can be resolved given the injection radius and the $\varepsilon_{\rm SFR}$. We find that this recommended density $\rho_{\rm rec}$ is decreasing with the injection radius and increasing with the $\varepsilon_{\rm SFR}$, e.g. for $r_{\rm inj}$= 4 pc, corresponding to 1 pc/cell spatial resolution, the $\varepsilon_{\rm SFR}$ has to be above 20% in a collapsing regions with an average density of 10^{-22} g/cm^3 to avoid the over-cooling of the SN remnant. However, the simulations presented here do not meet this criterion.

- We suggest two methods for solving the problem of over-cooling SN remnants. Given that improving the resolution to below one parsec can be problematic, one can either (i) model a more realistic ISM, improving the Schmidt-type SN driving to include the

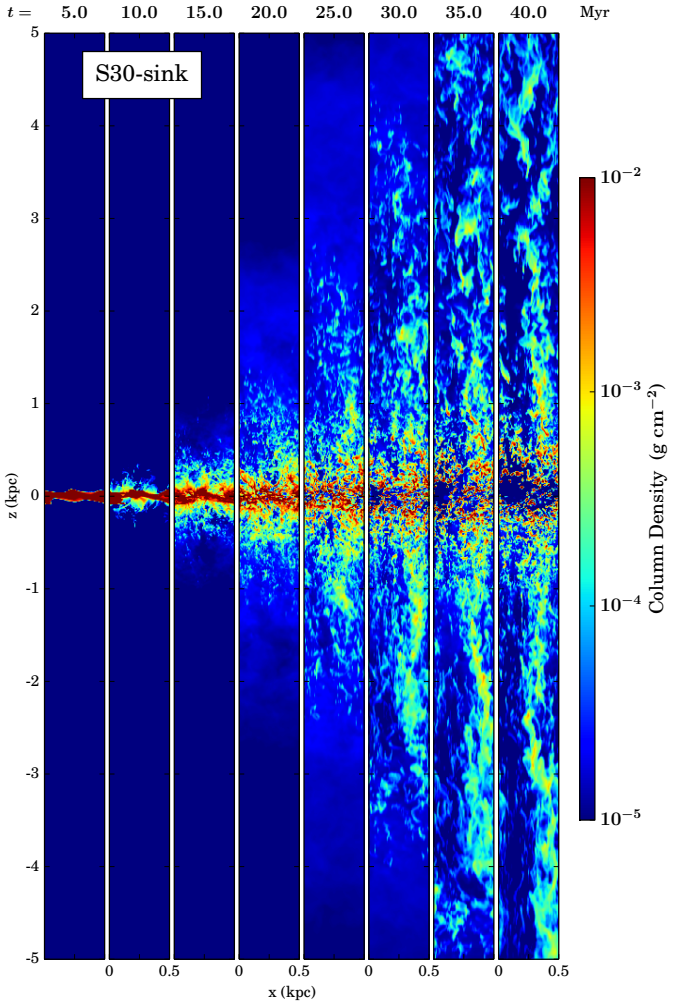

Figure 5.16: Column density sequence for S30-sink up to 40 Myr. There is much more gas being pushed to about ±5 kpc above and below the midd-plane after only a very short period of time.

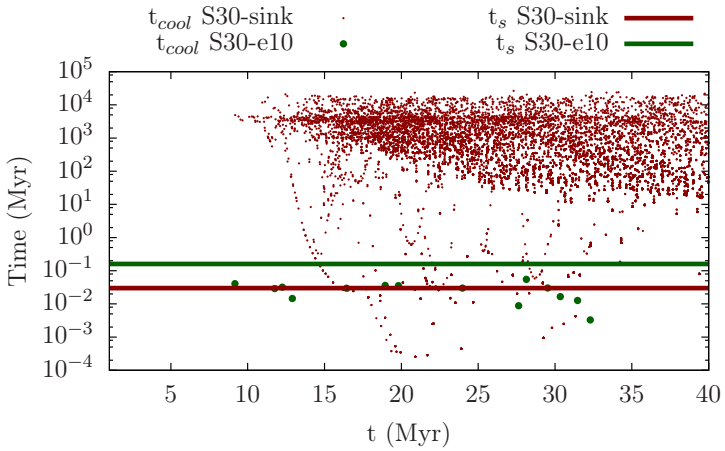

Figure 5.17: Cooling times for S30-e10-ld (dark-green dots) and S30-sink (small dark-red dots), along with the average sound-crossing times of S30-e10-ld (dark-green line) and S30-sink (dark-red line). The SN events in S30-sink are much more numerous and their cooling times are orders of magnitude larger than their sound crossing times, while in S30-e10-ld there are only a few events and all of them are affected by overcooling.

spatial displacement that massive runaway stars exhibit, and take into account that O and B-type stars have different lifetimes, or (ii) rearrange the density structure in the injection region by including a turbulent field due to stellar feedback mechanisms that cannot be resolved.

Summary

In this thesis, we use the 3D magnetohydrodynamic adaptive mesh refinement code FLASH (version 4) to study the structure of the galactic interstellar medium (ISM), while focusing on the connection between the ISM structure, molecular gas formation, and SN feedback. The FLASH 4 simulations can include an external potential, self-gravity, magnetic fields, heating and radiative cooling, time-dependent chemistry of H^+, H, H_2, C^+ and CO considering (self-) shielding, and supernova (SN) feedback. In Chapter 3 we investigate periodic boxes with a volume of $(256\,\mathrm{pc})^3$ seeded with different initial magnetic fields of varying strength. SNe are inserted as individual explosions at fixed observationally motivated rates (derived from the Kennicutt-Schmidt relation, assuming a Salpeter IMF with a low-mass cutoff at 0.01 $M_\odot$ and a high-mass cutoff at 60 $M_\odot$ we find the number of massive stars that will explode as Type II SN) and random locations. In Chapter 4 we use this setup but focus on the effect of SNe positioning. We vary the fraction of SNe exploding at density peaks - regions of their parental clouds - and at random locations. These simulations also include self-gravity, magnetic fields and two different initial gas densities of $n = 0.5$ and 3 cm^{-1}. In a second and more complex setup, we use $0.5 \times 0.5 \times \pm 5$ $(\mathrm{kpc})^3$ and models of stratified disks (Chapter 5) with different initial surface densities and star formation efficiencies to study a more self-consistent star formation model based on the local gas density and free-fall time (Schmidt-type star formation). The main results can be summarised as follows:

Magnetic fields have a significant impact on the multi-phase, chemical and thermal structure of the ISM. For a fixed SN rate, we investigate the multi-phase ISM structure, H_2 molecule formation and density-magnetic field scaling for various initial magnetic field strengths $B = 0$, 6×10^{-3}, 0.3 and 3 μG. All magnetic runs saturate at mass-weighted field strengths of $\sim 1 - 3$ μG, but the ISM structure is notably different. With higher initial field strengths (from $B = 6 \times 10^{-3}$ to $B = 3\mu$G), the simulations develop an ISM with a more homogeneous density and temperature structure, with increasing mass (from 5% to 85%) and volume filling fractions (from 4% to 85%) of warm (300 K $<$ T $<$ 8000 K) gas, with decreasing volume filling fractions (VFF) $\sim$ 35% to $\sim$ 12% of hot gas (T $> 10^5$ K), and with a decreasing H_2 mass fraction (from 70% to $<$ 1%). Meanwhile the mass fraction of gas in which the magnetic pressure dominates over the thermal pressure increases by a factor of 10, from $\beta = 0.07$ for an initial field of $B = 6 \times 10^{-3}$ μG to $\beta = 0.7$ for a 3 μG initial field. In all but the simulations with the highest initial field strengths, self-gravity promotes the formation of dense gas and H_2, but does not change any other

trends.

The positioning (i.e. ambient density) of SNe is critical for the evolution of the ISM. For a fixed SN rate, we study the evolution of the ISM including self-gravity and magnetic fields ($B = 0$ and $B = 0.3$ μG), and we vary the density of the gas (n = 0.5 and 3 cm^{-1}) as well as the SN rate (1.2 and 14 Myr^{-1}). We vary the fraction of SNe exploding in peak density regions from 0%, 10%, 20% to 100%, with 0% representing the case when the massive OB-type stars have a very high probability of exploding outside their parental MC, and the case of 100% representing a scenario in which none of the massive stars travel out of dense regions.

Small variations around critical peak fractions can cause significant changes in the H_2 mass fractions, hot gas VFFs, and thermal pressure. For example, the H_2 mass fractions for 10% and 20% peak fraction change from 20% to 2%, respectively. This is accompanied by a factor of 5 decrease in the hot gas VFFs. Self-gravity shifts the critical peak fractions to 30% and 40%, as the H_2 clumps have increased densities and need a higher number of SNe to explode within them in order to be dispersed, causing the H_2 mass fractions to decline from 40% to 2%. Magnetic fields saturate at an average value of 2 μG, and they suppress the formation of H_2 regardless of the SN peak fraction in simulations without self-gravity. With self-gravity included, they determine a transition in H_2 at a lower peak fraction (10-30%) due to the lower average density of the magnetised clouds than that of unmagnetised ones.

At higher star formation rates the ISM enters a thermal runaway state in which the volume is filled with hot, low density, and highly pressurised gas. The dense cold gas (mostly H_2) is compressed into very dense small clumps. The runaway transition occurs at a peak fractions of 60-80%, without self-gravity. When including self-gravity, thermal runaway characterises the simulations up to 80% peak fraction. Our findings qualitatively confirm to results of Gatto et al. (2015), who focused on non-magnetic runs without self-gravity.

To test a more self-consistent star formation model we implemented a Schmidt-type model where star formation rate is related to the local gas density and free-fall time: $\dot{\rho}_\star = \varepsilon_{\rm SFR} \times (\rho/t_{\rm ff})$, which is commonly used in lower resolution galaxy formation simulations. This model is tested in a stratified disk environment. We study the star formation rate, ISM structure and gaseous outflows for varying the initial gas surface densities $\Sigma_{\rm gas} = 10, 30$ and $50\,M_\odot\,{\rm pc}^{-2}$ and star formation efficiencies of $\varepsilon_{\rm SFR}$ =3%, 10% and 30%. The star formation rate surface densities $\Sigma_{\rm SFR}$ retrieved are comparable with the observed Kennicutt-Schmidt relation for $\Sigma_{\rm gas} = 10\,M_\odot\,{\rm pc}^{-2}$, while simulations with higher $\Sigma_{\rm gas}$ produce $\Sigma_{\rm SFR}$ further away from the relation (a factor of three and thirty higher, respectively).

The instantaneous explosion of SNe in high density collapsing regions leads to overcooling of the SN remnants and results in a cold environment with a lack of gaseous outflows for all the simulations. The SN remnants radiate away their thermal energy before they have a chance to expand. We derive a criterion that connects the average density of the SN environment, $\varepsilon_{\rm SFR}$, and the spatial resolution in order to insure that the remnants will not overcool (e.g. for $r_{\rm inj}$= 4 pc, corresponding to 1 pc/cell spatial resolution, the $\varepsilon_{\rm SFR}$ has to be above 20% in a collapsing regions with an average density of 10^{-22} g/cm^3 to ensure

that the cooling time is at least eight times longer than the sound-crossing time).

For using self-consistent Schmidt-type SN driving to produce a hot phase, we also suggest a more realistic treatment of the massive runaway and walkaway stars (involving their spatial displacement around the peak densities and their delayed explosions due to their different lifetimes) and a treatment of turbulent fields inside the injection regions due to unresolved stellar feedback. **We conclude that Schmidt-type star formation models have intrinsic problems if applied to simulations at high spatial resolution.**

Appendix A

The impact of magnetic fields

A.1 Resolution study

A.1.1 CO mass fractions

Figure A.1 shows the CO mass fraction[1] evolution over 250 Myr. The self-gravity runs form the most CO with fractions over 0.01% for KS-lowB-SG and KS-SG. The only simulation without self-gravity that forms mass fractions over 10^{-5} is KS-lowB.

"Zoom-in" simulations of molecular clouds carried out by Seifried et al. (in prep.) show that the CO fraction only converges once the spatial resolution is better than 0.25 pc. This requirement is consistent with the finding by Glover et al. (2010) and Glover and Clark (2012) that the CO abundance is resolved in their simulations of turbulent clouds, which have effective resolutions in the CO-rich gas of 0.3 pc or better. In addition, a new study also shows that CO-bright regions have a narrow distribution of temperatures between 10 and 30 K (Glover and Smith, 2016). In our simulations, there are only a few cells with gas within this temperature regime, namely 214 for KS, 572 for KS-lowB, 39 for KS-medB, 1 for KS-SG, 5 for KS-lowB-SG, 6 for KS-medB-SG and none for KS-highB and KS-highB-SG (at 150 Myr). Considering that these cells are deeply embedded in cold, dense molecular hydrogen clumps (that represent less than 3% of the total volume at most) and there are only a small number of cells temperatures relevant for CO, we conclude that a spatial resolution of 2 pc/cell is not sufficient for resolving the evolution of the CO.

A.1.2 Magnetic field amplification and H_2 mass fractions

MHD simulations are affected by numerical dissipation that acts on scales much larger than the scale on which real physical dissipation occurs. For example, in typical ISM conditions, after repeating the calculations by Balsara (1996) and Zweibel and Brandenburg (1997), Mac Low and Klessen (2004) obtained an ambipolar diffusion dissipation scale larger than 0.04 pc while the Kolmogorov dissipation scale is of the order of 10^{-5} pc (10^{14}

[1] Our simplified chemical network does not track the abundance of atomic carbon.

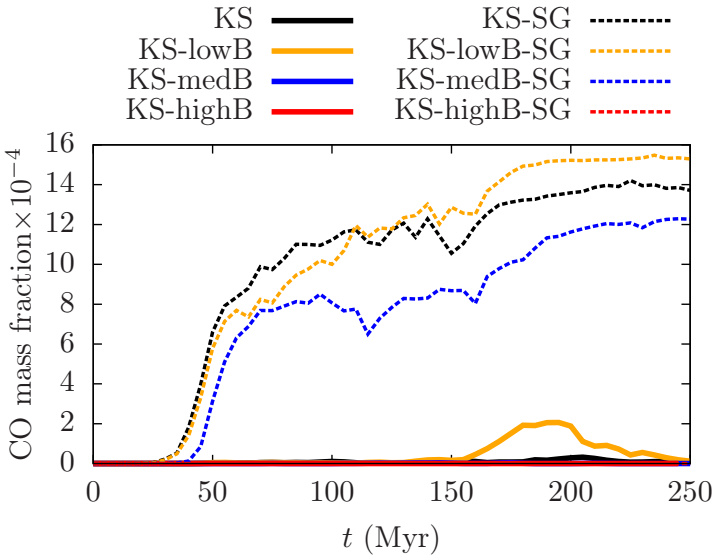

Figure A.1: CO mass fraction evolution over 250 Myr for the simulations: KS (solid black line), KS-lowB (solid orange line), KS-medB (solid blue line), KS-highB (solid red line), KS-SG (dashed black line), KS-lowB-SG (dashed orange line), KS-medB-SG (dashed blue line) and KS-highB-SG (dashed red line). The maximum CO mass fraction is reached in KS-lowB-SG with a maximum of 1.5×10^{-3}.

cm), calculated by Kritsuk et al. (2011). Both scales are orders of magnitude smaller than the spatial resolution in our simulations. The highest magnetic Prandtl number that can be resolved in numerical simulations is around unity while in a typical MC it is about an order of magnitude higher than that (see Federrath et al., 2014b). This means that the simulations themselves introduce artificial diffusivity, with effects that depend on the numerical resolution of the simulation (Balsara et al., 2004; Waagan et al., 2011).

We have tested the resolution dependence of the amplification of the magnetic seed field in our simulations (Fig. A.2, first and second panels) by performing simulations with 4, 5 and 6 refinement levels (runs KS-lowB-L4, KS-lowB, and KS-lowB-L6), corresponding to physical resolutions of 4 pc, 2 pc and 1 pc per cell, respectively. The early stages of the simulations ($t < 20$ Myr) capture the growth of the seed field and we find that during this period the difference between the three simulations is small. However, the field amplification occurs more rapidly with increasing numerical resolution. We follow the evolution of the mean magnetic field in runs KS-lowB-L4 and KS-lowB for a period of 200 Myr after saturation and find that the difference in the mass weighted field strengths is 63% between runs KS-lowB and KS-lowB-L6 and 29% between runs KS-lowB and KS-lowB-L4. The higher computational demands of run KS-lowB-L6 mean that we were only able to follow it until shortly after saturation, but it is nevertheless clear that the field strength in this run saturates at slightly higher value in comparison to the lower resolution runs. We therefore conclude that even though we do not recover a convergent behaviour

for the field strength, a resolution of 2 pc per cell is sufficient to model the global behaviour of the magnetic field in our simulations. We note that the resolution necessary to fully capture the behaviour of the small-scale turbulent dynamo can be estimated to be at least two orders of magnitude higher than this value (Sur et al., 2010), putting it far out of reach of current simulations.

The other important quantity that is potentially sensitive to resolution is the H_2 mass fraction. Work by Glover and Mac Low (2007b) and Micic et al. (2012) has shown that small-scale transient density enhancements produced by turbulence can significantly enhance the H_2 formation rate in interstellar gas, provided that the turbulent mixing time is shorter than the H_2 formation time in the over-dense regions. As we do not resolve the turbulent cascade, we potentially miss many of these small over-densities and hence underestimate the H_2 formation rate. In practice, however, this does not appear to be an important effect for the size scales and timescales considered here. In the last panel of Fig. A.2, we show how the H_2 mass fraction evolves with time in runs KS-lowB-L4, KS-lowB, and KS-lowB-L6. We see that although there are minor differences, there is no significant increase when we increase our resolution from 2 pc per cell (run KS-lowB) to 1 pc per cell (run KS-lowB-L6). This suggests that our fiducial resolution is high enough to yield converged results for the evolution of the H2 mass fraction on these timescales. Note, however, that we do find a small but systematic difference between the H2 mass fractions in runs KS-lowB-L4 and KS-lowB, suggesting that a resolution of 4 pc per cell is not sufficient to fully resolve H2 formation.

A.2 Self-gravity switched on at a later time

In Fig. A.3 (top panel) we compare the H_2 mass fraction for KS-medB-lateSG, KS-medB-SG and KS-medB. Once we switch on self-gravity at 150 Myr, the H_2 mass fraction increases rapidly. However, the impact of self-gravity on the total volume weighted field strength is negligible as gravity acts on the small dense clumps which have a low volume filling fraction (see e.g. Gatto et al., 2015). The effect on the mass weighed field strength is stronger as the compressed dense regions become denser and their magnetic field increases.

We have selected four values of the H_2 mass fraction (0.35, 0.45, 0.52 and 0.67) and noted the time it takes for KS-medB-SG and KS-medB-lateSG to reach these values. In Fig. A.4 we show column density snapshots for these two simulations at the times they reach the same H_2 mass fraction. In each column the H_2 mass fraction is equal in both simulations. What we see is that when self-gravity is acting on the dense regions from the beginning of the simulation the cold, dense clumps are embedded in dense gas. If we let the structures evolve before switching on self-gravity, the already formed structures will rapidly incorporate all the gas around them leaving the newly-formed dense clumps isolated. At 20 Myr after the time at which self-gravity was switched on, the clumps are still accreting the gas around them (Fig. A.4 left bottom row) while after 60 Myr they are already isolated.

Switching on self-gravity at a later time (150 Myr) yields a larger cold mass fraction

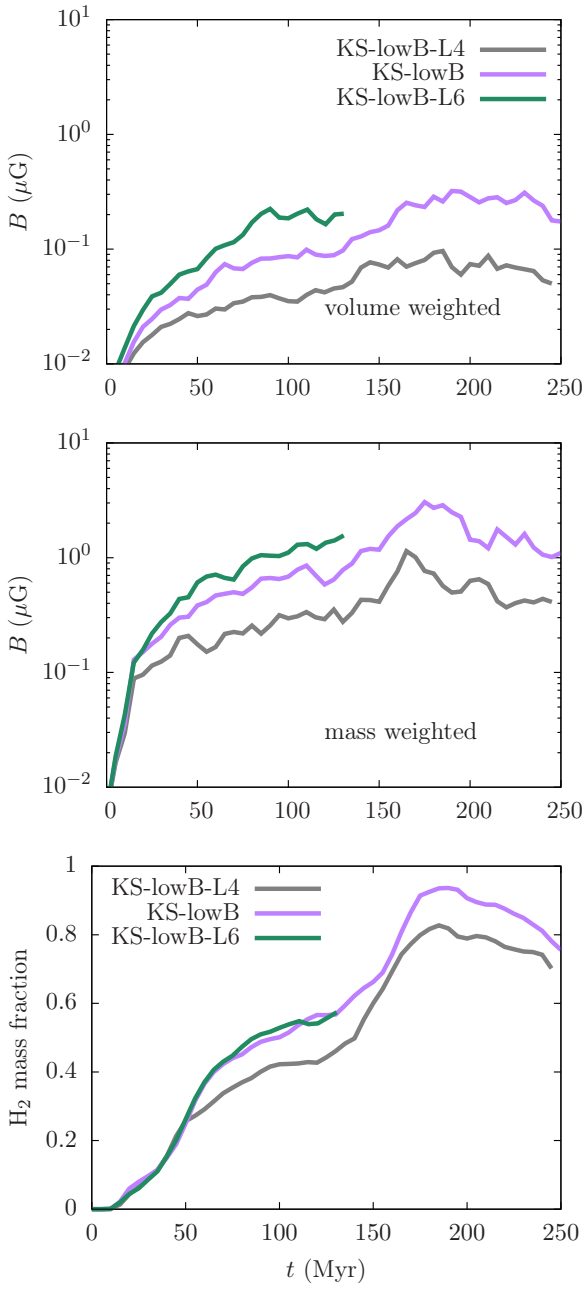

Figure A.2: Time evolution of the mean magnetic field strength and H_2 mass fraction for three different resolutions (grey line: 4 pc per cell, run KS-lowB-L4; purple line: 2 pc per cell, run KS-lowB-L5; green line: 1 pc per cell, run KS-lowB-L6). *Top panel*: volume weighted mean magnetic field strength. *Middle panel*: mass weighted mean magnetic field strength. *Bottom panel*: H_2 mass fraction. The magnetic field is stronger with higher resolution and the H_2 mass fraction as well, but not significantly.

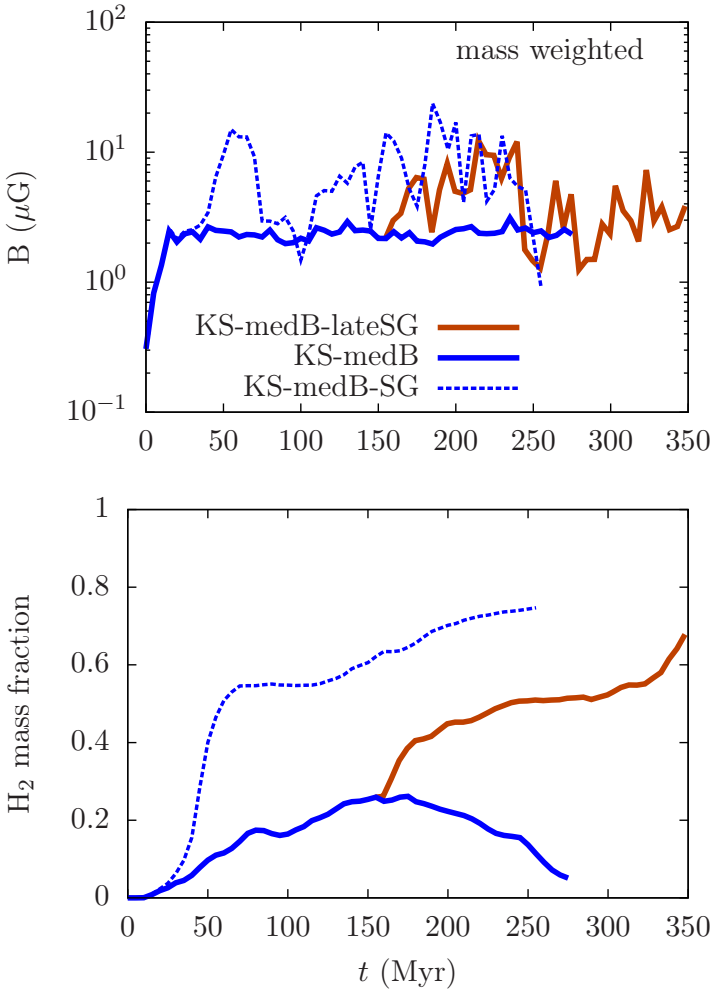

Figure A.3: *Top panel*: time evolution of the mean mass weighted magnetic field strength. *Bottom panel*: time evolution of the H_2 mass fraction. We compare runs KS-medB-lateSG (dark-orange line), KS-medB (blue solid line) and KS-medB-SG (blue dotted line). We see that the H_2 mass fraction increases dramatically once self-gravity is switched on at 150 Myr in run KS-med-lateSG. We also see an increase in the mass weighted mean magnetic field strength at the same time.

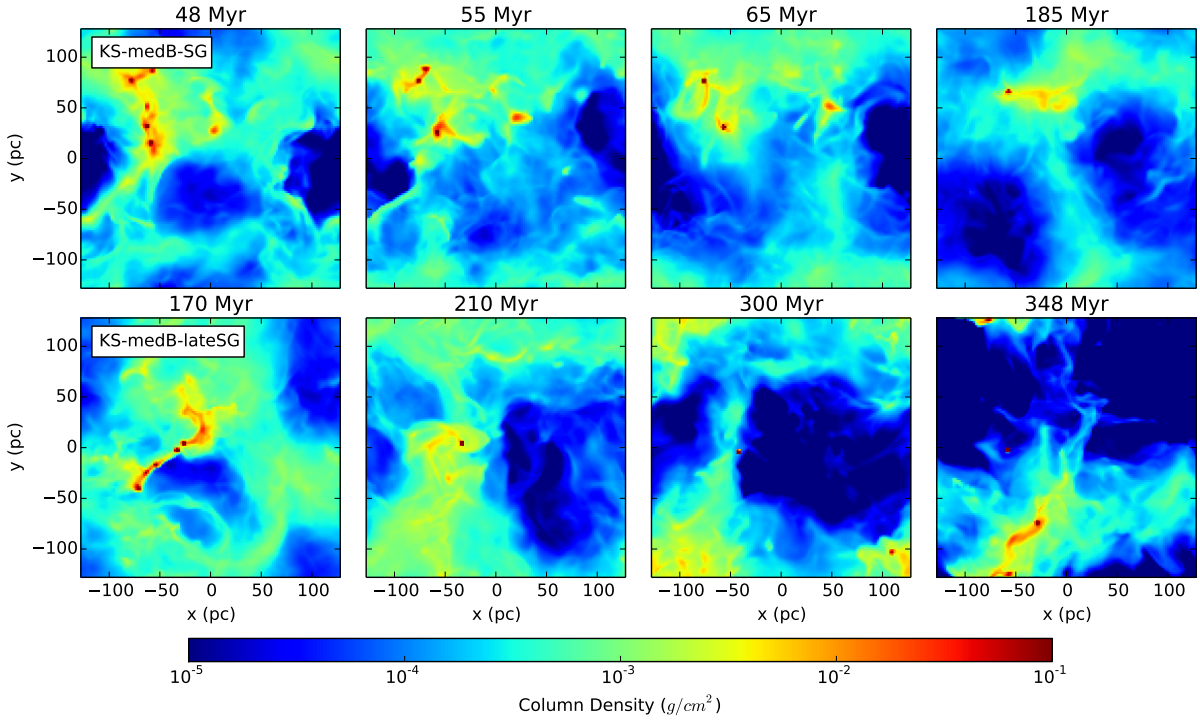

Figure A.4: Column density projection for KS-medB-SG (*first row*) and KS-medB-lateSG (*second row*). In each column, the snapshots compared have the same H_2 mass fraction. Note that as H_2 forms at a different rate in the two simulations, this means that we have to compare them at different output times. We see that the dense blobs formed in run KS-medB-SG are embedded in higher density gas than those in run KS-medB-lateSG. This occurs because in run KS-medB-lateSG, we switch on self-gravity after dense structures have already formed. Consequently, once they start to collapse, they very efficiently capture all of the dense gas surrounding them. This leads to more isolated dense blobs and a higher volume of the box dominated by hot, low density gas.

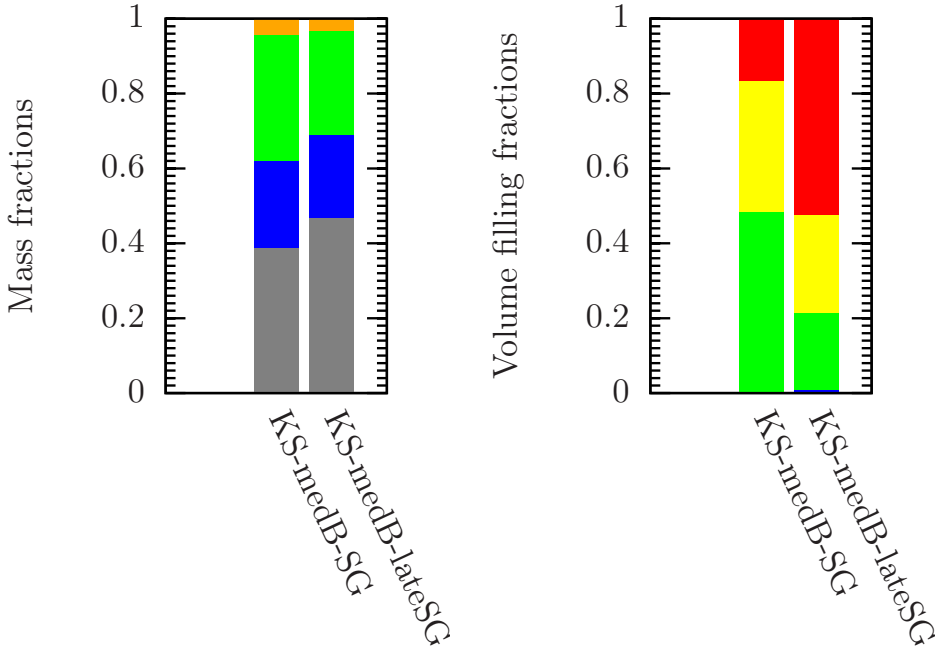

Figure A.5: Mass fractions (*left panel*) and VFFs (*right panel*) for runs KS-medB-SG and KS-medB-lateSG. We average over 5 Myr in both cases (63 to 68 Myr for KS-medB-SG and 297 to 302 Myr for KS-medB-lateSG: at these times, the H_2 mass fraction is the same in both simulations) to avoid discreteness effects due to the explosion of a single SN. The plots use the same colour-coding as in Fig. 3.12. The hot gas VFF is twice as high in KS-medB-lateSG as in KS-medB-SG.

(Fig. A.5) for the same amount of H_2 but not significantly in comparison to switching on self-gravity from the beginning of the simulation. It also yields a larger hot gas VFF in KS-medB-lateSG in comparison to KS-medB-SG. Because the already formed dense structures contract very suddenly, they incorporate a lot of the neighbouring gas. The cold clumps end up surrounded by low density gas that is easily heated by the exploding SNe, leading to a VFF of hot gas that is almost twice as high as in the run with self-gravity switched on from the beginning.

In Fig. A.6 we show the plasma-β parameter as a function of density for KS-medB-SG and KS-medB-lateSG at 65 Myr and 300 Myr when the H_2 mass fraction is 0.52 in both cases. In KS-medB-lateSG 31.6% of the gas mass is magnetically dominated in comparison to only 18% in KS-medB-SG. This suggests that switching on self-gravity at a later time, after dense structures have already formed, leads to a higher cold ($T < 30$ K) mass fraction that will be strongly magnetised (due to flux-freezing). This is an additional factor that decreases the H_2 mass fraction.

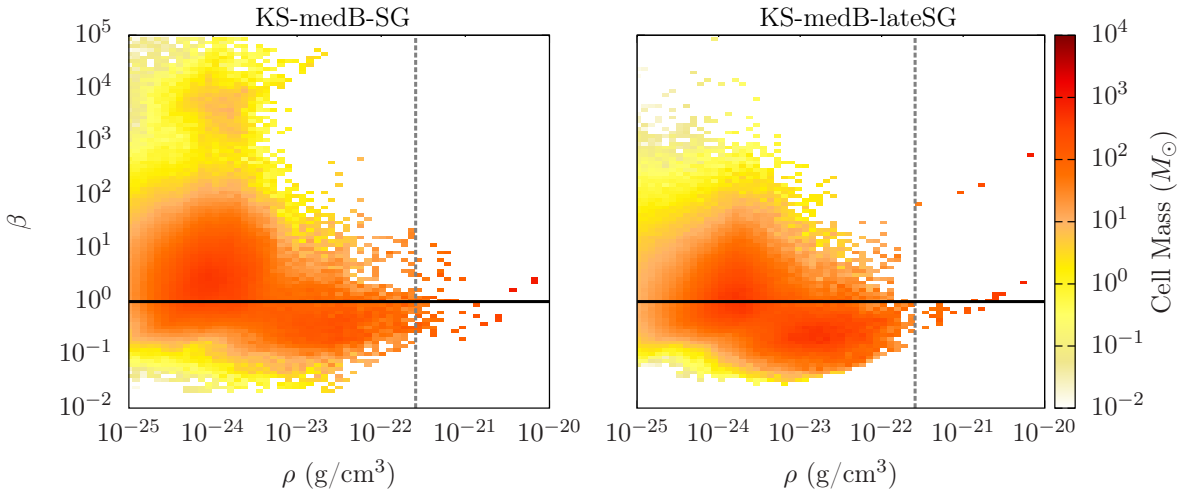

Figure A.6: Plasma-β as a function of density with mass colour-coding for KS-medB-SG (*left panel*) at 65 Myr and KS-medB-lateSG (*right panel*) at 300 Myr (when the H_2 mass fraction is the same in both simulations). The grey dotted line represents the maximum density we can resolve according to the Truelove criterion. In KS-medB-lateSG the gas mass that is magnetically dominated is almost double that in KS-med-SG.

A.3 RMS Mach number

We present, in Fig. A.7, the volume and mass weighted root mean square of the Mach numbers of all the simulations. We calculate the volume/mass weighted RMS of the local flow divided by the sound speed in every cell, with the adiabatic index equal to 1.4, if the cell is dominated by diatomic molecules, or 1.66, otherwise. In both cases the RMS Mach number is lower than unity for KS-highB and KS-highB-SG. The volume weighted values for KS-lowB and KS-lowB-SG decrease and reach a minimum between 150 and 200 Myr. At this point the very hot gas fills more than 80% of the volume of the simulation (see Fig. 3.12) and the high sound speed of this environment is affecting the overall Mach number of these simulations. The mass wighted values are about unity for KS-medB and between 1 and 10 for the rest of the simulations. The average sound speeds at 150 Myr are 100 km/s (KS), 150 km/s (KS-lowB), 21 km/s (KS-medB), 7 km/S (KS-highB), 68 km/s (KS-SG), 172 km/s (KS-lowB-SG), 63 km/s (KS-medB-SG) and 8 km/s (KS-highB-SG).

The highest RMS Mach numbers are obtained in the self-gravity runs where most of the mass is concentrated in small and very dense clumps. To illustrate better the difference between the runs with and without self gravity, we plot a 2D histogram of the RMS velocity and sound speed in Fig. A.8 for KS-medB (top panel) and KS-medB-SG (bottom panel), both at 150 Myr. The main difference is that while for KS-medB the RMS velocity is tightly correlated with the sound speed, explaining the close to unity RMS Mach number, in KS-medB-SG most of the mass resides in a few cell which have a high RMS velocity (between 1 and 10 km/s) but have low sound speeds (below 1 km/s).

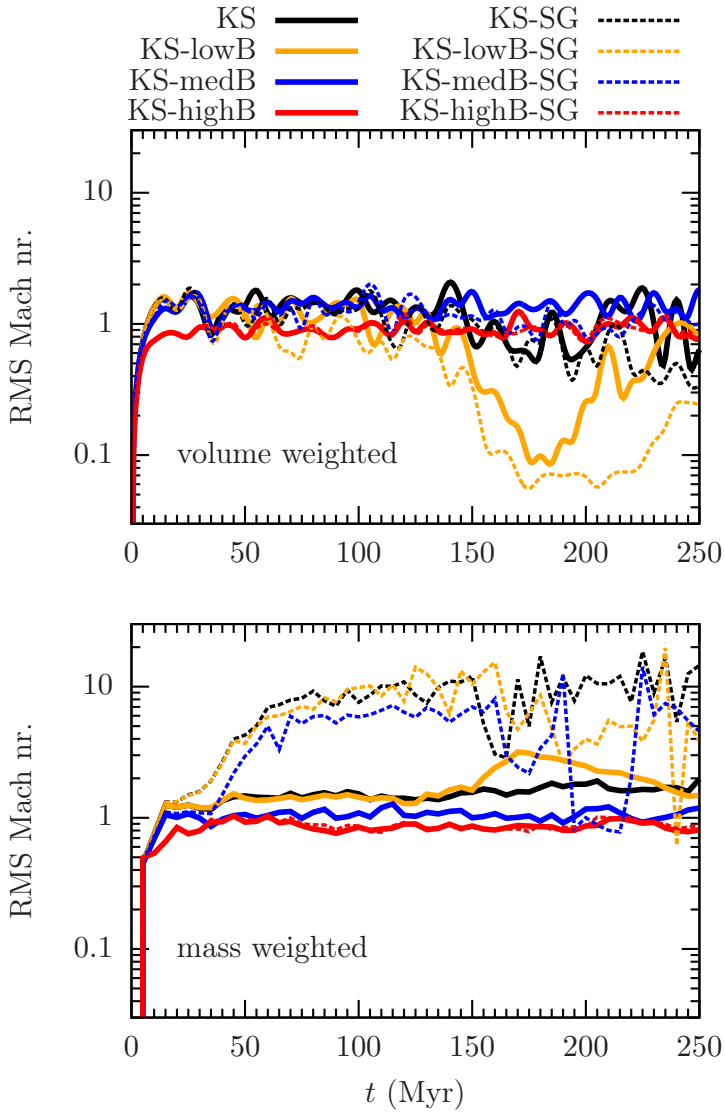

Figure A.7: Time evolution of the root mean square Mach number, volume weighted (*top panel*) and mass weighed (*bottom panel*) for KS (solid black line), KS-lowB (solid orange line), KS-medB (solid blue line), KS-highB (solid red line), KS-SG (dashed black line), KS-lowB-SG (dashed orange line), KS-medB-SG (dashed blue line) and KS-highB-SG (dashed red line). The volume weighted RMS Mach numbers are close to unity except for KS-lowB, KS-lowSG, KS-highB and KS-highB-SG. The mass weighted values are higher for the self-gravity runs than the rest, reaching values up to 10.

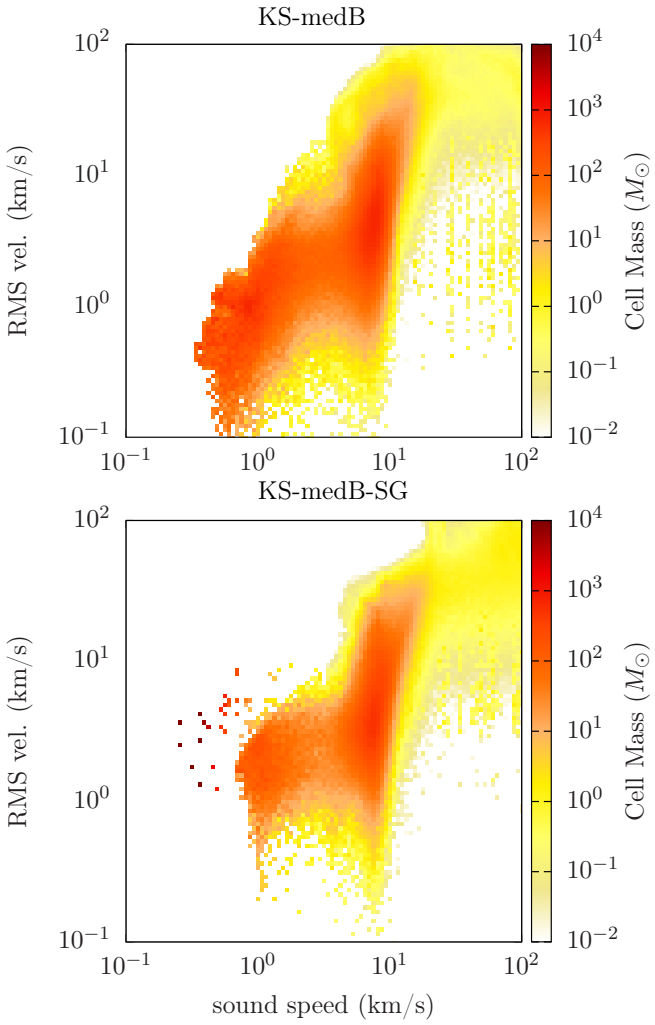

Figure A.8: RMS velocity as function of sound speed for KS-medB (*top panel*) and KS-medB-SG (*bottom panel*) at 150 Myr. Most of the mass in KS-medB has the RMS velocity increasing proportionally with the sound speed while in KS-medB-SG most of the mass is concentrated in a few cells having one order of magnitude higher RMS velocities for low sound speeds.

Appendix B

The impact of massive runaway stars

B.1 Temperature PDFs

As mentioned in Chapter 4, we show in Fig. B.1 the temperature PDFs for the fiducial simulations p10(B), p30(B), p90(B) and p90(B), mass and volume weighted, and for sg-p10(B), sg-p30(B), sg-p90(B) and sg-p90(B). In the mass weighted PDFs of sg-p10, sg-p10B and sg-p30, the peak at about 80000 K is related to the lower column density of the gas around the dense clumps that can be heated to high temperatures by the high percentage of randomly distributed SNe.

B.2 Chemical equilibrium

Figures B.2 and B.3 show the chemical evolution of the simulations without and with self-gravity, $n = 0.5$ g/cm^3. Right at the beginning of the simulations a very small fraction of H_2 forms in the shells of the first SNe but it is quickly dispersed by the subsequent blasts. After about 10 Myr H_2 starts forming in dense structures and rapidly reach mass fractions of 1-10% and further, as more than 12 SNe already exploded, the H_2 mass fractions evolve influenced by the peak fraction and magnetic field. For lower peak fractions the H_2 mass fractions keeps rising (p0, p0B, p10, p10B). All in all, it seems like the all the simulations pass the initial phase of H_2 after about 50 Myr.

B.3 Magnetic field evolution

Figure B.4 presents the evolution of the volume weighted and mass weighted magnetic field over 150 Myr, for (sg-)p0B, (sg-)p20B, (sg-)p40B, (sg-)p60B, (sg-)p80B and (sg-)p100B. While the volume weighted magnetic field evolution self-gravity does not impact significantly the saturated fields strength, in the mass weighted case, self-gravity makes an order or magnitude difference for sg-0B.

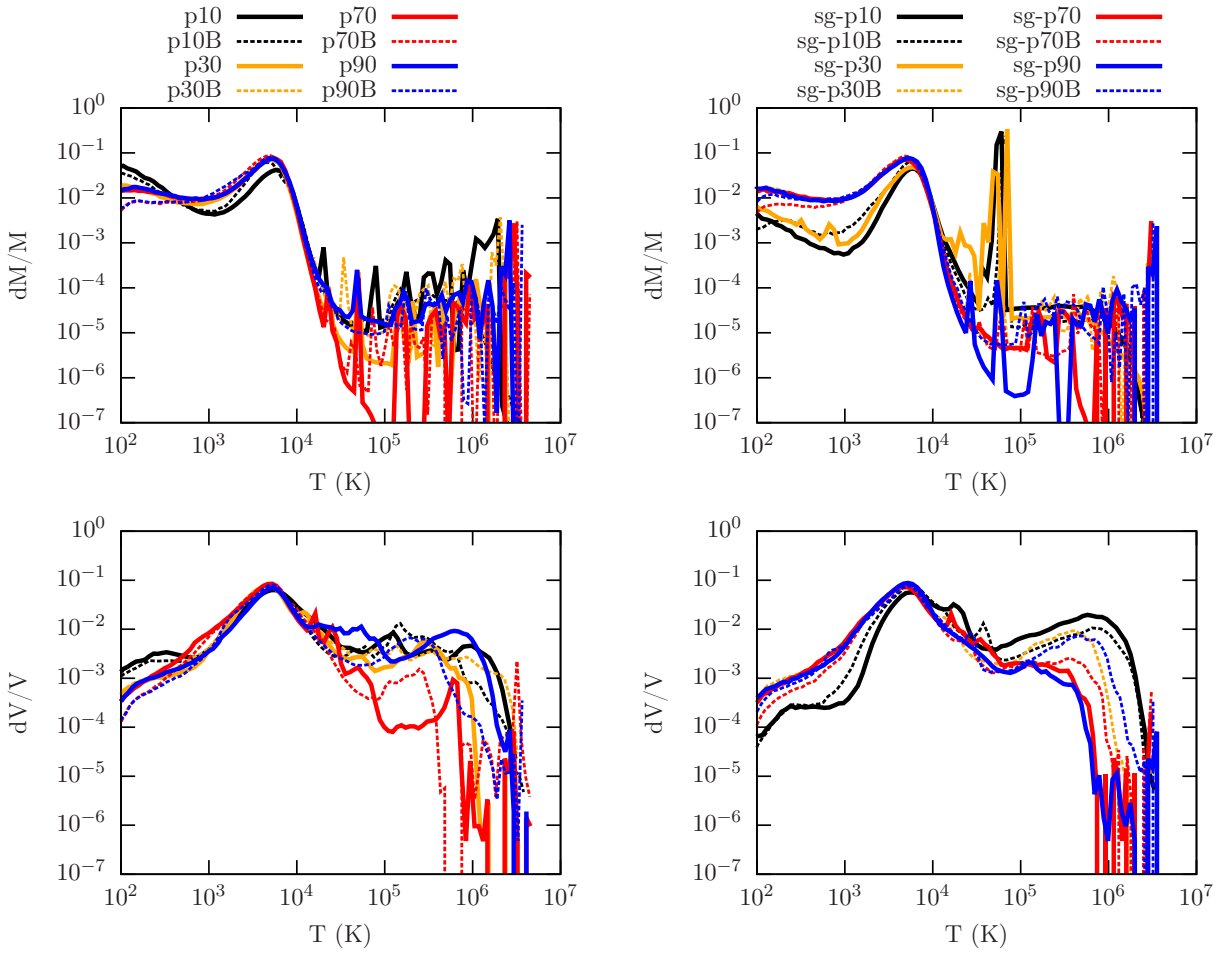

Figure B.1: Same as Fig, 4.2 but temperature PDFs. In the mass weighted self-gravity PDFs, there is one peak at about 80000 K for sg-p10, sg-p10B and sg-p30. This has to be related to the clumps, once they form, the column density of the gas around them is lower and it can be heated to high temperatures by the high percentage of randomly distributed SNe.

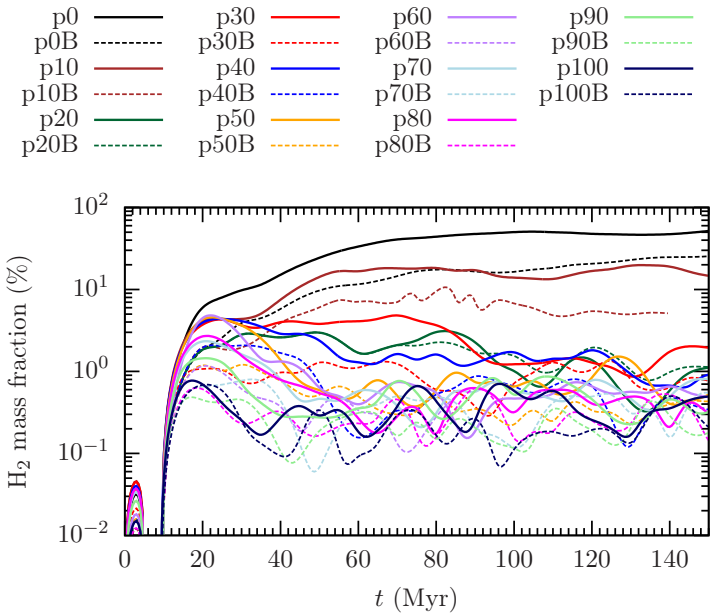

Figure B.2: H_2 mass fraction evolution in time for the fiducial runs, with and without magnetic fields: p0 (solid black line), p0B (dotted black line), p10 (solid brown line), p10B (dotted brown line), p20 (solid green line), p20B (dotted green line), p30 (solid red line), p30B (dotted red line), p40 (solid red line), p40B (dotted red line), p50 (solid orange line), p50B (dotted orange line), p60 (solid purple line), p60B (dotted purple line), p70 (solid light-blue line), p70B (dotted light-blue line), p80 (solid pink line), p80B (dotted pink line), p90 (solid light-green line), p90B (dotted light-green line), p100 (solid dark-blue line), p100B (dotted dark-blue line). The H_2 mass fraction seem to oscillate about an equilibrium value after roughly 50 Myr.

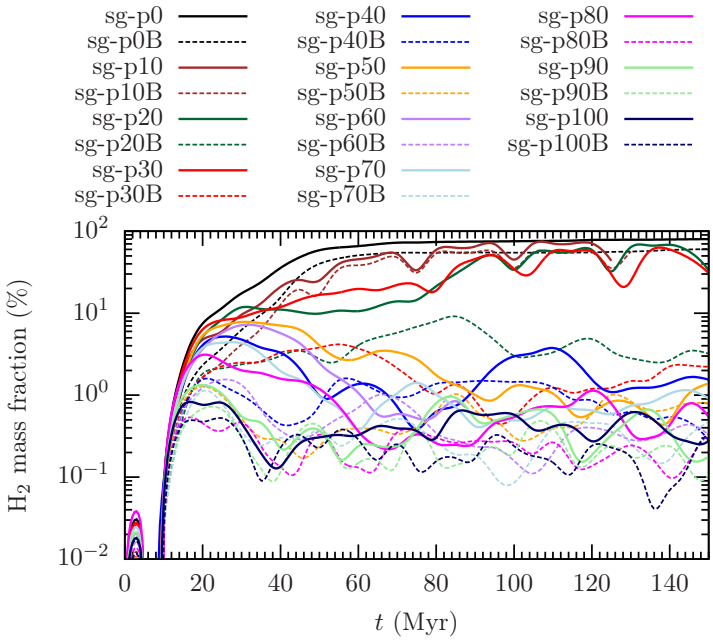

Figure B.3: Same as Fig. B.2 but for the self-gravity simulations. There is a clear difference between the H_2 mass fractions of sg-p0, sg-p0B, sg-p10, sg-p10B, sg-p20, sg-p30 and the rest of the simulations. While the simulations with low PF result in significant fractions of H_2, higher PF runs produce H_2 mass fractions of 1% and below.

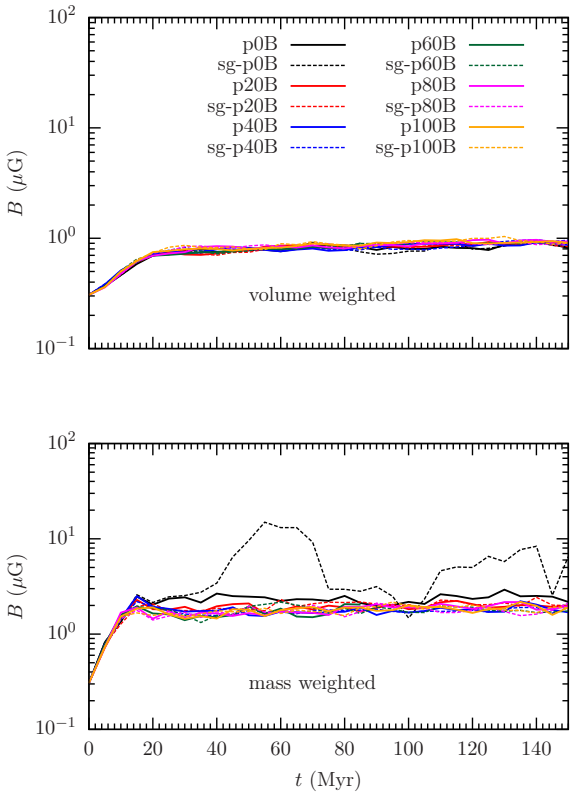

Figure B.4: Volume (top panel) and mass weighted (bottom panel) magnetic field to ilustrate the effect of self-gravity on the evolution of the field in runs with different peak fractions: p0B (black solid line), sg-p0B (black dotted line), p20B (red solid line), sg-p20B (red dotted line), p40B (blue solid line), sg-p40B (blue dotted line), p60B (green solid line), sg-p60B (green dotted line), p80B (purple solid line), sg-p80B (purple dotted line), p100B (orange solid line), sg-p100B (orange dotted line). In the volume weighted field evolution, there are no significant differences between runs with and without self-gravity while in the mass weighted case, self-gravity makes an order or magnitude difference for sg-0B.

B.4 Average values

We give the average values used in the figures in Chapter 3 for the H_2, H and H^+ mass fractions, for the cold gas VFF at ($T_1 \in [30, 300)$ K) and hot gas VFF ($T_2 > 3 \times 10^5$ K). We also give the average values for the volume and mass weighted magnetic field, the mass weighted magnetic field strength in H_2 , H, in cold gas (T_1), cool gas ($T_3 \in [300, 8000)$ K) and warm gas ($T_4 > 8000$ K) along with the mass fraction of the gas with $\beta < 1$.

Sim. name weighing	f_{H_2}	f_H	f_{H^+}	VFF (T_1)	VFF (T_2)	B [μG] volume	B [μG] mass	B (H_2) [μG] mass	B (H) [μG] mass	B (T_1) [μG] mass	B (T_3) [μG] mass	B (T_4) [μG] mass	$f_{\beta<1}$
p0	0.4	0.5	0.022	0.02	0.3								
p0B	0.2	0.8	0.023	0.02	0.13	0.82	2.35	2.7	2.3	2.7	1.9	1.9	0.39
p10	0.16	0.8	0.02	0.02	0.13								
p10B	0.07	0.9	0.02	0.017	0.08	0.8	1.97	2.6	1.9	2.5	1.6	2	0.26
p20	0.01	0.9	0.018	0.011	0.04								
p20B	0.01	0.9	0.018	0.013	0.04	0.86	1.94	2.6	1.9	2.7	1.7	1.8	0.23
p30	0.02	0.9	0.017	0.012	0.03								
p30B	0.01	0.9	0.018	0.01	0.02	0.83	1.82	2.7	1.8	2.6	1.6	1.7	0.19
p40	0.01	0.9	0.017	0.01	0.02								
p40B	0.004	0.9	0.018	0.007	0.02	0.84	1.75	2.8	1.8	2.7	1.6	1.6	0.15
p50	0.007	0.9	0.018	0.008	0.02								
p50B	0.004	0.9	0.017	0.007	0.02	0.85	1.72	2.6	1.7	2.5	1.6	1.8	0.14
p60	0.005	0.9	0.017	0.007	0.02								
p60B	0.003	0.9	0.017	0.007	0.03	0.83	1.81	3.2	1.8	3	1.6	1.7	0.16
p70	0.005	0.9	0.017	0.007	0.02								
p70B	0.003	0.9	0.018	0.007	0.02	0.86	1.79	2.9	1.8	2.8	1.6	1.7	0.16
p80	0.004	0.9	0.017	0.006	0.013								
p80B	0.002	0.9	0.018	0.006	0.02	0.88	1.87	3.1	1.9	3	1.7	1.6	0.17
p90	0.004	0.9	0.018	0.007	0.03								
p90B	0.002	0.9	0.017	0.006	0.02	0.88	1.85	3.2	1.8	3	1.7	1.7	0.16
p100	0.004	0.9	0.018	0.006	0.006								
p100B	0.002	0.9	0.017	0.006	0.01	0.89	1.84	3.5	1.8	3.2	1.7	1.7	0.15

Table B.1: List of simulations and parameters. From left to right we list the name of the simulation, the average H_2, H and H^+ mass fractions, the average cold gas VFF at ($T_1 = T \in [30, 300)$ K) and hot gas VFF ($T_2 = T > 3\times10^5$ K), the average volume and mass weighted magnetic field, the mass weighted magnetic field strength in H_2 , H, in cold gas ($T_1 = T \in [30, 300)$ K), cool gas ($T_3 = T \in [300, 8000)$ K) and warm gas ($T_4 = T > 8000$ K) and the mass fraction of the gas with $\beta < 1$

Sim. name weighing	f_{H_2}	f_H	f_{H^+}	VFF (T_1)	VFF (T_2)	B [μG] volume	B [μG] mass	B (H_2) [μG] mass	B (H) [μG] mass	B (T_1) [μG] mass	B (T_3) [μG] mass	B (T_4) [μG] mass	$f_{\beta<1}$
sg-p0	0.75	0.2	0.024	0.002	0.34								
sg-p0B	0.54	0.4	0.023	0.003	0.2	0.83	6.2	9.7	2.4	5.4	2.1	2	0.14
sg-p10	0.57	0.4	0.022	0.004	0.25								
sg-p10B	0.46	0.5	0.022	0.003	0.14	0.83	5.3	8.5	2.6	5.2	1.9	3.5	0.125
sg-p20	0.38	0.6	0.02	0.009	0.16								
sg-p20B	0.04	0.9	0.02	0.015	0.05	0.85	2	2.9	2	2.7	1.7	1.9	0.26
sg-p30	0.36	0.6	0.02	0.009	0.12								
sg-p30B	0.02	0.9	0.018	0.01	0.04	0.83	1.8	2.6	1.8	2.6	1.6	1.8	0.19
sg-p40	0.01	0.9	0.016	0.009	0.02								
sg-p40B	0.01	0.9	0.016	0.009	0.015	0.85	1.7	2.6	1.8	2.7	1.5	1.7	0.16
sg-p50	0.01	0.9	0.016	0.01	0.02								
sg-p50B	0.005	0.9	0.017	0.008	0.016	0.86	1.8	2.9	1.8	2.8	1.6	1.9	0.17
sg-p60	0.01	0.9	0.016	0.009	0.017								
sg-p60B	0.004	0.9	0.017	0.008	0.015	0.87	1.8	2.9	1.8	2.9	1.6	1.7	0.17
sg-p70	0.007	0.9	0.017	0.008	0.02								
sg-p70B	0.003	0.9	0.017	0.007	0.02	0.86	1.7	2.7	1.7	2.7	1.6	1.6	0.14
sg-p80	0.005	0.9	0.016	0.006	0.006								
sg-p80B	0.002	0.9	0.016	0.006	0.01	0.88	1.8	3	1.8	2.9	1.6	1.7	0.14
sg-p90	0.004	0.9	0.016	0.006	0.008								
sg-p90B	0.002	0.9	0.016	0.006	0.01	0.89	1.8	3.1	1.8	3	1.7	1.7	0.15
sg-p100	0.004	0.9	0.016	0.006	0.01								
sg-p100B	0.001	0.98	0.016	0.005	0.01	0.9	1.8	3.1	1.8	3.1	1.7	1.7	0.15

Table B.2: List of simulations and parameters. From left to right we list the name of the simulation, the average H_2, H and H^+ mass fractions, the average cold gas VFF at ($T_1 = T \in [30, 300)$ K) and hot gas VFF ($T_2 = T > 3 \times 10^5$ K), the average volume and mass weighted magnetic field, the mass weighted magnetic field strength in H_2 , H, in cold gas ($T_1 = T \in [30, 300)$ K), cool gas ($T_3 = T \in [300, 8000)$ K) and warm gas ($T_4 = T >$8000 K) and the mass fraction of the gas with $\beta < 1$

Sim. name weighing	f_{H_2}	f_H	f_{H^+}	VFF (T_1)	VFF (T_2)	B [μG] volume	B [μG] mass	B (H_2) [μG] mass	B (H) [μG] mass	B (T_1) [μG] mass	B (T_3) [μG] mass	B (T_4) [μG] mass	$f_{\beta<1}$
P0	0.94	0.05	0.007	0.004	0.97								
P0B	0.97	0.02	0.007	0.001	0.99	0.47	7.9	8	6.5	6.7	5	1.13	0.15
P20	0.86	0.12	0.006	0.005	0.96								
P20B	0.93	0.06	0.005	0.002	0.99	0.42	10.2	10.2	12	8.2	6.5	0.95	0.23
P40	0.76	0.23	0.005	0.006	0.96								
P60	0.66	0.33	0.005	0.01	0. 92								
P60B	0.59	0.4	0.004	0.04	0.86	0.73	8.83	9.22	8.2	7.6	5.4	1.4	0.7
P80	0.29	0.7	0.002	0.24	0.093								
P80B	0.29	0.7	0.002	0.24	0.091	0.78	2.58	2.7	2.5	2.6	1.4	0.92	0.52
P100	0.19	0.8	0.0006	0.25	0.001								
P100B	0.17	0.83	0.0008	0.25	0.0004	0.98	2.9	3.2	2.8	3.2	1.5	2.1	0.52
sg-P0	0.96	0.02	0.01	0.01	0.98								
sg-P0B	0.97	0.015	0.01	0.0003	0.99	0.62	13.9	14.2	9.18	10	8.2	1.6	0.01
sg-P20	0.97	0.01	0.01	0.0002	0.99								
sg-P20B	0.97	0.01	0.008	0.5×10^{-5}	0.99	0.68	5.5	5.4	12.1	6.9	12.3	3	0.006
sg-P40	0.97	0.01	0.01	0.0006	0.99								
sg-P40B	0.97	0.02	0.007	0.001	0.98	0.66	18.5	18.8	9	10.4	7	1.8	0.034
sg-P60	0.96	0.02	0.006	0.003	0.95								
sg-P60B	0.97	0.02	0.006	0.001	0.98	0.77	17.6	18	8.5	9.4	7.5	2.3	0.027
sg-P80	0.96	0.03	0.004	0.003	0.91								
sg-P80B	0.92	0,06	0.005	0.009	0.77	0.84	13.5	14.2	5.7	6.12	4.7	2.5	0.05
sg-P100	0.19	0.8	0.008	0.24	0.001								
sg-P100B	0.15	0.84	0.0007	0.24	0.0001	0.97	3	3.4	2.9	3.4	1.5	1.8	0.5

Table B.3: List of simulations and parameters. From left to right we list the name of the simulation, the average H_2, H and H^+ mass fractions, the average cold gas VFF at ($T_1 = T \in [30, 300)$ K) and hot gas VFF ($T_2 = T > 3 \times 10^5$ K), the average volume and mass weighted magnetic field, the mass weighted magnetic field strength in H_2 , H, in cold gas ($T_1 = T \in [30, 300)$ K), cool gas ($T_3 = T \in [300, 8000)$ K) and warm gas ($T_4 = T >$8000 K) and the mass fraction of the gas with $\beta < 1$.

Appendix C

Schmidt-type SN driving

C.1 Time-steps, cooling and sound crossing times

The left panel of Fig. C.1 shows the time-steps of all the simulations up to the first 15000 steps while in the right panel we present the free-fall times of individual events at the time they occur in the simulations: S10-e10, S10-e10-mag, S10-e30, S10-e03, S30-e10 and S50-e10 and compare them to the average time-steps of the same runs. While the free-fall times vary between 0.5 and 30 Myr, they decrease with increasing $\Sigma_{\rm gas}$. The lowest free-fall times ($\sim$ 0.6 Myr) correspond to the most massive events which occur in simulation S50-e10 due to the large amount of gas available in the disk. The average time-steps are about 0.005 Myr decreasing with $\Sigma_{\rm gas}$ as well.

C.2 The magnetic field strenght and evolution

In Fig.C.2, we show the evolution of the average mass and volume weighted magnetic field (top panel) and the fields strength in H^+, H and H_2 (bottom panel). While the volume weighted magnetic field is relatively constant in time (about 2-3 μG), the mass weighted field varies between 2 and 10 μG. There is a sudden drop from 6 to 2 μG around 70 Myr which corresponds to the most massive start burst event, described in Section 5.2. Due to flux-freezing, the magnetic field is strongest in the cold, dens regions. In Fig.C.2 bottom panel we show that the mass weighted magnetic field in H^+ is on average 1 μG while in atomic hydrogen it varies between 2 and 9 μG. The strongest magnetic field can be found in H_2, where the field can get up to 30 μG. These values are in agreement with observations of MCs which show a the magnetic field strength between 16 μG and 1.1 mG (Woody et al., 1989; Crutcher, 2004; Crutcher et al., 2009, 2010b; Crutcher, 2012).

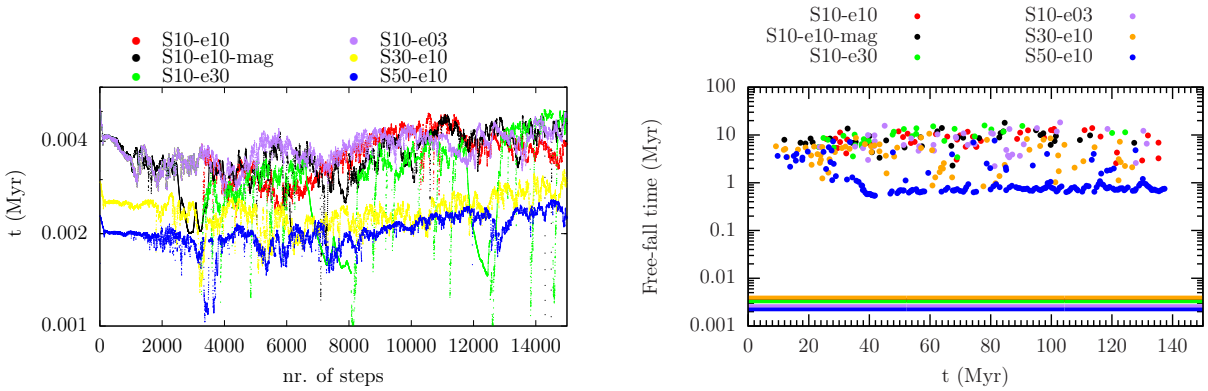

Figure C.1: The length of the time steps of simulations S10-e10 (red dots), S10-e10-mag (black dots), S10-e30 (green dots), S10-e03 (purple dots), S30-e10 (orange dots) and S50-e10 (blue dots) for the first 15000 steps (*left panel*) and the free-fall time of the SN events as they occur in time, for the same simulations and colour coding (*right panel*). We also show the average time-steps with lines of the corresponding colour. The time steps are lower with increasing initial surface density. The average free-fall time of events, in general, is about 10 Myr while the average time-steps are of the order of 3-4 $\times$ 10^{-3} Myr.

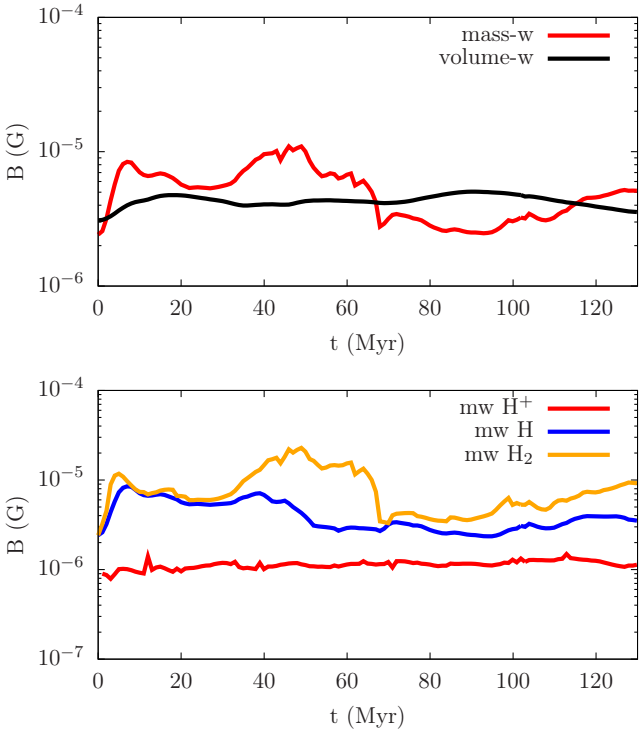

Figure C.2: Mass and volume weighted magnetic field evolution in S10-e10-mag (*top panel*) over 100 Myr and the field in different chemical species (*bottom panel*). The magnetic field in H_2 is stronger on average than in H or H^+.

No.	Sim. name	$\Sigma_{\rm gas}$ $[M_\odot/{\rm cp}^2]$	SN rate $[{\rm Myr}^{-1}]$	$f_{\rm rand}$
1	S10-rand	10	15	1
2	S10-peak	10	15	0
3	S10-mix	10	15	0.5
4	S10-clus	10	15	1

Table C.1: From the left to the right, we list the name of the simulations, the initial gas surface density $\Sigma_{\rm gas}$, the SN rate calculated using the KS relation and a Chabrier IMF (Chabrier, 2001) and the fraction of randomly places SNe.

C.3 Comparison to fixed rate SN rate simulations

We show a comparison of the $\Sigma_{\rm gas} = 10\ M_\odot\,{\rm pc}^{-2}$ simulations with runs of same initial conditions and comparable $\Sigma_{\rm SFR}$ but a fixed SN rate (see Table C.1). We note that the fixed SN rate simulations discussed here do not include self-gravity. The fixed SN rate are described and analysed by Walch et al. (2015) and Girichidis et al. (2016). The treatment of the SN positioning is:

- The random driving assumes that the SNe (Type II) are randomly distributed in the disk following a Gaussian distribution with a scale-height of 50 pc. This approach allows the modelling of massive OB-type stars that travel outside the molecular clods they were born in.
- In peak driving the Type II SNe are positioned in peak density regions, following a scenario where all the massive stars explode in their mother MC.
- For mixed driving the SNe locations are a mix of 50 % random and 50% local peak positioning of the SNe. For a detailed analysis on the percentage of random and peak density placed SNe and how they impact the ISM see the discussion in Chapter 3.
- The clustered driving is based on the idea that OB-type stars are born in clusters and the positions of the SNe, at the end of their lives, are correlated as well. The clusters have a 40 Myr lifetime (Oey and Clarke, 1997) and the number of SNe in each cluster is based on a truncated power law (Clarke and Oey, 2002) with the time between individual explosions of 40 Myr, within the cluster. The clustering methods we compare to accounts for 80% Type II SN with a 50 pc scale-heigth and the rest Type Ia SNe with 325 pc scale-height (Joung and Mac Low, 2006; Hill et al., 2012). 40% of the Type II SNe explode in random locations while 60% explode in clusters. For more details on the implementation see Walch et al. (2015).

The H_2 mass fractions (Fig. C.3) for S10-e10, S10-e10-mag and S10-e30 vary between the two extremes: random driving (40%) and peak driving ($\sim$ 2%). The SNe in S10-e30, due to their higher numbers in comparison to the other runs manage to disperse efficiently the H_2 formed in the densest regions, very similarly to the standard peak driving.

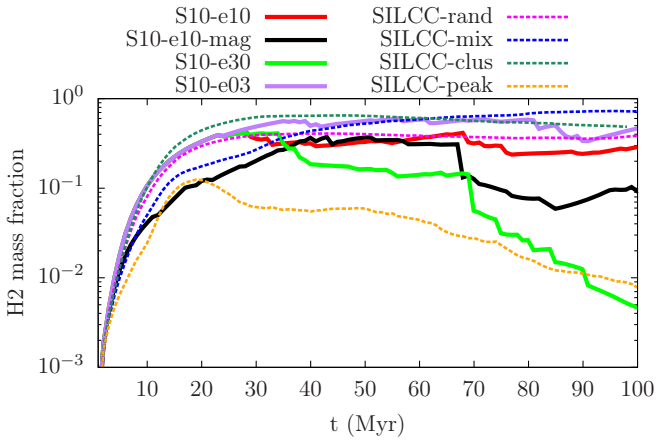

Figure C.3: H_2 mass fraction evolution for S10-e10 (black line), S10-e10-mag (red line), S10-e30 (green line), S10-e03 (purple line), SILCC-rand (magenta dotted line), SILCC-mix (blue dotted line), SILCC-clus (dark-green dotted line) and SILCC-peak (orange dotted line). The H_2 mass fractions the self-consistent runs lie between the random and peak fixed SN driving while S10-e03 is comparable to clustered driving.

Simulation S10-e03, because of the low $\varepsilon_{\rm SFR}$, creates relatively small SN events in the collapsing regions, comparable to the fixed SN rate clustered driving. Even though the random component is missing in S10-e03, the H_2 mass fraction is similar to clustered driving ($\sim 60\%$).

The cold gas VFFs (Fig. C.4) for S10-e10, S10-e10-mag and S10-e03 are comparable to the standard peak driving (with an average of 3.5%) mainly because they fail to efficiently destroy the high density collapsing areas the SNe explode in. On the other hand, S10-e03, due to its higher $\varepsilon_{\rm SFR}$, disperses the cold gas (see Fig. C.3) causing the cold VFF to decrease. However, the same simulation, is not as efficient at creating outflows as clustered driving and random driving is.

C.4 Dynamical evolution of S30-e10-ld

In Fig. C.5 we show the column density sequence for S30-e10-ld at 10, 20, 40, 60, 80, 90, 100 and 110 Myr. The gas in this simulation is being pushed to higher scale height than in S30-e10. On the other hand, there is a dense MC in the left part of the disk formed around 40 Myr into the simulation that is still present after 110 Myr.

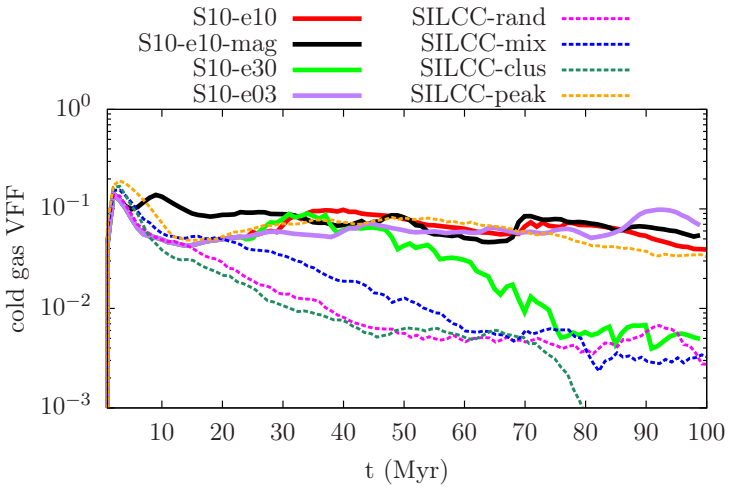

Figure C.4: Cold gas VFFs ($T < 300$ K) calculated for ± 100 pc around the galactic centre for the same simulations and colour coding as in Fig. C.3. All the simulations present the same high VFF as peak driving except for S10-e03 which has intermediate values, between peak and mixed.

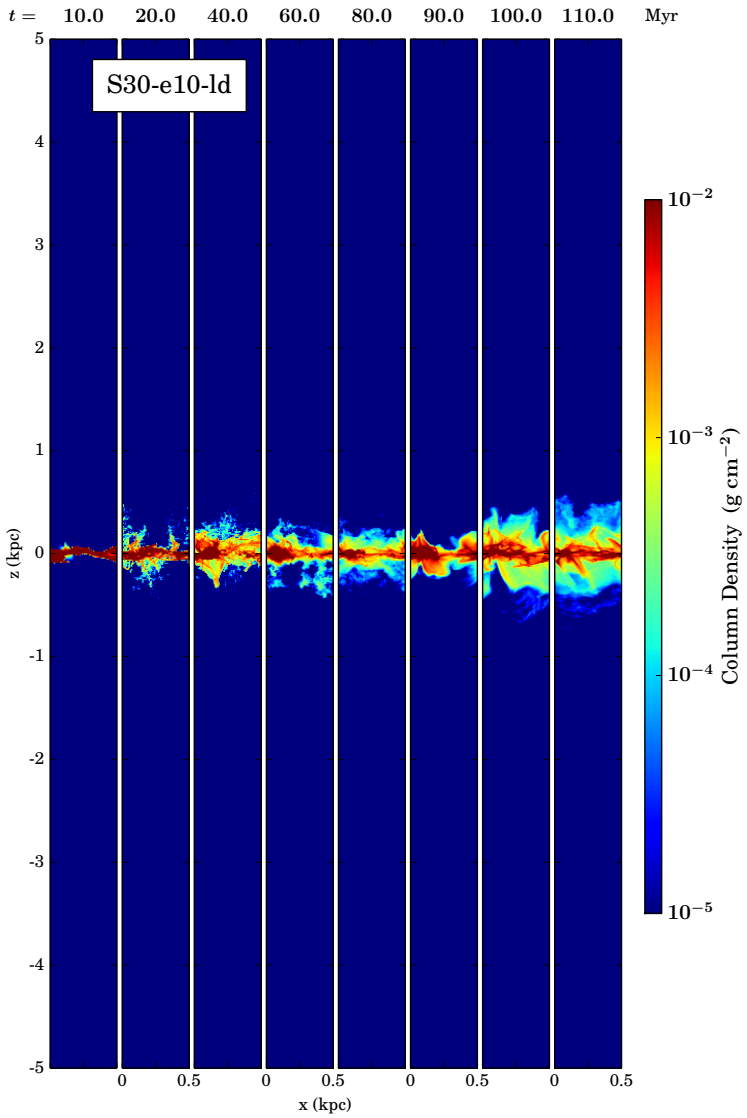

Figure C.5: Column density sequence for S30-e10-ld. There is more gas being pushed to higher scale height in comparison to S30-e10 however, there is a similar dense MC formed in the left part of the disk that is not dispersed after 110 Myr into the simulation.

Bibliography

O. Agertz, A. V. Kravtsov, S. N. Leitner, and N. Y. Gnedin. Toward a Complete Accounting of Energy and Momentum from Stellar Feedback in Galaxy Formation Simulations. *ApJ*, 770:25, June 2013. doi: 10.1088/0004-637X/770/1/25.

E. D. Alfvin, B. P. Miller, M. P. Haynes, E. Gallo, R. Giovanelli, R. A. Koopmann, E. Hodges-Kluck, and J. M. Cannon. The role of galactic cold gas in low-level supermassive black hole activity. *ArXiv e-prints*, June 2016.

F. O. Alves, P. Frau, J. M. Girart, G. A. P. Franco, F. P. Santos, and H. Wiesemeyer. On the radiation driven alignment of dust grains: Detection of the polarization hole in a starless core. *A&A*, 569:L1, September 2014. doi: 10.1051/0004-6361/201424678.

D. Arzoumanian, P. Andre, N. Peretto, and V. Konyves. Formation and evolution of interstellar filaments. Hints from velocity dispersion measurements. *A&A*, 553:A119, May 2013. doi: 10.1051/0004-6361/201220822.

I. Bagetakos, E. Brinks, F. Walter, W. J. G. de Blok, A. Usero, A. K. Leroy, J. W. Rich, and R. C. Kennicutt. The Porosity of the neutral ISM in 20 THINGS Galaxies. In M. Röllig, R. Simon, V. Ossenkopf, and J. Stutzki, editors, *EAS Publications Series*, volume 52 of *EAS Publications Series*, pages 103–106, November 2011. doi: 10.1051/eas/1152015.

J. Ballesteros-Paredes and L. Hartmann. Remarks on Rapid vs. Slow Star Formation. *RMxAA*, 43:123–136, April 2007.

J. Ballesteros-Paredes, E. Vázquez-Semadeni, and J. Scalo. Clouds as Turbulent Density Fluctuations: Implications for Pressure Confinement and Spectral Line Data Interpretation. *ApJ*, 515:286–303, April 1999. doi: 10.1086/307007.

J. Ballesteros-Paredes, R. S. Klessen, M.-M. Mac Low, and E. Vazquez-Semadeni. Molecular Cloud Turbulence and Star Formation. *Protostars and Planets V*, pages 63–80, 2007.

D. Balsara, R. A. Benjamin, and D. P. Cox. The Evolution of Adiabatic Supernova Remnants in a Turbulent, Magnetized Medium. *ApJ*, 563:800–805, December 2001. doi: 10.1086/323967.

D. S. Balsara. Wave Propagation in Molecular Clouds. *ApJ*, 465:775, July 1996. doi: 10.1086/177462.

D. S. Balsara, J. Kim, M.-M. Mac Low, and G. J. Mathews. Amplification of Interstellar Magnetic Fields by Supernova-driven Turbulence. *ApJ*, 617:339–349, December 2004. doi: 10.1086/425297.

R. Banerjee, E. Vazquez-Semadeni, P. Hennebelle, and R. S. Klessen. Clump morphology and evolution in MHD simulations of molecular cloud formation. *MNRAS*, 398:1082–1092, September 2009. doi: 10.1111/j.1365-2966.2009.15115.x.

M. R. Bate, I. A. Bonnell, and N. M. Price. Modelling accretion in protobinary systems. *MNRAS*, 277:362–376, November 1995. doi: 10.1093/mnras/277.2.362.

R. Beck. Galactic and Extragalactic Magnetic Fields. *SSRv*, 99:243–260, October 2001.

R. Beck. Magnetic Field Structure from Synchrotron Polarization. In M.-A. Miville-Deschênes and F. Boulanger, editors, *EAS Publications Series*, volume 23 of *EAS Publications Series*, pages 19–36, 2007. doi: 10.1051/eas:2007003.

R. Beck and R. Wielebinski. *Magnetic Fields in Galaxies*, page 641. 2013. doi: 10.1007/978-94-007-5612-0_13.

S. M. Benincasa, J. Wadsley, H. M. P. Couchman, and B. W. Keller. The anatomy of a star-forming galaxy: pressure-driven regulation of star formation in simulated galaxies. *MNRAS*, 462:3053–3068, November 2016. doi: 10.1093/mnras/stw1741.

E. A. Bergin, L. W. Hartmann, J. C. Raymond, and J. Ballesteros-Paredes. Molecular Cloud Formation behind Shock Waves. *ApJ*, 612:921–939, September 2004. doi: 10.1086/422578.

R. A. Bernstein, W. L. Freedman, and B. F. Madore. The First Detections of the Extragalactic Background Light at 3000, 5500, and 8000 Å. III. Cosmological Implications. *ApJ*, 571:107–128, May 2002. doi: 10.1086/339424.

H. Beuther, J. Kerp, T. Preibisch, T. Stanke, and P. Schilke. Hard X-ray emission from a young massive star-forming cluster. *A&A*, 395:169–177, November 2002. doi: 10.1051/0004-6361:20021261.

F. Bigiel, A. Leroy, F. Walter, E. Brinks, W. J. G. de Blok, B. Madore, and M. D. Thornley. The Star Formation Law in Nearby Galaxies on Sub-Kpc Scales. *ApJ*, 136:2846–2871, December 2008. doi: 10.1088/0004-6256/136/6/2846.

A. Blaauw. On the origin of the O- and B-type stars with high velocities (the "run-away" stars), and some related problems. 15:265, May 1961.

Francois Bouchut, Christian Klingenberg, and Knut Waagan. A multiwave approximate riemann solver for ideal mhd based on relaxation ii: numerical implementation with 3 and 5 waves. *Numerische Mathematik*, 115(4):647–679, 2010. ISSN 0945-3245. doi: 10.1007/s00211-010-0289-4.

A. Brandenburg. Hydromagnetic dynamo theory. *Scholarpedia*, 2(3):2309, 2007. revision 127681.

B. C. Bromley, S. J. Kenyon, M. J. Geller, E. Barcikowski, W. R. Brown, and M. J. Kurtz. Hypervelocity Stars: Predicting the Spectrum of Ejection Velocities. *ApJ*, 653: 1194–1202, December 2006. doi: 10.1086/508419.

W. R. Brown. Hypervelocity Stars. *ARAA*, 53:15–49, August 2015. doi: 10.1146/annurev-astro-082214-122230.

E. M. Burbidge, G. R. Burbidge, W. A. Fowler, and F. Hoyle. Synthesis of the Elements in Stars. *Reviews of Modern Physics*, 29:547–650, 1957. doi: 10.1103/RevModPhys.29.547.

B. J. Burn. On the depolarization of discrete radio sources by Faraday dispersion. *MNRAS*, 133:67, 1966. doi: 10.1093/mnras/133.1.67.

G. Chabrier. The Galactic Disk Mass Budget. I. Stellar Mass Function and Density. *ApJ*, 554:1274–1281, June 2001. doi: 10.1086/321401.

C.-Y. Chen and E. C. Ostriker. Formation of Magnetized Prestellar Cores with Ambipolar Diffusion and Turbulence. *ApJ*, 785:69, April 2014. doi: 10.1088/0004-637X/785/1/69.

R. Chini, V. H. Hoffmeister, A. Nasseri, O. Stahl, and H. Zinnecker. A spectroscopic survey on the multiplicity of high-mass stars. *MNRAS*, 424:1925–1929, August 2012. doi: 10.1111/j.1365-2966.2012.21317.x.

P. C. Clark, S. C. O. Glover, and R. S. Klessen. TreeCol: a novel approach to estimating column densities in astrophysical simulations. *MNRAS*, 420:745–756, February 2012. doi: 10.1111/j.1365-2966.2011.20087.x.

C. Clarke and M. S. Oey. Galactic porosity and a star formation threshold for the escape of ionizing radiation from galaxies. *MNRAS*, 337:1299–1308, December 2002. doi: 10.1046/j.1365-8711.2002.05976.x.

D. C. Collins, P. Padoan, M. L. Norman, and H. Xu. Mass and Magnetic Distributions in Self-gravitating Super-Alfvénic Turbulence with Adaptive Mesh Refinement. *ApJ*, 731: 59, April 2011. doi: 10.1088/0004-637X/731/1/59.

D. P. Cox and B. W. Smith. Large-Scale Effects of Supernova Remnants on the Galaxy: Generation and Maintenance of a Hot Network of Tunnels. *ApJL*, 189:L105, May 1974. doi: 10.1086/181476.

P. Creasey, T. Theuns, R. G. Bower, and C. G. Lacey. Numerical overcooling in shocks. *MNRAS*, 415:3706–3720, August 2011. doi: 10.1111/j.1365-2966.2011.19001.x.

R. M. Crutcher. Observations of Magnetic Fields in Molecular Clouds. In B. Uyaniker, W. Reich, and R. Wielebinski, editors, *The Magnetized Interstellar Medium*, pages 123–132, February 2004.

R. M. Crutcher. Magnetic Fields in Molecular Clouds. *ARAA*, 50:29–63, September 2012. doi: 10.1146/annurev-astro-081811-125514.

R. M. Crutcher, T. H. Troland, A. A. Goodman, C. Heiles, I. Kazes, and P. C. Myers. OH Zeeman observations of dark clouds. *ApJ*, 407:175–184, April 1993. doi: 10.1086/172503.

R. M. Crutcher, N. Hakobian, and T. H. Troland. Testing Magnetic Star Formation Theory. *ApJ*, 692:844–855, February 2009. doi: 10.1088/0004-637X/692/1/844.

R. M. Crutcher, N. Hakobian, and T. H. Troland. Self-consistent analysis of OH Zeeman observations. *MNRAS*, 402:L64–L66, February 2010a. doi: 10.1111/j.1745-3933.2009.00802.x.

R. M. Crutcher, B. Wandelt, C. Heiles, E. Falgarone, and T. H. Troland. Magnetic Fields in Interstellar Clouds from Zeeman Observations: Inference of Total Field Strengths by Bayesian Analysis. *ApJ*, 725:466–479, December 2010b. doi: 10.1088/0004-637X/725/1/466.

J. E. Dale. The modelling of feedback in star formation simulations. *NewAR*, 68:1–33, October 2015. doi: 10.1016/j.newar.2015.06.001.

J. E. Dale, J. Ngoumou, B. Ercolano, and I. A. Bonnell. Before the first supernova: combined effects of H II regions and winds on molecular clouds. *MNRAS*, 442:694–712, July 2014. doi: 10.1093/mnras/stu816.

C. Dalla Vecchia and J. Schaye. Simulating galactic outflows with thermal supernova feedback. *MNRAS*, 426:140–158, October 2012. doi: 10.1111/j.1365-2966.2012.21704.x.

T. M. Dame, D. Hartmann, and P. Thaddeus. The Milky Way in Molecular Clouds: A New Complete CO Survey. *ApJ*, 547:792–813, February 2001. doi: 10.1086/318388.

M. A. de Avillez and D. Breitschwerdt. Global dynamical evolution of the ISM in star forming galaxies. I. High resolution 3D simulations: Effect of the magnetic field. *A&A*, 436:585–600, June 2005. doi: 10.1051/0004-6361:20042146.

M. A. de Avillez and D. Breitschwerdt. The Generation and Dissipation of Interstellar Turbulence: Results from Large-Scale High-Resolution Simulations. *ApJL*, 665:L35–L38, August 2007. doi: 10.1086/521222.

R. Dgani, D. van Buren, and A. Noriega-Crespo. The Transverse Acceleration Instability for Bow Shocks in the Nonlinear Regime. *ApJ*, 461:372, April 1996. doi: 10.1086/177065.

C. L. Dobbs. GMC formation by agglomeration and self gravity. *MNRAS*, 391:844–858, December 2008. doi: 10.1111/j.1365-2966.2008.13939.x.

C. L. Dobbs, A. Burkert, and J. E. Pringle. The properties of the interstellar medium in disc galaxies with stellar feedback. *MNRAS*, 417:1318–1334, October 2011. doi: 10.1111/j.1365-2966.2011.19346.x.

B. T. Draine. Photoelectric heating of interstellar gas. *ApJS*, 36:595–619, April 1978. doi: 10.1086/190513.

B. T. Draine and F. Bertoldi. Structure of Stationary Photodissociation Fronts. *ApJ*, 468: 269, September 1996. doi: 10.1086/177689.

A. Dubey, R. Fisher, C. Graziani, G. C. Jordan, IV, D. Q. Lamb, L. B. Reid, P. Rich, D. Sheeler, D. Townsley, and K. Weide. Challenges of Extreme Computing using the FLASH code. In N. V. Pogorelov, E. Audit, and G. P. Zank, editors, *Numerical Modeling of Space Plasma Flows*, volume 385 of *Astronomical Society of the Pacific Conference Series*, page 145, April 2008.

H. Egan, B. W. O'Shea, E. Hallman, J. Burns, H. Xu, D. Collins, H. Li, and M. L. Norman. Length Scales and Turbulent Properties of Magnetic Fields in Simulated Galaxy Clusters. *ArXiv e-prints*, January 2016.

J. J. Eldridge, N. Langer, and C. A. Tout. Runaway stars as progenitors of supernovae and gamma-ray bursts. *MNRAS*, 414:3501–3520, July 2011. doi: 10.1111/j.1365-2966.2011.18650.x.

B. G. Elmegreen. Star Formation in a Crossing Time. *ApJ*, 530:277–281, February 2000. doi: 10.1086/308361.

B. G. Elmegreen and A. Parravano. When star formation stops: Galaxy edges and low surface brightness disks. *ApJL*, 435:L121–124, November 1994. doi: 10.1086/187609.

V. Eswaran and S. B. Pope. An examination of forcing in direct numerical simulations of turbulence. *Computers & Fluids*, 16:257–278, 1988. doi: 0045-7930/88.

C. Federrath and R. S. Klessen. On the Star Formation Efficiency of Turbulent Magnetized Clouds. *ApJ*, 763:51, January 2013. doi: 10.1088/0004-637X/763/1/51.

C. Federrath, R. Banerjee, P. C. Clark, and R. S. Klessen. Modeling Collapse and Accretion in Turbulent Gas Clouds: Implementation and Comparison of Sink Particles in AMR and SPH. *ApJ*, 713:269–290, April 2010. doi: 10.1088/0004-637X/713/1/269.

C. Federrath, G. Chabrier, J. Schober, R. Banerjee, R. S. Klessen, and D. R. G. Schleicher. Mach Number Dependence of Turbulent Magnetic Field Amplification: Solenoidal versus Compressive Flows. *Physical Review Letters*, 107(11):114504, September 2011a. doi: 10.1103/PhysRevLett.107.114504.

C. Federrath, S. Sur, D. R. G. Schleicher, R. Banerjee, and R. S. Klessen. A New Jeans Resolution Criterion for (M)HD Simulations of Self-gravitating Gas: Application to Magnetic Field Amplification by Gravity-driven Turbulence. *ApJ*, 731:62, April 2011b. doi: 10.1088/0004-637X/731/1/62.

C. Federrath, J. Schober, S. Bovino, and D. R. G. Schleicher. The Turbulent Dynamo in Highly Compressible Supersonic Plasmas. *ApJL*, 797:L19, December 2014a. doi: 10.1088/2041-8205/797/2/L19.

C. Federrath, M. Schrön, R. Banerjee, and R. S. Klessen. Modeling Jet and Outflow Feedback during Star Cluster Formation. *ApJ*, 790:128, August 2014b. doi: 10.1088/0004-637X/790/2/128.

R. Feldmann, N. Y. Gnedin, and A. V. Kravtsov. The X-factor in Galaxies. I. Dependence on Environment and Scale. *ApJ*, 747:124, March 2012. doi: 10.1088/0004-637X/747/2/124.

K. M. Ferrière. The interstellar environment of our galaxy. *Reviews of Modern Physics*, 73:1031–1066, October 2001. doi: 10.1103/RevModPhys.73.1031.

G. B. Field, D. W. Goldsmith, and H. J. Habing. A Theoretical Model for the Interstellar Medium. In *Bulletin of the American Astronomical Society*, volume 1 of *BAAS*, page 240, June 1969.

P. Frau, J. M. Girart, M. T. Beltrán, M. Padovani, G. Busquet, O. Morata, J. M. Masqué, F. O. Alves, Á. Sánchez-Monge, G. A. P. Franco, and R. Estalella. Young Starless Cores Embedded in the Magnetically Dominated Pipe Nebula. II. Extended Data Set. *ApJ*, 759:3, November 2012. doi: 10.1088/0004-637X/759/1/3.

R. A. Freedman and W. J. Kaufmann. *Universe: Stars & Galaxies w/Starry Night Enthusiast*. 2008.

B. Fryxell, K. Olson, P. Ricker, F. X. Timmes, M. Zingale, D. Q. Lamb, P. MacNeice, R. Rosner, J. W. Truran, and H. Tufo. FLASH: An Adaptive Mesh Hydrodynamics Code for Modeling Astrophysical Thermonuclear Flashes. *ApJS*, 131:273–334, November 2000. doi: 10.1086/317361.

M. S. Fujii and S. Portegies Zwart. The Origin of OB Runaway Stars. *Science*, 334:1380, December 2011. doi: 10.1126/science.1211927.

Y. Fukui, Y. Moriguchi, K. Tamura, H. Yamamoto, Y. Tawara, N. Mizuno, T. Onishi, A. Mizuno, Y. Uchiyama, J. Hiraga, T. Takahashi, K. Yamashita, and S. Ikeuchi. Discovery of Interacting Molecular Gas toward the TeV Gamma-Ray Peak of the SNR G 347.3–0.5. *PASJ*, 55:L61–L64, October 2003. doi: 10.1093/pasj/55.5.L61.

B. M. Gaensler, G. J. Madsen, S. Chatterjee, and S. A. Mao. The Vertical Structure of Warm Ionised Gas in the Milky Way. *PASA*, 25:184–200, November 2008. doi: 10.1071/AS08004.

D. Garcia-Senz, C. Badenes, and N. Serichol. Is There a Hidden Hole in Type Ia Supernova Remnants? *ApJ*, 745:75, January 2012. doi: 10.1088/0004-637X/745/1/75.

A. Gatto, F. Fraternali, J. I. Read, F. Marinacci, H. Lux, and S. Walch. Unveiling the corona of the Milky Way via ram-pressure stripping of dwarf satellites. *MNRAS*, 433: 2749–2763, August 2013. doi: 10.1093/mnras/stt896.

A. Gatto, S. Walch, M.-M. M. Low, T. Naab, P. Girichidis, S. C. O. Glover, R. Wunsch, R. S. Klessen, P. C. Clark, C. Baczynski, T. Peters, J. P. Ostriker, J. C. Ibanez-Mejia, and S. Haid. Modelling the supernova-driven ISM in different environments. *MNRAS*, 449:1057–1075, May 2015. doi: 10.1093/mnras/stv324.

A. Gatto, S. Walch, T. Naab, P. Girichidis, R. Wunsch, S. C. O. Glover, R. S. Klessen, P. C. Clark, T. Peters, D. Derigs, C. Baczynski, and J. Puls. The SILCC project: III. Regulation of star formation and outflows by stellar winds and supernovae. *ArXiv e-prints*, June 2016.

S. Geier, T. Kupfer, U. Heber, B. N. Barlow, P. F. L. Maxted, C. Heuser, V. Schaffenroth, E. Ziegerer, R. H. Ostensen, and B. T. Gansicke. The Population of White Dwarf Binaries with Hot Subdwarf Companions. In P. Dufour, P. Bergeron, and G. Fontaine, editors, *19th European Workshop on White Dwarfs*, volume 493 of *Astronomical Society of the Pacific Conference Series*, page 475, June 2015.

F. A. Gent, A. Shukurov, A. Fletcher, G. R. Sarson, and M. J. Mantere. The supernova-regulated ISM - I. The multiphase structure. *MNRAS*, 432:1396–1423, June 2013a. doi: 10.1093/mnras/stt560.

F. A. Gent, A. Shukurov, G. R. Sarson, A. Fletcher, and M. J. Mantere. The supernova-regulated ISM - II. The mean magnetic field. *MNRAS*, 430:L40–L44, March 2013b. doi: 10.1093/mnrasl/sls042.

R. Giovanelli and M. P. Haynes. Extragalactic HI surveys. *A&ARv*, 24:1, December 2016. doi: 10.1007/s00159-015-0085-3.

P. Girichidis, S. Walch, T. Naab, A. Gatto, R. Wunsch, S. C. O. Glover, R. S. Klessen, P. C. Clark, T. Peters, D. Derigs, and C. Baczynski. The SILCC (SImulating the LifeCycle of molecular Clouds) project - II. Dynamical evolution of the supernova-driven ISM and the launching of outflows. *MNRAS*, 456:3432–3455, March 2016. doi: 10.1093/mnras/stv2742.

S. C. O. Glover and P. C. Clark. Approximations for modelling CO chemistry in giant molecular clouds: a comparison of approaches. *MNRAS*, 421:116–131, March 2012. doi: 10.1111/j.1365-2966.2011.20260.x.

S. C. O. Glover and M.-M. Mac Low. Simulating the Formation of Molecular Clouds. I. Slow Formation by Gravitational Collapse from Static Initial Conditions. *ApJS*, 169: 239–268, April 2007a. doi: 10.1086/512238.

S. C. O. Glover and M.-M. Mac Low. Simulating the Formation of Molecular Clouds. II. Rapid Formation from Turbulent Initial Conditions. *ApJ*, 659:1317–1337, April 2007b. doi: 10.1086/512227.

S. C. O. Glover and R. J. Smith. CO-dark gas and molecular filaments in Milky Way-type galaxies - II. The temperature distribution of the gas. *MNRAS*, 462:3011–3025, November 2016. doi: 10.1093/mnras/stw1879.

S. C. O. Glover, C. Federrath, M.-M. Mac Low, and R. S. Klessen. Modelling CO formation in the turbulent interstellar medium. *MNRAS*, 404:2–29, May 2010. doi: 10.1111/j.1365-2966.2009.15718.x.

O. Gnat and G. J. Ferland. Ion-by-ion Cooling Efficiencies. *ApJS*, 199:20, March 2012. doi: 10.1088/0067-0049/199/1/20.

P. Goldreich and N. D. Kylafis. On mapping the magnetic field direction in molecular clouds by polarization measurements. *ApJL*, 243:L75–L78, January 1981. doi: 10.1086/183446.

D. W. Goldsmith, H. J. Habing, and G. B. Field. Thermal Properties of Interstellar Gas Heated by Cosmic Rays. *ApJ*, 158:173, October 1969. doi: 10.1086/150181.

H. Gong and E. C. Ostriker. Implementation of Sink Particles in the Athena Code. *ApJL*, November 2012.

A. Gualandris, S. Portegies Zwart, and M. S. Sipior. Three-body encounters in the Galactic Centre: the origin of the hypervelocity star SDSS J090745.0+024507. *MNRAS*, 363:223–228, October 2005. doi: 10.1111/j.1365-2966.2005.09433.x.

J. Guillochon and A. Loeb. The Fastest Unbound Stars in the Universe. *ApJ*, 806:124, June 2015. doi: 10.1088/0004-637X/806/1/124.

H. J. Habing. The interstellar radiation density between 912 A and 2400 A. *BAIN*, 19: 421, January 1968.

J. Han. The magnetic structure of our Galaxy: a review of observations. In K. G. Strassmeier, A. G. Kosovichev, and J. E. Beckman, editors, *Cosmic Magnetic Fields: From Planets, to Stars and Galaxies*, volume 259 of *IAU Symposium*, pages 455–466, April 2009. doi: 10.1017/S1743921309031123.

J. L. Han. The Large-Scale Magnetic Field Structure of Our Galaxy: Efficiently Deduced from Pulsar Rotation Measures. In B. Uyaniker, W. Reich, and R. Wielebinski, editors, *The Magnetized Interstellar Medium*, pages 3–12, February 2004.

J. L. Han, R. N. Manchester, A. G. Lyne, G. J. Qiao, and W. van Straten. Pulsar Rotation Measures and the Large-Scale Structure of the Galactic Magnetic Field. *ApJ*, 642:868–881, May 2006. doi: 10.1086/501444.

Z. Han. A possible solution for the lack of EHB binaries in globular clusters. *A&A*, 484: L31–L34, June 2008. doi: 10.1051/0004-6361:200809614.

H. Hanayama and K. Tomisaka. Long-Term Evolution of Supernova Remnants in Magnetized Interstellar Medium. *ApJ*, 641:905–918, April 2006. doi: 10.1086/500527.

C. Heiles. The Local Direction and Curvature of the Galactic Magnetic Field Derived from Starlight Polarization. *ApJ*, 462:316, May 1996. doi: 10.1086/177153.

C. Heiles and T. H. Troland. The Millennium Arecibo 21 Centimeter Absorption-Line Survey. II. Properties of the Warm and Cold Neutral Media. *ApJ*, 586:1067–1093, April 2003. doi: 10.1086/367828.

F. Heitsch and L. Hartmann. Rapid Molecular Cloud and Star Formation: Mechanisms and Movies. *ApJ*, 689:290-301, December 2008. doi: 10.1086/592491.

F. Heitsch and L. Hartmann. Accretion and diffusion time-scales in sheets and filaments. *MNRAS*, 443:230–240, September 2014. doi: 10.1093/mnras/stu1147.

F. Heitsch, M.-M. Mac Low, and R. S. Klessen. Gravitational Collapse in Turbulent Molecular Clouds. II. Magnetohydrodynamical Turbulence. *ApJ*, 547:280–291, January 2001. doi: 10.1086/318335.

F. Heitsch, T. Naab, and S. Walch. Flow-driven cloud formation and fragmentation: results from Eulerian and Lagrangian simulations. *MNRAS*, 415:271–278, July 2011. doi: 10.1111/j.1365-2966.2011.18694.x.

P. Hennebelle and O. Iffrig. Simulations of magnetized multiphase galactic disc regulated by supernovae explosions. *A&A*, 570:A81, October 2014. doi: 10.1051/0004-6361/201423392.

P. Hennebelle, R. Banerjee, E. Vazquez-Semadeni, R. S. Klessen, and E. Audit. From the warm magnetized atomic medium to molecular clouds. *AAp*, 486:L43–L46, August 2008. doi: 10.1051/0004-6361:200810165.

P. Hennebelle, B. Commercon, M. Joos, R. S. Klessen, M. Krumholz, J. C. Tan, and R. Teyssier. Collapse, outflows and fragmentation of massive, turbulent and magnetized prestellar barotropic cores. *A&A*, 528:A72, April 2011. doi: 10.1051/0004-6361/201016052.

J. W. Hewitt and F. Yusef-Zadeh. Discovery of New Interacting Supernova Remnants in the Inner Galaxy. *ApJL*, 694:L16–L20, March 2009. doi: 10.1088/0004-637X/694/1/L16.

M. Heyer and T. M. Dame. Molecular Clouds in the Milky Way. *ARAA*, 53:583–629, August 2015. doi: 10.1146/annurev-astro-082214-122324.

R. H. Hildebrand. Magnetic fields and stardust. *QJRAS*, 29:327–351, September 1988.

A. S. Hill, M. R. Joung, M.-M. Mac Low, R. A. Benjamin, L. M. Haffner, C. Klingenberg, and K. Waagan. Vertical Structure of a Supernova-driven Turbulent, Magnetized Interstellar Medium. *ApJ*, 750:104, May 2012. doi: 10.1088/0004-637X/750/2/104.

J. G. Hills. Hyper-velocity and tidal stars from binaries disrupted by a massive Galactic black hole. *NATURE*, 331:687–689, February 1988. doi: 10.1038/331687a0.

T. Hoang and A. Lazarian. Radiative torque alignment: essential physical processes. *MNRAS*, 388:117–143, July 2008. doi: 10.1111/j.1365-2966.2008.13249.x.

D. J. Hollenbach and H. A. Thronson, Jr., editors. *Summer School on Interstellar Processes: Abstracts of contributed papers*, October 1986.

M. Honma, Y. Sofue, and N. Arimoto. The molecular front in galaxies. II. Galactic-scale gas phase transition of HI and H_2_. *A&A*, 304:1, December 1995.

P. F. Hopkins, E. Quataert, and N. Murray. Self-regulated star formation in galaxies via momentum input from massive stars. *MNRAS*, 417:950–973, October 2011. doi: 10.1111/j.1365-2966.2011.19306.x.

P. F. Hopkins, D. Narayanan, and N. Murray. The meaning and consequences of star formation criteria in galaxy models with resolved stellar feedback. *MNRAS*, 432:2647–2653, July 2013. doi: 10.1093/mnras/stt723.

I. D. Howarth, P. L. Dufton, P. R. Dunstall, C. J. Evans, L. A. Almeida, A. Z. Bonanos, J. S. Clark, N. Langer, H. Sana, S. Simon-Diaz, I. Soszynski, and W. D. Taylor. The VLT-FLAMES Tarantula Survey. XXIII. Two massive double-lined binaries in 30 Doradus. *A&A*, 582:A73, October 2015. doi: 10.1051/0004-6361/201526408.

D. A. Hubber, S. Walch, and A. P. Whitworth. An improved sink particle algorithm for SPH simulations. *MNRAS*, 430:3261–3275, April 2013. doi: 10.1093/mnras/stt128.

A. Hughes, T. Wong, J. Ott, E. Muller, J. L. Pineda, Y. Mizuno, J.-P. Bernard, D. Paradis, S. Maddison, W. T. Reach, L. Staveley-Smith, A. Kawamura, M. Meixner, S. Kim, T. Onishi, N. Mizuno, and Y. Fukui. Physical properties of giant molecular clouds in the Large Magellanic Cloud. *MNRAS*, 406:2065–2086, August 2010. doi: 10.1111/j.1365-2966.2010.16829.x.

J. C. Ibáñez-Mejía, M.-M. Mac Low, R. S. Klessen, and C. Baczynski. Gravitational Contraction versus Supernova Driving and the Origin of the Velocity Dispersion-Size Relation in Molecular Clouds. *ApJ*, 824:41, June 2016. doi: 10.3847/0004-637X/824/1/41.

R. Jansson and G. R. Farrar. A New Model of the Galactic Magnetic Field. *ApJ*, 757:14, September 2012. doi: 10.1088/0004-637X/757/1/14.

E. B. Jenkins and T. M. Tripp. The Distribution of Thermal Pressures in the Diffuse, Cold Neutral Medium of Our Galaxy. II. An Expanded Survey of Interstellar C I Fine-structure Excitations. *ApJ*, 734:65, June 2011. doi: 10.1088/0004-637X/734/1/65.

T. W. Jones, D. H. Porter, D. Ryu, and J. Cho. MHD Turbulence Simulation in a Cosmic Structure Context. *ArXiv e-prints*, August 2011.

M. K. R. Joung and M.-M. Mac Low. Turbulent Structure of a Stratified Supernova-driven Interstellar Medium. *ApJ*, 653:1266–1279, December 2006. doi: 10.1086/508795.

M. R. Joung, M.-M. Mac Low, and G. L. Bryan. Dependence of Interstellar Turbulent Pressure on Supernova Rate. *ApJ*, 704:137–149, October 2009. doi: 10.1088/0004-637X/704/1/137.

D. Kasen and E. Ramirez-Ruiz. Optical Transients from the Unbound Debris of Tidal Disruption. *ApJ*, 714:155–162, May 2010. doi: 10.1088/0004-637X/714/1/155.

N. Katz. Dissipational galaxy formation. II - Effects of star formation. *ApJ*, 391:502–517, June 1992. doi: 10.1086/171366.

N. Kazantsev. Enhancement of a magnetic filed by a conducting fluid. *Soviet J. Exp. Theor. Phys.*, 26:1031–1034, May 1968.

R. C. Kennicutt and N. J. Evans. Star Formation in the Milky Way and Nearby Galaxies. *ARA&A*, 50:531–608, September 2012. doi: 10.1146/annurev-astro-081811-125610.

R. C. Kennicutt, Jr. The star formation law in galactic disks. *ApJ*, 344:685–703, September 1989. doi: 10.1086/167834.

R. C. Kennicutt, Jr. The Global Schmidt Law in Star-forming Galaxies. *ApJ*, 498:541–552, May 1998. doi: 10.1086/305588.

S. J. Kenyon, B. C. Bromley, M. J. Geller, and W. R. Brown. Hypervelocity Stars: From the Galactic Center to the Halo. *ApJ*, 680:312-327, June 2008. doi: 10.1086/587738.

S. J. Kenyon, B. C. Bromley, W. R. Brown, and M. J. Geller. Predicted Space Motions for Hypervelocity and Runaway Stars: Proper Motions and Radial Velocities for the Gaia Era. *ApJ*, 793:122, October 2014. doi: 10.1088/0004-637X/793/2/122.

W. E. Kerzendorf, B. P. Schmidt, M. Asplund, K. Nomoto, P. Podsiadlowski, A. Frebel, R. A. Fesen, and D. Yong. Subaru High-Resolution Spectroscopy of Star G in the Tycho Supernova Remnant. *ApJ*, 701:1665–1672, August 2009. doi: 10.1088/0004-637X/701/2/1665.

C.-G. Kim and E. C. Ostriker. Momentum Injection by Supernovae in the Interstellar Medium. *ApJ*, 802:99, April 2015a. doi: 10.1088/0004-637X/802/2/99.

C.-G. Kim and E. C. Ostriker. Vertical Equilibrium, Energetics, and Star Formation Rates in Magnetized Galactic Disks Regulated by Momentum Feedback from Supernovae. *ApJ*, 815:67, December 2015b. doi: 10.1088/0004-637X/815/1/67.

C.-G. Kim and E. C. Ostriker. Momentum Injection by Supernovae in the Interstellar Medium. *ApJ*, 802:99, April 2015c. doi: 10.1088/0004-637X/802/2/99.

C.-G. Kim, W.-T. Kim, and E. C. Ostriker. Regulation of Star Formation Rates in Multiphase Galactic Disks: Numerical Tests of the Thermal/Dynamical Equilibrium Model. *ApJ*, 743:25, December 2011. doi: 10.1088/0004-637X/743/1/25.

C.-G. Kim, E. C. Ostriker, and W.-T. Kim. Three-dimensional Hydrodynamic Simulations of Multiphase Galactic Disks with Star Formation Feedback. I. Regulation of Star Formation Rates. *ApJ*, 776:1, October 2013. doi: 10.1088/0004-637X/776/1/1.

R. S. Klessen and S. C. O. Glover. Physical Processes in the Interstellar Medium. *Star Formation in Galaxy Evolution: Connecting Numerical Models to Reality, Saas-Fee Advanced Course, Volume 43. ISBN 978-3-662-47889-9. Springer-Verlag Berlin Heidelberg, 2016, p. 85*, 43:85, 2016. doi: 10.1007/978-3-662-47890-5_2.

A. G. Kritsuk, S. D. Ustyugov, M. L. Norman, and P. Padoan. Simulating supersonic turbulence in magnetized molecular clouds. In *Journal of Physics Conference Series*, volume 180 of *Journal of Physics Conference Series*, page 012020, July 2009. doi: 10.1088/1742-6596/180/1/012020.

A. G. Kritsuk, Å. Nordlund, D. Collins, P. Padoan, M. L. Norman, T. Abel, R. Banerjee, C. Federrath, M. Flock, D. Lee, P. S. Li, W.-C. Müller, R. Teyssier, S. D. Ustyugov, C. Vogel, and H. Xu. Comparing Numerical Methods for Isothermal Magnetized Supersonic Turbulence. *ApJ*, 737:13, August 2011. doi: 10.1088/0004-637X/737/1/13.

M. R. Krumholz and C. D. Matzner. The Dynamics of Radiation-pressure-dominated H II Regions. *ApJ*, 703:1352–1362, October 2009. doi: 10.1088/0004-637X/703/2/1352.

M. R. Krumholz, C. F. McKee, and J. Tumlinson. The Star Formation Law in Atomic and Molecular Gas. *ApJ*, 699:850–856, July 2009. doi: 10.1088/0004-637X/699/1/850.

T. Kudoh and S. Basu. Three-dimensional MHD simulations of magnetized molecular cloud fragmentation with turbulence and ion-neutral friction. In B. G. Elmegreen and J. Palous, editors, *Triggered Star Formation in a Turbulent ISM*, volume 237 of *IAU Symposium*, pages 437–437, 2007. doi: 10.1017/S1743921307002256.

T. Kudoh and S. Basu. Three-dimensional Simulation of Magnetized Cloud Fragmentation Induced by Nonlinear Flows and Ambipolar Diffusion. *ApJL*, 679:L97, June 2008. doi: 10.1086/589618.

R. M. Kulsrud and E. G. Zweibel. On the origin of cosmic magnetic fields. *Reports on Progress in Physics*, 71(4):046901, April 2008. doi: 10.1088/0034-4885/71/4/046901.

C. J. Lada. Star Formation in the Local Milky Way. In J. H. Kastner, B. Stelzer, and S. A. Metchev, editors, *Young Stars & Planets Near the Sun*, volume 314 of *IAU Symposium*, pages 8–15, January 2016. doi: 10.1017/S1743921315005955.

R. B. Larson. A model for the formation of a spherical galaxy. *MNRAS*, 145:405, 1969. doi: 10.1093/mnras/145.4.405.

A. Lazarian. Magnetic Fields via Polarimetry: Progress of Grain Alignment Theory. *JQSRT*, 79:881, 2003. doi: 10.1016/S0022-4073(02)00326-6.

A. Lazarian. Reconnection Diffusion, Star Formation, and Numerical Simulations. In N. V. Pogorelov, E. Audit, and G. P. Zank, editors, *Numerical Modeling of Space Plasma Flows (ASTRONUM2012)*, volume 474 of *Astronomical Society of the Pacific Conference Series*, page 15, April 2013.

M. D. Lehnert, L. Le Tiran, N. P. H. Nesvadba, W. van Driel, F. Boulanger, and P. Di Matteo. On the self-regulation of intense star-formation in galaxies at z = 1-3. *A&A*, 555:A72, July 2013. doi: 10.1051/0004-6361/201220555.

A. K. Leroy, F. Walter, E. Brinks, F. Bigiel, W. J. G. de Blok, B. Madore, and M. D. Thornley. The Star Formation Efficiency in Nearby Galaxies: Measuring Where Gas Forms Stars Effectively. *Aj*, 136:2782–2845, December 2008. doi: 10.1088/0004-6256/136/6/2782.

D. L. Li, J. Esimbek, J. J. Zhou, Y.-Q. Lou, G. Wu, X. D. Tang, and Y. X. He. Filament L1482 in the California molecular cloud. *A&A*, 567:A10, July 2014. doi: 10.1051/0004-6361/201323122.

H.-B. Li and T. Henning. The alignment of molecular cloud magnetic fields with the spiral arms in M33. *Nature*, 479:499–501, November 2011. doi: 10.1038/nature10551.

M. Li, J. P. Ostriker, R. Cen, G. L. Bryan, and T. Naab. Supernova Feedback and the Hot Gas Filling Fraction of the Interstellar Medium. *ApJ*, 814:4, November 2015a. doi: 10.1088/0004-637X/814/1/4.

P. S. Li, C. F. McKee, and R. I. Klein. Magnetized interstellar molecular clouds - I. Comparison between simulations and Zeeman observations. *MNRAS*, 452:2500–2527, September 2015b. doi: 10.1093/mnras/stv1437.

M.-M. Mac Low. From Gas to Stars over Cosmic Time. In T. Wong and J. Ott, editors, *Molecular Gas, Dust, and Star Formation in Galaxies*, volume 292 of *IAU Symposium*, pages 3–15, March 2013. doi: 10.1017/S1743921313000161.

M.-M. Mac Low and R. S. Klessen. Control of star formation by supersonic turbulence. *Reviews of Modern Physics*, 76:125–194, January 2004. doi: 10.1103/RevModPhys.76.125.

M.-M. Mac Low, D. S. Balsara, J. Kim, and M. A. de Avillez. The Distribution of Pressures in a Supernova-driven Interstellar Medium. I. Magnetized Medium. *ApJ*, 626:864–876, June 2005. doi: 10.1086/430122.

S. A. Mao, N. M. McClure-Griffiths, B. M. Gaensler, M. Haverkorn, R. Beck, D. McConnell, M. Wolleben, S. Stanimirović, J. M. Dickey, and L. Staveley-Smith. Magnetic Field Structure of the Large Magellanic Cloud from Faraday Rotation Measures of Diffuse Polarized Emission. *ApJ*, 759:25, November 2012. doi: 10.1088/0004-637X/759/1/25.

E. Marietta, A. Burrows, and B. Fryxell. Type IA Supernova Explosions in Binary Systems: The Impact on the Secondary Star and Its Consequences. *ApJS*, 128:615–650, June 2000. doi: 10.1086/313392.

C. F. McKee and E. C. Ostriker. Theory of Star Formation. *ARA&A*, 45:565–687, September 2007. doi: 10.1146/annurev.astro.45.051806.110602.

C. F. McKee and J. P. Ostriker. A theory of the interstellar medium - Three components regulated by supernova explosions in an inhomogeneous substrate. *ApJ*, 218:148–169, November 1977. doi: 10.1086/155667.

C. P. McNally, J. Wadsley, and H. M. P. Couchman. Self-Gravity and Angular Momentum Transport in Extended Galactic Disks. *ApJL*, 697:L162–L166, June 2009. doi: 10.1088/0004-637X/697/2/L162.

G. Meynet, A. Maeder, G. Schaller, D. Schaerer, and C. Charbonnel. Grids of massive stars with high mass loss rates. V. From 12 to 120 M_{sun-} at Z=0.001, 0.004, 0.008, 0.020 and 0.040. *A&AS*, 103, January 1994.

M. Micic, S. C. O. Glover, C. Federrath, and R. S. Klessen. Modelling H_2 formation in the turbulent interstellar medium: solenoidal versus compressive turbulent forcing. *MNRAS*, 421:2531–2542, April 2012. doi: 10.1111/j.1365-2966.2012.20477.x.

A. Mizuno and Y. Fukui. Physical properties of molecular clouds as revealed by NANTEN CO survey: from the galactic center to the galactic warp. In D. Clemens, R. Shah, and T. Brainerd, editors, *Milky Way Surveys: The Structure and Evolution of our Galaxy*, volume 317 of *Astronomical Society of the Pacific Conference Series*, page 59, December 2004.

P. Monaco, G. Murante, S. Borgani, and K. Dolag. Schmidt-Kennicutt relations in SPH simulations of disc galaxies with effective thermal feedback from supernovae. *MNRAS*, 421:2485–2497, April 2012. doi: 10.1111/j.1365-2966.2012.20482.x.

T. C. Mouschovias. Nonhomologous contraction and equilibria of self-gravitating, magnetic interstellar clouds embedded in an intercloud medium: Star formation. I Formulation of the problem and method of solution. *ApJ*, 206:753–767, June 1976. doi: 10.1086/154436.

T. Naab and J. P. Ostriker. Theoretical Challenges in Galaxy Formation. *ArXiv e-prints*, December 2016.

F. Nakamura and Z.-Y. Li. Binary and Multiple Star Formation in Magnetic Clouds: Bar Growth and Fragmentation. *ApJ*, 594:363–378, September 2003. doi: 10.1086/376862.

R. P. Nelson and W. D. Langer. The Dynamics of Low-Mass Molecular Clouds in External Radiation Fields. *ApJ*, 482:796–826, June 1997.

M. S. Oey and C. J. Clarke. The superbubble size distribution in the interstellar medium of galaxies. *MNRAS*, 289, August 1997. doi: 10.1093/mnras/289.3.570.

R. M. O'Leary and A. Loeb. Production of hypervelocity stars through encounters with stellar-mass black holes in the Galactic Centre. *MNRAS*, 383:86–92, January 2008. doi: 10.1111/j.1365-2966.2007.12531.x.

J. H. Oort. Dynamics of the galactic system in the vicinity of the Sun. 4:269, November 1928.

D. E. Osterbrock and N. G. Bochkarev. Book-Review - Astrophysics of Gaseous Nebulae and Active Galactic Nuclei. *SvA*, 33:694, November 1989.

E. C. Ostriker and R. Shetty. Maximally Star-forming Galactic Disks. I. Starburst Regulation Via Feedback-driven Turbulence. *ApJ*, 731:41, April 2011. doi: 10.1088/0004-637X/731/1/41.

E. C. Ostriker, C. F. McKee, and A. K. Leroy. Regulation of Star Formation Rates in Multiphase Galactic Disks: A Thermal/Dynamical Equilibrium Model. *ApJ*, 721:975–994, October 2010. doi: 10.1088/0004-637X/721/2/975.

P. Padoan, L. Pan, T. Haugbolle, and Å. Nordlund. Supernova Driving. I. The Origin of Molecular Cloud Turbulence. *ApJ*, 822:11, May 2016. doi: 10.3847/0004-637X/822/1/11.

R. Pakmor, F. K. Ropke, A. Weiss, and W. Hillebrandt. The impact of type Ia supernovae on main sequence binary companions. *A&A*, 489:943–951, October 2008. doi: 10.1051/0004-6361:200810456.

A. Pardi, P. Girichidis, T. Naab, S. Walch, T. Peters, F. Heitsch, S. C. O. Glover, R. S. Klessen, R. Wunsch, and A. Gatto. The impact of magnetic fields on the chemical evolution of the supernova-driven ISM. *MNRAS*, 465:4611–4633, March 2017. doi: 10.1093/mnras/stw3071.

V. I. Pariev, S. A. Colgate, and J. M. Finn. A Magnetic α-ω Dynamo in AGN Disks. II. Magnetic Field Generation, Theories, and Simulations. *ApJ*, 658:129–160, March 2007. doi: 10.1086/510735.

M. D. Pavel, D. P. Clemens, and A. F. Pinnick. Testing Galactic Magnetic Field Models Using Near-infrared Polarimetry. *ApJ*, 749:71, April 2012. doi: 10.1088/0004-637X/749/1/71.

H. B. Perets and L. Subr. The Properties of Dynamically Ejected Runaway and Hyper-runaway Stars. *ApJ*, 751:133, June 2012. doi: 10.1088/0004-637X/751/2/133.

T. Peters, R. Banerjee, R. S. Klessen, and M.-M. Mac Low. The Interplay of Magnetic Fields, Fragmentation, and Ionization Feedback in High-mass Star Formation. *ApJ*, 729:72, March 2011. doi: 10.1088/0004-637X/729/1/72.

T. Peters, D. R. G. Schleicher, R. S. Klessen, R. Banerjee, C. Federrath, R. J. Smith, and S. Sur. The Impact of Thermodynamics on Gravitational Collapse: Filament Formation and Magnetic Field Amplification. *ApJL*, 760:L28, December 2012. doi: 10.1088/2041-8205/760/2/L28.

T. Peters, T. Naab, S. Walch, S. C. O. Glover, P. Girichidis, E. Pellegrini, R. S. Klessen, R. Wünsch, A. Gatto, and C. Baczynski. The SILCC project — IV. Impact of dissociating and ionising radiation on the interstellar medium and Halpha emission as a tracer of the star formation rate. *ArXiv e-prints*, October 2016a.

T. Peters, S. Zhukovska, T. Naab, P. Girichidis, S. Walch, S. C. O. Glover, R. S. Klessen, P. C. Clark, and D. Seifried. The turbulent life of dust grains in the supernova-driven, multi-phase interstellar medium. *ArXiv e-prints*, October 2016b.

T. Piffl, C. Scannapieco, J. Binney, M. Steinmetz, R.-D. Scholz, M. E. K. Williams, R. S. de Jong, G. Kordopatis, G. Matijevič, O. Bienaymé, J. Bland-Hawthorn, C. Boeche, K. Freeman, B. Gibson, G. Gilmore, E. K. Grebel, A. Helmi, U. Munari, J. F. Navarro, Q. Parker, W. A. Reid, G. Seabroke, F. Watson, R. F. G. Wyse, and T. Zwitter. The RAVE survey: the Galactic escape speed and the mass of the Milky Way. *A&A*, 562:A91, February 2014. doi: 10.1051/0004-6361/201322531.

J. L. Pineda, W. D. Langer, T. Velusamy, and P. F. Goldsmith. A Herschel [C ii] Galactic plane survey. I. The global distribution of ISM gas components. *A&A*, 554:A103, June 2013. doi: 10.1051/0004-6361/201321188.

R. A. Piontek and E. C. Ostriker. Models of Vertically Stratified Two-Phase ISM Disks with MRI-Driven Turbulence. *ApJ*, 663:183–203, July 2007. doi: 10.1086/518103.

Planck Collaboration. Planck intermediate results. I. Further validation of new Planck clusters with XMM-Newton. *A&A*, 543:A102, July 2012. doi: 10.1051/0004-6361/201118731.

Planck Collaboration. Planck intermediate results. III. The relation between galaxy cluster mass and Sunyaev-Zeldovich signal. *A&A*, 550:A129, February 2013a. doi: 10.1051/0004-6361/201219398.

Planck Collaboration. Planck intermediate results. IV. The XMM-Newton validation programme for new Planck galaxy clusters. *A&a*, 550:A130, February 2013b. doi: 10.1051/0004-6361/201219519.

Planck Collaboration, AMI Collaboration, P. A. R. Ade, N. Aghanim, M. Arnaud, M. Ashdown, J. Aumont, C. Baccigalupi, A. Balbi, A. J. Banday, and et al. Planck intermediate results. II. Comparison of Sunyaev-Zeldovich measurements from Planck and from the Arcminute Microkelvin Imager for 11 galaxy clusters. *A&A*, 550:A128, February 2013. doi: 10.1051/0004-6361/201219361.

S. F. Portegies Zwart, S. L. W. McMillan, and H. Baumgardt. Life and Death of Young Dense Star Clusters near the Galactic Center. In H. J. G. L. M. Lamers, L. J. Smith, and A. Nota, editors, *The Formation and Evolution of Massive Young Star Clusters*, volume 322 of *Astronomical Society of the Pacific Conference Series*, page 439, December 2004.

S. F. Portegies Zwart, S. L. W. McMillan, and J. Makino. Star cluster ecology - VII. The evolution of young dense star clusters containing primordial binaries. *MNRAS*, 374: 95–106, January 2007. doi: 10.1111/j.1365-2966.2006.11142.x.

A. Poveda, J. Ruiz, and C. Allen. Run-away Stars as the Result of the Gravitational Collapse of Proto-stellar Clusters. *Boletin de los Observatorios Tonantzintla y Tacubaya*, 4:86–90, April 1967.

D. J. Price and M. R. Bate. The effect of magnetic fields on star cluster formation. *MNRAS*, 385:1820–1834, April 2008. doi: 10.1111/j.1365-2966.2008.12976.x.

N. Przybilla, M. F. Nieva, A. Tillich, U. Heber, K. Butler, and W. R. Brown. HVS 7: a chemically peculiar hyper-velocity star. *A&A*, 488:L51–L54, September 2008. doi: 10.1051/0004-6361:200810455.

R. Pudritz. Accretion power and the origin of astrophysical jets. In *APS Meeting Abstracts*, November 2004.

O. H. Ramirez-Agudelo, H. Sana, A. de Koter, F. Tramper, N. J. Grin, F. R. N. Schneider, N. Langer, J. Puls, N. Markova, J. M. Bestenlehner, N. Castro, P. A. Crowther, C. J. Evans, M. Garcia, G. Grafener, A. Herrero, B. van Kempen, D. J. Lennon, J. Maiz Apellaniz, F. Najarro, C. Sabin-Sanjulian, S. Simon-Diaz, W. D. Taylor, and J. S. Vink. The VLT-FLAMES Tarantula Survey XXIV. Stellar properties of the O-type giants and supergiants in 30 Doradus. *ArXiv e-prints*, January 2017.

R. J. Rand and S. R. Kulkarni. The local Galactic magnetic field. *ApJ*, 343:760–772, August 1989. doi: 10.1086/167747.

F. Renaud, F. Bournaud, E. Emsellem, B. Elmegreen, R. Teyssier, J. Alves, D. Chapon, F. Combes, A. Dekel, J. Gabor, P. Hennebelle, and K. Kraljic. A sub-parsec resolution simulation of the Milky Way: global structure of the interstellar medium and properties

of molecular clouds. *MNRAS*, 436:1836–1851, December 2013. doi: 10.1093/mnras/stt1698.

R. J. Reynolds, L. M. Haffner, and S. L. Tufte. Evidence for an Additional Heat Source in the Warm Ionized Medium of Galaxies. *ApJL*, 525:L21–L24, November 1999. doi: 10.1086/312326.

A. Rimoldi, S. Portegies Zwart, and E. M. Rossi. Simulations of stripped core-collapse supernovae in close binaries. *Computational Astrophysics and Cosmology*, 3:2, March 2016. doi: 10.1186/s40668-016-0015-4.

W. W. Roberts, Jr. and C. Yuan. Application of the Density-Wave Theory to the Spiral Structure of the Milky way System. III. Magnetic Field: Large-Scale Hydromagnetic Shock Formation. *ApJ*, 161:887, September 1970. doi: 10.1086/150592.

H. Rogers and J. M. Pittard. Feedback from winds and supernovae in massive stellar clusters - I. Hydrodynamics. *MNRAS*, 431:1337–1351, May 2013. doi: 10.1093/mnras/stt255.

E. E. Salpeter. The Luminosity Function and Stellar Evolution. *ApJ*, 121:161, January 1955. doi: 10.1086/145971.

H. Sana, S. E. de Mink, A. de Koter, N. Langer, C. J. Evans, M. Gieles, E. Gosset, R. G. Izzard, J.-B. Le Bouquin, and F. R. N. Schneider. Binary Interaction Dominates the Evolution of Massive Stars. *Science*, 337:444, July 2012. doi: 10.1126/science.1223344.

V. Schaffenroth, N. Przybilla, K. Butler, A. Irrgang, and U. Heber. Observations of the extreme runaway HD271791: nucleosynthesis in a core-collapse supernova. *ArXiv e-prints*, January 2015.

J. Schaye. Star Formation Thresholds and Galaxy Edges: Why and Where. *ApJ*, 609: 667–682, July 2004. doi: 10.1086/421232.

J. Schaye and C. Dalla Vecchia. On the relation between the Schmidt and Kennicutt-Schmidt star formation laws and its implications for numerical simulations. *MNRAS*, 383:1210–1222, January 2008. doi: 10.1111/j.1365-2966.2007.12639.x.

J. et al. Schaye. The EAGLE project: simulating the evolution and assembly of galaxies and their environments. *MNRAS*, 446:521–554, January 2015. doi: 10.1093/mnras/stu2058.

M. Schmidt. The Rate of Star Formation. *ApJ*, 129:243, March 1959. doi: 10.1086/146614.

M. Schmidt. The Rate of Star Formation. II. The Rate of Formation of Stars of Different Mass. *ApJ*, 137:758, April 1963. doi: 10.1086/147553.

J. Schober, D. Schleicher, S. Bovino, and R. S. Klessen. Small-scale dynamo at low magnetic Prandtl numbers. *PhysRev*, 86(6):066412, December 2012. doi: 10.1103/PhysRevE.86.066412.

J. Schober, D. R. G. Schleicher, C. Federrath, S. Bovino, and R. S. Klessen. Saturation of the turbulent dynamo. *PhysRev*, 92(2):023010, August 2015. doi: 10.1103/PhysRevE.92.023010.

A. Schruba, A. K. Leroy, F. Walter, F. Bigiel, E. Brinks, W. J. G. de Blok, G. Dumas, C. Kramer, E. Rosolowsky, K. Sandstrom, K. Schuster, A. Usero, A. Weiss, and H. Wiesemeyer. A Molecular Star Formation Law in the Atomic-gas-dominated Regime in Nearby Galaxies. *AJ*, 142:37, August 2011. doi: 10.1088/0004-6256/142/2/37.

L. I. Sedov. *Similarity and Dimensional Methods in Mechanics*. 1959.

D. Seifried and S. Walch. The impact of turbulence and magnetic field orientation on star-forming filaments. *MNRAS*, 452:2410–2422, September 2015. doi: 10.1093/mnras/stv1458.

K. R. Sembach, J. C. Howk, R. S. I. Ryans, and F. P. Keenan. Modeling the Warm Ionized Interstellar Medium and Its Impact on Elemental Abundance Studies. *ApJ*, 528:310–324, January 2000. doi: 10.1086/308173.

D. S. Shepherd and E. Churchwell. Bipolar Molecular Outflows in Massive Star Formation Regions. *ApJ*, 472:225, November 1996. doi: 10.1086/178057.

R. Shetty and E. C. Ostriker. Maximally Star-forming Galactic Disks. II. Vertically Resolved Hydrodynamic Simulations of Starburst Regulation. *ApJ*, 754:2, July 2012. doi: 10.1088/0004-637X/754/1/2.

F. H. Shu, S. Lizano, and F. C. Adams. Star formation in molecular cloud cores. In M. Peimbert and J. Jugaku, editors, *Star Forming Regions*, volume 115 of *IAU Symposium*, pages 417–433, 1987.

M. D. V. Silva and R. Napiwotzki. Ejection velocities of high Galactic latitude runaway stars. *MNRAS*, 411:2596–2614, March 2011. doi: 10.1111/j.1365-2966.2010.17864.x.

A. D. Slyz, J. E. G. Devriendt, G. Bryan, and J. Silk. Towards simulating star formation in the interstellar medium. *MNRAS*, 356:737–752, January 2005. doi: 10.1111/j.1365-2966.2004.08494.x.

S. J. Smartt. Progenitors of Core-Collapse Supernovae. *ARA&A*, 47:63–106, September 2009. doi: 10.1146/annurev-astro-082708-101737.

S. J. Smartt. Observational Constraints on the Progenitors of Core-Collapse Supernovae: The Case for Missing High-Mass Stars. *PASA*, 32:e016, April 2015. doi: 10.1017/pasa.2015.17.

S. L. Snowden, R. Egger, D. P. Finkbeiner, M. J. Freyberg, and P. P. Plucinsky. Progress on Establishing the Spatial Distribution of Material Responsible for the 1 4 keV Soft X-Ray Diffuse Background Local and Halo Components. *ApJ*, 493:715–729, January 1998. doi: 10.1086/305135.

J. B. Spencer. The Discovery of the Zeeman Effect in Sunspots. *Leaflet of the Astronomical Society of the Pacific*, 9:273, 1965.

L. Spitzer, Jr. The Dynamics of the Interstellar Medium. III. Galactic Distribution. *ApJ*, 95:329, May 1942. doi: 10.1086/144407.

V. Springel and L. Hernquist. Cosmological smoothed particle hydrodynamics simulations: a hybrid multiphase model for star formation. *MNRAS*, 339:289–311, February 2003. doi: 10.1046/j.1365-8711.2003.06206.x.

G. Stinson, A. Seth, N. Katz, J. Wadsley, F. Governato, and T. Quinn. Star formation and feedback in smoothed particle hydrodynamic simulations - I. Isolated galaxies. *MNRAS*, 373:1074–1090, December 2006. doi: 10.1111/j.1365-2966.2006.11097.x.

K. Subramanian. Dynamics of fluctuating magnetic fields in turbulent dynamos incorporating ambipolar drifts. *ArXiv Astrophysics e-prints*, August 1997.

X.-H. Sun and W. Reich. The Galactic halo magnetic field revisited. *Research in Astronomy and Astrophysics*, 10:1287–1297, December 2010. doi: 10.1088/1674-4527/10/12/009.

S. Sur, A. Shukurov, and K. Subramanian. Galactic dynamos supported by magnetic helicity fluxes. *MNRAS*, 377:874–882, May 2007. doi: 10.1111/j.1365-2966.2007.11662.x.

S. Sur, D. R. G. Schleicher, R. Banerjee, C. Federrath, and R. S. Klessen. The Generation of Strong Magnetic Fields During the Formation of the First Stars. *ApJL*, 721:L134–L138, October 2010. doi: 10.1088/2041-8205/721/2/L134.

J. C. Tan, M. T. Beltran, P. Caselli, F. Fontani, A. Fuente, M. R. Krumholz, C. F. McKee, and A. Stolte. Massive Star Formation. *Protostars and Planets VI*, pages 149–172, 2014. doi: 10.2458/azu_uapress_9780816531240-ch007.

E. J. Tasker and J. C. Tan. Star Formation in Disk Galaxies. I. Formation and Evolution of Giant Molecular Clouds via Gravitational Instability and Cloud Collisions. *ApJ*, 700: 358–375, July 2009. doi: 10.1088/0004-637X/700/1/358.

T. M. Tauris. Maximum speed of hypervelocity stars ejected from binaries. *MNRAS*, 448: L6–L10, March 2015. doi: 10.1093/mnrasl/slu189.

G. Taylor. The Formation of a Blast Wave by a Very Intense Explosion. I. Theoretical Discussion. *Proceedings of the Royal Society of London Series A*, 201:159–174, March 1950. doi: 10.1098/rspa.1950.0049.

N. Tetzlaff, R. Neuhäuser, and M. M. Hohle. A catalogue of young runaway Hipparcos stars within 3 kpc from the Sun. *MNRAS*, 410:190–200, January 2011. doi: 10.1111/j.1365-2966.2010.17434.x.

N. Tetzlaff, B. Dinccel, R. Neuhauser, and V. V. Kovtyukh. The origin of the young pulsar PSR J0826+2637 and its possible former companion HIP 13962. *MNRAS*, 438: 3587–3593, March 2014. doi: 10.1093/mnras/stt2478.

J. K. Truelove, R. I. Klein, C. F. McKee, J. H. Holliman, II, L. H. Howell, and J. A. Greenough. The Jeans Condition: A New Constraint on Spatial Resolution in Simulations of Isothermal Self-gravitational Hydrodynamics. *ApJL*, 489:L179–L183, November 1997. doi: 10.1086/310975.

D. van Buren. Stellar Wind Bow Shocks. In J. P. Cassinelli and E. B. Churchwell, editors, *Massive Stars: Their Lives in the Interstellar Medium*, volume 35 of *Astronomical Society of the Pacific Conference Series*, page 315, January 1993.

E. Vazquez-Semadeni, J. Kim, M. Shadmehri, and J. Ballesteros-Paredes. The Lifetimes and Evolution of Molecular Cloud Cores. *ApJ*, 618:344–359, January 2005. doi: 10.1086/425951.

S. Veilleux, G. Cecil, and J. Bland-Hawthorn. Galactic Winds. *ARAA*, 43:769–826, September 2005. doi: 10.1146/annurev.astro.43.072103.150610.

K. Waagan, C. Federrath, and C. Klingenberg. A robust numerical scheme for highly compressible magnetohydrodynamics: Nonlinear stability, implementation and tests. *Journal of Computational Physics*, 230:3331–3351, May 2011. doi: 10.1016/j.jcp.2011.01.026.

S. Walch and T. Naab. The energy and momentum input of supernova explosions in structured and ionized molecular clouds. *MNRAS*, 451:2757–2771, August 2015. doi: 10.1093/mnras/stv1155.

S. Walch, P. Girichidis, T. Naab, A. Gatto, S. C. O. Glover, R. Wunsch, R. S. Klessen, P. C. Clark, T. Peters, D. Derigs, and C. Baczynski. The SILCC (SImulating the LifeCycle of molecular Clouds) project - I. Chemical evolution of the supernova-driven ISM. *MNRAS*, 454:238–268, November 2015. doi: 10.1093/mnras/stv1975.

B. Wang and Z. Han. Companion stars of type Ia supernovae and hypervelocity stars. *A&A*, 508:L27–L30, December 2009. doi: 10.1051/0004-6361/200913326.

B. Wang and Z. Han. Companion stars of Type Ia supernovae and single low-mass white dwarfs. *MNRAS*, 404:L84–L88, May 2010. doi: 10.1111/j.1745-3933.2010.00840.x.

J. C. Weingartner and B. T. Draine. Dust Grain-Size Distributions and Extinction in the Milky Way, Large Magellanic Cloud, and Small Magellanic Cloud. *ApJ*, 548:296–309, February 2001. doi: 10.1086/318651.

F. P. Wilkin. Exact Analytic Solutions for Stellar Wind Bow Shocks. *ApJL*, 459:L31, March 1996. doi: 10.1086/309939.

C. J. E. Wolf and G. Rayet. Spectroscopie stellaire. *Academie des Sciences Paris Comptes Rendus*, 65:292–296, 1867.

M. G. Wolfire, D. Hollenbach, C. F. McKee, A. G. G. M. Tielens, and E. L. O. Bakes. The neutral atomic phases of the interstellar medium. *ApJ*, 443:152–168, April 1995. doi: 10.1086/175510.

M. G. Wolfire, C. F. McKee, D. Hollenbach, and A. G. G. M. Tielens. Neutral Atomic Phases of the Interstellar Medium in the Galaxy. *ApJ*, 587:278–311, April 2003. doi: 10.1086/368016.

T. Wong and L. Blitz. The Relationship between Gas Content and Star Formation in Molecule-rich Spiral Galaxies. *ApJ*, 569:157–183, April 2002. doi: 10.1086/339287.

D. P. Woody, S. L. Scott, N. Z. Scoville, L. G. Mundy, A. I. Sargent, S. Padin, C. G. Tinney, and C. D. Wilson. Interferometric observations of 1.4 millimeter continuum sources. *ApJL*, 337:L41–L44, February 1989. doi: 10.1086/185374.

T. M. Yoast-Hull, J. E. Everett, J. S. Gallagher, III, and E. G. Zweibel. Winds, Clumps, and Interacting Cosmic Rays in M82. *ApJ*, 768:53, May 2013. doi: 10.1088/0004-637X/768/1/53.

J. S. Young. Molecular clouds in external galaxies and the efficiency of star formation. In M. Peimbert and J. Jugaku, editors, *Star Forming Regions*, volume 115 of *IAU Symposium*, pages 557–583, 1987.

Q. Yu and S. Tremaine. Ejection of Hypervelocity Stars by the (Binary) Black Hole in the Galactic Center. *ApJ*, 599:1129–1138, December 2003. doi: 10.1086/379546.

H. Zinnecker and H. W. Yorke. Toward Understanding Massive Star Formation. *ARA&A*, 45:481–563, September 2007. doi: 10.1146/annurev.astro.44.051905.092549.

B. Zuckerman and N. J. Evans, II. Models of massive molecular clouds. *ApJL*, 192:L149–L152, September 1974. doi: 10.1086/181613.

B. Zuckerman and P. Palmer. Radio radiation from interstellar molecules. *ARAA*, 12:279–313, 1974. doi: 10.1146/annurev.aa.12.090174.001431.

E. G. Zweibel and A. Brandenburg. Current Sheet Formation in the Interstellar Medium. *ApJ*, 478:563–568, March 1997. doi: 10.1086/303824.

Danksagung

I would like to thank in the first place Dr. Thorsten Naab, Dr. Philipp Girichidis and Prof. Dr. Simon White for supervising my work and progress as a PhD student. I am also grateful for the support and useful discussions with my research group, the SILCC collaboration (especially Prof. Dr. Stefanie Walch-Gassner) and to PhD and postdoc community of the Max Planck Institute for Astrophysics.

My special thanks to Dr. Philipp Girichidis for his dedication, patience and help through the years. His guidance will be forever invaluable to me. He is a true model that I look up to.

I would like to also acknowledge the love, understanding, help and support of my family, especially my mother, my sister and Imran.

I am very grateful to my close friends for time spent together, discussions, moral support and proof-reading of this thesis (on short notice): Matteo Frigo, Aoife Boyle, Malin Renneby, Maximilian Eisenreich, Ricard Ardevol, Vlas Sokolov, Talytha Barbosa, Philipp Busch, Andreas Schmidt, Andrea Gatto and Alessandro Ballone.

My long distance friends also kept my spirit high along the way through Skype chats: Krisztian Herman and Salman Hassan Shams.